Investigation of Dipion Final State Interactions in $pp \rightarrow pp\eta[\eta \rightarrow \pi^+\pi^-\gamma]$ with the WASA-at-COSY Facility

Dissertation zur Erlangung des Grades
Doktor der Naturwissenschaften
am Fachbereich für Mathematik und Naturwissenschaften
der Bergischen Universität Wuppertal

vorgelegt von
Daniel Lersch
aus Köln

Oktober 2014

Die Dissertation kann wie folgt zitiert werden:

urn:nbn:de:hbz:468-20150204-112638-3
[http://nbn-resolving.de/urn/resolver.pl?urn=urn%3Anbn%3Ade%3Ahbz%3A468-20150204-112638-3]

To my family, friends and my physics teacher Dr. Zeiske.

Contents

Chapter 1

Abstract and Motivation

1.1 German version

Der Zerfallskanal $\eta \rightarrow \pi^+\pi^-\gamma$ erlaubt Einblicke in den anomalen Sektor der Quanten Chromodynamik, da die Zerfallsstärke dieses Kanals sensitiv zur sogenannten Box Anomalie ist. Diese Anomalie ist Bestandteil des Wess-Zumino-Witten Lagrangians, welcher Mesonenzerfälle im chiralen Grenzfall (d.h. vernachlässigbare Quarkmassen) beschreibt. Allerdings ist dieser chirale Grenzfall im Experiment nicht realisiert und damit ist die Grundvoraussetzung für die Sensitivität von $\eta \rightarrow \pi^+\pi^-\gamma$ zur Box Anomalie nicht mehr gegeben. Ferner wird die Anomalie von Wechselwirkung zwischen den beiden geladenen Pionen dominiert. Diese Wechselwirkungen müssen in der Beschreibung des Zerfalls $\eta \rightarrow \pi^+\pi^-\gamma$ berücksichtigt werden, was durch mehrere theoretische Vorhersagen bewerkstelligt wird [1,2,3,4]. Diese Modelle können im Experiment durch Messung des relativen Verzweigungsverhältnisses zwischen $\eta \rightarrow \pi^+\pi^-\gamma$ und $\eta \rightarrow \pi^+\pi^-\pi^0$ sowie der Energieverteilung des Photons aus $\eta \rightarrow \pi^+\pi^-\gamma$ untersucht bzw. überprüft werden.

Zur Bestimmung dieser beiden Größen gab es verschiedene experimentelle Ansätze (z.B. Messungen der CLEO [5], KLOE [6] und der WASA-at-COSY Kollaboration [7]). Um beide Observablen simultan mit ausreichend statistischer Signifikanz zu bestimmen, wurde der Kanal $\eta \rightarrow \pi^+\pi^-\gamma$ in der Proton-Proton induzierten Reaktion $pp \rightarrow pp\eta[\eta \rightarrow \pi^+\pi^-\gamma]$ am WASA-at-COSY Experiment gemessen. Der WASA Detektor deckt nahezu den gesamten Raumwinkel ab und erlaubt es alle an der Reaktion beteiligten Teilchen inklusive ihrer Energien und Winkel zu rekonstruieren.

Die Hauptaufgabe bei der Analyse von Proton-Proton induzierten η Zerfällen besteht in der Differenzierung zwischen dem eigentlichen η Signal und den Untergrundsignalen aus Multi-Pion Produktionsmechanismen, welche mit der Produktion der η Mesonen einhergehen. Für den vorliegenden Zerfallskanal kommen noch erschwerend Untergrundbeiträge des Referenzkanals $\eta \rightarrow \pi^+\pi^-\pi^0$ hinzu. Dies erfordert eine detaillierte Analyse, in der das $\eta \rightarrow \pi^+\pi^-\gamma$ Signal aus dem oben genannten Untergrund heraus gefiltert werden kann.

Die vorliegende Arbeit befasst sich mit der Analyse des $pp \rightarrow pp\eta$ Datensatz, welcher im Jahr 2010 am WASA-at-COSY Experiment gemessen wurde. Neben der Rekonstruktion des Zerfalls $\eta \rightarrow \pi^+\pi^-\gamma$, die den Hauptanteil dieser Arbeit stellen wird, werden die mit der Analyse einhergehenden systematischen Effekte untersucht und diskutiert. Die in dieser Arbeit erzielten Ergebnisse werden im Rahmen der systematischen Unsicherheiten bewertet und mit bereits existierenden Daten wie auch vorhandenen theoretischen Modellen verglichen.

1.2 English version

The radiative decay $\eta \rightarrow \pi^+\pi^-\gamma$ provides the opportunity to investigate anomalies in Quantum Chromo Dynamics as well as pion final state interactions.
In the limit of vanishing quark masses the decay amplitude of this reaction is solely driven by the box anomaly term which is part of the Wess-Zumino-Witten Lagrangian. However, when going to physical quark masses, the decay amplitude is dominated by pion-pion final state interactions which are described by several theoretical models [1,2,3,4]. The experimental observables to characterise this decay and to test the theoretical models are the relative branching ratio between $\eta \rightarrow \pi^+\pi^-\gamma$ and $\eta \rightarrow \pi^+\pi^-\pi^0$ as well as the photon energy distribution of the single photon in $\eta \rightarrow \pi^+\pi^-\gamma$.
Several experimental efforts have been made (e.g. by the CLEO [5], KLOE [6] and WASA-at-COSY collaboration [7]) in order to determine one of those quantities. In order to measure both observables simultaneously within one data set with high statistics, the reaction $pp \rightarrow pp\eta[\eta \rightarrow \pi^+\pi^-\gamma]$ has been investigated with the WASA-at-COSY facility. The measurement represents a large statistics data set and provides the possibility to determine the relative branching ratio and the photon energy distribution simultaneously. The WASA detector covers nearly the full solid angle and is able to measure all final state particles with their corresponding momenta as well as their angular distributions.
The essential challenge of measuring the decay $\eta \rightarrow \pi^+\pi^-\gamma$ in proton-proton reactions, is to disentangle between: (i) contributions related to this decay, (ii) events stemming from multi-pion-production reactions,which come along with the production of η mesons, and (iii) events related to the decay $\eta \rightarrow \pi^+\pi^-\pi^0$. Thus, a dedicated analysis is needed where the $\eta \rightarrow \pi^+\pi^-\gamma$ signal is filtered out of the background reactions (ii) and (iii).
This work deals with the analysis of the $pp \rightarrow pp\eta$ data set which has been acquired in 2010 with the WASA-at-COSY experiment. Besides the reconstruction of $\eta \rightarrow \pi^+\pi^-\gamma$ events (which will be the major part within this work), systematical errors that come along with the analysis are investigated and discussed. Finally, the achieved results will be interpreted within those errors and compared to previously acquired experimental results and theoretical predictions.

Chapter 2

The decay $\eta \rightarrow \pi^+\pi^-\gamma$

The η-meson is a suitable tool to study symmetry violation processes and to test the standard model on an energy scale of several GeV. Furthermore the decay $\eta \rightarrow \pi^+\pi^-\gamma$ allows to explore the chiral limit of QCD and investigate final state interactions between the two charged pions. This chapter will focus on that specific decay in the framework of QCD and chiral pertubation theory.

2.1 The Standard Model

The Standard Model of particle physics is a fundamental tool to describe particle interactions on a microscopic scale. Phenomena or reactions which are correlated to the electromagnetic, weak or strong interaction (or force) are explained by this model.

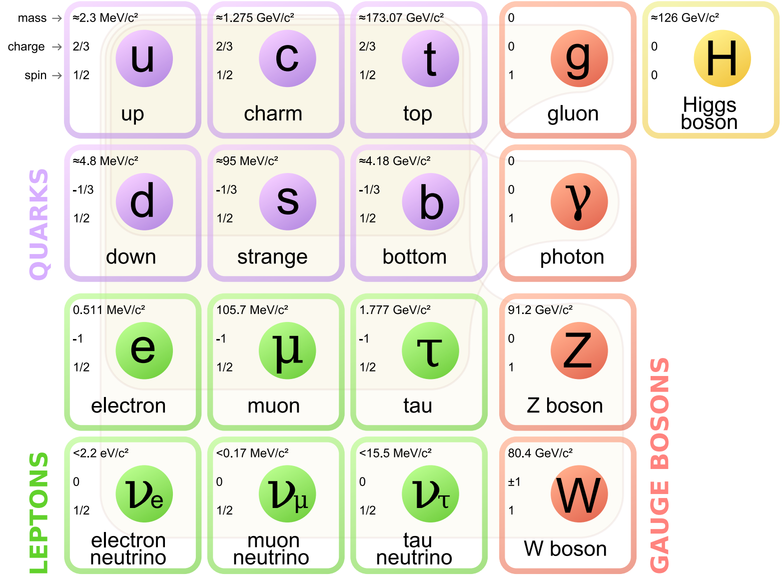

Figure 2.1: *Fundamental particles and force carriers of the Standard Model of particle physics [8].*

The underlying principle of that model is that every fundamental interaction/force between particles is described by the exchange of a boson between them. The electromagnetic interaction between two charged particles, for example, is explained by the exchange of a neutral photon. This (well-known) theory is called Quantum Electrodynamics (QED). The same principle is applied for the weak interaction, where W and Z-bosons are the force carriers. The interaction between quarks (strong interaction) is described by QCD which will be discussed in the next section.

2.2 The QCD Lagrangian

The behaviour of quarks is described by the QCD Lagrangian $\mathscr{L}_{QCD}$ which is derived from the Lagrangian $\mathscr{L}_{free}$ of free quarks including the gauge principle with respect to the SU(3) colour group. This introduces interactions between quarks and gluons and interactions between gluons as well. The Lagrangian $\mathscr{L}_{QCD}$ reads as [9]:

$$\mathscr{L}_{QCD} = \sum_{f=u,d,s,c,b,t} \underbrace{\bar{q}_f(i\gamma^\mu D_\mu - m_f)q_f}_{(I)} \underbrace{-\frac{1}{4}G^a_{\mu\nu}G_{a\mu\nu}}_{(II)} \tag{2.1}$$

where f refers to the quark flavours: up, down, strange, charme, bottom and top (see Fig. 2.1). For each flavour a colour triplet is introduced which leads to the quark field q_f:

$$q_f = \begin{pmatrix} q_{f,1} \\ q_{f,2} \\ q_{f,3} \end{pmatrix} \tag{2.2}$$

The propagation of the quark fields and their interaction with the gluonic fields are summarised in part (I) of Equation 2.1, where $D_\mu = (\partial_\mu + ig_3 A^a_\mu \frac{\lambda^a_{\text{col}}}{2})$ is the covariant derivative. The partial derivative ∂_μ corresponds to the propagation of the quarks. The interaction of the vector potentials A^a_μ results from the applied gauge principle and can be identified with the quark-gluon-interaction. The strong coupling constant is given by g_3 and λ^a_{col} represent the Gell-Mann matrices for the colour.

$G_{a\mu\nu}$ is the field-strength tensor: $G_{a\mu\nu} = \partial_\mu A_{a\mu} - \partial_\nu A_{a\mu} - g_3 f_{abc} A_{b\mu} A_{c\nu}$ with the SU(3) structure constant f_{abc} [a]. The pure gluonic part (i.e. the propagation of gluons and their self-interaction) is described by part (II) respectively. The main difference between this Lagrangian and the QED one is related to the non-abelian term: $-g_3 f_{abc} A_{b\mu} A_{c\nu}$, which describes the interaction between gluons. Since photons do not interact with each other, this term is missing in the QED Lagrangian.

2.2.1 Quark masses and chiral symmetry

The six quark flavours u, d, s, c, b, t might be divided by their masses which is shown in Table 2.1.

Strongly interacting particles observed in the energy regime of $\sim 1\,\text{GeV}$ are hadrons (e.g. protons, neutrons), having the light quarks as constituents. Trying to explain the masses of hadrons by the quark masses leads to a surprising result: The difference between the proton mass and the current quark masses (of the proton), for example, is:

$$m_p \approx 100 \cdot (2m_u + m_d) \tag{2.3}$$

One important question that arises from Eq. 2.3 is, how this large mass difference can be explained. This question is one of the main topics investigated in hadron

---

[a] The values of this constant can be found in [9].

light quarks	mass [GeV]	heavy quarks	mass [GeV]
up	$(2.3^{+0.7}_{-0.5}) \cdot 10^{-3}$	charm	1.275 ± 0.025
down	$(4.8^{+0.5}_{-0.3}) \cdot 10^{-3}$	bottom	4.18 ± 0.03 (MS scheme)
strange	$(95 \pm 5) \cdot 10^{-3}$	top	$173.21 \pm 0.51 \pm 0.71$

Table 2.1: *The six quark flavours and their corresponding current masses [10] are divided into light and heavy particles with respect to the energy of* 1 GeV.

physics. Eq. 2.3 motivates the assumption that QCD phenomena at $\sim 1\,\mathrm{GeV}$ can be described by neglecting the light quark masses: $m_u, m_d, m_s \to 0$, which is called the chiral limit. In that limit the mass and properties of a hadron are described by the interaction of point-like quarks (and gluons).

A vanishing mass m_f in the QCD Lagrangian leads to a decoupling of quarks with a left-handed chiral[b] component $q_{f,L}$ and a right-handed component $q_{f,R}$, respectively. Thus the QCD Lagrangian has global $U(3)_L \times U(3)_R$ symmetry [9] which can be written in:

$$U(3)_L \times U(3)_R = SU(3)_L \times SU(3)_R \times U(1)_V \times U(1)_A \tag{2.4}$$

The invariance of $\mathscr{L}_{QCD}$ under $SU(3)_L \times SU(3)_R$ in the chiral limit is then called chiral symmetry.

2.2.2 The Goldstone Theorem and QCD

Generally speaking the Goldstone Theorem describes the appearance of massless bosons, if a continuous (and global) symmetry is spontaneously broken. This shall be explained in the following example: Consider a rotational invariant system with a potential $V(x, y)$ as shown in Fig. 2.2. The energy of that system shall be bound from below, that means the ground state corresponds to the minima of $V(x, y)$. All minima are located at the radius R_{min} of the so-called Mexican hat in Fig.2.2. Thus, all ground states are degenerated. The rotational invariance of this system holds as long as the potential is at the maximum: $V(x = 0, y = 0)$. Decreasing the energy until one particular ground state of the system is reached (see minimum of the Mexican hat in Fig. 2.2), leads to a breaking of the rotational symmetry. At that point, the Goldstone Theorem states that the spontaneous breakdown of a symmetry in the ground state leads to bosons which are massless in addition to the usual bosons with a mass depending on the quantitative details of the potential. The former are called Goldstone bosons. Looking at Fig. 2.2 again, it is shown that the Goldstone bosons can be interpreted as excitations along the minimum which demand no additional energy. In contrast, excitations perpendicular to the minimum demand energy, which manifests in massive bosons.

According to Noether's Theorem, each symmetry is connected to a conserved current. In a quantum field theory picture this corresponds to a charge operator $\hat{Q}$, which either creates or annihilates states and commutes with the Hamiltonian $\hat{H}$. Thus, each symmetry operation $\hat{U}$ is connected to a set of those operators:

$$\hat{U} = \exp\{i \sum_k \alpha_k \hat{Q}_k\} \tag{2.5}$$

---

[b] For massless particles, chirality might be interpreted as helicity. Particles with a spin parallel/anti-parallel to their momentum are called right/left-handed.

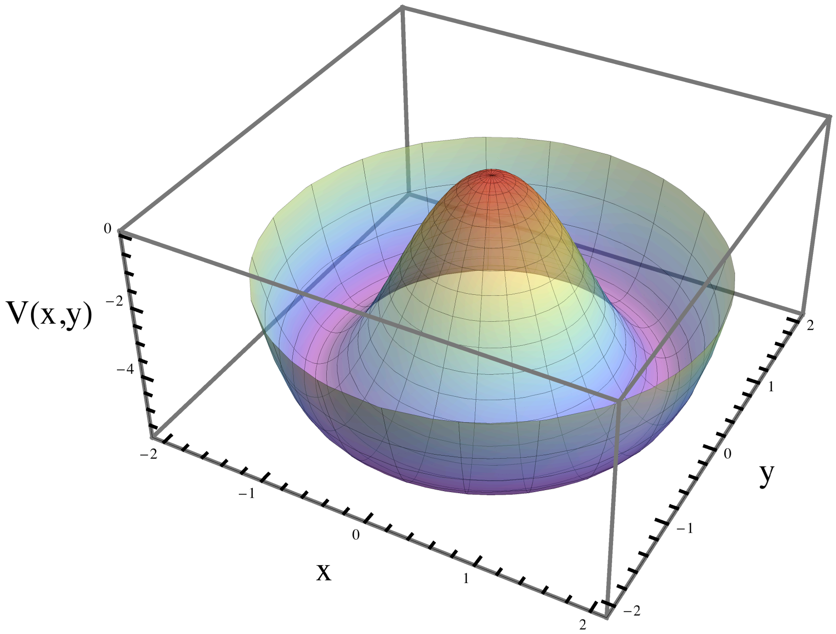

Figure 2.2: *Plot of a Mexican hat potential:* $V(x,y) = \frac{\lambda}{4}(x^2+y^2)^2 + m^2 \cdot (x^2+y^2)$*, with* $m^2 < 0$*. The minima of* V *are located at the radius* $R_{min} = \sqrt{\frac{-2m^2}{\lambda}}$*.*

and fulfills the conditions (according to $[\hat{Q}_k, \hat{H}] = 0$):

$$\hat{U}\hat{H}\hat{U}^\dagger = \hat{H} \tag{2.6}$$

$$\hat{U}\hat{U}^\dagger = \mathbf{1} \tag{2.7}$$

Two states A and B which are connected by such a transformation: $\hat{U}|A\rangle = |B\rangle$ have the energies:

$$E_A = \langle A|\hat{H}|A\rangle = \langle A|\hat{U}^\dagger\hat{U}\hat{H}\hat{U}^\dagger\hat{U}|A\rangle = \langle B|\hat{H}|B\rangle = E_B \tag{2.8}$$

Every state that can be reached from A by a symmetry transformation $\hat{U}$ has the same energy. If A is now identified with the vacuum ground state $|0\rangle$, Eq. 2.8 shows that all states B are degenerate with the vacuum. In case of spontaneous symmetry breaking the ground state is no longer invariant under a symmetry transformation which means that there is at least one operator $\hat{Q}_k$ with: $\hat{Q}_k|0\rangle \neq 0$. The vacuum state is said to be broken. Every operator, that breaks the vacuum, leads to a massless Goldstone boson. The global symmetry of the QCD Lagrangian in the chiral limit is chiral symmetry. The corresponding symmetry operation $\hat{U}_{L/R}$ on left-handed (L) and right handed (R) quark fields is given by [9]:

$$\hat{U}_{L/R} = \exp\Big(-i \cdot \sum_{a=1}^{8} \Theta_{L/R,a} \frac{\lambda^a_{\text{col}}}{2} \Big) \cdot e^{-i\Theta_{L/R}} \tag{2.9}$$

where λ^a_{col} represent the Gell-Mann matrices and $\Theta_{R/L,a}$ denotes a smooth real function in Minkowski space. If this symmetry would hold for ground states, one should observe parity doubles which are characterised by particles with same quantum numbers, same mass but opposite parity. Table 2.2 shows two examples of such parity pairs observed in nature.

Particle	Parity P	Momentum I	Mass $[MeV]$
p	$+$	$1/2$	938.27
$N(1535)$	$-$	$1/2$	$1,535$
$a_1(1260)$	$+$	1	$1,230$
ρ	$-$	1	775.26

Table 2.2: *Parity doubles of observed/measured nucleons and mesons [10].*

If chiral symmetry would be present, all pairs should have the same mass, which is not the case. This is an indication that the chiral symmetry is spontaneously broken and there must be a certain number of Goldstone bosons. According to Eq. 2.9, there are 16 generators (2 × 8 Gell-Mann-matrices) of the chiral symmetry group: $SU(3)_L \times SU(3)_R$. Due to the spontaneous symmetry breaking the ground state is still invariant under $S(3)_{L+R} = SU(3)_V$. This group has 8 generators which leave the vacuum invariant. This implies that there are $16 - 8 = 8$ massless Goldstone bosons. They are identified as the 8 lightest pseudoscalar mesons [9]: $\pi^+, \pi^-, \pi^0, \eta, K^+, K^-, K^0$ and $\bar{K}^0$.

In reality those mesons are not massless at all, because quarks do have a (small) mass which leads to an explicit symmetry breaking. And yet the Goldstone theorem still applies, with the difference, that the Goldstone bosons have a small mass and interact with each other. This will be of importance when discussing the decay dynamics of $\eta \to \pi^+\pi^-\gamma$.

The spontaneous breaking of the chiral symmetry leads to the abundance of light mesons (baryons) and thus explains part of the hadron spectrum observed in nature.

2.3 The η-meson

It has been shown in the last section, that the lightest mesons can be identified with the Goldstone bosons which occur due to the spontaneous break down of the chiral symmetry. In this picture they are related to the quark condensate $\langle 0|\bar{q}q|0\rangle$. Following the $SU(3)$ flavour symmetry of QCD, which has been discussed in Section 2.2, the three lightest quarks (u, d, s) allow for nine combinations and are grouped into an octet and a singlet: $3 \bigotimes \bar{3} = 8 \bigoplus 1$ (see Fig. 2.3).

The η-meson observed in nature is a linear combination of the octet and singlet states [10]:

$$\begin{aligned}
\eta_{\text{octet}} &= \frac{1}{\sqrt{6}} \cdot (u\bar{u} + d\bar{d} - 2s\bar{s}) && (2.10)\\
\eta_{\text{singlet}} &= \frac{1}{\sqrt{3}} \cdot (u\bar{u} + d\bar{d} + s\bar{s}) && (2.11)\\
\eta &= \cos(\theta) \cdot \eta_{\text{octet}} - \sin(\theta) \cdot \eta_{\text{single}} && (2.12)\\
& && (2.13)
\end{aligned}$$

The mixing angle θ between the two states is experimentally given by: $\theta = (-15.5 \pm 1.3)^\circ$ [12]. The η-meson has a mass of (547.862 ± 0.018)MeV [10] and a mean lifetime of $\approx 5 \cdot 10^{-19}$s (corresponding to the decay width of $\Gamma_\eta = (1.31 \pm 0.05)\,\text{keV}$ [10]).

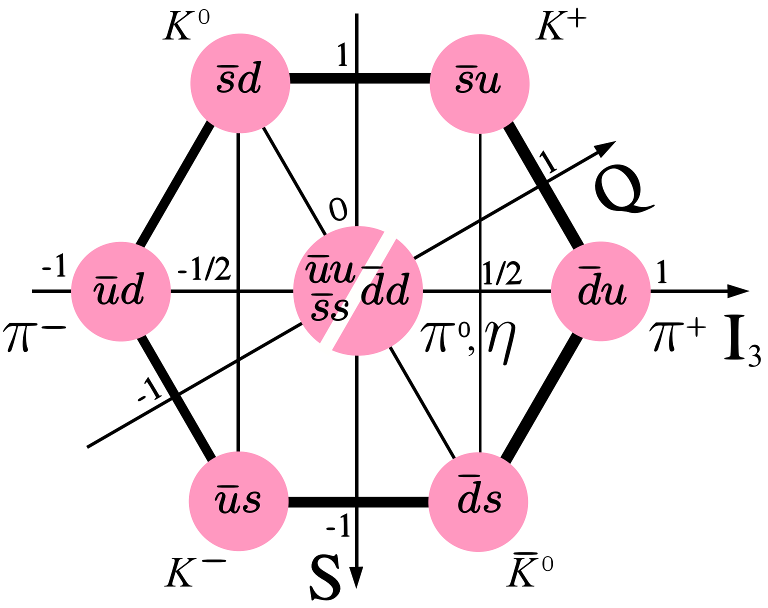

Figure 2.3: *The arrangement of the eight mesons with respect to the z-component of the isospin I_3 (x-axis), the charge Q (y-axis) and strangeness S (z-axis) form the $SU(3)$ octet [11]. The axes are related by the Gell-Mann-Nishijam-Relation [10]: $Q = e \cdot \left[I_3 + \frac{1}{2} \cdot (B + S + C)\right]$ where B is the baryon number and C the charm number.*

2.3.1 Quantum numbers

The parity P of a two particle system is given by: $P(1,2) = p_1 p_2 \cdot (-1)^\ell$ where p_1,p_2 are the eigen-parities of particle 1,2 and ℓ is the relative momentum [13]. According to Dirac, fermions and anti-fermions have an opposite parity. This leads to the total parity of a meson:

$$P(q, \bar{q}) = p_q p_{\bar{q}} \cdot (-1)^\ell = -1 \cdot (-1)^\ell = (-1)^{\ell+1} \tag{2.14}$$

The spins of the two quarks can be aligned parallel or antiparallel. Thus the relative spin s of the two quarks can only take the value 0 or 1. The charge conjugation C of a meson is then given by [13]:

$$C = (-1)^{\ell+s} \tag{2.15}$$

The total spin J of the meson is defined by the following limitations:

$$|\ell - s| \leq J \leq |\ell + s| \tag{2.16}$$

Including the total isospin I, the G-parity of a meson reads as [13]:

$$G = (-1)^{\ell+s+I} \tag{2.17}$$

Using Equations 2.14 to 2.16 and the limitation for s helps to calculate all possible meson states which are denoted by J^{PC}. For example all states with $P = +1$ and $C = -1$ have to have $\ell = 1, 3, 5, ...$ and $s = 0$. According to Equation 2.16 the total spin is given by: $J = \ell = 1, 3, 5, ...$ This leads to the meson states: $1^{+-}, 3^{+-}, etc.$. Other meson multiplets which are in accordance with the quark

P	C	Restriction on ℓ	Restriction on s	J^{PC}
-1	$+1$	$0, 2, 4, ...$	0	$0^{-+}, 2^{-+}, 4^{-+}, ..$
-1	-1	$0, 2, 4, ...$	1	$\lvert\ell+1\rvert^{--}, ..., \lvert\ell-1\rvert^{--}$
$+1$	-1	$1, 3, 5, ...$	0	$1^{+-}, 3^{+-}, 5^{+-}, ..$
$+1$	$+1$	$1, 3, 5, ...$	1	$\lvert\ell+1\rvert^{++}, ..., \lvert\ell-1\rvert^{++}$

Table 2.3: *Possible quantum numbers for a $q\bar{q}$-system. The limitations of the relative / total spin s / J, lead to a restriction on the allowed J^{PC} meson-multiplets.*

model mentioned above, are listed in Table 2.3. According to that table the meson states $J^{PC} = 0^{--}, 1^{-+}, 3^{-+}, 5^{-+}, 0^{+-}, 2^{+-}, 4^{+-}$, *etc.* are forbidden as $q\bar{q}$ states and this leads to a limitation of allowed particle decays, if C or CP-invariance is realised. The η-meson has $\ell = s = 0$ and is therefore called a **pseudoscalar** with $J^{PC} = 0^{-+}$. An alignment of the quark spins to $s = 1$ would cost more energy. This increases the mass of the $q\bar{q}$-system and leads to a particle with $J^{PC} = 1^{--}$ which is the $\rho(770)$-meson. Particles with $J^{PC} = 1^{--}$ are called **vector mesons**.

2.3.2 η-decays

The η-meson is a C, P, G and CP eigenstate with eigenvalues: $C(\eta) = +1$, $P(\eta) = -1$, $G(\eta) = 1$ and $CP(\eta) = -1$. The lifetime of the η-meson is quite long compared to other mesons, like the ω-meson with a life time of $(7.75 \pm 0.07) \cdot 10^{-23}$s. This is due to the fact that all electromagnetic and strong decays are forbidden or suppressed in lowest order by C-, P-, G- or CP-violation. In this context some decays will be discussed briefly:

- All electromagnetic decays with an odd number of decay photons, like $\eta \rightarrow \gamma\gamma\gamma$ or $\eta \rightarrow \pi^0\gamma$, are forbidden by conservation of C-parity, because $C(\eta) = 1$, but $C(n\gamma) = (-1)^n$.

- All strong decays, such as $\eta \rightarrow \pi^+\pi^-$, are forbidden to first order. The η-meson has an orbital angular momentum $\ell = 0$ which leads to a parity -1. The two pion-system has a parity: $P(\pi^+\pi^-) = p_{\pi^+}p_{\pi^-} \cdot (-1)^\ell = (-1)^\ell$. In order to conserve parity, the relative angular momentum of the two pions has to be odd which is in contrast to momentum conservation of $\ell = 0$. Thus the decay $\eta \rightarrow \pi^+\pi^-$ is suppressed because of P-violation (and also CP-violation).

- The charged decay $\eta \rightarrow \pi^+\pi^-\pi^0$ is forbidden in first order because it violates G-Parity. However, this decay is observed in nature because its decay amplitude is proportional to the non-zero quark mass difference $(m_u - m_d)$ [1, 14].

- The radiative decay $\eta \rightarrow \pi^+\pi^-\gamma$ is C-conserving [10]: The η-meson has the C-eigenvalue: $C(\eta) = 1$ and the C-eigenvalue for the single photon is $C(\gamma) = -1$. The two-pion system has: $C(\pi^+\pi^-) = (-1)^\ell$. According to that, C-invariance is only given for odd ℓ-values[c]. However, states with $\ell > 1$ are suppressed with respect to $\ell = 1$. The CP-eigenvalue of η is -1. The two pions have $CP(\pi^+\pi^-) = (-1)^{2\ell}$. As shown before, the relative momentum ℓ is odd, which leads to $CP(\pi^+\pi^-) = 1$. The photon has P-eigenvalues which are either $(-1)^j$ for electric E_j or $(-1)^{j+1}$ for magnetic M_j transitions. According to that,

---

[c] There might be a relative momentum between the photon and the $\pi^+\pi^-$ system. Therefore $\ell = 3, 5, ..$ could also be realised.

> the reaction $\eta \to \pi^+\pi^-\gamma$ is CP-conserving for M_1 and E_2 transitions and CP-violating for E_1 transitions respectively. All those processes contribute to the decay mechanism, which leads to the comparable low branching ratio (see Table 2.4), because some of the transitions are suppressed by CP-violation. On the other hand this decay could be a suitable tool to investigate CP-violation in case of an E_1 transition. But the information about the transition and thus about the CP-violation, is hidden in the polarisation of the single photon. This observable is difficult to measure within an experiment. However there is the possibility, that the single photon is virtual and decays into a dilepton-pair: $\gamma^* \to e^+e^-$. This leads to a different η-decay: $\eta \to \pi^+\pi^-e^+e^-$ which is experimentally accessible. The observable in that case would be the angle between the $\pi^+\pi^-$ and e^+e^- planes [10].

A collection of charged η-decays is summarised in Table 2.4. The gap between the first and last groups of rows separates common from rare decay modes (according to the branching ratio). Since most η-decays are forbidden/suppressed in lowest order it is possible to investigate higher order processes (e.g. the triangle anomaly). Furthermore it is possible to examine C-, or CP-violation phenomena (see Table 2.4). This makes the η-meson a suitable tool to investigate symmetry breaking phenomena as well as quantum anomalies in a low energy regime $\sim$ 1 GeV. The issues related to the decay $\eta \to \pi^+\pi^-\gamma$ (highlighted in red in Table 2.4) will be discussed in the following section.

Decay mode	Ratio $\Gamma(\eta \to ...)/\Gamma_\eta$	Issue
$\eta \to \pi^+\pi^-\pi^0$	$(22.92 \pm 0.28)\%$	Dalitz plot parameter, quark masses
$\eta \to \pi^+\pi^-\gamma$	$(4.22 \pm 0.08)\%$	Box anomaly, $\pi^+\pi^-$-interaction
$\eta \to e^+e^-\gamma$	$(0.69 \pm 0.04)\%$	Single-off-shell transition form factor
$\eta \to \pi^+\pi^-e^+e^-$	$(2.68 \pm 0.11) \cdot 10^{-4}$	CP-violation
$\eta \to e^+e^-e^+e^-$	$(2.40 \pm 0.22) \cdot 10^{-5}$	Double-off-shell transition form factor
$\eta \to e^+e^-\pi^0$	$< 4 \cdot 10^{-5}$	C-violation
$\eta \to e^+e^-$	$< 5.6 \cdot 10^{-6}$	Physics beyond the standard model

Table 2.4: *Summary of a fraction of charged η-decay modes with related physics issues. The decays are ordered according to their branching ratio [10].*

2.4 The anomalous sector of QCD

As explained in Section 2.2.1, the quark fields can be separated into right- and left-handed fields, if quark masses are neglected. According to Noether's Theorem, each symmetry is associated with a conserved current. In case of the chiral symmetry, two currents are present. The first one is called vector current:

$$V_\mu = R_\mu + L_\mu \tag{2.18}$$

where all left-handed and all right-handed quarks are transformed by the same phase. This current is conserved, which leads to conservation of the baryon number B [9]. The second current is called axial current:

$$A_\mu = R_\mu - L_\mu \tag{2.19}$$

where all left-handed quark fields are transformed with the same phase opposite to all right-handed quark fields. On a classical level, this current would be conserved, which is not the case when going to quantum fields. Those non-zero terms are so called quantum anomalies, because they occur due to the quantisation of a classical theory. The charge operators of the vector currents leave the QCD vacuum invariant, whereas the corresponding operators for the axial current do not. These are exactly those eight (spontaneously broken) generators which are responsible for the eight Goldstone bosons / light mesons [9].

2.4.1 ChPT and the effective Lagrangian

The most general QCD Lagrangian, discussed in Section 2.2, describes the interaction between quarks and gluons. In a low energy regime $\lesssim$ 1GeV, only light quarks with vanishing masses are present (compare Table 2.1). Left- and right-handed quark fields are decoupled and the Lagrangian underlies the global $SU(3)_L \times SU(3)_R$ chiral symmetry. This symmetry is broken in the ground state by axial transformations which lead to 8 massless Goldstone bosons: (π, K, η). Hence for low energies, the whole system can be described by the light mesons and their interactions instead of the more fundamental quarks and gluons. This is done by Chiral Pertubation Theory (ChPT) which is in fact, the effective low-energy theory of QCD including the chiral symmetry properties of QCD [9]. Effective Field Theories (EFT) are used to describe a physical system at low energies (low compared to a certain scale) including the underlying fundamental theory. Consequently, instead of applying the full theory (valid for all energy scales) on that system, the theory is restricted to the low-energy domain of interest. Thus at low-energies, a detailed understanding / description of the theory at large energies is not necessary.
This leads to an effective Lagrangian, using different degrees of freedom than the underlying ones, but having the same symmetry properties. In case of low-energy QCD, the *effective* low-energy degrees of freedom are not the fundamental quarks and gluons anymore but the lightest pseudoscalar mesons:

$$\mathscr{L}_{QCD}(q, \bar{q}, g) \to \mathscr{L}_{eff}(\pi, K, \eta) = \sum_N \mathscr{L}_{2N}(U) \tag{2.20}$$

The effective (and most general) Lagrangian shown in Equation 2.20 is written in terms of increasing derivatives of U. Their number has to be even, because of parity conservation [9]. The matrix U is given by [9]:

$$U(\Phi) = \exp\left(\frac{i\Phi}{F_\pi}\right) \tag{2.21}$$

F_π is the pion-decay constant and the matrix Φ includes exactly the eight Goldstone bosons [9]:

$$\Phi = \begin{pmatrix} \pi^0 + \frac{1}{\sqrt{3}}\eta & \sqrt{2}\pi^+ & \sqrt{2}K^+ \\ \sqrt{2}\pi^- & -\pi^0 + \frac{1}{\sqrt{3}}\eta & \sqrt{2}K^0 \\ \sqrt{2}K^- & \sqrt{2}\bar{K}^0 & -\frac{2}{\sqrt{3}}\eta \end{pmatrix} \tag{2.22}$$

By definition of $U(\Phi)$, the Lagrangian shown in Equation 2.20 is consistent with the chiral symmetry.

2.4.2 The box anomaly

Looking at the decay $\eta \to \pi^+\pi^-\gamma$, shows that there are three light mesons (η, π^+, π^-) and one photon involved. By partial conservation of the axial current, the pseudoscalar mesons can be related to axial currents. The divergence of the latter might be affected by the chiral anomaly. The photon on the other hand is correlated to a vector current and couples to the light mesons. Within the framework of current algebra, the coupling of (axial/vector) currents has been investigated by J. Wess, B. Zumino and E. Witten and are summarised in the Wess-Zumino-Witten Lagrangian L_{WZW} [15, 16]. This Lagrangian incorporates all interactions of dimension four between axial currents and vector currents and thus all anomalies of QCD. Taking Eq. 2.20 into account leads to the effective Lagrangian [15,16]:

$$\mathscr{L} = \underbrace{\frac{F_\pi^2}{16} \cdot \int d^4x Tr[D_\mu U D_\mu U^\dagger]}_{(I)} + n \cdot \overbrace{[\underbrace{\Gamma}_{(II)} + \underbrace{\Gamma_A}_{(III)}]}^{=L_{WZW}} \tag{2.23}$$

The features of Eq. 2.23 shall be discussed in the following [9,15,16]:

(I) This is the lowest order effective Lagrangian as shown in Eq. 2.20 with only two derivatives of U. The photon introduces a field A_μ which couples to the mesons. In order to keep the Lagrangian invariant under global charge rotations, the derivative $\partial_\mu U$ has to be changed to; $D_\mu U = \partial_\mu U - ieA_\mu^a[Q, U]$, where Q represents the quark charge matrix. In principle, this term describes the propagation of the Goldstone bosons through space.

(II) Γ refers to the Wess-Zumino-Witten Lagrangian (in the absence of external fields) and is given by [15,16] :

$$\Gamma = \frac{1}{240\pi^2 F_\pi^5} \cdot \int d^4x \epsilon^{\mu\nu\alpha\beta} Tr[\Phi \partial_\mu \Phi \partial_\nu \Phi \partial_\alpha \Phi \partial_\beta \Phi] + \text{higher orders} \tag{2.24}$$

Φ is the matrix from Eq. 2.22. Γ contains five fields of Φ and describes the coupling of five axial currents / light mesons. In the chiral limit, this term is related to the process: $K^+K^- \rightarrow \pi^+\pi^-\pi^0$, also known as the quintangle anomaly.

(III) In the presence of an electromagnetic field, the term Γ is extended by the final term Γ_A [16], which reads as:

$$\Gamma_A = \frac{1}{48\pi^2} \epsilon^{\mu\nu\alpha\beta} \cdot \int d^4x \Big[eA_\mu \cdot Tr(Q(R_\nu R_\alpha R_\beta + L_\nu L_\alpha L_\beta)$$
$$-ie^2(\partial_\mu A_\nu)A_\alpha \cdot 2Tr\Big(Q^2(R_\beta + L_\beta) + \frac{1}{2} \cdot (QU^\dagger QUR_\beta + QUQU^\dagger L_\beta)\Big)\Big] \tag{2.25}$$

With the electromagnetic field: A_μ, the quark charge matrix Q and:
$R_\mu = (\partial_\mu U)U^\dagger$, $L_\mu = U^\dagger \partial_\mu U$.

The third term of Eq. 2.23 describes the coupling between the mesons, which are represented by U, and the photon, represented by A. Because of the existence of an electromagnetic field, the quark charges have to be taken in to account. This is done by including the quark charge matrix Q. The number n is an integer, which can be identified with the number of quark colours N_c, when matching these terms to the anomalies calculated in terms of quarks and gluons. The corresponding QCD anomalies, that are described by Γ_A are presented in Fig. 2.4 and will be discussed in the following. It should be mentioned, that also the coupling to external fields different to electromagnetism can be (with restrictions) included [9,16]. From

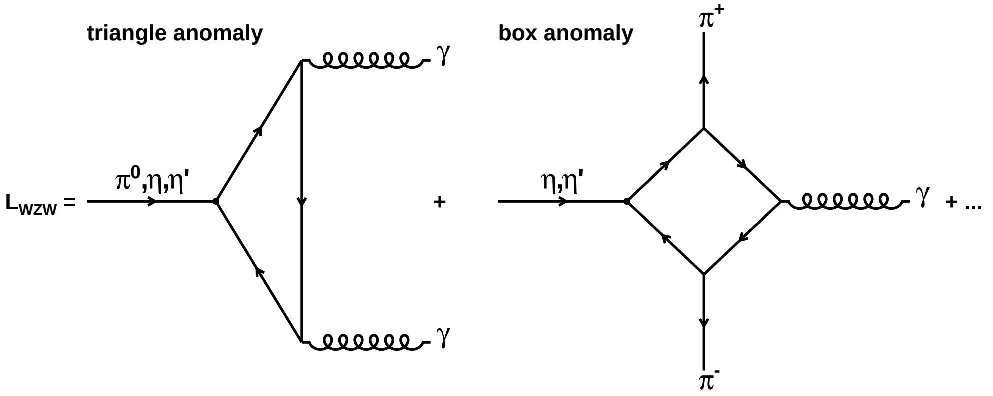

Figure 2.4: *Schematic description of the anomalous part of the Wess-Zumino-Witten Lagrangian L_{WZW} by showing Feynman diagrams for the triangle and box anomaly. The triangle anomaly is responsible for decays: $(\pi^0, \eta, \eta') \to \gamma\gamma$. The box anomaly describes (in the chiral limit) the decays: $(\eta, \eta') \to \pi^+\pi^-\gamma$.*

Eq. 2.23 several Lagrangians dedicated to certain decays can now be calculated. For example the decay: $\pi^0 \to \gamma\gamma$ is described by [9]:

$$\mathscr{L}_{\pi^0\gamma\gamma} = -\frac{n}{N_c}\frac{e^2}{32\pi^2}\epsilon^{\mu\nu\rho\sigma}F_{\mu\nu}F_{\rho\sigma}\frac{\pi^0}{F_\pi^2} \tag{2.26}$$

Eq. 2.26 contains only the electromagnetic field strength tensor, because all decay particles are photons. π^0 denotes the neutral pion from Eq. 2.22. N_c denotes the number of quark colours. The Lagrangian for $\eta \to \pi^+\pi^-\gamma$ has the form [9]:

$$\mathscr{L}_{\eta\pi^+\pi^-\gamma} = \frac{ien}{12\sqrt{3}\pi^2F_\pi^3} \cdot \epsilon^{\mu\nu\rho\sigma}A_\mu\partial_\nu\eta\partial_\rho\pi^+\partial_\sigma\pi^- \tag{2.27}$$

Again, the coupling between the photon (A_μ) and the three mesons: η, π^+, π^- can instantly be recognised. The corresponding Feynman diagrams to Eq. 2.26 and 2.27 are shown in Fig. 2.4. Due to the shape, the Feynman diagram for $(\pi^0, \eta, \eta') \to \gamma\gamma$ is called the triangle anomaly. The corresponding diagram for $(\eta, \eta') \to \pi^+\pi^-\gamma$ is called the box anomaly.

The decay amplitude $A_{\eta\to\pi^+\pi^-\gamma}(0,0,0)$ of the decay mode $\eta \to \pi^+\pi^-\gamma$ is (in the chiral limit) solely determined by the box anomaly term and thus directly correlated to Eq. 2.27 [1]:

$$A_{\eta\to\pi^+\pi^-\gamma}(0,0,0) = \frac{eN_c}{12\sqrt{3}\pi^2F_\pi^3} \cdot \left(\frac{F_\pi}{F_8}\cos\theta - \sqrt{2}\frac{F_\pi}{F_0}\sin\theta\right)\epsilon^{\mu\nu\rho\sigma}\epsilon^*_\mu p^+_\nu p^-_\rho k^\gamma_\sigma \tag{2.28}$$

$p_\pm$ are the momenta of the two charged pions and k^γ denotes the photon momentum, which has the polarisation ϵ^*. The η-meson is described by the decay constants F_0 and F_8 for the single and octet η states, which are coupled by the mixing angle θ.

2.4.3 Final state interactions

When going to physical meson masses, i.e. leaving the chiral limit, the Goldstone bosons gain a finite mass and may also interact with each other. This introduces final state interactions between the two pions in the decay $\eta \to \pi^+\pi^-\gamma$.

On the other hand, the interaction between two charged pions can be described by the exchange of vector mesons V, which have the same quantum numbers J^{PC} as photons (see Tab. 2.3). According to that, the real photon is replaced by a (virtual) vector meson, which directly decays into hadrons (e.g. the two pions). This effect is described by the Vector Meson Dominance (VMD) model [17]: A photon couples to hadrons via an intermediate vector meson. By taking this into account, the triangle anomaly might be rewritten as: $\eta \to \gamma V[V \to \pi^+\pi^-]$ with V being the vector meson. Thus, a decay which was originally driven by the triangle anomaly ends up with the same final state particles (see Fig. 2.5), as the decay $\eta \to \pi^+\pi^-\gamma$, which is driven by the box anomaly. Hence, contributions coming from the triangle or box anomaly are indistinguishable. It turns out, that for physical meson masses the box anomaly is dominated by the triangle anomaly because of final state interactions between the two pions. Besides the scenario shown in Fig. 2.5, the two pions of the box anomaly term might rescatter and thus contribute to final state interactions of the pions. A first indication for the presence of pion interactions can be seen by comparing the calculated decay width: $\Gamma^{\mathrm{calc}}(\eta \to \pi^+\pi^-\gamma) = 35.7\,\mathrm{eV}$ [1] with the experimental width: $\Gamma^{\mathrm{exp}}(\eta \to \pi^+\pi^-\gamma) = (55 \pm 2)\,\mathrm{eV}$ [10].

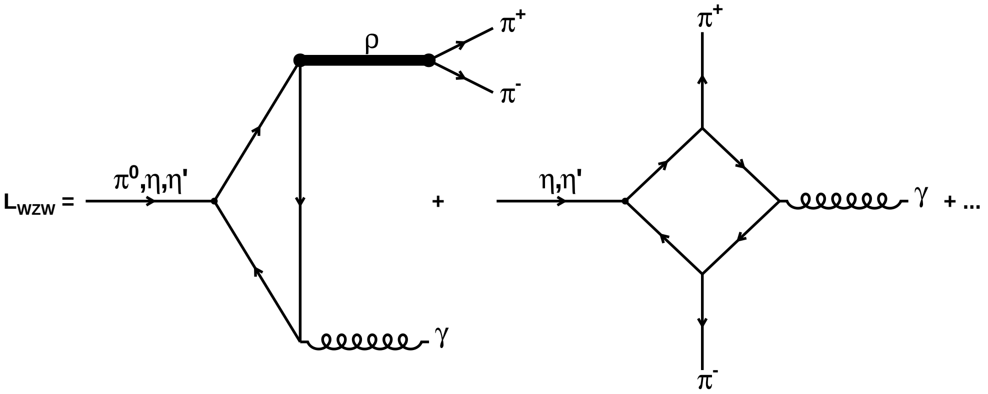

Figure 2.5: Same schematic representation as shown in Fig. 2.4. In this scenario, one photon stemming from the triangle anomaly is replaced by a virtual ρ-meson, which decays into two charged pions [18].

In order to overcome this discrepancy, the Lagrangian L_{WZW} has to be extended by including those final state interactions. For that purpose, several theoretical models are at hand. Three of them shall be described briefly in the following.

a) The pion final state interactions are taken into account within this approach by considering contributions from vector meson dominance as well as one-loop chiral corrections [1]. This leads to a modification of Eq. 2.28 by a form factor having an N/D structure [1]: $\left(1-c+c\cdot\frac{1+as_{\pi\pi}}{D_1(s_{\pi\pi})}\right)$. This factor comprises P-wave $\pi\pi$ scattering phase shifts, which are incorporated via the Omnes function $D_1(s_{\pi\pi})$ (this expression might be identified with the pion loop correction). The parameters c, a are set to be $c = 1$ and $a = \frac{1}{2m_\rho^2}$ [1]. The variable $s_{\pi\pi}$ denotes the dipion invariant mass squared, which would be zero in the chiral limit (where both the η and the pion masses vanish). The modified decay width using this approach reads as: $\Gamma^{N/D}(\eta \to \pi^+\pi^-\gamma) = 65.7\,\mathrm{eV}$.

b) Another approach is given by using the Hidden Local Symmetries (HLS) model [2], which basically describes $\gamma - V$ transitions. Within this model, the effective Lagrangian incorporates L_{WZW} and additional vector meson dominance terms. For instance, one of those terms describes the coupling of two vector mesons with one pseudoscalar meson (e.g. $\eta \to VV$). The resulting decay width is given by: $\Gamma^{HLS}(\eta \to \pi^+\pi^-\gamma) = (56.3 \pm 1.7)\,\mathrm{eV}$.

c) The third and last model discussed here comprises pion loop corrections and higher order momenta $O(p^6)$ [3] (the box anomaly term is of the order $O(p^4)$) in order to correct Eq. 2.28. This leads to the decay width $\Gamma^{O(p^6)+1-\mathrm{loop}}(\eta \to \pi^+\pi^-\gamma) = 47\,\mathrm{eV}$.

All theoretical approaches presented above result in a modification of the decay amplitude by multiplying it with a form factor, which depends on the underlying model.

A different approach to describe final state interactions, without using an explicit model, has been developed recently [4]. Basically, the decay amplitude in Eq. 2.28 is multiplied by the pion vector form factor $F_{PV}(s_{\pi\pi})$ and a polynomial in the squared invariant mass $s_{\pi\pi}$ of the two pion system [4]:

$$|A_{\eta\to\pi^+\pi^-\gamma}(s_{\pi\pi})|^2 = |\underbrace{(1+\delta)}_{\equiv f_S} \cdot A_{\eta\to\pi^+\pi^-\gamma}(0,0,0) \cdot F_{PV}(s_{\pi\pi}) \cdot (1+\alpha\cdot s_{\pi\pi})|^2 \tag{2.29}$$

The pion vector form factor describes the interaction between two (final state) pions, independent of the underlying reaction mechanism. Hence, this factor is applicable for any reaction, including pions. The linear term $(1+\alpha s_{\pi\pi})$ on the contrary, is reaction specific and has to be determined for each decay individually. The parameter α indicates how large the contribution from final state interactions (i.e. $s_{\pi\pi}$) is and can be obtained from fitting Eq. 2.29 to experimental data. The constant δ is chosen such, that the partial decay width fits the PDG value [4]. By comparing this equation with different theoretical models (e.g. VMD, pion loop correction, etc.), different α- and δ- parameters can be found and compared to the α- / δ- parameter found in data. This might point out which model is, to some extent, suitable for including final state interactions for the reaction $\eta \to \pi^+\pi^-\gamma$.

The scaling factor $(1+\delta)$ in Eq. 2.29 will be called f_S in the following.

2.5 Experimental observables and recent measurements

An experimental access to test the validity of the models explained in the previous section, is given by measuring the observables of $\eta \to \pi^+\pi^-\gamma$, which are: (i) The relative branching ratio $\frac{\Gamma(\eta\to\pi^+\pi^-\gamma)}{\Gamma(\eta\to\pi^+\pi^-\pi^0)}$ and (ii) The energy distribution E_γ of the photon in the η-rest frame. Observable (ii) is correlated to the Dalitz plot [d] of $\eta \to \pi^+\pi^-\gamma$, which represents the decay dynamics (see Fig. 2.7).

2.5.1 Relative branching ratio

The recent measurements of the relative branching ratio as well as the theoretical predicted values, according to the models discussed above, are summarised in Table 2.5. The errors of the ratio quoted for the KLOE and CLEO collaboration

---

[d] The Dalitz plot variables are given by any two combinations of the two invariant mass squared of $\pi^\pm$ and γ.

represent the sum of the statistical and systematical error. The theoretical values for the relative branching ratio have been determined according to:

$$\frac{\Gamma(\eta \to \pi^+\pi^-\gamma)}{\Gamma(\eta \to \pi^+\pi^-\pi^0)}(theor) = \frac{\Gamma^{theor}(\eta \to \pi^+\pi^-\gamma)}{\Gamma_\eta(PDG) \cdot \frac{\Gamma(\eta\to\pi^+\pi^-\pi^0)}{\Gamma_\eta}(PDG)} \tag{2.30}$$

$\Gamma^{theor}(\eta \to \pi^+\pi^-\gamma)$ corresponds to the predicted decay widths, which have been presented in items a) to c) in Section 2.4.3. The remaining values refer to the actual PDG values given in [10]. The errors of the theoretical ratios have been calculated accordingly. According to Table 2.5, the experimental results for the relative branching ratio might be split into two groups. The first group refers to the results of Gormley and Thaler et al. [19, 20], with ratios $\gtrsim 0.2$. The second group, based on the results from the CLEO and KLOE collaboration [5, 6], is in favour of ratios < 0.19. The results of the latter group define the actual PDG value. From a theoretical point of view, the HLS model would describe the recent results, whereas the N/D model would confirm the observation made by Gormley and Thaler.

Experiment / Theory	Relative branching ratio
Gormley et al. [19]	0.202 ± 0.006
Thaler et al. [20]	0.209 ± 0.004
CLEO [5]	0.175 ± 0.013
KLOE [6]	0.1856 ± 0.003
PDG [10]	0.1847 ± 0.003
N/D [1]	0.2188 ± 0.0088
HLS [2]	0.1875 ± 0.0094
$O(p^6) + 1 - \text{loop}$ [3]	0.1565 ± 0.0063
Box anomaly only [1]	0.119 ± 0.0048

Table 2.5: *Summary of measured and predicted values for the relative branching ratio* $\frac{\Gamma(\eta\to\pi^+\pi^-\gamma)}{\Gamma(\eta\to\pi^+\pi^-\pi^0)}$. *The red highlighted row presents the current PDG value for the relative branching ratio. The last row represents the ratio based on Eq. 2.28 without any final state interactions.*

2.5.2 The photon energy distribution E_γ

The two pion invariant mass squared distribution $s_{\pi\pi}$ is sensitive to contributions from final state interactions. Thus, it allows a more detailed investigation of the problem. The dynamic range of this distribution is (outside the chiral limit) given by [7]:

$$4m_{\pi^\pm}^2 \leq s_{\pi\pi} \leq m_\eta^2 \tag{2.31}$$

where $m_{\pi^\pm}$ and m_η are the masses of the charged pions and the η-meson respectively. The photon energy E_γ (in the η rest frame) is related to $s_{\pi\pi}$ by the following equation [7]:

$$E_\gamma = \frac{1}{2} \cdot \left(m_\eta - \frac{s_{\pi\pi}}{m_\eta}\right) \tag{2.32}$$

This makes the distribution of the single photon energy suitable for studying contributions from final state interactions. According to Eq. 2.31, the E_γ-distribution is kinematically limited by:

$$0 \leq E_\gamma \leq \frac{1}{2} \cdot \left(m_\eta - \frac{4m_{\pi^\pm}^2}{m_\eta}\right) \tag{2.33}$$

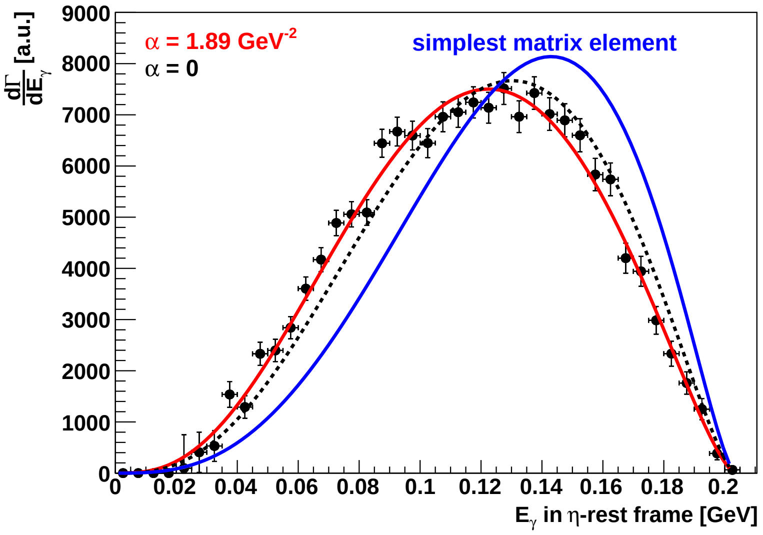

Figure 2.6: *Measured photon energy distribution E_γ in the η rest frame (data points and α-values taken from [7]). The measurement was done for the reaction $pd \rightarrow {}^3\mathrm{He}\eta[\eta \rightarrow \pi^+\pi^-\gamma]$ at the WASA-at-COSY-facility. The black points represent the measured data with error bars indicating the statistical uncertainties. The blue solid curve corresponds to the calculated E_γ-distribution using Eq. 2.28 only. The black dashed curve is obtained by using Eq. 2.29 with $\alpha = 0$ and is shown for comparison. The fit of Eq. 2.29 to the experimental distribution of E_γ is shown by the red solid curve. In that case α was found to be: $\alpha = (1.89 \pm 0.25_{stat} \pm 0.59_{sys} \pm 0.02_{theo})\,\mathrm{GeV}^{-2}$.*

Several experimental efforts have been made to measure this distribution. One of the latest results is shown in Fig. 2.6 [7]. The measured data (black points) is compared to the calculated single photon energy distribution using: Eq. 2.28 (blue solid curve), Eq. 2.29 with $\alpha = 0$ (black, dashed curve) and fitting Eq. 2.29 to data (red solid curve). As discussed in the previous section, the α parameter determines reaction specific contributions from pion-pion-interactions. According to that, $\alpha = 0$ corresponds to a scenario, where the pion final state interactions are purely described by the pion vector form factor (see Eq. 2.29). This value is independent of any reaction dynamics. Any α value different from zero is related to decay dependent final state interactions. The α-parameter obtained from fitting the data points in Fig. 2.6 is $\alpha = (1.89 \pm 0.25_{stat} \pm 0.59_{sys} \pm 0.02_{theo})\,\mathrm{GeV}^{-2}$ [7].

However, the distribution presented in Fig. 2.6 might to some extend be described by the black dashed curve which is related to $\alpha = 0$.

Further measurements as well as theoretical predictions related to the photon energy distribution are listed in Table 2.6. The α values for all measurements where calculated in [4]. The theoretical predicted values can be found in [7]. Since the data points in Fig. 2.6 are given in arbitrary units, the fitted curves imply the scaling factor f_S presented in Eq. 2.29.

The values of the GAMS-200 and CRYSTAL BARREL collaboration are not considered in the following discussion, because the α-value for $\eta' \rightarrow \pi^+\pi^-\gamma$ is expected to differ from the one corresponding to $\eta \rightarrow \pi^+\pi^-\gamma$. The measured α values presented in Table 2.6 show a clear tendency towards values $> 1\,\mathrm{GeV}^{-2}$ (except the result obtained from Layter et al.). In contrast, the three models presented in Section 2.4.3 predict values $< 0.7\,\mathrm{GeV}^{-2}$.

Experiment / Theory	α [GeV^{-2}]
Gormley et al. [19, 4]	1.8 ± 0.4
Layter et al. [21, 4]	-0.9 ± 0.1
GAMS-200 [22, 4]	2.7 ± 0.1
CRYSTAL BARREL [23, 4]	1.8 ± 0.53
KLOE [6, 4]	1.32 ± 0.2
WASA-at-COSY [7]	1.89 ± 0.86
N/D [1, 7]	0.64 ± 0.02
HLS [2, 7]	0.23 ± 0.01
$O(p^6) + 1 - \text{loop}$ [3, 7]	-0.7 ± 0.1

Table 2.6: *Summary of the measured and predicted values for α. The results of the GAMS-200 and CRYSTAL BARREL collaboration where obtained from measuring $\eta' \to \pi^+\pi^-\gamma$. The errors for α obtained from the KLOE and WASA-at-COSY collaboration represent the linear sum of all errors.*

2.5.3 The pion-photon opening angle

The left side of Fig. 2.7 shows the Dalitz plot (squared invariant mass of π^- and γ as a function of the squared invariant mass of π^+ and γ) for the decay $\eta \to \pi^+\pi^-\gamma$. The black dashed line indicates the symmetry line. Any deviation from a uniform yield, when reflecting about this diagonal would give hint to a C-violating process, because the distribution of positive and negative charged pion momenta would be unequal and allow for even relative momenta $\ell = 2, 4, \ldots$. This would be in contradiction to C-symmetry, which strictly demands odd relative momenta (see also discussion in Section 2.3.2). One observable connected to testing of the C-violation is the opening angle between the positive pion and the photon measured in the (π^+, π^-)-rest frame (see right side of Fig. 2.7). This differential distribution is obtained by a projection perpendicular to the symmetry line shown in the left frame of Fig. 2.7. The angular

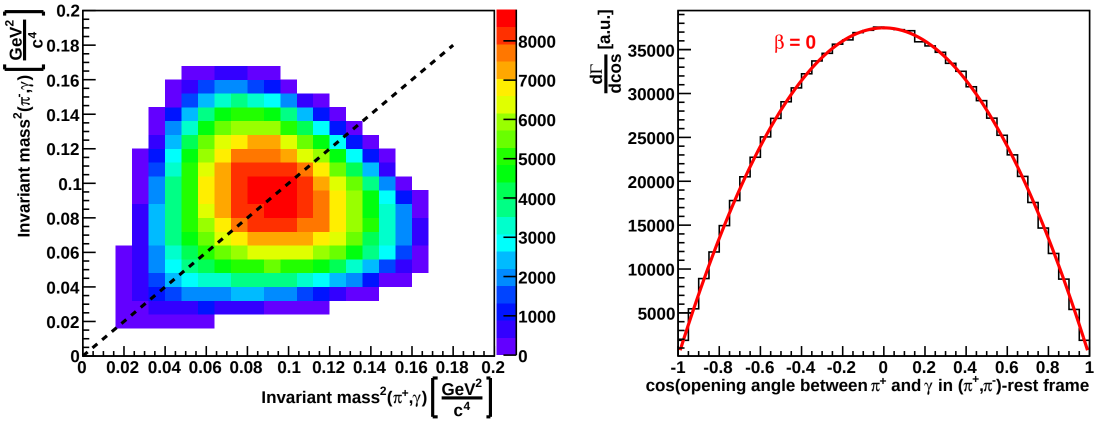

Figure 2.7: **Left:** *Dalitz plot of the decay $\eta \to \pi^+\pi^-\gamma$. The black dashed line represents the symmetry line.* **Right:** *Cosine of the opening angle between the charged pion and the photon in the dipion rest frame. The red line represents a fit of Eq. 2.34. Both distributions shown here are obtained from an event generator called Pluto, which will be presented in Chapter 4.*

distribution might be parameterised by the following equation [24]:

$$f(\cos[\angle(\pi^+,\gamma)]) = A \cdot \sin^2[\angle(\pi^+,\gamma)] \cdot (1 + \beta \cdot \cos^2[\angle(\pi^+,\gamma)]) \tag{2.34}$$

The angle $\angle(\pi^+,\gamma)$ denotes the opening angle between the positively charged pion and the photon in the dipion rest frame. The parameter A is a scaling parameter, whereas β is a measure for the strength of D-wave ($\ell = 2$) contributions, which imply C-violation. The value $\beta = 0$ is given in case of no C-violation (see red curve in the right frame of Fig. 2.7). Recent measurements of the β-parameter are presented in Table 2.7. All results shown there (except the observation from Thaler et al.) confirm contributions from P-waves ($\ell = 1$) only, which is in agreement with C-symmetry. The β-parameter will also be investigated to a certain extent within this thesis. The main aspects of this work are sumarised in the following section.

Experiment	β
Gormley et al. [19]	-0.06 ± 0.065
Thaler et. al. [24]	0.12 ± 0.06
Jane et al. [25]	0.11 ± 0.11
PDG [10]	-0.02 ± 0.07
PhD CFR [26]	0.236 ± 0.430

Table 2.7: *Summary of the measured β parameters. The observed value from Thaler et al. is not considered within the recent PDG value (highlighted in red).*

2.6 Aim of this work

The aim of this work is to measure the relative branching ratio $\frac{\Gamma_{\eta\to\pi^+\pi^-\gamma}}{\Gamma_{\eta\to\pi^+\pi^-\pi^0}}$ and the photon energy E_γ within one experiment with high statistics, using the reaction $pp \to pp\eta[\eta \to \pi^+\pi^-\gamma]$. The basic questions addressed to this measurement are:

i) Will the measured relative branching ratio confirm the Gormley / Thaler results [19,20] or the latest measurements of the CLEO- and KLOE-collaborations [5, 6]?

ii) Can the α-parameter of the previous WASA-result [7] be confirmed and will the E_γ-distribution measured in this experiment allow a clearer distinction between $\alpha = 0$ and $\alpha \neq 0$?

iii) Will this experiment give insight into the significant deviation between the theoretical and experimental values of α?

Chapter 3

The WASA-at-COSY Experiment

The experimental tool for measuring and determining the observables of the anomalous decay $\eta \to \pi^+\pi^-\gamma$ is the WASA-at-COSY facility, located at the research center Jülich, Germany. The main feature of this experiment is, that all particle momenta in the final state of every eta decay can be reconstructed. The η production can be operated at high luminosities so that rare decays like the double Dalitz decay $\eta \to e^+e^-e^+e^-$ or $\eta \to e^+e^-$ can be measured. Fig. 3.1 shows a CAD drawing of the WASA-at-COSY experiment representing the WASA detector, the COSY beamline and the pellet target station, which is mounted on top of WASA. These three components are discussed in detail in the following sections.

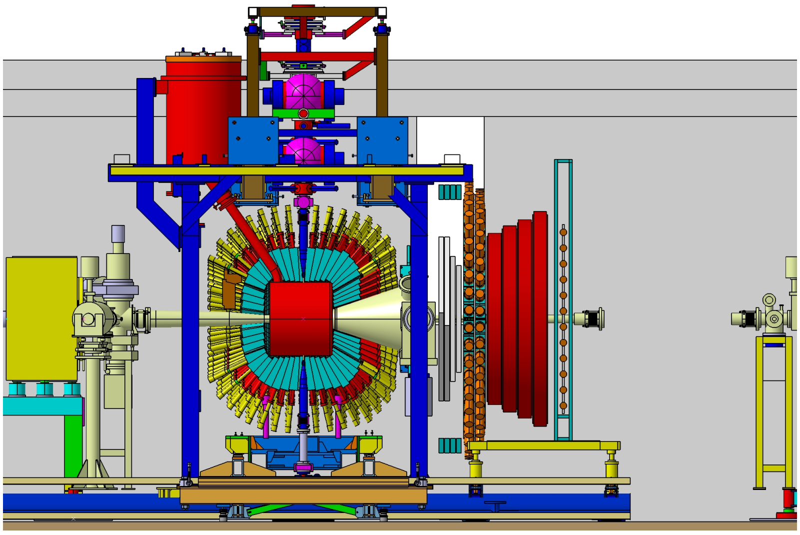

Figure 3.1: *CAD drawing of the WASA detector inside the COSY ring.*

3.1 The COSY accelerator

The η mesons are produced in the reaction $pp \to pp\eta$. The beam protons used in this experiment are provided by the COSY accelerator and have a kinetic energy of 1.4 GeV. The COoler SYnchrotron accelerator (COSY) is a storage ring (see Fig. 3.2 left) with a circumference of 184 m. It provides (polarised/unpolarised) proton or deuteron beams in the momentum range 0.3 GeV/c to 3.7 GeV/c [27,28]. The proton (deuterium) beam is produced by H^- (D^-) ions which are preaccelerated up to 45 MeV (76 MeV) by a cyclotron and injected into the COSY ring. The electrons are stripped by a $\sim 20 - 25\,\mu\text{g/cm}^2$ thick carbon foil [28]. One unique feature of COSY

is the beam cooling which leads to a beam momentum resolution of $\frac{\Delta p}{p} \approx 1 \cdot 10^{-4}$. Two cooling techniques are used: The first one is electron cooling. This technique is applied at injection energies in order to prepare a low-emittance beam. For beam energies larger than 1.5 GeV, stochastic cooling is used instead [27, 28].
For the WASA-at-COSY experiment none of those techniques was applied, because they are insufficient to correct for the energy loss after the beam interacted with the pellet target. This effect is compensated by running the accelerator in the barrier bucket mode. In this mode beam particles are grouped into single bunches and the mean energy loss after interacting with the target is compensated by a radio-frequency cavity [29].

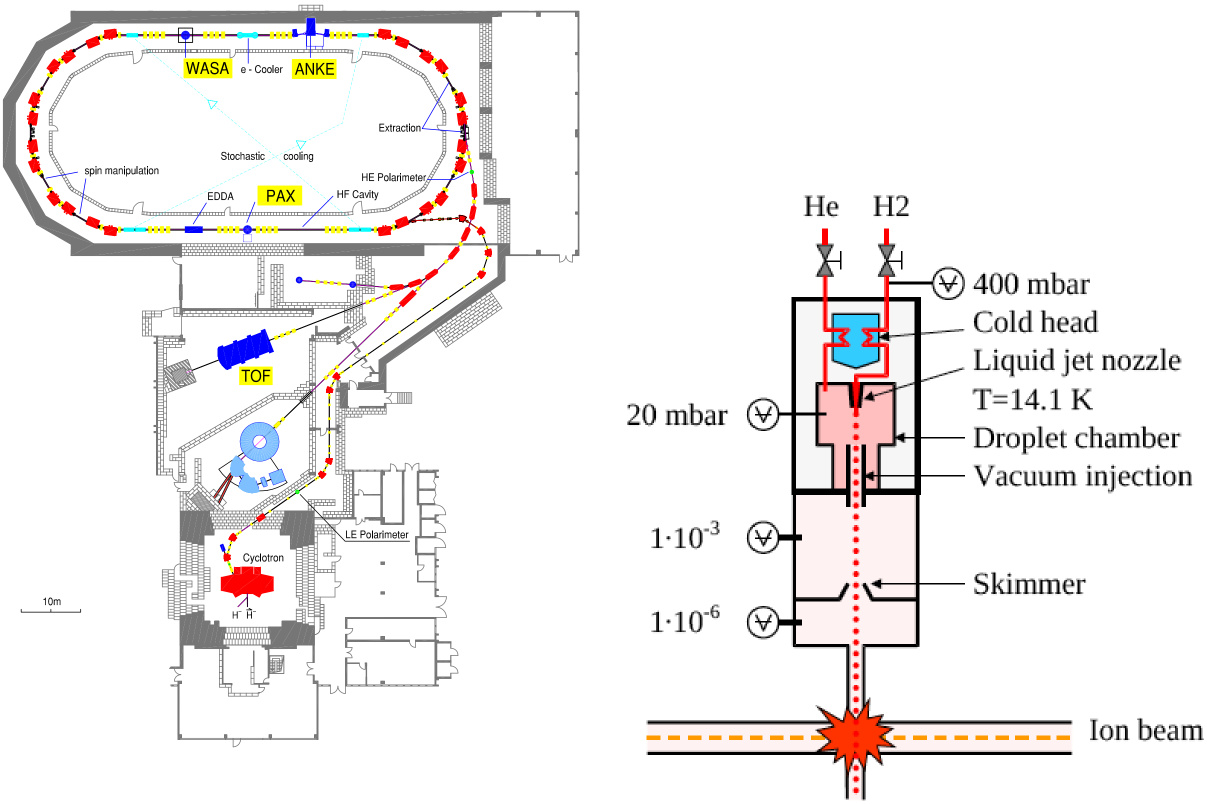

Figure 3.2: **Left:** *Floor plan of the COSY accelerator, showing the beam line and internal experiments like WASA, ANKE and PAX.* **Right:** *Schematic drawing of the WASA pellet target station.*

3.2 The pellet target

WASA is built as an internal experiment thus the target has been designed in a way that background reactions stemming from secondary beam target interactions are suppressed. Otherwise a clean detection of the eta decay products would not be possible. Additionally, a thick target would lead to large energy losses of the incoming proton beam. A thin target on the other hand is also not applicable, since the luminosity would be too low to be able to collect sufficient statistics. Furthermore, rare eta decays could not be measured. In order to meet those requirements a high density pellet target (see Fig. 3.2 right) has been developed for the WASA experiment.

Hydrogen (or helium) gas is liquified by passing a cold head where it is cooled down. Afterwards it passes a vibrating nozzle into the droplet chamber. The vibrating nozzle is a key element of that target, because it breaks up the continuous stream of liquid into droplets. Those droplets enter the vacuum chamber through a capillary. Due to the pressure gradient between the droplet chamber and the vacuum chamber the droplets will cool further to frozen pellets. The final pellets have a diameter of $\sim 35\,\mu$m [30]. A 2 m long tube with a diameter of 7 mm (skimmer) guides the pellet stream into the scattering chamber where they interact with the proton (deuterium) beam. The pellets inside the stream have a mean velocity of $\sim 80\,\frac{\mathrm{m}}{s}$ and the pellet stream diameter at the interaction point is between 2 mm and 4 mm. After crossing the beam line, the pellets are collected in the pellet dump. In summary the pellet stream corresponds to an effective target thickness $\gtrsim 10^{15}$ atoms/cm^2.
The achievable luminosities using this target are of the order of $10^{32}\,\mathrm{cm}^{-2}\mathrm{s}^{-1}$ and the beam life time is about several minutes. Furthermore, the interaction vertex is well defined in space. However, this device also has disadvantages. The pellets might evaporate further in the beam pipe, which leads to rest gas and might interact outside the primary interaction region with beam protons. This influences the resolution of the primary vertex and has to be taken into account for the analysis [18]. Another aspect of this target is, that the luminosity is directly correlated to the pellet rate. A higher pellet rate increases the interaction rate between beam protons and pellets and therefore might lead to systematic effects. For further information see [31].

3.3 Wide Angle Shower Apparatus (WASA)

All final particles of the reaction $pp \rightarrow pp\eta[\eta \rightarrow \pi^+\pi^-\gamma]$ are measured with the Wide Angle Shower Apparatus (WASA) which is designed as a 4π detector (see Fig. 3.3). The protons are reconstructed in the forward part of WASA which consists of tracking detectors and a range hodoscope with a maximum proton stopping power of ~ 360 MeV. The decay products (pions and photons) are reconstructed in the central part which has an onion-like structure. The inner most part contains a tracking detector which reconstructs the particle momenta. This detector is surrounded by a plastic scintillator delivering energy and time information. Further outside a superconducting solenoid is implemented, providing a magnetic field used for momentum reconstruction. The most outer part of the Central Detector is a calorimeter, mainly used for reconstructing photons and electrons. The following sections will not focus on all detector parts of WASA, but on those which are relevant for the decay channel of this analysis.
The momenta of all particles are described in a right handed (cartesian/spherical) coordinate system. The origin of that system is defined by the mean interaction point between the proton and pellet beam (see Fig. 3.3). The Z-axis of that system is aligned parallel to the proton beam, the Y-axis is aligned antiparallel to the pellet beam. The X-axis points outside of the COSY-ring.
All particle momenta are expressed in spherical coordinates (p, θ, ϕ), where p is the momentum, θ the polar and ϕ the azimuthal angle.

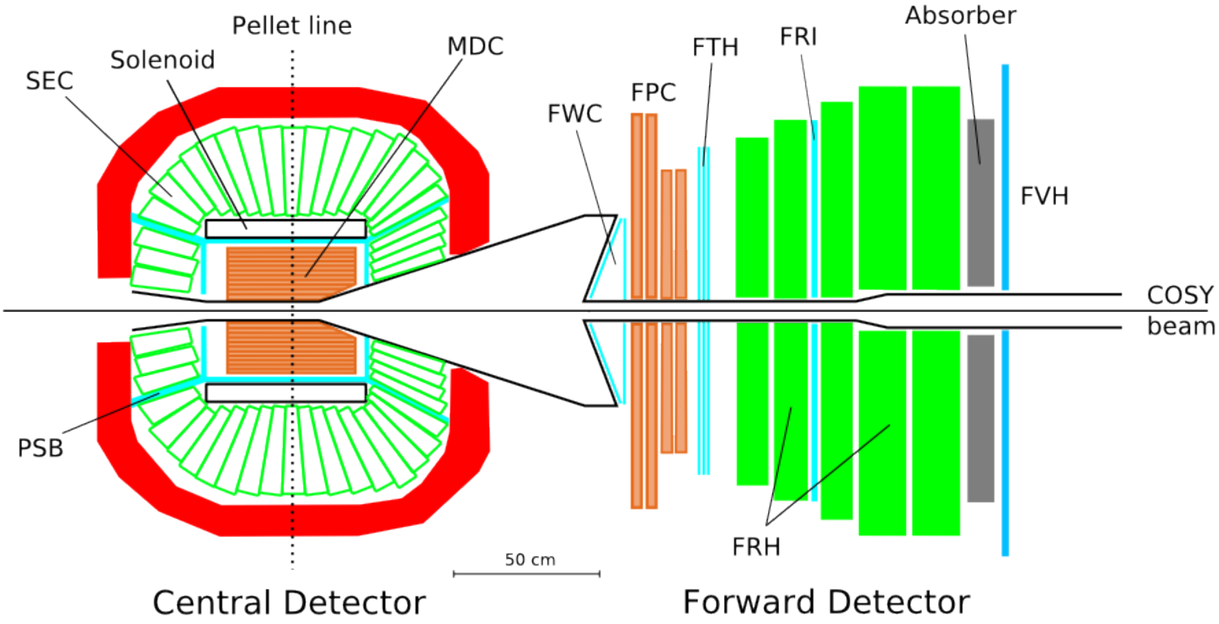

Figure 3.3: *Schematic drawing of the WASA detector. The proton beam provided by COSY is coming from the left hand side and enters the Central Detector first. The various labels are assigned to different detector parts and are explained in the text below.*

3.4 The Forward Detector (FD)

The scattered or recoil protons are reconstructed in the forward part of WASA. It basically consists of a range hodoscope (see green bars in right part of Fig. 3.3), which is used for energy reconstruction. Angular information is provided by tracking detectors (see Fig. 3.3). Besides protons, it is also possible to detect pions, deuterons, alpha partilces and neutrons inside the Forward Detector.

3.4.1 Forward Range Hodoscope (FRH)

A particle interacts with matter by ionising or scattering the valence electrons of the atoms inside that matter. This leads to an energy loss of the incoming particle. The correlation between this energy loss and the initial kinetic energy of the particle is given by the Bethe-Bloch-Formular [13]:

$$-\frac{1}{\rho}\cdot\frac{dE}{dx} = K\cdot\frac{Z}{M_r}\cdot z^2\cdot\left(\frac{1}{2\beta^2(E)}\cdot\ln\left[\frac{2m_ec^2\beta^4\gamma^2(E)\nu(E)}{I^2}\right]-1\right) \tag{3.1}$$

with:

$$\beta^2(E) = 1-\left(\frac{Mc^2}{E}\right)^2,\ \gamma^2(E) = \frac{1}{1-\beta^2(E)},\ \nu(E) = \frac{2E^2}{2Em_e+m_e^2+M^2} \tag{3.2}$$

K is a constant, Z the charge number of the interacting matter, M_r is the atomic mass and ρ is the density. I is the average ionisation energy of all electrons (with mass m_e) within an atom of the interacting matter. z is the charge number and M the mass of the incoming particle. Every particle passing through the FRH will deposit energy in some of the plastic scintillators (see Fig. 3.4). By measuring this energy deposit and using Eq. 3.1 with the appropriate constants, it is possible to calculate the initial kinetic energy of that particle (see top picture of Fig. 3.4).

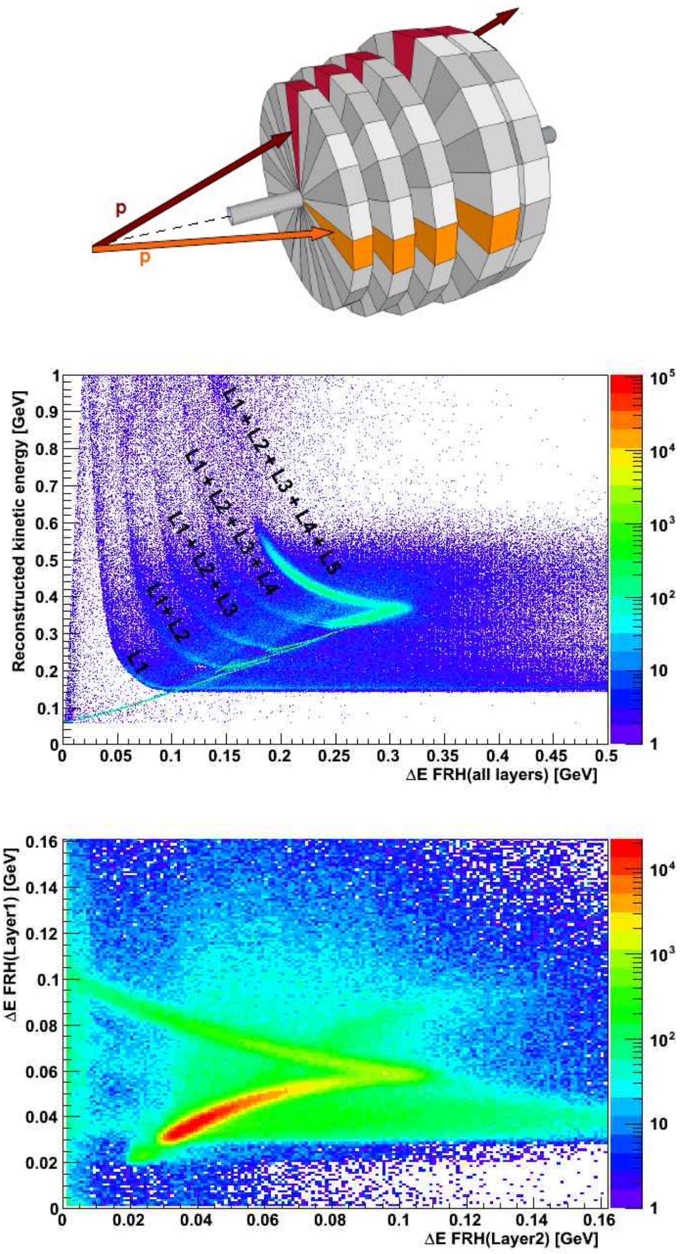

Figure 3.4: **Top:** *Schematic drawing of the Forward Range Hodoscope (FRH) [18]. It consists of five layers with 24 wedge-shaped plastic scintillators each. In addition, two incoming protons are drawn (red and orange arrows). One proton (red arrow) passes through the whole hodoscope and deposits energy in all layers, while the other one (orange arrow) is stopped in the fourth layer.* **Centre:** *Reconstructed kinetic energy of a proton hitting the FRH module shown as function of the deposited energy in all layers of the FRH. There are five structures visible, each corresponding to a layer that was hit by the proton. The second structure for example (labeled with L1+L2) corresponds to a proton which is stopped in the second layer of the FRH.* **Bottom:** *Deposited energy of a proton in the first layer of the FRH plotted as function of the deposited energy in the second layer. The "banana" like shape of the energy loss pattern is characteristic for protons.*

Another feature of this detector device is its ability to identify particles. According to Eq. 3.1, the deposited energy of a particle depends on its kinetic energy and its mass. That is why particles with different masses (and kinetic energies) cause different energy loss patterns. The bottom picture of Fig. 3.4 shows the energy loss pattern in the first two FRH layers of (simulated) single protons hitting the FRH. The most prominent structure is a “banana” shaped band which is characteristic for protons. Other structures in that plot are related to nuclear interactions between the protons and the detector material. One way of selecting proton candidates would be the rejection of all entries which are not lying (within some boundary) on the band. This will be discussed in Chapter 5.

3.4.2 Tracking detectors and track reconstruction

The two main detectors, which are used for reconstructing the angles of the particle are the Forward Proportional Chamber (FPC) and the Forward Trigger Hodoscope (FTH) (see corresponding labels in Fig. 3.3). The FTH consists of three layers with a total of 96 plastic scintillators. Each of them has a thickness of 5 mm and 48 of those scintillators are wedge shaped and built in the first layer of the FTH (see Fig. 3.5). The second and third layer contain the remaining 48 elements shaped in oppositely-orientated Archimedian spirals. A particle passing the FTH module will leave a signal in each of the three layers. Due to the different geometry of each layer, a combination of all three signals leads to a unique pixel. The line connecting the interaction point to this pixel defines a direction vector which should have the same azimuthal and polar angle as the measured particle. If at least two layers of the FTH are hit (within a certain time window), the angular information and average time of the FTH hits are assigned to the particle track. Further information from other detector parts (e.g. the energy information from the FRH) are added to the track, if a geometrical and time overlap between hits in the FTH and hits of the corresponding detector is found [32].

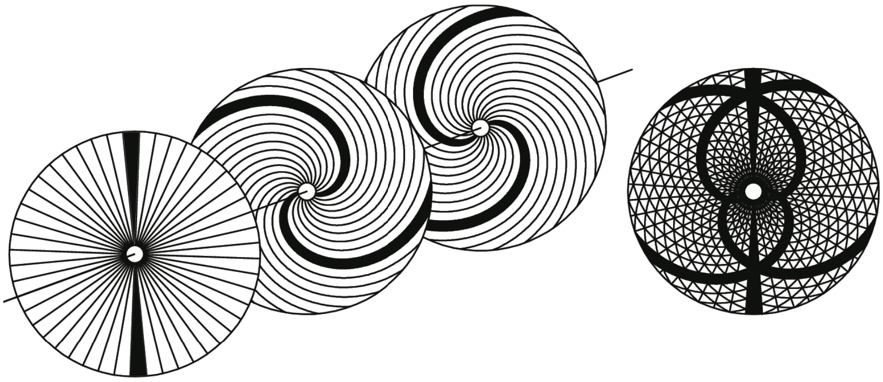

Figure 3.5: *Drawing of all three FTH layers. A combination of the signals left in each layer allow for a reconstruction of the azimuthal and polar angle of a particle hitting this detector. In the scenario drawn above, the reconstruction of two particles (black curves) is shown. The outer radius of each layer is (with respect to the beam line)* $\sim 1.1\,\mathrm{m}$

In addition to the FTH, the Forward Proportional Chamber (FPC) (see Fig. 3.6 right) is used for the angular reconstruction as well. The FPC consists of 122 straw tubes, which are divided onto four modules, where each module has four layers of those straws.

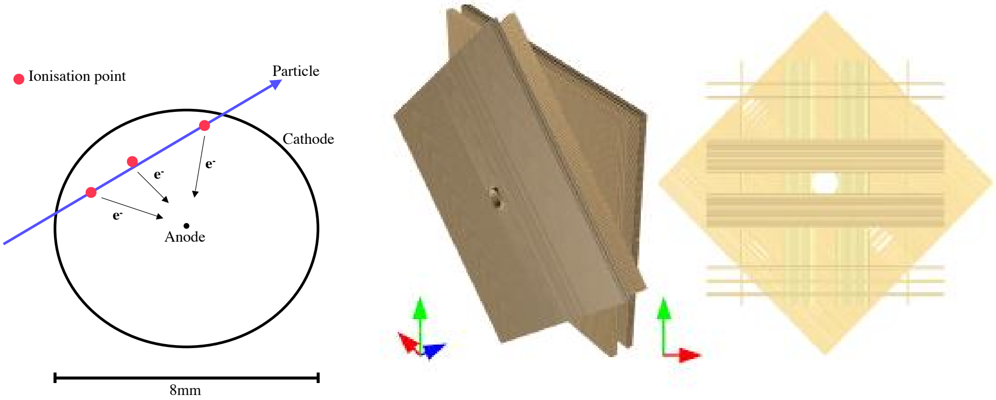

Figure 3.6: **Left:** *Schematic drawing of a single straw tube (2D front view). A particle (blue) hits the tube and ionises the gas inside (red points). The electrons travel towards the anode (indicated by black arrows) and ionise the gas further in the region close to the anode, where the electrical field strength has its maximum.* **Right:** *3D drawing of the FPC module (left) and front view (right) of the FPC, where not all straws are shown.*

The modules are aligned such that the first and second module are rotated by ±45° with respect to the X-axis. The third and fourth modules are aligned parallel to the X- and Y-axis, respectively [26].

Each straw (see Fig. 3.6 left) consists of a stainless steel wire (anode) which is surrounded by a 8 mm thin aluminised mylar foil tube (cathode) and set under high voltage. The tube is filled with a gas mixture of 80% argon and 20% ethane. Particles that hit the straw will ionise the gas and the resulting electrons get accelerated towards the anode due to the electrical field. The field strength of that field increases with decreasing distance to the wire [13] and the primary electrons can ionise the gas further in the region close to the wire. This leads to an electron cascade. Argon is used as drift gas and ensures that the electrons do not recombine with positive ions on their way to the anode. A small amount of ethane is mixed to the drift gas in order to adjust the drift velocity.

The distance between a particle hitting a straw tube and the central cathode of this straw is directly correlated to the measured drift time for the electron cloud to travel to the anode (see Fig. 3.6 left). This allows for an accurate position determination. The same technique is used for reconstructing charged particles in the Central Detector which will be discussed in the next section.

The angular information of a particle track is refined by the information of the FPC, if a geometrical overlap between this detector and the FTH exists. This procedure improves the polar as well as azimuthal angular resolution by a factor of two [26].

3.5 The Central Detector (CD)

The decay particles, such as pions or photons are reconstructed in the Central Detector of WASA. Charged particles (e.g. pions and electrons) are mainly reconstructed by the MDC (see orange bars in Fig. 3.3). Further information, that can be used for particle identification, is obtained from the PSB (see blue lines in Fig. 3.3) and the SEC (see green bars in left part of Fig. 3.3). Neutral particles are reconstructed in the SEC only.

3.5.1 The Mini Drift Chamber (MDC)

One feature of WASA is the ability to reconstruct the momentum and direction of charged particles. For that purpose a superconducting solenoid is used which provides a nearly homogeneous magnetic field $\vec{B}$, which was set to 1 T for this experiment. Charged particles with velocity $\vec{v}$ entering that field, will be affected by the Lorentz force [a]: $\vec{F}_L = q \cdot [(\vec{v} \times \vec{B})]$ which leads to helix like trajectory (see Fig. 3.7 right). The handiness of that helix depends on the sign of the measured particle charge Q.

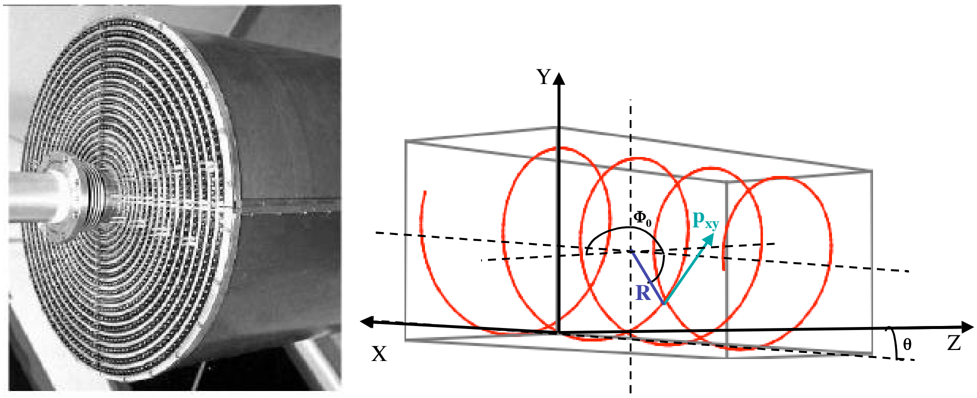

Figure 3.7: **Left:** *Photograph of the back part of the Mini Drift Chamber (MDC). The drift wires are arranged in layers around the beam pipe.* **Right:** *Schematic drawing of a particle traveling along the beam direction (z-axis) with a helix like trajectory due to the magnetic field [18]. The blue line indicates the radius R of the helix and the green arrow the transverse momentum p_{xy} of the particle (in the xy-plane) respectively. The polar angle between the helix centre and the origin of the coordinate system is denoted by Φ_0. Depending on $\vec{v}$, the helix could also be tilted by θ with respect to the z-axis. It is the major task of the MDC to reconstruct and determine those parameters. The helix shown here does not represent a realistic event, since the proportions are chosen arbitrary.*

The magnetic field $\vec{B}$ is aligned parallel to the z-axis. That is why only the transverse part $\vec{v}_{xy}$ of $\vec{v}$ has to be taken into account and the Lorentz-force is restricted to the xy-plane and thus equal to the centripetal force: $F_L = qv_{xy}B = \frac{\gamma v_{xy}^2 m}{R}$. R is the radius of the helix (see Fig. 3.7 right), m the particle mass and γ the relativistic factor. This leads to:

$$p_{xy} = mv_{xy} = \frac{q}{\gamma} \cdot R \cdot B \tag{3.3}$$

Further parameters which can be deduced from the reconstructed helix, are the polar angle Φ_0 and the azimuthal angle θ (see Fig. 3.7). Using those additional parameters and p_{xy} lead to the reconstructed momentum vector $\vec{p}$ of the measured particle [18]:

$$\vec{p} = p_{xy} \cdot \begin{pmatrix} \cos(\Phi_0) \\ \sin(\Phi_0) \\ \cot(\theta) \end{pmatrix} \tag{3.4}$$

The MDC is composed of 1738 straw tubes [33, 34] working as described in Section 3.4.2. The straws are arranged in 17 layers (see Fig. 3.7 left) surrounding the beam pipe in radii between 41 mm and 203 mm [30]. Nine of those layers are parallel to the beam axis, as the remaining eight layers are skewed by ∼ 9° in order to

---

[a] Contributions from electrical fields can be neglected.

reconstruct the $z-$component of a track. A particle detected within the MDC will cause a certain hit-pattern, due to the responding straws. Those hits define a group called a tracklet. Assuming a homogeneous magnetic field, the tracklet is fit by a helix. The fit provides the parameters mentioned above: R, Φ_0, θ plus the charge Q, the z-component z_0 of the closest approach from the helix center to the origin in the XY-plane and R_0, the helix axis coordinate in the XY-plane [35]. Those parameters are assigned to a single particle track. In a second step, the track values are refined using a final fit where the track is traced back from the outer layers of the MDC towards the beam target interaction region, using a Kalman filter [35]. The initial values of the final fit are given by the helix parameters found in the pattern recognition. One important feature of that final fit is that effects like multiple Coulomb scattering and energy loss within the detector itself are taken into account. Furthermore, the assumption of a homogeneous magnetic field is corrected by including a map of the actual solenoid field [35]. A more detailed description of the track reconstruction within the MDC and the drift time calibration can be found in [18, 26].

3.5.2 The Plastic Scintillator Barrel (PSB)

The MDC is surrounded by 146, 8mm [30, 36] thick BC408 plastic scintillators [26], which are arranged as a barrel (see Fig. 3.8). Each of the detecting elements is read out by a photomultiplier tube. This barrel consists of three main parts: [30, 36] i) The forward part (containing 48 scintillators and an outer diameter of $\sim 51\,\mathrm{cm}$), ii) The central part (containing 50 scintillators) and iii) The backward part (also containing 48 scintillators and an outer diameter of $\sim 42\,\mathrm{cm}$) .

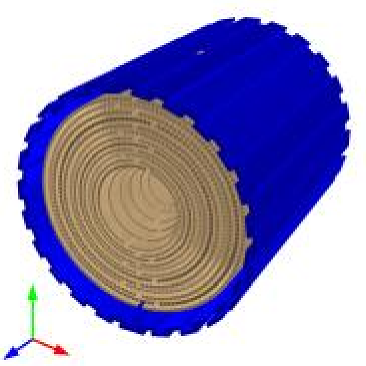

Figure 3.8: *3D drawing of the central part of the PSB (blue) surrounding the MDC (brown).*

The forward part of the PSB is flat shaped and perpendicular to the beam axis and the backward part has a conical surface. Each scintillator element of the central part has small overlap ($\sim$ 6mm [30]) with its neighbour, in order to avoid particles passing the detector without being registered.

The PSB provides fast signals resulting in a good time resolution for charged particles. Furthermore, the PSB signal can be used as a first level trigger for selecting charged decays [30].

Hits detected in the PSB are grouped by a clustering routine and used later on for track assignment.

3.5.3 The Scintillator Electromagnetic Calorimeter (SEC)

Neutral particles (in this case photons) are detected by the WASA calorimeter (see Fig. 3.9). Electrons, positrons and pions with an energy up to 800 MeV can also be reconstructed with this detector as well. The calorimeter is composed of 1020 sodium doped CsI scintillators which are shaped as truncated pyramids. Each of those scintillators is connected to a photomultiplier tube. The photomultipliers are protected from the magnetic field by a return iron yoke (red circle in Fig. 3.3). The polar angular acceptance of the calorimeter is between 20° and 170°. As indicated in Fig. 3.9, the scintillators are arranged in rings which are labelled from 151 (backward part) to 174 (front part).

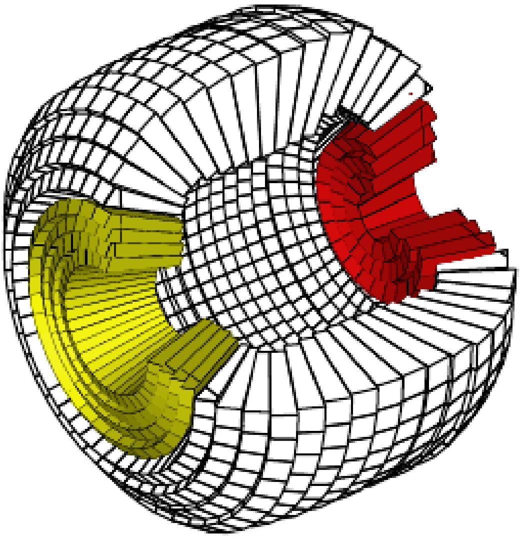

Figure 3.9: *Schematic drawing of the WASA calorimeter. It consists of three parts: The front part (yellow), central part (white) and the backward part (red). The* 1020 *crystals are arranged in* 24 *polar angle dependant rings. The crystal length varies from* 25 cm *in the forward part, to* 30 cm *in the central part and* 20 cm *in the backward part [30]. The calorimeter surrounds the solenoid, the PSB and the MDC.*

High energy particles hitting the calorimeter cause a particle shower. The two main mechanisms for creating such showers at large energies are pair creation (in case of photons) and bremsstrahlung (in case of electrons). If a photon with energy $E > 2m_e$ hits the calorimeter, it will create an electron positron pair with energy about $E/2$ after a typical radiation depth d. Those particles emit two photons with energy about $E/4$ after $2d$ which again create electron positron pairs and so on. After Nd radiation depths 2^N particles with an average energy $\frac{E}{2^N}$ each have been created. The whole process stops when the average energy falls below the critical energy E_{crit}. Thus, the maximum depth of the shower (expressed in N) is given by: $N_{max} \leq \frac{\ln(E/E_{crit})}{\ln(2)}$ [13]. The lateral expansion of the shower inside the calorimeter is expressed by the Molière radius: $R_M = \frac{d \cdot 21\,\mathrm{MeV}}{E_{crit}}$ [13] which comprises the two main characteristics of a shower: d and E_{crit}. The relative energy resolution $\sigma(E)$ for photons of the WASA calorimeter is parameterised to be [36]:

$$\frac{\sigma(E)}{E} \approx \frac{5\%}{\sqrt{E}} \tag{3.5}$$

Charged pions deposit their energy via ionisation or cause a delayed shower by decaying into: $\pi^\pm \rightarrow \mu^\pm \nu_\mu(\bar{\nu}_\mu)$ with: $\mu^\pm \rightarrow e^\pm + \nu_e(\bar{\nu}_e) + \nu_\mu$. The corresponding energy resolution FWHM is of the order of ≈ 3% [36]. Figure 3.10 shows a very simplified scheme of the track reconstruction within the calorimeter. For simplicity, detector elements are drawn as rectangles. If a photon hits the calorimeter a shower spreads over several elements. The particles within such a shower interact with the valence shell electrons of the crystal which results in an electron-hole pair. This pair recombines again to a photon which is detected by the corresponding photomultiplier. Since the crystals are doped, the effect of recombination is amplified. The coloured rectangles in Fig. 3.10 represent elements which have interacted with the shower caused by an incoming photon. The track reconstruction is performed by a cluster-finding-algorithm [37]: Detector elements with an energy deposit $\geq 5\,\text{MeV}$ are taken as the central cluster (dark red rectangles in Fig. 3.10). Neighbouring elements with a minimum energy of 2 MeV (red and light red rectangles in Fig. 3.10) and a time difference smaller than 50ns (with respect to the central cluster) are assigned to that cluster.

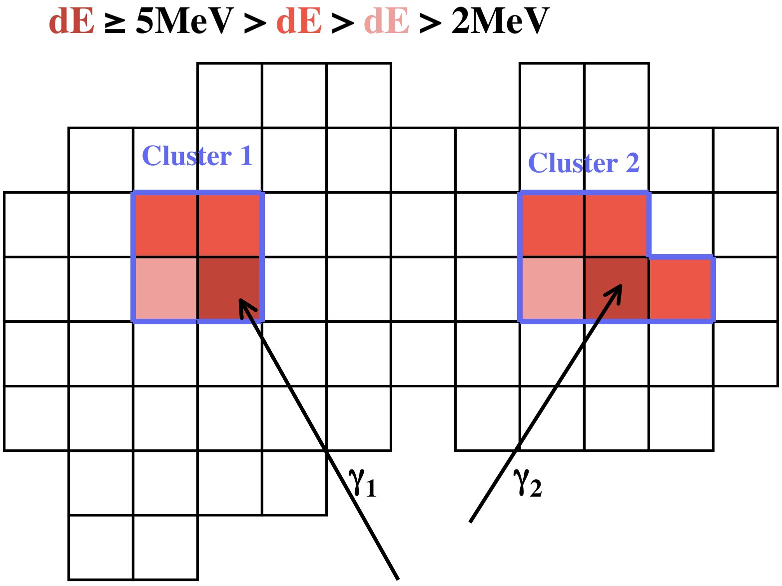

Figure 3.10: *Simplified schematic representation of the cluster finding procedure: Detector elements of the calorimeter are drawn as white/red rectangles. All elements with an energy deposit smaller than* 2 MeV *are coloured white and elements with an energy larger than* 2 MeV *are coloured red. In this scenario two photons hit the calorimeter and are reconstructed as two different clusters (blue lines represent the borders of one cluster) with a minimum distance of four elements from each other.*

The procedure stops if at least one non-hit element is found on each side of the cluster (see blue lines in Fig. 3.10). This final cluster is assigned to a track. The cluster-finding-algorithm is applied again on all remaining hits which have not been grouped to a cluster. The whole procedure ends, if all hits are assigned to clusters (see Fig. 3.10). The position $\vec{X}_{clu}$ of a cluster is defined by the individual position $\vec{x}_i$ of each crystal belonging to the cluster and its weighted energy E_i [37]:

$$\vec{X}_{clu} = \frac{\sum\limits_i w_i \vec{x}_i}{\sum\limits_i w_i} \tag{3.6}$$

$$w_i = \text{MAX}\Big[0,\ 5 + \ln\Big(\frac{E_i}{\sum\limits_i E_i}\Big)\Big] \tag{3.7}$$

The properties of a (neutral) track (i.e. position) are defined by $\vec{X}_{clu}$.

3.5.4 Calibration of the SEC

In order to be sensitive to the single photon energy distribution E_γ of $\eta \rightarrow \pi^+\pi^-\gamma$, a good calibration of the calorimeter is necessary. The following section will describe briefly the energy and time calibration of this detector [38] with a main focus on the energy calibration.

3.5.4.1 Energy calibration

In order to calibrate the SEC, the reaction: $pp \rightarrow pp\pi^0[\pi^0 \rightarrow \gamma\gamma]$ has been measured with a kinetic beam energy $\sim 500\,\mathrm{MeV}$. The π^0 has a mass of $0.135\,\mathrm{GeV/c^2}$ and decays into two photons. Both of them are used to calibrate the calorimeter because their invariant mass has to be at the π^0 mass. The invariant mass of two photons is given by:

$$\text{Invariant mass } (\gamma_1, \gamma_2) = \sqrt{2E_{\gamma_1}E_{\gamma_2} \cdot (1 - \cos[\angle(\gamma_1, \gamma_2)])} \tag{3.8}$$

where E_{γ_1}, E_{γ_2} are the energies of the two photons and $\angle(\gamma_1, \gamma_2)$ is the opening angle (in the laboratory system) between them. The invariant mass is not a discrete value but rather a distribution, because the detector has a finite resolution. If the calibration is done properly, the maximum of this distribution should be located at $m_{\pi^0} = 0.135\,\mathrm{GeV/c^2}$. Fig. 3.11 shows the invariant mass distribution dedicated to the measurement of: $pp \rightarrow pp\pi^0$. The black curve shows the distribution before calibration and the red curve after calibration. The enhancement at low invariant masses $\sim 0.01 - 0.02\,\mathrm{GeV/c^2}$ is mainly related to incorrectly reconstructed, low energy photons which will be discussed later. Even though the π^0-signal is quite dominant[b], there is still a smooth background related to combinatorics (i.e. combination of (incorrectly) reconstructed photons which do not belong to the same

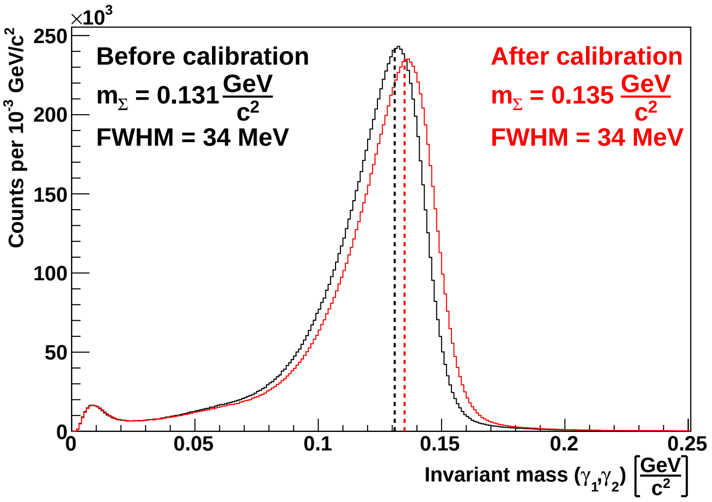

Figure 3.11: *Invariant mass distributions obtained from a fraction of data taken from the measurement of: $pp \rightarrow pp\pi^0$. The dashed lines indicate the peak position of that distribution before (black) and after (red) the calibration. Both distributions are obtained by requesting exactly two reconstructed neutral clusters in the calorimeter.*

---

[b] Due to the request of exactly two reconstructed clusters in the calorimeter within one event.

$\pi^0 \rightarrow \gamma\gamma$ event). The peak position of the invariant mass distribution (before and after calibration) is denoted by m_Σ. Before calibration, the peak position is at $m_\Sigma = 0.131\frac{\text{GeV}}{c^2}$. Thus, the detector has to be calibrated in order to have m_Σ at the correct value. The calibration procedure is based on the assumption, that the

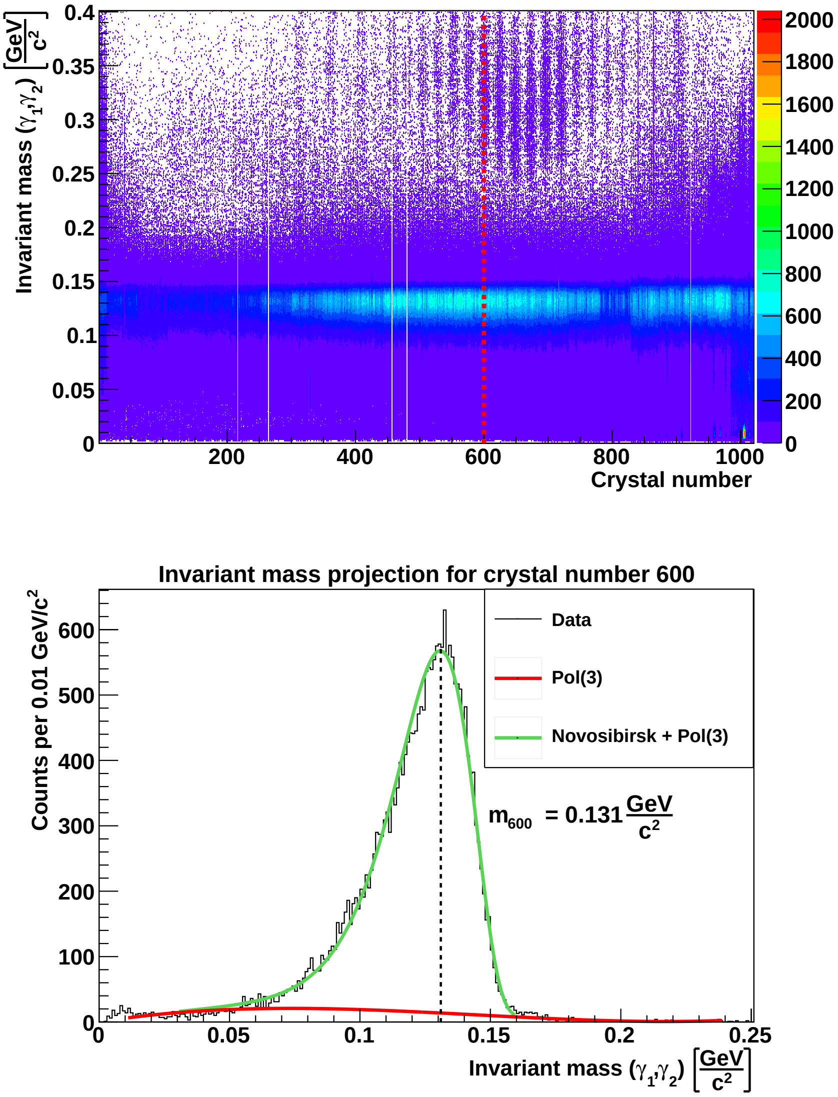

Figure 3.12: **Top:** *Invariant mass of two photons as function of the individual crystal that was hit by one of the two photons. The red dashed line indicates the projection of the invariant mass on a specific crystal number (600 in this case).* **Bottom:** *Projection of the invariant mass for crystal 600. The background is fit by a third order polynomial (red line). The total signal is fit by a Novosibirsk function (see Fig. 3.13) and a third order polynomial (green line). The position m_i of the invariant mass distribution for that crystal is (before calibration) at 0.131 GeV/c^2.*

energy of each detected photon is mainly described by the deposited energy in the central crystal of the corresponding cluster. The invariant mass m_{ij} of two central crystals i and j is approximated by [39]:

$$m_{ij} \sim \sqrt{E_i E_j} \tag{3.9}$$

Taking one particular (central) crystal i which is hit by a photon and assuming that the contribution of the remaining 1019 crystals to the invariant mass of that crystal

i and every other crystal j averages out [39], leads to:

$$m_i \equiv \frac{1}{1020} \cdot \sum_{i \neq j} m_{ij} \sim \sqrt{E_i \cdot \kappa} \tag{3.10}$$

where κ is a (global) calibration correction factor. The obvious choice for κ is: $\kappa = \frac{m_{\pi^0}}{m_\Sigma}$, such that the final invariant mass distribution is shifted to the π^0-mass. Additionally, the individual contribution of each element i to the global invariant mass shown in Fig. 3.11 has to be taken into account. This can be done by introducing the factor: $\frac{m_\Sigma}{m_i}$. Using this and Eq. 3.10 leads to an energy correction per element [38,39]:

$$E_i \to E_i \cdot \left(\frac{m_\Sigma}{m_i}\right)^2 \cdot \frac{m_{\pi^0}}{m_\Sigma} \tag{3.11}$$

In order to calculate m_i for each detector element, the invariant mass before calibration (black distribution shown in Fig. 3.11) is plotted as a function of the individual crystal number (see top of Fig. 3.12). After that, the projection of Invariant mass (γ_1, γ_2) is done for every crystal number and the peak position is determined (see bottom of Fig. 3.12). This peak position can be directly identified with m_i shown in Eq. 3.11.

Fig. 3.12 shows the procedure described above for crystal 600. As already explained for the distributions shown in Fig. 3.11, the distribution here does not only contain $\pi^0 \to \gamma\gamma$ events but also a smooth combinatorial background. There is still a small enhancement at small invariant masses, due to incorrectly reconstructed photons.

In order to obtain m_i, the whole invariant mass distribution has been fit. The smooth background is described by a third order polynomial (red curve in Fig. 3.12 bottom). The signal part which is related to $\pi^0 \to \gamma\gamma$ events, is described by the Novosibirsk function [40]:

$$f(x) = A \cdot \exp\left[-0.5 \cdot \left(\frac{\log(1 + \Lambda \cdot (x - x_0))}{\tau}\right)^2 + \tau^2 \right] \tag{3.12}$$

with:

$$\Lambda = \frac{\sinh(\tau \cdot \sqrt{\log(4)})}{\sigma \cdot \sqrt{\log(4)}} \tag{3.13}$$

This function basically describes an asymmetric Gaussian distribution with resolution σ, peak position x_0 and scaling factor A. The asymmetry can be adjusted by the parameter τ. Fig. 3.13 shows several plots of Eq. 3.12 for different asymmetry parameters. The black dashed line indicates the symmetry line (considering the Gaussian distribution represented by the blue curve) located at the peak position $x_0 = 0.135$. Plotting Eq. 3.12 with negative τ-values leads to a Gaussian-like distribution with a tail on the left side (green curve in Fig. 3.13). Positive τ-values cause a tail on the right side (red curve in Fig. 3.13). For vanishing τ-values, the distribution converges to a Gaussian distribution (blue, dashed curve in Fig. 3.13). This function was chosen, because the response function of the calorimeter (encoded in the π^0-signal) represents itself as a Gaussian-like distribution with a tail towards smaller invariant masses. Thus, Eq. 3.12 using negative τ-values is fit to the π^0-peak in Fig. 3.12. The resulting peak position from that fit is $m_i = 0.131\,\mathrm{GeV/c^2}$. Knowing that $m_\Sigma = 0.131\,\mathrm{GeV/c^2}$ and using Eq. 3.12 leads to a calibration (correction) factor of 1.035 for crystal 600. This procedure is done for all 1020 crystals belonging to the calorimeter. Afterwards, the analysis of the $pp \to pp\pi^0$ data is redone with the updated calibration constants. The overall invariant mass peak

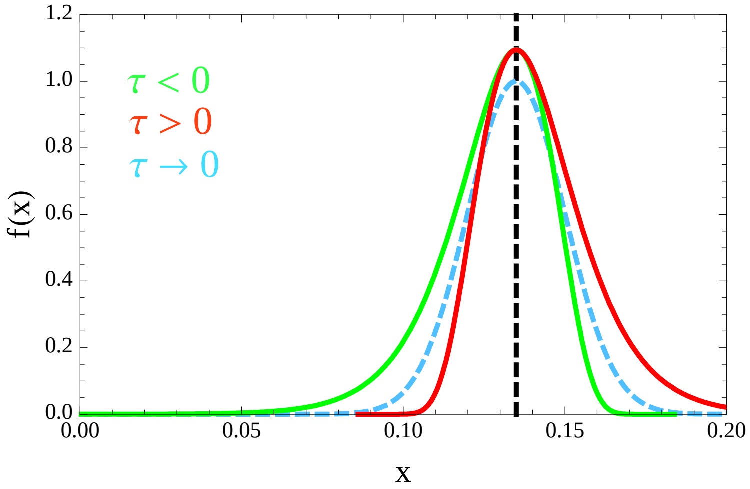

Figure 3.13: *Plot of Eq. 3.12 for different values of the τ-parameter. All other parameters are fixed to: $x_0 = 0.135$ (black, dashed line), $\sigma = 0.015$ and $A = 1$. The green curve corresponds to: $\tau = -0.3$ and the red curve to: $\tau = 0.3$. The Novosibirsk distribution converges to a Gauss distribution if $\tau \to 0$ (blue dashed curve). The black dashed line indicates the symmetry line of the Gaussian distribution.*

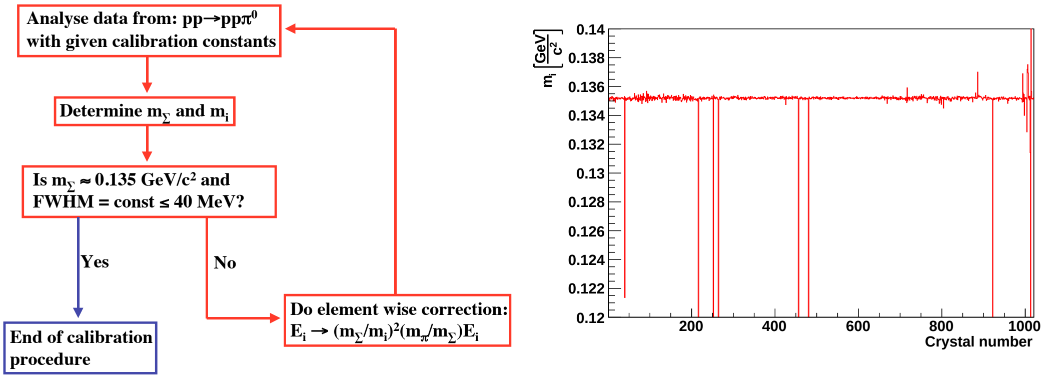

Figure 3.14: **Left:** *Schematic representation of the calorimeter calibration procedure.* **Right:** *Plot of m_i versus the corresponding crystal number after the third iteration of the procedure shown in the left frame. The vertical lines indicate defect elements.*

position m_Σ and the individual energies m_i of the crystals are checked again. The calibration procedure is finished, if m_Σ is at the π^0 mass and the corresponding FWHM does not change significantly after further iteration steps and is $\leq 40\,\text{MeV}$. Otherwise, it has to be repeated (see left hand side of Fig. 3.14) until $m_\Sigma = m_{\pi^0}$ and FWHM $= const \leq 40\,\text{MeV}$. The right side of Fig. 3.14 shows the energy m_i of each crystal as function of the crystals number after iterating the calibration procedure three times. All crystals (which are not broken or defect) have nearly the same energy around $0.135\,\text{GeV/c}^2$. The final overall invariant mass spectrum after calibration has already been shown and discussed in Fig. 3.11. The energy resolution σ of the calorimeter obtained for the current $\pi^0 \to \gamma\gamma$ calibration runs is $\sim 14\,\text{MeV}$.

3.5.4.2 Time calibration

The procedure for calibrating the time for each element is very similar to the one for the energy calibration. Fig. 3.15 shows the time measured in the SEC as function of the individual crystal number. By taking the projection for each crystal number i, the individual time distribution $x_{chn}(i)$ (see Fig. 3.16 left) given in SQDC channels can be obtained. This spectrum is fit with a Gaussian function (see red curve in Fig. 3.16 left) and the peak $x_{peak}(i)$ position is determined. After that, the SQDC time information $x_{chn}(i)$ of crystal i is transformed by the function:

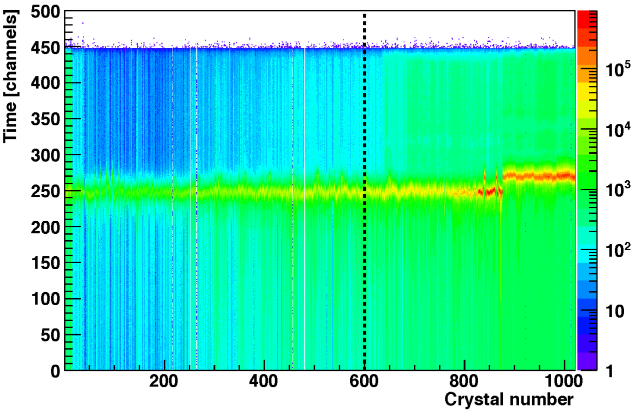

Figure 3.15: *Measured time in the SEC (in SQDC channels and relative to the main trigger) as function of the individual crystal number before the time calibration. The black dashed line indicates the projection of the time on crystal number 600.*

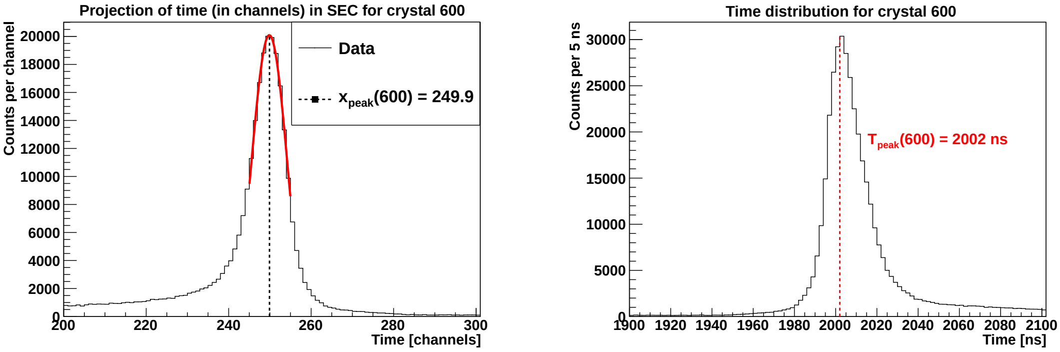

Figure 3.16: **Left:** *Time spectrum for crystal 600, obtained from the projection shown on Fig. 3.15. The peak position $x_{peak}(600)$ (black dashed line) found after fitting a Gaussian function (red curve) to that spectrum is at 249.9 channels.* **Right:** *Time distribution of crystal 600 after calibration according to Eq. 3.14. The peak centre is at 2002 ns.*

$$x_{time}(i) = -\frac{12.5}{8}\,\mathrm{ns} \cdot \left[\mathrm{x_{chn}(i) - x_{peak}(i)}\right] + 2000\,\mathrm{ns} \tag{3.14}$$

which results in a time distribution $x_{time}(i)$ given in ns with a maximum at 2000 ns (see right side of Fig. 3.16). This procedure is done, in most cases, once for each crystal in the calorimeter. The time resolution σ for each element is about ~ 7 ns.

3.5.5 Track assignment and particle identification

The decision whether a detected particle is neutral or charged depends on which detector elements fired. Table 3.1 shows all combinations of the Central Detector components which might be assigned to a track. The hits in each detector that has fired within one event, are grouped into clusters (PSB, SEC) or tracklets (MDC). The clusters of one detector are checked for geometrical and time overlap with the clusters of the remaining detectors. The parameters for checking the overlap can be adjusted in the software, which will be discussed later.

	Scenario	Responding detectors	charged/neutral
a)	Particle stopped in MDC	MDC	charged
b)	Particle stopped in PSB, or solenoid	MDC, PSB	charged
c)	Particle punching through SEC	MDC, PSB, SEC	charged
d)	Particle punching through SEC, but undetected in PSB	MDC, SEC	charged
e)	Particle punching through SEC, but undetected in MDC	PSB, SEC	charged
f)	Particle stopped in PSB, or solenoid, but undetected in MDC	PSB	charged
g)	Particle detected in SEC only	SEC	neutral

Table 3.1: *Different scenarios for the detection of a (neutral/charged) particle in the Central Detector [26].*

The track assignment algorithm works basically in three steps [26] by propagating a particle track from the beam-target interaction point (inside the MDC) to the outside of the Central Detector (SEC):

Step 1: The procedures done in this step refer to scenarios a) - d) in Tab. 3.1 and are shown in Fig. 3.17: At first, all tracklets found in the MDC are checked for geometrical/time overlap with clusters found in the PSB. For each match that is found, all clusters from the SEC are checked for a geometrical/time overlap with the MDC tracklet. A check between calorimeter and PSB clusters in this case is optional. If no overlap between MDC and PSB is found, clusters of SEC and tracklets of MDC are checked for overlap. Finally, the information provided by the MDC and every other detector which has a geometrical/time overlap with the MDC, are assigned to the charged particle track. If no match between MDC and the other detectors is found, the particle track is defined by the MDC information only.

Step 2: If all MDC tracklets and the matching clusters from PSB/SEC are assigned to tracks, the remaining clusters from PSB, which have no overlap with MDC, are checked for overlap with clusters from the calorimeter. Afterwards the particle track is updated with information from the PSB and SEC, if an overlap is found. Otherwise the track contains PSB information only. All particle tracks reconstructed in this step correspond to scenarios e) - f) in Tab. 3.1.

Step 3: The final step deals with tracks which are supposed to be caused by neutral particles (scenario g) in Tab. 3.1): All remaining SEC cluster which have no geometrical/time overlap either with the MDC or with the PSB are identified as neutral particle tracks.

A more detailed description of the track assignment done in the Central Detector can be found in [18, 26]. Anyhow, one aspect of checking the overlap between MDC tracklets and SEC clusters shall be discussed briefly because it is an important step in the analysis of $\eta \to \pi^+\pi^-\gamma$.

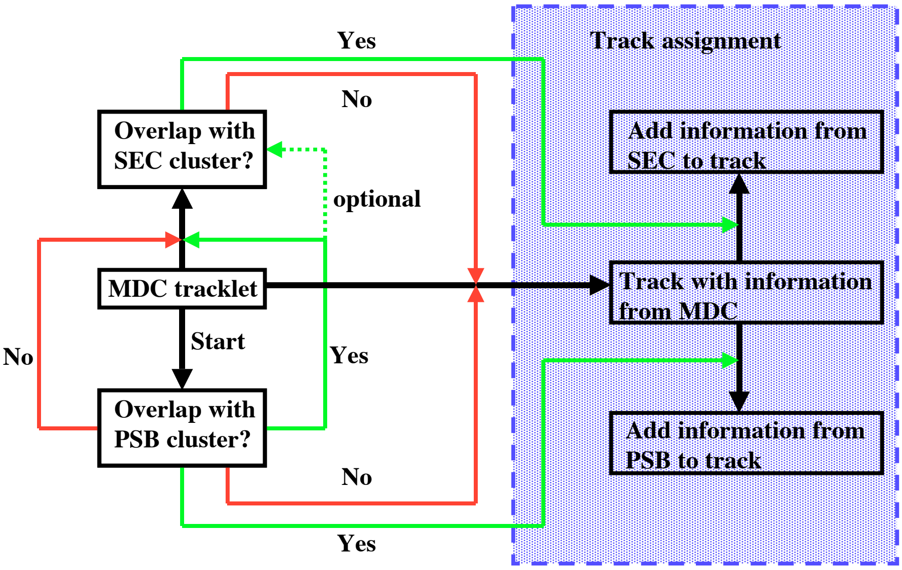

Figure 3.17: *Schematic flow diagram of the track assignment in the Central Detector of WASA. The procedure shown here is done if a particle is registered by the MDC and thus refer to the scenarios a) - d) listed in Tab. 3.1. Procedures shown on the left hand side of the blue box deal with checking geometrical/time overlap between the detectors. The final track assignment is shown inside the blue box respectively.*

3.5.5.1 Propagating MDC tracklets into the calorimeter

A charged particle inside the Central Detector is bent to a helix-like curve due to the magnetic field of the solenoid (see red curve in inset to Fig. 3.18). If the particle is not stopped in the MDC, PSB or solenoid, it will travel towards the calorimeter. However, after leaving the solenoid, the particle is not affected by the magnetic field anymore. Thus it will have a linear trajectory which is tangential to the end of its previous helix curvature. If the particle is finally detected in the calorimeter, it will be reconstructed as a cluster according to the procedure described in the previous section. This cluster is defined by a vector pointing straight from the origin to the central crystal. The method to assign this particular cluster to the charged track is shown in Fig. 3.18. In addition to the particle momentum, its charge and helix parameters, the Mini Drift Chamber also provides information about the exit point v_{EP} where the particle leaves the MDC and its direction v_{ED} pointing towards the calorimeter. The vector v_{ED} is normalised to its length. If a cluster v_{SE} originally belongs to a charged particle with given v_{EP} and v_{ED}, then the relation (see Fig. 3.18 insert):

$$|v_{SE}| = |s \cdot v_{ED} + v_{EP}| \tag{3.15}$$

has to be fulfilled for a given scaling factor s. This equation is applied to all combinations of MDC tracklets and SEC clusters. For each combination the scaling factor

s is calculated and inserted in Eq. 3.15 again. Finally the opening angle between v_{SE} and $s \cdot v_{ED} + v_{EP}$ is calculated (see insert in Fig. 3.18). Depending on that angle, the calorimeter cluster is assigned to the charged particle track. The default maximum angle for matching SEC clusters and MDC tracklets is 20° (see red dashed line in Fig. 3.18). That means all clusters and tracklets with a larger opening angle are expected to have no geometrical overlap. This procedure also plays an important part in the determination of $\eta \rightarrow \pi^+\pi^-\gamma$ events and will be discussed again in Chapter 5.

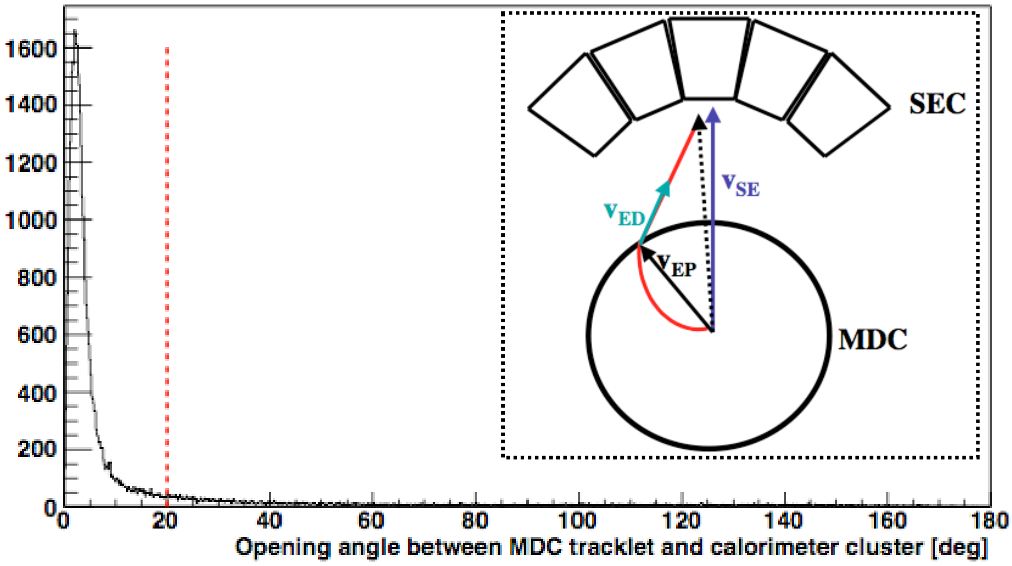

Figure 3.18: *Plot of the opening between the vector of the calorimeter cluster (purple arrow in the insert) and the reconstructed particle track without magnetic field (black, dashed arrow in the insert). The opening angle has been calculated for simulated π^+-tracks. The red dashed line indicates the selection criteria for assigning a calorimeter cluster to a charged track.* **Inset:** *Schematic drawing of a charged particle leaving the Mini Drift Chamber and flying towards the calorimeter crystals (red curve) [26]. The purple arrow indicates a vector reconstructed from a calorimeter cluster. The point, where the charged particle leaves the MDC is denoted by the vector v_{EP} (black arrow). The green arrow represents the direction vector v_{ED} which is parallel to the flight direction of the particle when leaving the MDC. By using the two vectors v_{EP} and v_{ED} it is possible to reconstruct the direction the charged particle should have without the solenoid field (black, dashed arrow).*

Finally, after assigning all detector information to tracks, particle identification can be done.

3.5.5.2 Particle identification

Fig. 3.19 shows two particle identification plots for 42% of the 2010 $pp \rightarrow pp\eta$ data. Electrons and pions have a different energy loss pattern due to their mass difference, which results in different bands separated by the red lines in Fig. 3.19. A particle identification can be performed by selecting one particular band. Furthermore, these particle identification plots can be used to optimise the analysis for a certain particle type.

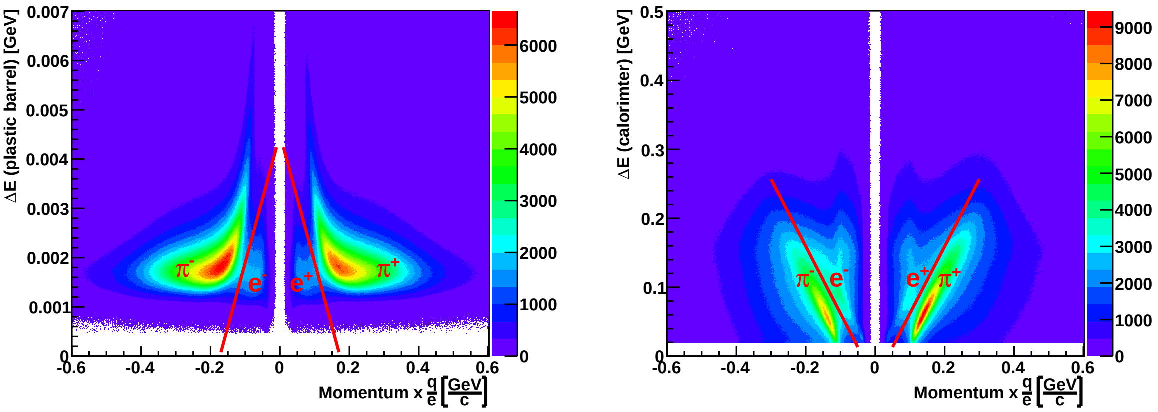

Figure 3.19: *Plot of the deposited energy in the PSB (left) and the SEC (right) as function of the momentum reconstructed in the MDC times the particle charge. The red lines are drawn for visualising the different bands caused by pions and electrons/positrons. SEC clusters with an energy smaller than* 20 MeV *are rejected.*

3.6 Data acquisition and trigger

The data acquisition system used in WASA is responsible for reading out the detector signals and providing them to a computer storage so that they can be processed for further analysis. Fig. 3.20 shows a schematic diagram of the data acquisition. In a first step, the information of each detector (analogue signal) has to be digitised where the response of each detector module has to be taken into account [41]. Signal pulses from the calorimeter for example have a much longer tail than those stemming from the plastic scintillator barrel.

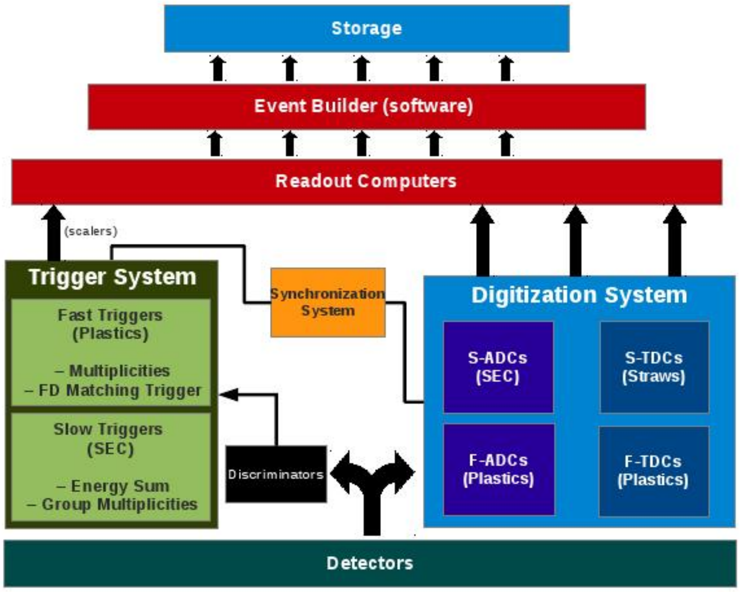

Figure 3.20: *Schematic representation of the WASA data acquisition system [18].*

3.6.1 Read out and digitisation

The detectors used in WASA (except the straw tubes) provide two pieces of information about a detected particle: (i) its energy and (ii) the time when the particle has been detected. The energy information of the particle is stored in the integrated detector signal - the charge Q. This charge is digitised by a Charge-to-Digital Converter (QDC) as the main component of that device is an Analogue-to-Digital Converter (ADC). The time is compared to a reference time and digitised by the Time-to-Digital Converter (TDC). Fig. 3.20 shows how the different detector components are read out. As mentioned before, signals coming from the calorimeter, time and as well as charge, have a long decay time and can both be readout by ADCs with a low sampling rate $\sim 80\,\mathrm{MHz}$ [41]. Those ADCs are called slow ADCs or s-ADCs (see Fig. 3.20). The straw detectors are read by slow TDCs (s-TDCs) [41].
The plastic scintillators (FRH and PSB) deliver signals with a short decay time and have to be read out by ADCs with a high sampling rate $\sim 160\,\mathrm{MHz}$ and fast TDCs [42].
As indicated in Fig. 3.20 the detector signals are split into two parts. One part is digitised (see blue box in Fig. 3.20) whereas the second part passes discriminators and is fed into the trigger system (see green box in Fig. 3.20). Signals passing the trigger have to fulfill certain conditions (see next section) and are scaled depending on the trigger that has been chosen. If a trigger fires a time stamp and an event number is generated by the synchronisation system [42]. This information is distributed to the digitisation modules. Only if the time of the detector signals is within a certain time interval around the time stamp, the digitised data is passed to the read out system. Thus the signals coming from the trigger are synchronised in time with those coming from the digitisation.

3.6.2 The trigger

The high luminosities $\sim 10^{32}\,\mathrm{cm}^{-2}\mathrm{s}^{-1}$ which can be achieved in the WASA experiment would cause a high event rate $\sim 5\,\mathrm{MHz}$ which can not be handled by the data acquisition system, having a readout capability of $\sim 20\,\mathrm{kHz}$ [43]. In order to reduce the amount of data flow, a three level trigger system is used [43].
The first trigger level comprises information from plastic scintillators in the forward and central detector parts of WASA. As indicated in Fig. 3.20, signals coming from plastic scintillators are filtered by their hit multiplicity, coincidence and track alignment [43].
The second level trigger is dedicated to events inside the calorimeter, which are filtered by their analogue energy sum and the cluster multiplicities, i.e. number of clusters above a certain energy threshold [43]. Information from the straw detectors (MDC and FPC) are not considered for the rate reduction. The first two trigger levels are implemented in hardware, because they require short processing delay times ($\sim 100\,\mathrm{ns}$ for the first and $\sim 500\,\mathrm{ns}$ for the second trigger) [43].
The third trigger level on the contrary, is software based and dedicated to a full event reconstruction [43]. For that purpose the basic trigger conditions of the different detector elements are combined by an AND-logic. The reaction $pp \to pp\eta[\eta \to \pi^+\pi^-\gamma]$ for example could be realised by the final trigger as follows:

i) At least two hits in the second FRH element are above a given energy threshold and the corresponding tracks are aligned properly. This corresponds to two protons in the Forward Detector.

ii) In addition to i): At least two clusters in the Plastic Scintillator Barrel are above a given energy threshold. This refers to the two charged pions.

iii) In addition to i) and ii): At least one cluster in the calorimeter is above a given energy threshold. This condition refers to the single photon.

These conditions are also suitable for selecting decays like $\eta \rightarrow \pi^+\pi^-\pi^0$ or $\eta \rightarrow e^+e^-\gamma$. Thus, the trigger condition mentioned above would be suitable for selecting all events which are supposed to be charged eta decays including photons.

A trigger including condition i) and at least two clusters in the calorimeter only, would be selective for $\eta \rightarrow \gamma\gamma$ events. This neutral decay is the most predominant one and can be suppressed by a prescaling factor x, i.e. only every x-th event that fires the trigger is taken. A more detailed description of the trigger system can be found in [43].

Chapter 4

Analysis Tools and the $pp\eta$ Data Set

The measured data is stored on computer clusters and processed further by the data analysis software package ROOT, which is described in the following sections. Additionally, the measured data is compared to a simulated data set in order to understand the detector response and physics background. The input of the simulated data is given by an event generator which incorporates the kinematics related to the physics of the decay channel of interest.

4.1 RootSorter

The data handling and particle track reconstruction is done by an analysis package called RootSorter which has initially been developed for the COSY-Apparatus for Studies of Nucleon and Kaon Ejectiles (ANKE) collaboration [44]. The basis of RootSorter is the ROOT data analysis framework which is an object-oriented, C++ based, software package [45]. ROOT was initially designed for high energy particle physics and has been developed at the European centre of nuclear physics research (CERN). The basic functions of ROOT contain data handling, event processing, creating and fitting of histograms and other functions that are related to data analysis. The benefits of such a framework are easy data processing on the one hand and common analysis conditions which do not depend on the individual reaction that is investigated on the other hand. The data storage and track reconstruction in each detector are assigned to individual C++ classes within RootSorter and may be called in the individual analysis scripts.

Fig. 4.1 shows a diagram representing the data flow and data processing. The hit information of each detector element is stored in object classes (hit banks) and grouped into clusters by a cluster finding routine which is part of the RootSorter analysis modules. The clusters are stored in cluster banks and finally processed by track finding routines. The tracks are stored in track banks respectively and can be processed in the final analysis which is related to a certain physics reaction (e.g. $\eta \to \pi^+\pi^-\gamma$).

4.2 The Pluto event generator

The input information for the simulated data is provided by the Pluto event generator (see Fig. 4.1) which is dedicated to hadron-physics reactions and has been designed within the HADES collaboration [46]. The input for Pluto are the particles that participate at the reaction of interest and the beam kinetic energy.

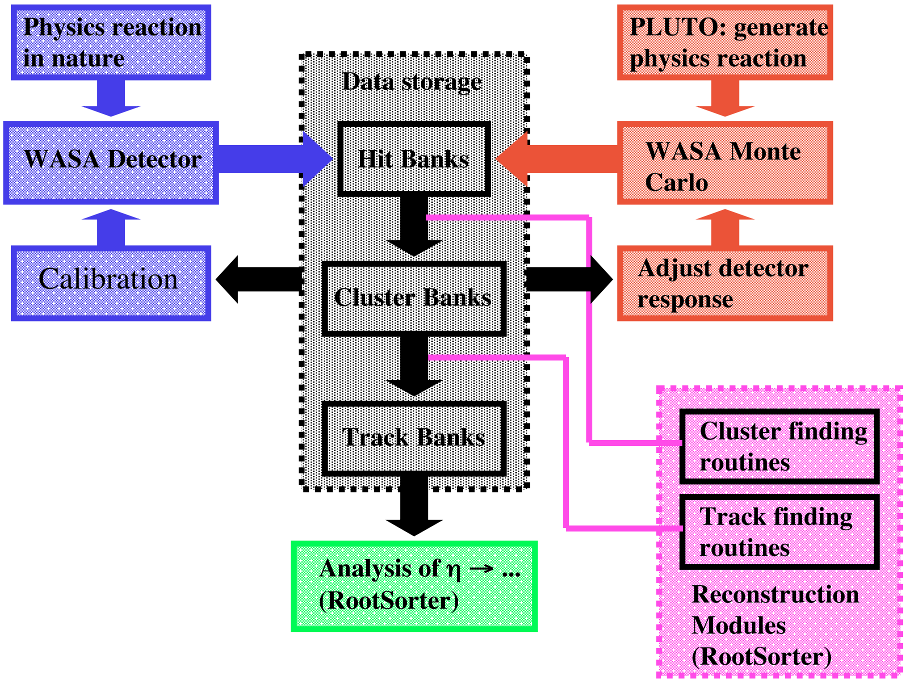

Figure 4.1: *Schematic representation of the data flow before analysis.*

The kinematics of all particles are, by default, defined by an isotropic phase space distribution, but it is also possible to incorporate the underlying physics of a certain reaction which defines the kinematics of the particle final states.
The kinematics of the generated decay $\eta \to \pi^+\pi^-\gamma$ for example, are implemented and defined in Pluto by the decay amplitude discussed in Chapter 2. The final output of Pluto are the momenta, angles and energies of all particles that have been defined in the input.

4.3 The WASA Monte Carlo (WMC) simulation package

After generating hadronic reactions with Pluto, the response of the WASA detector to those events is simulated with the WMC program which is based on GEometry ANd Tracking (GEANT) [47]. This program is a tool for simulating the response of a (virtual) detector on (simulated) particles propagating through it. The interactions between the propagating particles and the detector components are computed by calculating the energy losses of the particles in active and non-active detector material. Furthermore, physical effects like photon conversion or secondary particle decays are included. Additional inputs for the WMC program might be information about the individual detector parts, e.g. dead tubes in the drift chamber, or shower losses in the individual parts of the calorimeter. The final output of the WMC simulations are data files containing events with hit information of each detector but also information about the initial kinematic variables of each particle. Those files can be passed to the analysis chain shown in Fig. 4.1 and processed in exactly the same way as the measured data. This procedure allows to study the measured data in various aspects because the output of the WMC simulations is well defined by the generated physics events and the detector information that has been put in.
It is also possible to generate single particle tracks by using an internal event gener-

ator which is built in the WMC package and does not depend on Pluto. In this case single particle tracks are simulated with in isotropic energy and angular distribution. This method will be important when performing the error parameterisation for the kinematic fit which will be discussed in Chapter 5.
The comparison between the measured and simulated data sets is only possible, if the measured data is calibrated and the detector response in the simulation is adjusted properly.
The adjustment of the detector response in WMC is done in such a way that detector thresholds, the energy resolution or drift distances can be adapted by the user. This method has the benefit, that effects which are not implemented in the Monte Carlo (MC) simulations can be taken into account (e.g. gain instabilities during the measurement). The energy resolution of the plastic scintillators for example can be changed by introducing an absolute or relative Gaussian smearing to the deposited energy ΔE in the scintillator:

$$\Delta E \mapsto \Delta E + \mathrm{Gauss}_{\mathrm{random}}(0, \sigma_{smear,abs}) \tag{4.1}$$

$$\Delta E \mapsto \Delta E \cdot \mathrm{Gauss}_{\mathrm{random}}(1, \sigma_{smear,rel}) \tag{4.2}$$

The first equation represents the absolute Gaussian smearing and the second equation represents the relative Gaussian smearing respectively. The function $\mathrm{Gauss}_{\mathrm{random}}$ returns a random number from a Gaussian distribution with mean value 0/1 and resolution $\sigma_{smear,abs}/\sigma_{smear,rel}$. The resolution σ_{smear} is a variable which can be adjusted by the user. Different values for σ_{smear} result in different resolutions of the corresponding detector. The resolution or response of the straw tubes is mainly adjusted by changing the drift times. The resolution of the calorimeter is tuned by varying the parameter $\frac{\sigma(E)}{\sqrt{E}}$ which has already been discussed in Chapter 3.
A correct description of the WMC generated data with respect to the measured data is tremendously important, because otherwise a detailed understanding of the final analysis will not be possible.

4.4 The data set

In the WASA-at-COSY experiment there are two production mechanisms for the η meson available. The first one is $pd \rightarrow {}^3\mathrm{He}\eta$ and the second one is $pp \rightarrow pp\eta$ which was employed for the data set of this analysis. Each of them has its advantages and disadvantages which are discussed in the following section.

4.4.1 η production at WASA-at-COSY

Table 4.1 summarises the characteristics of the two η production methods mentioned above. T_{beam} denotes the kinetic beam energy which is used in each case and refers to an excess energy of $\sim 60\,\mathrm{MeV}$. The cross section of the corresponding η production process is described by $\sigma(\eta)$. Table 4.1 shows that the η production cross section for the reaction $pp \rightarrow pp\eta$ is about 24 times larger than the corresponding cross section for $pd \rightarrow {}^3\mathrm{He}\eta$. This allows on the one hand to study rare decay processes such as $\eta \rightarrow e^+e^-$ but has the drawback of a large background contribution from multi-pion production (see Table 4.2). This is not the case when using the reaction $pd \rightarrow {}^3\mathrm{He}\eta$. The multi-pion production rate is lower (see Table 4.2) but the price for that is the insufficient statistics to measure rare η decay processes. Another advantage, that comes along with the analysis of $pd \rightarrow {}^3\mathrm{He}\eta$ decays is the easy tagging of the η

	pd → ^{3}Heη	**pp → ppη**
$\boldsymbol{T_{beam}}$	1 GeV	1.4 GeV
$\boldsymbol{\sigma(\eta)}$ [48, 49]	$(0.412 \pm 0.016)\,\mu$b	$(9.8 \pm 1)\,\mu$b
Suited for	study of not-so-rare η decays	study of (not-so-) rare η decays
Background	low multi-pion background	high multi-pion background

Table 4.1: *Short summary of the main aspects of the two different η production mechanisms used for the WASA-at-COSY experiment.*

Reaction	$\boldsymbol{T_{beam}}$**[GeV]**	$\boldsymbol{\sigma[\mu}$**b]** [49, 50]
$pd \rightarrow {}^3\mathrm{He}\pi^0\pi^0$	0.893	2.8 ± 0.3
$pd \rightarrow {}^3\mathrm{He}\pi^+\pi^-$	0.893	5.1 ± 0.5
$pp \rightarrow pp\pi^+\pi^-\pi^0$	1.36	4.6 ± 1.5
$pp \rightarrow pp\pi^0\pi^0$	1.36	200 ± 30
$pp \rightarrow pp\pi^+\pi^-$	1.36	660 ± 100

Table 4.2: *Summary of multi-pion production cross sections that compete with the different η production mechanisms.*

meson, because the ^{3}He particle is mainly stopped by the thin plastic scintillators in the Forward Trigger Hodoscope and thus can be easily identified. Protons stemming from the reaction $pp \rightarrow pp\eta$ might punch through the whole Forward Detector and deposit their energy throughout the whole Forward Range Hodoscope.
There is no single argument that determines which η production process is better or worse. It depends on the experimentalists purpose such as the ability to study, more or less, background free but not-so-rare decay processes or rather rare decays which come along with a large multi-pion background.
The aim of studying $\eta \rightarrow \pi^+\pi^-\gamma$ in $pp \rightarrow pp\eta$ is to improve the statistical uncertainty. It also allows to cross check the results which have already been gained from the analysis $pd \rightarrow {}^3\mathrm{He}\eta[\eta \rightarrow \pi^+\pi^-\gamma]$ because each production mechanism comes along with different systematic uncertainties.
Table 4.2 shows the cross sections of multi-pion production reaction for beam kinetic energies in the region of the η production. In case of $pp \rightarrow pp\eta$ there are three multi-pion production reactions which dominate the background and may overwhelm the η signal. Thus, the challenge of this work is to sufficiently eliminate the background without loosing too much acceptance for the η signal.

4.4.2 Preselection and experimental trigger

The WASA-at-COSY experiment has taken $pp \rightarrow pp\eta$ data in three different periods which are listed in Table 4.3. Taking all those data sets into account leads to $\lesssim 1 \cdot 10^9$ expected η events stored on tape. The file size per data run is ~ 21 GB (see Appendix A) which is still not sufficiently small to be stored on a hard disk cluster, if all runs are analysed. According to the previous section the $pp\eta$ data contains a large fraction of events stemming from multi-pion production reactions, which are not needed for the analysis. The time needed to analyse the whole data set with a well tuned and sophisticated analysis program would be in the order of a year[a], which is not feasable. Thus, a reduction of the taken data is needed in order to decrease the amount of data stored on disk and to limit the time needed for offline

---

[a] This estimation is based on the usage of the recent analysis code.

analysis. For that purpose a preselection has been done in which events are selected that are supposed to be related to charged η decays.

Data taken in	Duration of beamtime	Quantity of stored data [TB]
Winter 2008	2 weeks	35
Spring 2010	7 weeks	98
Spring 2012	8 weeks	118

Table 4.3: *$pp \to pp\eta$ data taken by the WASA-at-COSY fascility. The right column in this table shows the file size of the taken data which is stored on tapes. The red coloured row refers to the data set which will be discussed and analysed within this thesis.*

4.4.2.1 Preselection of the 2010 $pp\eta$ data set

Fig 4.2 shows the two selection criteria that have been implemented in the preselection. The first selection step is dedicated to the two protons in the final state which are reconstructed in the Forward Detector. For that purpose the missing mass deduced from the two initial and two final protons is investigated. The missing mass is defined by all measured particles in the reaction $p_{beam}p_{target} \to p_1p_2\eta$:

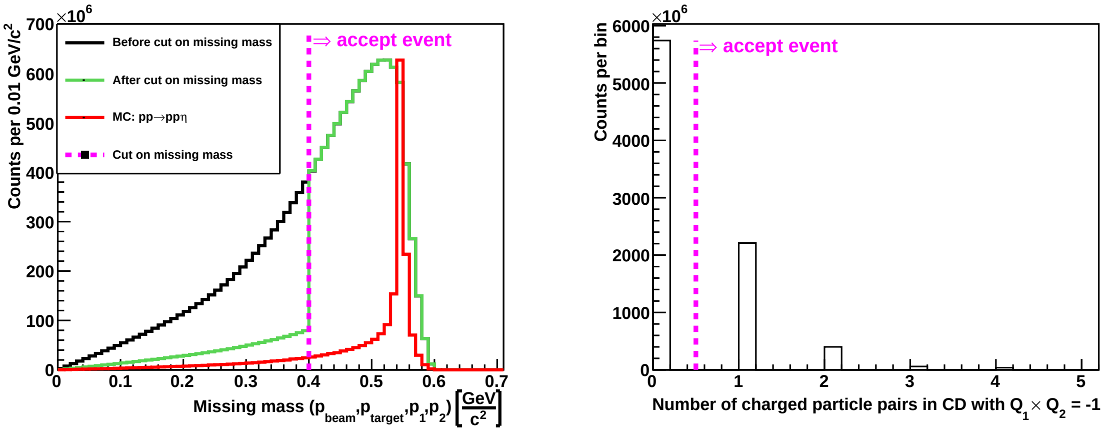

Figure 4.2: **Left:** *Missing mass distribution of the measured data before and after applying a missing mass cut (purple dashed line). The red curve shows the missing mass distribution of the MC simulated reaction $pp \to pp\eta$. The purple dashed line indicates the first preselection condition.* **Right:** *Multiplicity of charged particle pairs in the Central Detector with opposite charge. The purple dashed line indicates the second preselection condition.*

$$\text{Missing mass } (p_{beam}, p_{target}, p_1, p_2) = |\mathbf{P}_{p_{beam}} + \mathbf{P}_{p_{target}} - (\mathbf{P}_{p_1} + \mathbf{P}_{p_2})| \tag{4.3}$$

where $\mathbf{P}_i$ is the four momentum vector of a particle i:

$$\mathbf{P}_i = \begin{pmatrix} p_x \\ p_y \\ p_z \\ E \end{pmatrix}, \ |\mathbf{P}_i| = \sqrt{E^2 - (p_x^2 + p_y^2 + p_z^2)} = m_i \tag{4.4}$$

The η meson is unmeasured but its mass can be calculated by Eq. 4.3 and Eq. 4.4 due to energy and momentum conservation. The missing mass in Eq. 4.3 is a distribution with maximum at the η mass because the reconstruction of the proton

variables is influenced by the detector properties (e.g. resolution, efficiency, etc.). The missing mass only depends on the proton pair p_1, p_2 which are reconstructed in the Forward Detector because the beam and target protons are fixed and well defined.
The left side of Fig. 4.2 shows a plot of Eq. 4.3 related to Monte Carlo simulations of $pp \rightarrow pp\eta$ (see red curve). This distribution has a maximum at the η mass $m_\eta = 0.5478\,\mathrm{GeV/c^2}$ and fast dropping tails. The corresponding spectrum deduced from the 2010 data set is represented by the black curve in Fig. 4.2. This distribution shows no clear η signal because of the dominating multi-pion background. In order to reduce this background, a cut on the missing mass has been introduced (purple dashed line in Fig. 4.2). This cut is defined in a way that all events are accepted which contain at least one pair of reconstructed protons with a missing mass larger than $0.4\,\mathrm{GeV/c^2}$. The event is rejected if no such proton pair exists. The missing mass spectrum which is related to that condition is represented by the green curve in Fig. 4.2. The tail at missing masses smaller than $0.4\,\mathrm{GeV/c^2}$ is caused by events where more than two proton tracks are reconstructed.
The cut on the missing mass distribution has been chosen in that particular way in order to meet three requirements. The first one implies that the largest fraction possible of background related events should be filtered out. In addition to that, the minimum possible signal events should be affected by the missing mass cut. The third requirement is that the selection of signal events should not be too sensitive to the calibration of the Forward Detector, because this might be optimised later. The left side of Fig. 4.2 shows that the missing mass cut only effects the left tail of the MC generated missing mass distribution and therefore has no influence on the signal region around the η-mass.
The second preselection condition, which is done in addition to the first one, is shown on the right hand side of Fig. 4.2. All events that contain at least one pair of reconstructed charged tracks in the Central Detector with opposite sign are accepted. This condition implies the track reconstruction by the Mini Drift Chamber and therefore demands a sufficient pre-calibration of the drift times. The final fitting routine, which is implemented in the MDC track reconstruction, has not been used because only the charge information was needed. This also ensures a less restrictive event selection. Applying both preselection conditions on the 2010 data set leads

	Acceptance [%]		
Simulated reaction	MM. cut	Geom.	Presel.
$\eta \rightarrow \pi^+\pi^-\pi^0$	86	59	27
$\eta \rightarrow \pi^+\pi^-\gamma$	86	65	32
$\eta \rightarrow e^+e^-\gamma$	86	83	35
$pp \rightarrow pp\pi^+\pi^-\pi^0$	66	54	18
$pp \rightarrow pp\pi^0\pi^0$	19	n.a.	0.2
$pp \rightarrow pp\pi^+\pi^-$	23	66	10

Table 4.4: *Acceptance for different simulated reactions related to: (i) The cut on the missing mass shown in Fig. 4.2 (ii) Geometrical acceptance of charged particles in the Central Detector and (iii) Requesting condition (i) and at least one charged pair in the Central Detector with opposite sign.*

to a file size of ~ 1.9 GB (see Appendix A) per run (including file compression). This is nearly a factor ten reduction of the original raw data file size, which will decrease the time for analysing the complete data set by roughly the same factor.

The acceptance of the whole preselection procedure is shown in Table 4.4 for different simulated reactions. According to this table, the acceptance for $\eta \rightarrow \pi^+\pi^-\gamma$ is $\sim$ 32%. This number shall be explained briefly in the following: Fig. 4.3 shows the geometrical acceptance for protons and pions stemming from the decay $\eta \rightarrow \pi^+\pi^-\gamma$, which is reconstructed in WASA. The geometrical acceptance for one proton being registered in the Forward Detector is $\sim$ 94%. The corresponding acceptance for a charged pion pair is $\sim$ 65% (see also third column in table 4.4). A cut on the proton missing mass refers to an efficiency of $\sim$ 86% (see second column in Table 4.4) and already includes the geometrical acceptance for protons. The remaining part of the event reduction is given by the reconstruction efficiency of a charged particle within the Mini Drift Chamber, which turned out to be in the order of $\sim 70 - 75\%$ (according to the values presented in Table 4.4). Taking all this into account leads to the total preselection efficiency of 32% for $\eta \rightarrow \pi^+\pi^-\gamma$.

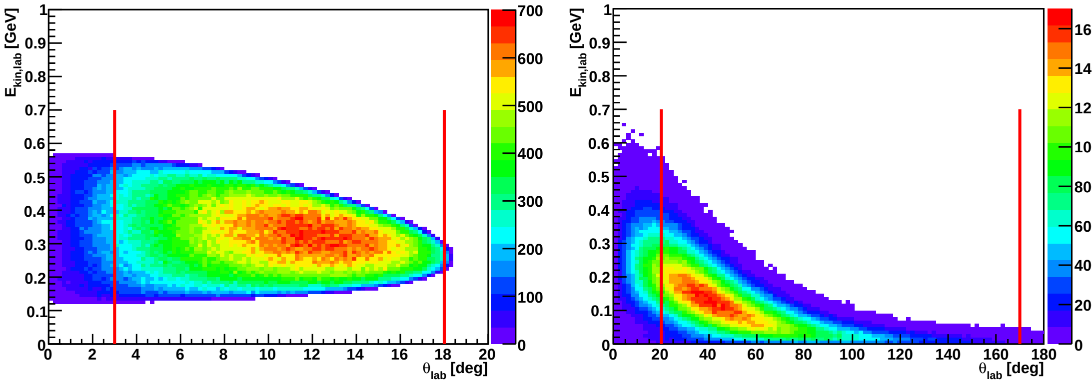

Figure 4.3: *Kinetic energy of protons (left) and pions (right) in the laboratory system as a function of the polar angle in the laboratory system. Both plots have been obtained from Pluto generated $\eta \rightarrow \pi^+\pi^-\gamma$ events. The red lines indicate the geometrical acceptance for protons in the Forward Detector (left) and pions in the Central Detector(right). Most of the pions are boosted into the forward direction.*

The different η decays listed in Table 4.4 show different preselection efficiencies which will be explained in the following: The efficiency related to the missing mass cut shown in Fig. 4.2 is unique for all eta decays, because the eta production mechanism and thus the corresponding proton missing mass distribution is decay independent. The geometrical acceptance for a charged particle pair in the Central Detector (see second column in Table 4.4) is different for each decay, due to the individual kinematics. Therefore, the preselection efficiency slightly changes for different η decays. Table 4.4 shows the capability for rejecting events stemming from direct pion production reactions, which is solely given by the missing mass condition. The production of two neutral pions is additionally suppressed by the request of two charged tracks in the Central Detector.

4.4.2.2 Experimental trigger for the 2010 $pp\eta$ data set

The main experimental trigger used during taking the 2010 data set is composed of two parts. The first part deals with hits in the Forward Detector which are supposed to be the final state protons of the reaction $pp \rightarrow pp\eta$. For that purpose at least two hits in the second layer of the Forward Range Hodoscope with a geometrical overlap to the forward tracking detectors are required. The second part of the trigger is dedicated to the decay products of charged η decays and therefore demands at least two hits in the Plastic Scintillator Barrel and at least one hit in the calorimeter. The constraint on the PSB hit multiplicity refers to charged particles and shall ensure that they passed the Mini Drift Chamber which is used for track reconstruction. Photons are requested by hits in the calorimeter. Fig. 4.4 summarises the trigger and preselection statistics done for $\sim 20\%$ of the 2010 $pp\eta$ data set. Every time the trigger or preselection condition (or a combination of both) is fulfilled within one event the corresponding histogram bin is filled. The results of that study show a 96% overlap between the preselection conditions and the experimental trigger (i.e. between third and fourth horizontal bar in Fig. 4.4). Thus, an explicit request of that trigger (i.e. selecting only events, where this trigger fired) during data analysis is not needed. This simplifies the comparison between simulated and measured data, because the experimental trigger conditions are more difficult to implement (e.g. detector thresholds) in the analysis of simulated events than the preselection conditions.

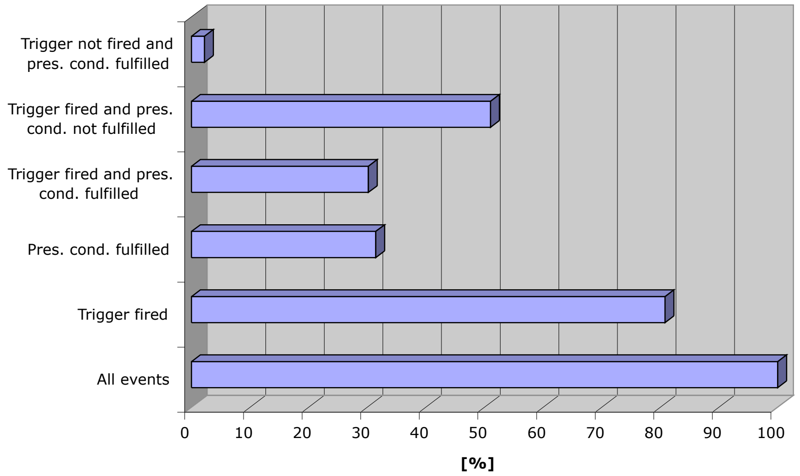

Figure 4.4: *Trigger statistics for* $\sim 20\%$ *of the analysed 2010 $pp\eta$ data set.*

4.5 Matching simulations to data

A very important issue in data analysis is the comparison to simulations. This is only possible if the experimental conditions are sufficiently reproduced in the simulated data sets.

4.5.1 π^0 peak position and calorimeter resolution

The first step in matching the measured and simulated data sets is the adjustment of the π^0 peak position and resolution. For that purpose the two photon π^0 invariant mass (see Eq. 3.8) has been monitored for each individual run during the preselection of the 2010 $pp\eta$ data set, as well as for the simulated decay $\eta \rightarrow \pi^+\pi^-\pi^0$. The π^0 peak position and resolution were determined according to Eq. 3.12. The results of this procedure are shown in Fig. 4.5. The top left diagram shows, that the π^0 peak position is for a large fraction of the runs at $\sim 0.142\,\mathrm{GeV/c^2}$. The reasons for such a run dependent resolution might have several reasons, such as gain instabilities or periods of varying detector rates. The total invariant mass spectrum of all analysed runs is shown at the top right corner of Fig. 4.5. This distribution was fit with a combination of the Novosibirsk function and a third order polynomial. The peak position deduced from that fit is $m_{\pi^0,fit} = 0.141\,\mathrm{GeV/c^2}$, as the corresponding fit error is negligible. In order to get the individual and overall peak position at the physical π^0 mass, a correction factor $\kappa(i)$ is introduced for each run i:

$$\kappa(i) = \frac{0.135\,\mathrm{GeV/c^2}}{m_{\pi^0}(i)} \tag{4.5}$$

$m_{\pi^0}(i)$ is the π^0 peak position of the invariant mass spectrum referring to run i which is shown in the top left of Fig. 4.5. This correction factor is multiplied by the calibration correction factor discussed in Eq. 3.11. After applying this correction, the overall invariant mass spectrum has its peak position at $0.135\,\mathrm{GeV/c^2}$ and a resolution of 16 MeV (The corresponding spectra will be shown and discussed in the lower part of this section). The average π^0 peak position per run improved to $\sim 0.134\,\mathrm{GeV/c^2}$. Additionally, the position of the $\eta \to \gamma\gamma$ peak per run was checked, in order to cross check the run dependent correction factor. The average

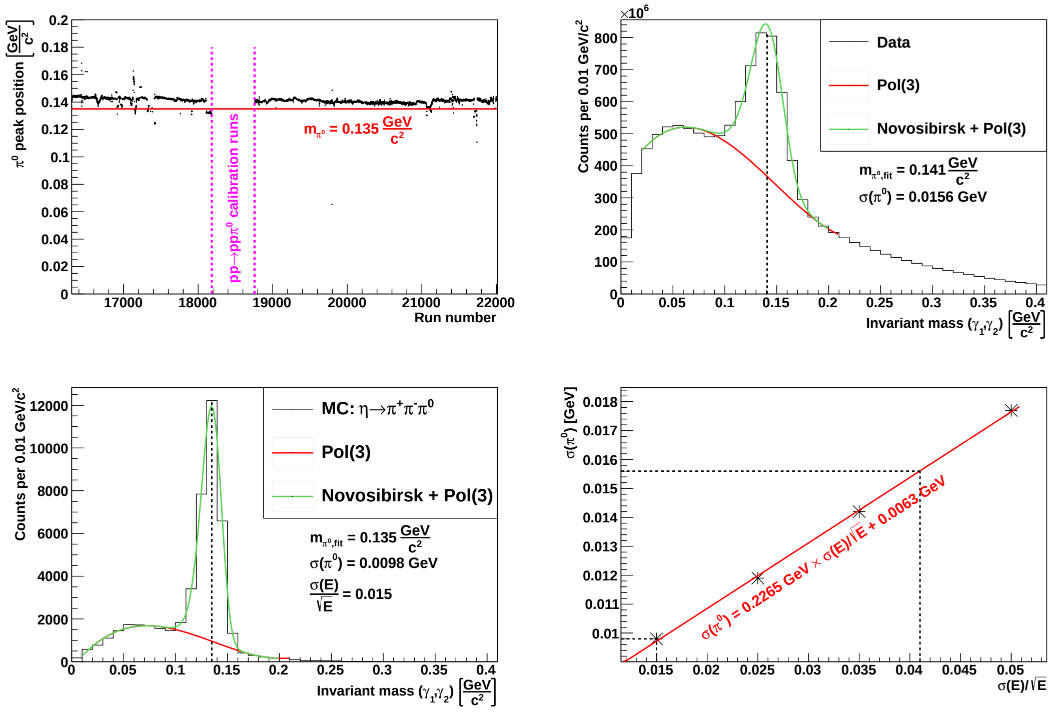

Figure 4.5: **Top left:** *Calculated π^0 peak position for each run of the 2010 $pp\eta$ data set. The red line indicates the nominal π^0 mass. The area between the purple lines shows no entries, because those runs belong to the $pp \to pp\pi^0$ calibration data set.* **Top right:** *Invariant mass distribution deduced from two photons for all runs stemming from the 2010 $pp\eta$ data set.* **Bottom left:** *Invariant mass distribution deduced from two photons for Monte Carlo (MC) simulated $\eta \to \pi^+\pi^-\pi^0$ events. The peak resolution $\sigma(\pi^0)$ has been adjusted by a smearing factor $\frac{\sigma(E)}{\sqrt{E}} = 0.015$. The background of both invariant mass distributions shown in the top right and bottom left frame is fit by a third order polynomial (red curve). The total signal is described by the Novosibirsk function plus a third order polynomial (green curve).* **Bottom right:** *π^0 peak resolution $\sigma(\pi^0)$ for different smearing parameters $\frac{\sigma(E)}{\sqrt{E}}$ for simulated $\eta \to \pi^+\pi^-\pi^0$ events. The red curve represents a linear fit to the four data points.*

eta mass per run is $\sim 0.546\,\mathrm{GeV/c^2}$, which is in good agreement with the expected eta mass [10].

In a next step, the resolution of the π^0 peak deduced from the simulated data has to be adjusted to the resolution from the data. For that purpose, simulated $\eta \rightarrow \pi^+\pi^-\pi^0$ events are analysed for different $\frac{\sigma(E)}{\sqrt{E}}$ parameters (see e.g. Fig. 4.5 lower left) which are responsible for the energy smearing in the calorimeter. The invariant mass distribution is again fit by a third order polynomial plus a Novosibirsk function (see green curves in top right and bottom left frame of Fig. 4.5). Afterwards the obtained π^0 peak resolution is plotted as function of $\frac{\sigma(E)}{\sqrt{E}}$ which is shown in the bottom right diagram of Fig. 4.5. The data points are fit by a linear function. Using this function and the π^0 peak resolution obtained from the measured data, it is possible to calculate the appropriate smearing parameter $\frac{\sigma(E)}{\sqrt{E}}$ which was determined to be 0.041 (see dashed line in bottom right diagram in Fig. 4.5).

After adjusting the calorimeter resolution within the simulated data, the π^0 and $\eta \rightarrow \gamma\gamma$ peak position is determined for simulated $\eta \rightarrow \pi^+\pi^-\pi^0$ and $\eta \rightarrow \gamma\gamma$ events. Ideally, the simulated π^0 and η two photon invariant masses should be in agreement with the average mass values obtained from the experimental data. The two photon invariant mass distributions deduced from simulated $\eta \rightarrow \pi^+\pi^-\pi^0$ and $\eta \rightarrow \gamma\gamma$ events are presented in Fig. 4.6. Each distribution is again fit by a third order polynomial plus a Novosibirsk function (see green curves in top row of Fig. 4.6) and

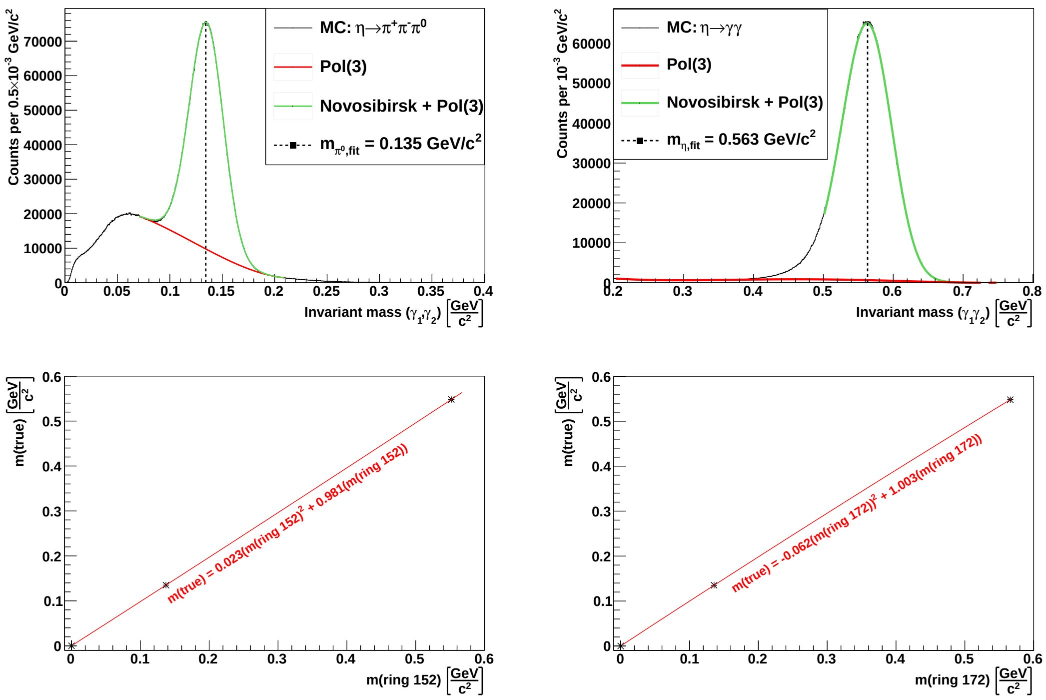

Figure 4.6: **Top:** *Two photon invariant mass distributions obtained from simulated* $\eta \rightarrow \pi^+\pi^-\pi^0$ *(left frame) and* $\eta \rightarrow \gamma\gamma$ *(right frame) events. The red curves in each diagram represent a third order polynomial, which was fit to the background. The green curves represent the polynomial plus a Novosibirsk function, which describes the signal peak. The black dashed lines refer to the peak position, which was found by fitting the green curve to the simulated distributions.* **Bottom:** *True* π^0 *and* η *mass as function of the corresponding mass determined from the spectra shown in the top frame for calorimeter ring number 152 (left) and 172 (right). The red curves represent a quadratic fit. In order to avoid non-physical invariant mass offsets, the point* $(0, 0)$ *is included.*

the individual peak position is determined. The value obtained for the two photon π^0 invariant mass is in agreement with the average mass value estimated for the measured data (see value in the box in the top left diagram of Fig. 4.6). In contrast, the η mass value deduced from simulations (see value in the box in the top right diagram of Fig. 4.6) shows a clear disagreement and is $\approx 3\%$ larger than the true value. According to that, the individual energy of a photon stemming from $\eta \rightarrow \gamma\gamma$ is a few percent too large, because $E_\gamma \sim \sqrt{\text{Invariant mass}}$.

Photons stemming from $\eta \rightarrow \pi^+\pi^-\gamma$ reactions cover the energy range of low energy $\pi^0 \rightarrow \gamma\gamma$ as well as high energy $\eta \rightarrow \gamma\gamma$ photons. Thus, the simulated E_γ-distribution is effected by the disagreement between the true and reconstructed $\eta \rightarrow \gamma\gamma$ mass. This mismatch has to be solved, otherwise the description of the decay $\eta \rightarrow \pi^+\pi^-\gamma$ is not consistent within the simulated and measured data set. In a first approach (which is not shown here), a global correction factor was introduced, which shifts the $\eta \rightarrow \gamma\gamma$ spectrum towards smaller mass. As a consequence, the η mass was adjusted properly, but the obtained π^0 mass was too small. This problem was overcome, by introducing a calorimeter ring (see Section 3.5.3) dependent photon energy correction for the simulated data set. The corrected photon energy $E_{\gamma,corr}(i)$ is given as function of the calorimeter ring number i and the corresponding energy $E_\gamma(i)$, which was reconstructed in that ring:

$$E_{\gamma,corr}(i) = \left[a(i) \cdot \sqrt{E_\gamma(i)} + b(i)\right]^2 \cdot f_{glob} \tag{4.6}$$

This correction is equivalent to the element-wise calibration presented in Eq. 3.11. The only difference is the additional parameter $b(i)$, which ensures the proper relative adjustment of the π^0 and $\eta \rightarrow \gamma\gamma$ peak position. The parameters $a(i)$ and $b(i)$ (listed in Appendix B) were found by deducing the invariant mass distributions of simulated $\eta \rightarrow \pi^+\pi^-\pi^0$ and $\eta \rightarrow \gamma\gamma$ events for each individual calorimeter ring i. The corresponding peak positions were determined, by fitting a Novosibirsk function plus a third order polynomial to each distribution. The obtained, ring dependent, two photon invariant masses are compared to the true values of the η and π^0 mass. The bottom row of Fig. 4.6 shows an example of this procedure for a ring in the back part (number 152) and in the front part (number 172) of the calorimeter. All three points are fit by a quadratic function[b] (see red curves). The coefficients of that function correspond to the parameters $a(i)$ and $b(i)$ in Eq. 4.6. This procedure was done for all 24 ring elements within the calorimeter. The global factor f_{glob} in Eq. 4.6 is adjusted by fine tuning the global (i.e. over all rings) invariant mass distributions towards the true π^0 and η masses.

The final results of this procedure are shown in Fig. 4.7. The peak position of the individual invariant mass distribution is presented as function of the single photon energy (first row) and the corresponding ring (second row). The final overall distributions are plotted in the third row. Applying no energy correction causes the π^0 masses to fluctuate between $\sim 0.13\,\text{GeV/c}^2$ and $\sim 0.145\,\text{GeV/c}^2$ for photon energies $\leq 0.4\,\text{GeV}$ (see black points in top left diagram of Fig. 4.7) and different rings (see black points in centre left diagram). After applying the correction (purple points), the peak position as function of the single photon energy / ring number increases within the order of $\lesssim 2\,\text{MeV} = 1.5\%$. The η invariant mass for each ring / energy range is reduced by $\lesssim 15\,\text{MeV} = 2.7\%$, if the energy correction is applied. For both simulated decay channels, the change of the individual invariant mass peak position is in the order of a few percent, which was expected. The right column of

---

[b] Here, a quadratic function was used, in order to include the point $(0, 0)$ within the fit.

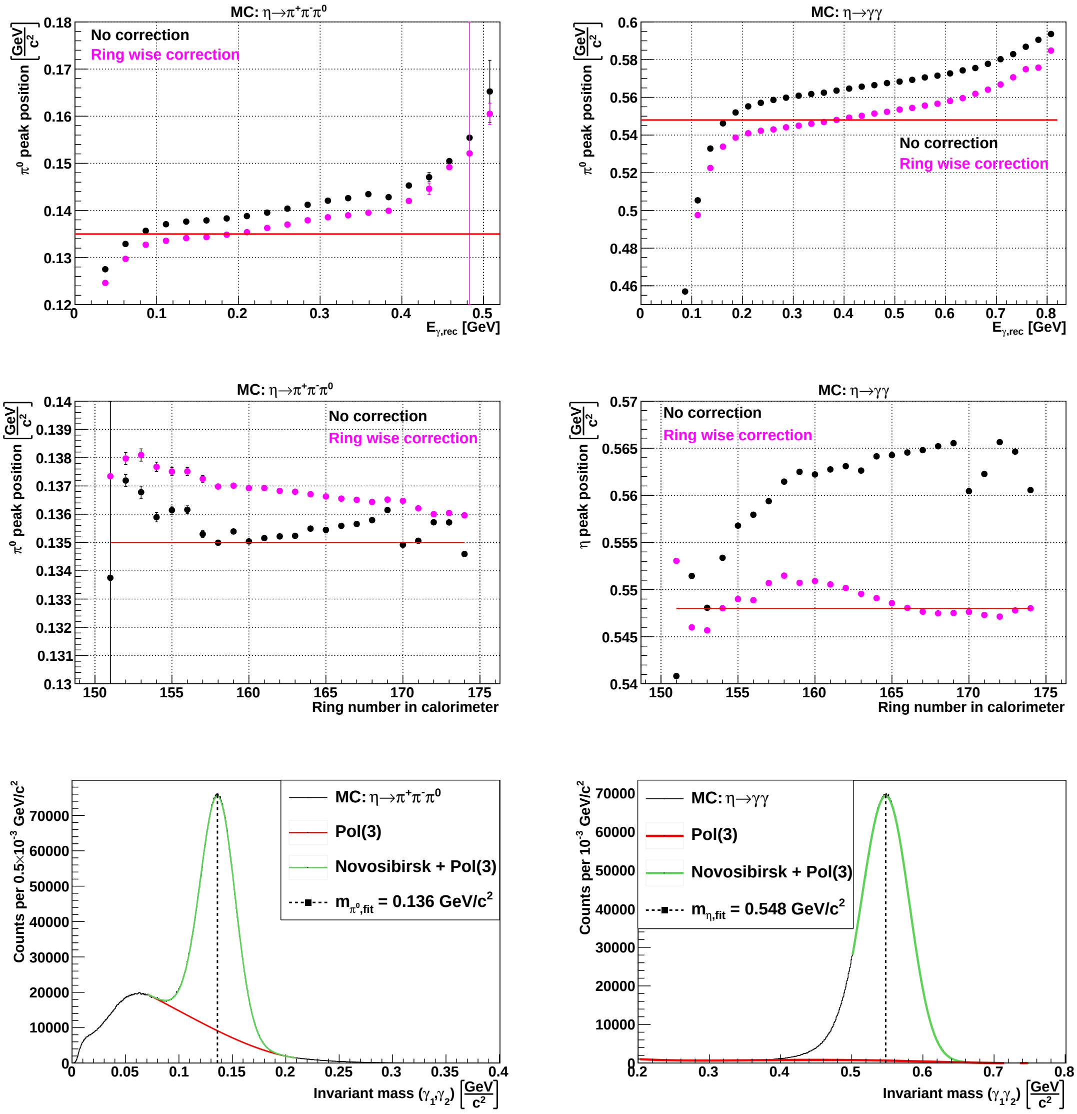

Figure 4.7: *Peak position of the two photon invariant mass distribution deduced from simulated $\eta \rightarrow \pi^+\pi^-\pi^0$ (left) and $\eta \rightarrow \gamma\gamma$ (right) events as function of:* **Top:** *The reconstructed energy of a single photon.* **Centre:** *The ring number within the calorimeter. The numbering starts at 151 (ring in the back part) and ends at 174 (ring in the front part). Peak positions calculated with /without the correction shown in Eq. 4.6, are presented by purple / black data points. The error bars represent the parameter errors obtained from fitting a Novosibirsk function plus a third order polynomial. The red lines represent the true values $m_{\pi^0} = 0.135\,\mathrm{GeV/c^2}$ and $m_\eta = 0.5478\,\mathrm{GeV/c^2}$.* **Bottom:** *Overall two photon invariant mass spectra for simulated $\eta \rightarrow \pi^+\pi^-\pi^0$ (left) and $\eta \rightarrow \gamma\gamma$ (right) decays, including the ring wise energy correction. The black dashed lines refer to the peak position, which was found by fitting a Novosibirsk function plus third order polynomial (green curve) to the simulated distributions.*

Fig. 4.7 shows that the deviation of the $\eta \rightarrow \gamma\gamma$ peak from the true value (indicated by red line) is significantly improved by introducing the ring and energy dependent correction. The peak position of the overall invariant mass spectra are indicated by the black, dashed lines in the bottom diagrams of Fig. 4.7. The π^0 peak position changed from $0.135\,\mathrm{GeV/c^2}$ to $0.136\,\mathrm{GeV/c^2}$, whereas the $\eta \rightarrow \gamma\gamma$ peak position changed from $0.563\,\mathrm{GeV/c^2}$ to $0.548\,\mathrm{GeV/c^2}$, respectively. Thus, the two photon invariant mass distributions for simulated $\eta \rightarrow \pi^+\pi^-\pi^0$ and $\eta \rightarrow \gamma\gamma$ reactions are adjusted relative to each other properly and are comparable with the measured data set.

4.5.2 FRH resolution

The resolution of each layer in the Forward Range Hodoscope is adjusted in a similar way as discussed above: The relative energy smearing $\sigma_{smear,rel}(i)$ (see Eq. 4.2) for simulated energy deposits in FRH layer i is varied and the corresponding energy resolution $\Delta E(i)$ is determined. The relation between both parameters is found to be linear: $\Delta E(i) \propto \sigma_{smear,rel}(i)$. By comparing $\Delta E(i)$ to the corresponding energy resolution obtained from measured data, the parameter $\sigma_{smear,rel}(i)$ is determined. This whole procedure is done for all layers in the Forward Range Hodoscope. Similarly the time resolution of each plastic scintillator is adjusted. However, it turned out, that the above described adjustment of the individual FRH energy resolution is connected to considerable large systematic uncertainties, which will be discussed in Chapter 6. This section will focus on the observed mismatch between the simulated and measured FRH resolution, depending on the reconstructed proton angle θ.

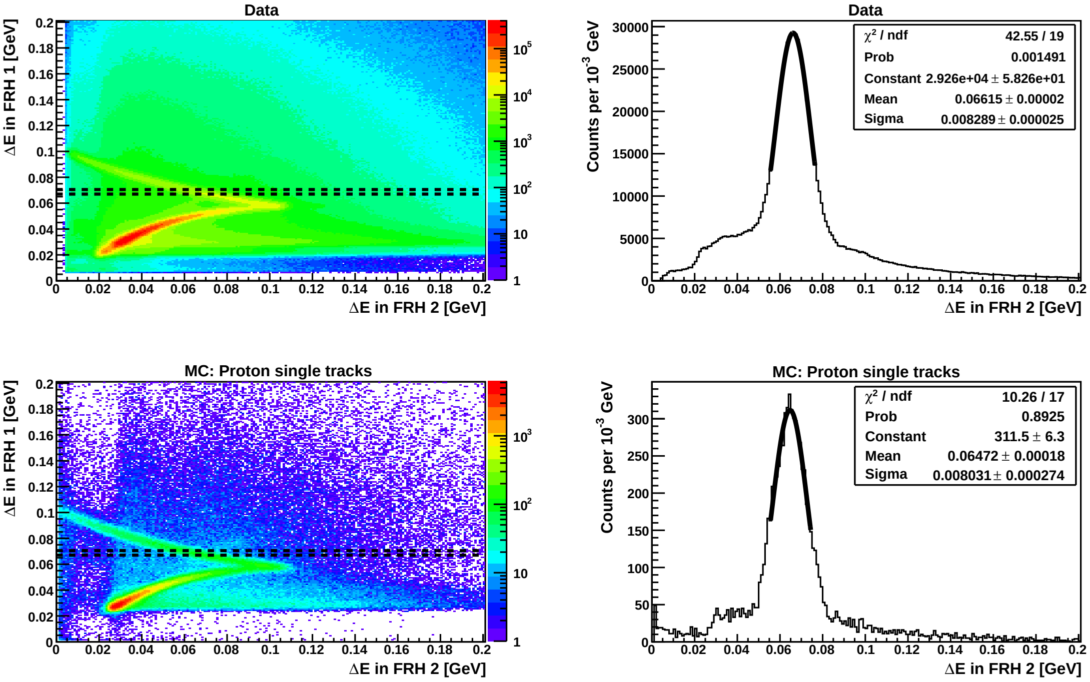

Figure 4.8: **Left:** *Deposited energy for measured (top row) and simulated (bottom row) protons in FRH layer 1 as a function of the corresponding deposited energy in FRH layer 2. The black dashed lines indicate as an example the range:* $\Delta E(FRH1) \in [0.067\,\mathrm{GeV}, 0.0705\,\mathrm{GeV}]$, *for which a projection of the deposited energy in FRH 2 is obtained. This range is varied along the upper part of the proton energy loss band.* **Right:** *Projection of the deposited energy in FRH 2 for measured (top diagram) and simulated (bottom diagram) protons.*

The left hand side of Fig. 4.8 shows the deposited energies of measured (top diagram) and simulated (bottom diagram) protons in the first FRH layer versus the corresponding deposited energy in the second FRH layer. The resulting energy loss band was scanned, by performing a projection onto the x-axis for different energy ranges, as indicated by the black dashed lines in the left panel of Fig. 4.8. The lower part of each band (i.e. deposited energies in FRH 1, that are smaller than 0.06 GeV) is not taken into account, in order to avoid resolution effects from nuclear interactions, minimum ionising particles or misidentified charged pions (the latter one is of course only observed in measured data). The width and position of a projection window i is defined according to:

$$0.06\,\mathrm{GeV} + 0.0035 \cdot \mathrm{i} \leq \Delta\mathrm{E}(\mathrm{FRH\ 1}) < 0.06 + 0.0035 \cdot (\mathrm{i}+1),\ \ \mathrm{i} = 0, ..., 9 \tag{4.7}$$

The right hand side of Fig. 4.8 presents the obtained projections for: $0.067\,\mathrm{GeV} \leq \Delta\mathrm{E}(\mathrm{FRH\ 1}) < 0.0705\,\mathrm{GeV}$. Each of those distributions corresponds to the deposited energy in the second FRH layer for all energy deposits in FRH layer 1, which are within the energy range discussed above. These distributions are fit by a Gaussian function (see black curves in right frame of Fig. 4.8) and the fit parameters (mean value μ and resolution σ) are determined. This procedure is repeated for all combinations of FRH layers and for different proton polar angles. Fig. 4.9 shows the mean deposited energy μ and resolution σ (deduced from the Gaussian fit) of FRH 2 as a function of the energy projection window, which corresponds to a certain range of deposited energy within FRH 1. The coloured markers refer to different ranges of the proton polar angle. The right side of Fig. 4.9 shows, that the energy resolution determined for data and simulations fluctuates for different polar angles. However, the variation of the experimental energy resolution is larger than the variation of the simulated resolution values.

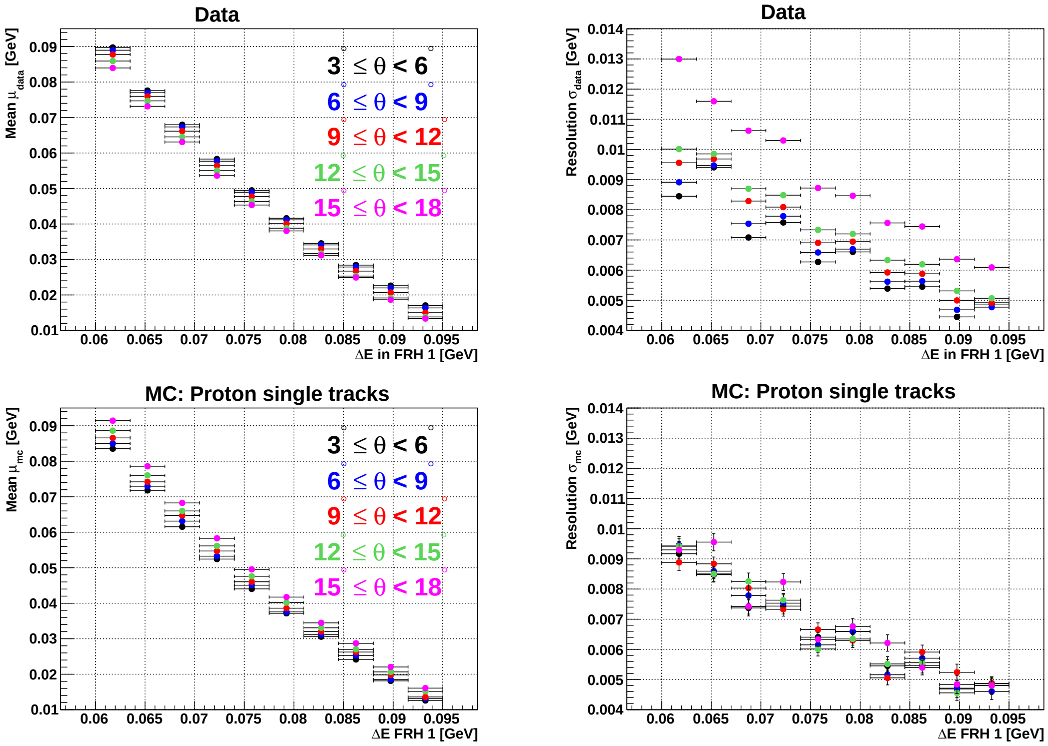

Figure 4.9: *Mean value μ (left column) and resolution σ (right column), deduced from a Gaussian fit to the projections of the deposited energies in the second FRH layer, as function of different deposited energies in FRH layer one.* **Top:** *For measured data.* **Bottom:** *For simulated proton single tracks. The horizontal error bars represent the width of each projection window and the vertical errors bars refer to the errors of the fit parameters. The coloured markers correspond to different θ ranges, which are listed in the left frames.*

In order to have a better visualisation of the differences between measured and simulated deposited energies, the fit parameters μ and σ are plotted as functions of the various θ ranges, but for a fixed projection window. The result is presented in Fig. 4.10. According to the blue data points in the left diagram, the simulated mean deposited energy in FRH layer two increases with increasing θ angle. This is reasonable, because the protons have to travel a longer path through the scintillating material for larger polar angles. The corresponding mean values obtained from the measured data show an opposite pattern. Here, the mean deposited energy decreases for larger proton angles. This behaviour might be related to the calibration procedure of the Forward Range Hodoscope: In the experiment, the deposited energy of a particle being detected in the FRH is collected as digitised ADC values, which show a θ dependency. In order to translate the ADC-values into deposited energy, the non-uniformity is corrected by a third order polynomial. Thus, it is naively assumed, that this correction might lead to the effects shown by the red points in Fig. 4.10. The measured energy resolution is also influenced by this effect, which can be seen in the right diagram of Fig. 4.10. For polar angles $\theta \leq 12°$, the simulated and measured resolutions continuously increase between 0.007 GeV and 0.008 GeV. Going to larger angles, leads to a jump of the measured values up to 0.011 GeV, whereas the simulated values stay below 0.0085 GeV. Thus, the experimental resolution of the second FRH layer varies about $\sim 50\%$ for different angles. In contrast, the corresponding simulated resolution shows a variation of $\sim 20\%$. Similar observations were made for the remaining energy projection windows and the remaining FRH layer combinations.

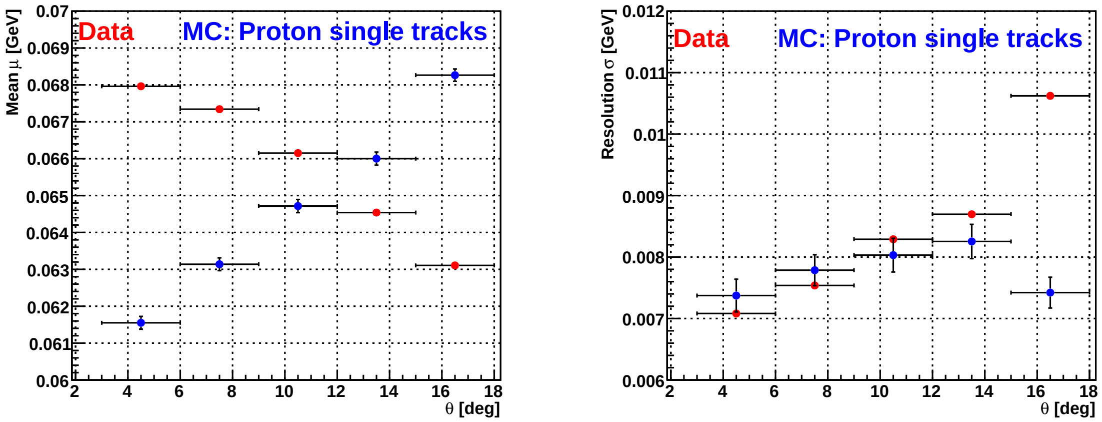

Figure 4.10: *Mean energy deposit μ (left diagram) and resolution σ (right diagram) of FRH 2 for the energy projection window:* $0.067\,\mathrm{GeV} \leq \Delta\mathrm{E}(\mathit{FRH}\,1) < 0.0705\,\mathrm{GeV}$ *as a function of different ranges of the proton polar angle. Red points refer to measured data and blue points refer to simulated data respectively. The horizontal error bars represent the width* ±1.5° *of the angular range. The vertical error bars refer to the fit error of each parameter.*

The reconstruction of the proton kinetic energy as well as the identification of proton candidates relies on the deposited energy within the FRH scintillators. Hence, a deviation between the simulated and measured FRH energy resolutions leads to different and incomparable responses with respect to the same decay analysis conditions. In a first approach, the simulated FRH detector resolutions are matched to the measured ones, by incorporating an artificial θ dependency . This is done within the following steps:

Step 1: The relative energy smearing parameter $\sigma_{smear,rel}$ was set to 0.015 for all FRH layers, in order to ensure, that the simulated energy resolution is better than the resolution observed within the experiment.

Step 2: The procedure shown and discussed in Fig. 4.8 and 4.9 is repeated for the readjusted smearing parameters. The simulated and measured energy resolution $\sigma_{MC}(i,j,\theta)$ / $\sigma_{data}(i,j,\theta)$ of FRH layer i within the energy projection window j is calculated for the different θ ranges.

Step 3: In order to be independent of the deposited energies in the previous FRH layer $i-1$, the average resolutions $\bar{\sigma}_{MC}(i,\theta) = 0.1 \cdot \sum\limits_{j=0}^{9} \sigma_{MC}(i,j,\theta)$ and $\bar{\sigma}_{data}(i,\theta) = 0.1 \cdot \sum\limits_{j=0}^{9} \sigma_{data}(i,j,\theta)$ are calculated.

Step 4: The deviation between simulated and measured resolution in layer i is determined according to: $\Delta\sigma(i,\theta) = \sqrt{\bar{\sigma}^2_{data}(i,\theta) - \bar{\sigma}^2_{MC}(i,\theta)}$. Due to the requirements in step 1, the expression under the squared root is always ≥ 0, which avoids mathematical undefined results for $\Delta\sigma(i,\theta)$.

Step 5: The simulated energy deposit $\Delta E(i)$ (which is related to $\sigma_{smear,rel}$ by Eq. 4.2) in FRH layer i is updated to:
$\Delta E(i)_{corr} = \Delta E(i) + \text{Gauss}_{\text{random}}(0, \Delta\sigma(i,\theta))$

As explained in Eq. 4.2, the function $\text{Gauss}_{\text{random}}$ returns a random number from a Gaussian distribution with mean value 0 and width $\Delta\sigma(i,\theta)$. Thus, the simulated and corrected deposited energies within the FRH plastic scintillator is still related to a Gaussian distribution, as indicated by Eq. 4.2. By definition of $\Delta\sigma(i,\theta)$, the updated resolution $\Delta E_{corr}(i)$ of FRH layer i is θ dependent. In principle, the procedure discussed in steps 1 to 5 could be done for any smearing value $\sigma_{smear,rel}$, as long as $\bar{\sigma}_{data}(i,\theta) \geq \bar{\sigma}_{MC}(i,\theta)$. The updated resolutions are representatively shown for FRH 2 in Figures 4.11 and 4.12. According to the diagrams shown on the right side of Fig. 4.11, the θ dependent variation of the simulated FRH 2 resolution values has been increased and shows now a different θ dependency than presented in Fig. 4.9. This effect can be seen more clearly in Fig. 4.12. The simulated resolution of FRH 2 increases with increasing polar angle θ, which is equivalent to the pattern of the experimental resolution. The same observations were also made for different layer combinations.

After applying the angle dependant energy resolution for simulated tracks, the acceptance studies shown in Table 4.4 were repeated. It turned out, that the missing mass acceptance for the charged η decays changed from 86% to 85%, which has an negligible effect on the final preselection efficiency.

The effect of the θ dependent energy correction of simulated proton tracks on the final data analysis and observables of $\eta \rightarrow \pi^+\pi^-\gamma$ will be investigated and discussed in Chapter 6.

However, the procedure presented here for implementing resolution effects in the simulated data, that have been observed in the measured data, should not taken as a final solution. Instead, it is an intermediate step to understand the underlying systematic effects and to have a reference setup for comparison with different (and more sophisticated) approaches. The right column of Fig. 4.11 shows that the correlation between resolution and polar angle is similar (i.e. increasing resolution for increasing polar angle) for the measured and simulated data, but the absolute

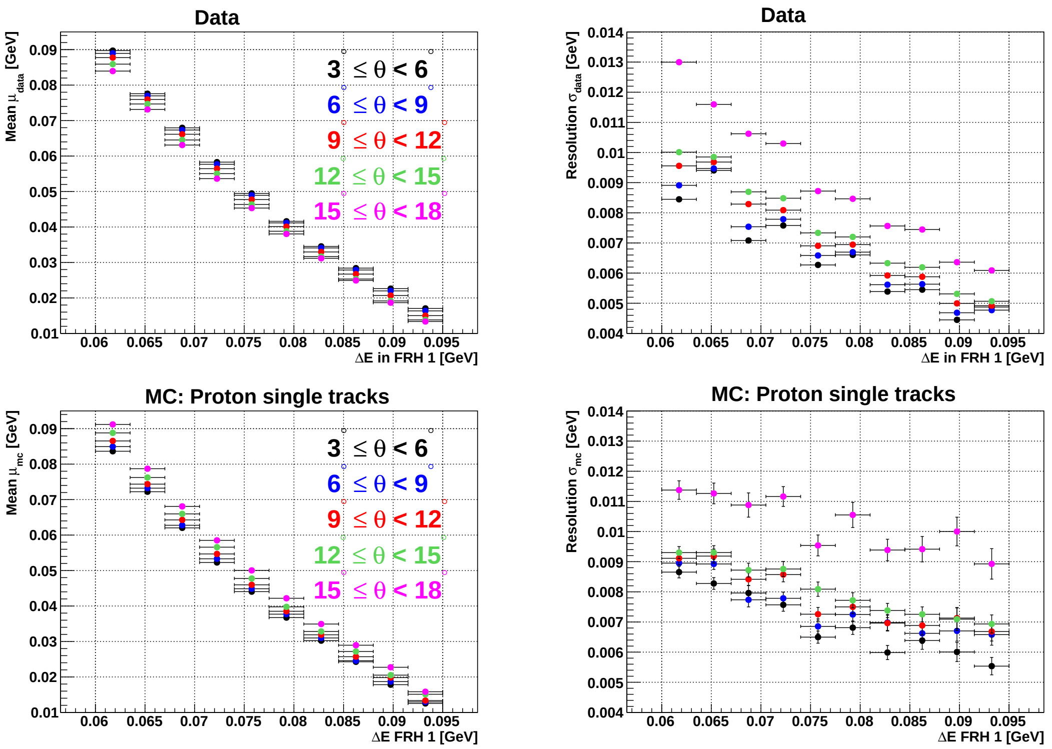

Figure 4.11: *Mean deposited energy μ (left column) and resolution σ (right column) of FRH 2 as a function of different deposited energies in FRH 1. The values are obtained in the same way as done for Fig. 4.9. The simulated resolution values σ_{MC} for FRH 2 were corrected according to the five steps discussed above. The error bars and coloured markers have the same meaning as in Fig. 4.9.*

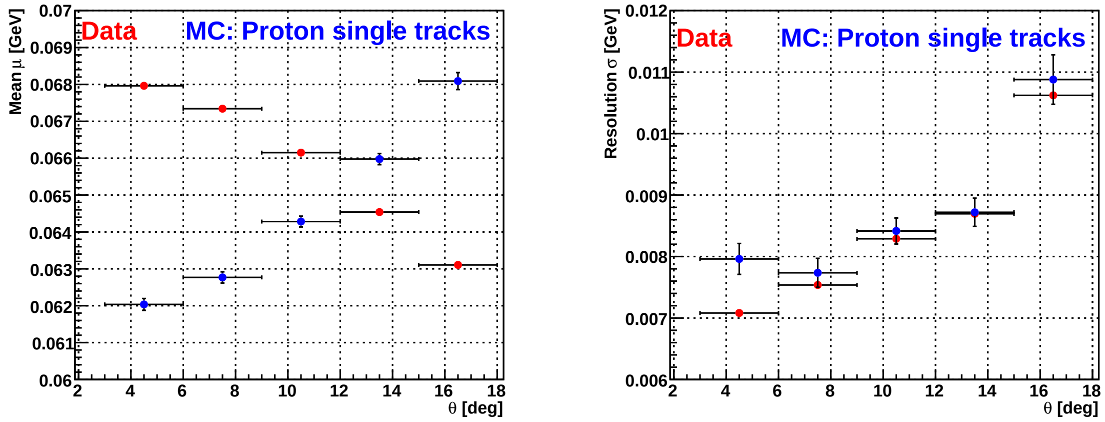

Figure 4.12: *Mean deposited energy μ (left diagram) and resolution σ (right diagram) of FRH 2 for the energy projection window: $0.067\,\mathrm{GeV} \leq \Delta\mathrm{E}(FRH\ 1) < 0.0705\,\mathrm{GeV}$ as a function of the different ranges of the proton polar angle. The results for the simulated proton tracks detected in FRH 2 include the θ dependent energy smearing. For further explanation see the caption to Fig. 4.10.*

values are in disagreement. The procedure shown in steps 1 to 5 is based on the simplification, that the deposited energy in the various FRH layers are not correlated with each other. This is, for sure, not the case in a real measurement and has to be taken into account in future energy correction / calibrations procedures.

4.5.3 Other detector components

The response of other detector components (e.g. MDC, FTH or FPC) have also been checked in simulations and matched to the experimental data when necessary. The matching of the simulated detector response to those in the experiment allows to compare the several steps which are necessary for the analysis of $\eta \to \pi^+\pi^-\gamma$.

“It’s up to you”

James Joseph “Duffy” Waldorf, Jr.

Chapter 5

Analysis

In order to reconstruct $\eta \rightarrow \pi^+\pi^-\gamma$ and $\eta \rightarrow \pi^+\pi^-\pi^0$ events, the presorted and calibrated 2010 $pp \rightarrow pp\eta$ data set is passed to the analysis programme schematically shown in Fig. 5.1. The input of this programme (top blue box in Fig. 5.1) has already been discussed in Chapter 4. Hence, the present chapter will focus on the features of the analysis (i.e. the black dashed box in Fig. 5.1) and the final output (bottom blue box in Fig. 5.1). It turns out that the analysis steps of $\eta \rightarrow \pi^+\pi^-\gamma$ and $\eta \rightarrow \pi^+\pi^-\pi^0$ are very similar, as indicated by the diagram below. The underlying statistics for the analysis corresponds to $\sim 42\%$ of the total 2010 $pp\eta$ data. Due to time constraints, the remaining data could not be analysed within the present work. However, it will be shown in Chapter 6 that analysing more data runs will not improve the final results significantly due to the dominating systematical errors.

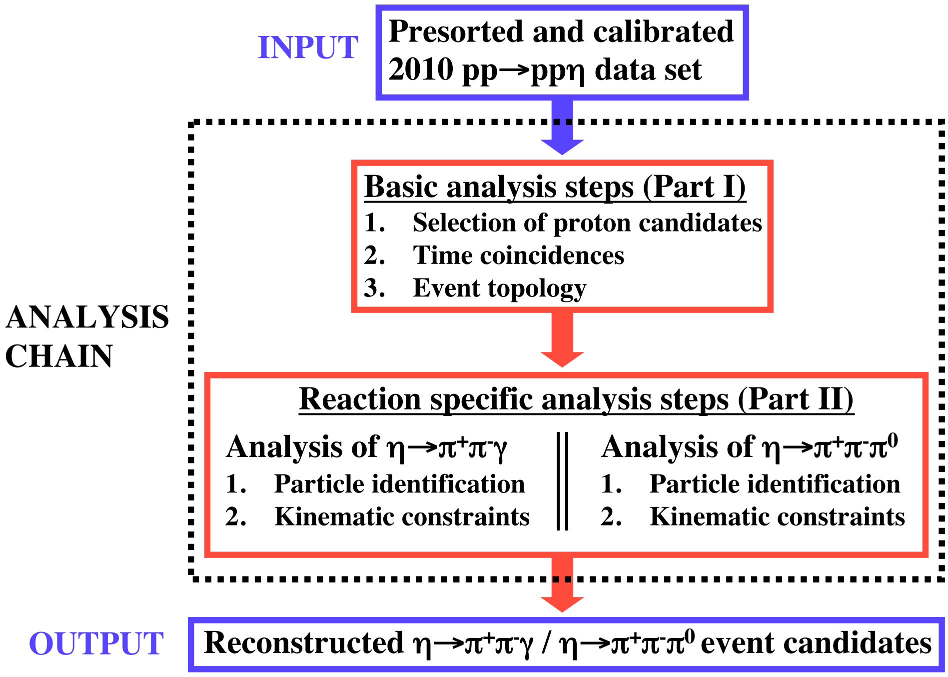

Figure 5.1: *Schematic representation of the analysis procedure, used for reconstructing* $\eta \rightarrow \pi^+\pi^-\gamma$ *and* $\eta \rightarrow \pi^+\pi^-\pi^0$ *events. The content inside the black dashed box represents the essential parts of the analysis, which will be discussed in the following sections.*

5.1 Basic analysis steps

The analysis consists of two main parts (see Fig. 5.1). The first part deals with the selection and combination of particles reconstructed in the Forward and Central Detector. It is more general and applicable for all charged η decays with at least one neutral particle.

5.1.1 Selection of proton candidates

Particles which have been reconstructed in the Forward Detector are identified as protons by their deposited energy $\Delta E(i)$ / $\Delta E(j)$ in the layers i / j of the Forward Range Hodoscope. Those deposited energies define a point $(\Delta E(i), \Delta E(j))$

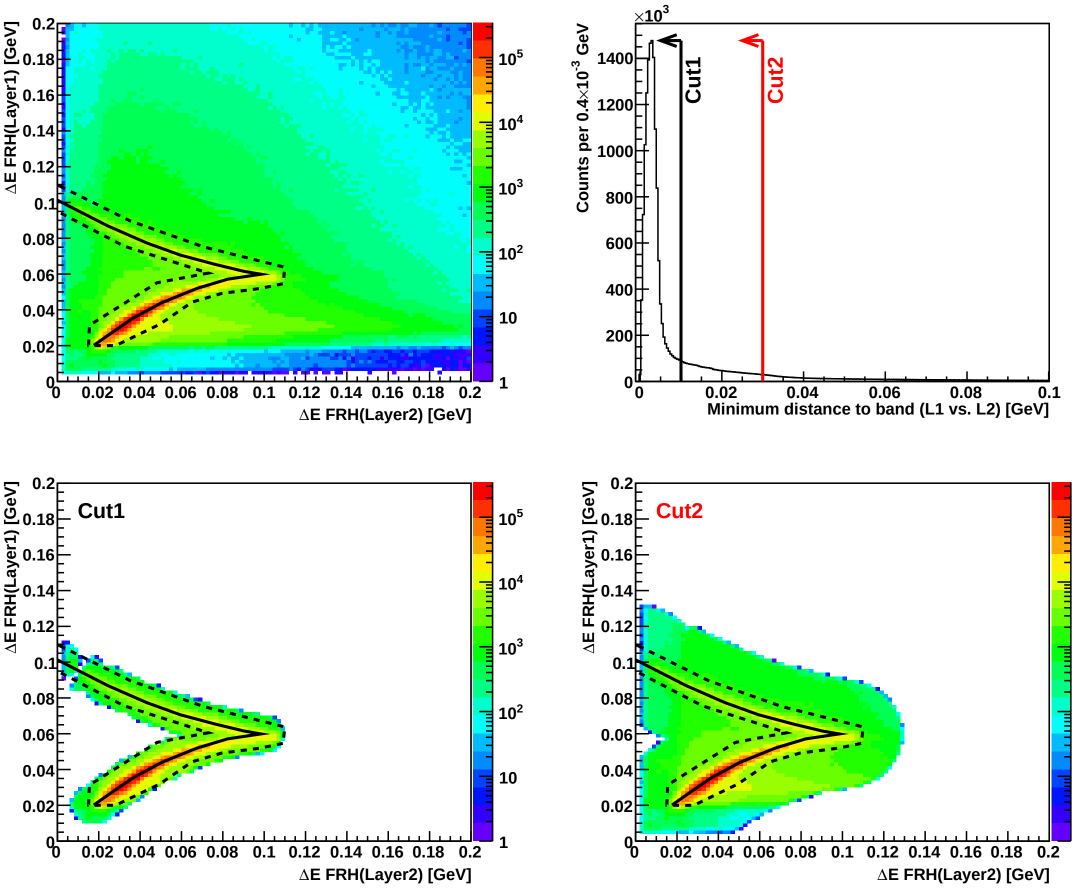

Figure 5.2: **Top left:** *Deposited energy of measured charged tracks in the first and second layer of the FRH detector.* **Top right:** *Minimum distance according to Eq. 5.2 for charged tracks being detected in FRH layers one and two. The black and red lines indicate the selection of all proton tracks with a minimum distance smaller than* 0.01 GeV *and* 0.03 GeV*, respectively.* **Bottom:** *Deposited energy of measured charged tracks in the first and second layer of the FRH detector after selecting a minimum distance of* 0.01 GeV *(left) and* 0.03 GeV *(right). The black line in the top left and bottom plots describes an ideal energy loss pattern for protons. The black dashed lines are drawn in order to visualise the edges of the measured proton energy loss pattern.*

in a two dimensional plot (see Fig. 5.2). The top left diagram of Fig. 5.2 shows the deposited energy of measured charged tracks in the first two layers of the FRH. The borders of the measured proton energy loss pattern are highlighted by the black dashed lines. The black solid line indicates the ideal deposited energy (according to the Bethe Bloch equation) of protons without any detector resolution effects. Those ideal lines are defined by a fixed set of N_{ideal} deposited energy points: $(\Delta E_{ideal}(i,k), \Delta E_{ideal}(j,k))$, $k = 1, ..., N_{ideal}$. Possible proton candidates are selected by their minimum distance d_{ij} to those points:

$$\begin{aligned} d_{ij} &= \text{Minimum}\{D(i,j)_1, ..., D(i,j)_{N_{ideal}}\} && (5.1) \\ D(i,j)_k &= \sqrt{(\Delta E(i) - \Delta E_{ideal}(i,k))^2 + (\Delta E(j) - \Delta E_{ideal}(j,k))^2} && (5.2) \end{aligned}$$

The top right diagram of Fig. 5.2 shows the distribution of the minimum distance for deposited energies in the first two FRH layers. This distribution suggests to select charged tracks with a minimum distance smaller than 0.01 GeV (see black line in top right frame of Fig. 5.2). Doing so leads to the correlation plot shown in the bottom left frame of Fig. 5.2. Nearly all entries outside the borders of the measured proton energy loss pattern (see black dashed lines) are removed by this selection. Unfortunately, entries inside the black dashed lines (which should not be affected) are also removed[a]. According to that, the minimum distance d_{ij} has been chosen such that proton candidates which are inside the black dashed lines (and thus belong to the measured energy loss pattern for protons) are not affected. Therefore, all charged tracks reconstructed in the Forward Detector with a minimum distance smaller than 0.03 GeV (see red line in top right frame of Fig. 5.2) are finally chosen as possible proton candidates. The corresponding correlation plot for deposited energies in FRH 1 and FRH 2 is shown in the bottom right panel of Fig. 5.2.

The procedure described above is done for every possible combination of adjacent FRH layers (e.g. layer 2 vs. layer 3, layer 4 vs. layer 5, etc.), where the corresponding deposited energies are not zero.

According to Monte Carlo based simulation studies, this analysis condition corresponds to a relative reconstruction efficiency of $\sim 62\%$ for proton single tracks. In order to proceed with the next analysis steps, two protons have to pass this identification criterium.

5.1.2 Time coincidences

When a proton pair has been selected, the time difference between the protons is checked. The top left diagram in Fig. 5.3 shows the corresponding spectrum. The black solid lines represent the time window which has been chosen to accept proton candidates. All proton pairs with a time difference $\leq$ 6 ns are accepted and the average proton time:

$$\bar{t}(\text{proton}) = \frac{1}{2} \cdot (t(\text{proton1}) + t(\text{proton2})) \tag{5.3}$$

is calculated. Afterwards the time difference between $\bar{t}(\text{proton})$ and the time of the reconstructed charged/neutral tracks in the Central Detector are investigated (see top right and bottom diagram in Fig. 5.3). The time conditions are the following:

- A charged track with time $t(\pi)$ inside the Central Detector is accepted for further analysis, if: $2\,\text{ns} \leq [\bar{\text{t}}(\text{proton}) - \text{t}(\pi)] \leq 14\,\text{ns}$. This time cut is not symmetric, because the corresponding time spectrum (see top right picture of Fig. 5.3) is not centred at zero.

---

[a] This is related to the fact that the number of ideal energy deposit points N_{ideal} is finite and chosen with respect to the computational time needed to calculate the minimum distance d_{ij} for each particle and each adjacent FRH layer combination.

- A neutral track with time $t(\gamma)$ inside the Central Detector is accepted for further analysis, if: $|\bar{t}(\text{proton}) - t(\gamma)| \leq 30\,\text{ns}$.

The time difference spectra of $\bar{t}(\text{proton}) - t(\pi)$ and $\bar{t}(\text{proton}) - t(\gamma)$ are not centred at zero, because the time response functions of the corresponding detector parts[b] are different. This is also the reason why the bottom spectrum in Fig. 5.3 has a larger width than the top right distribution in Fig. 5.3. The plastic scintillators inside the barrel have a faster time response than the crystals inside the calorimeter.

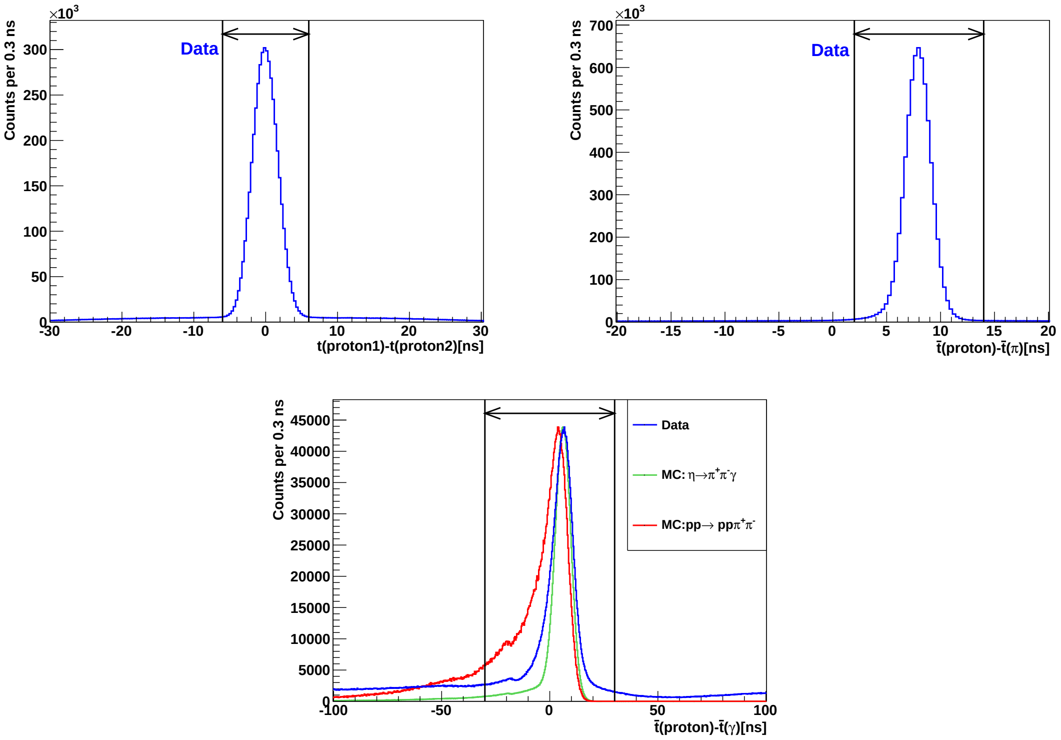

Figure 5.3: **Top left:** *Time difference between two reconstructed proton candidates.* **Top Right:** *Difference between the average proton time and the time of a charged track reconstructed in the Central Detector.* **Bottom:** *Difference between the average proton time and the time of a neutral track reconstructed in the Central Detector. The green and red curves correspond to simulated $\eta \rightarrow \pi^+\pi^-\gamma$ and $pp \rightarrow pp\pi^+\pi^-$ events. Each of the two distributions is scaled to the blue curve. The black solid lines in each diagram represent the time window which is used to select a particle candidate.*

The bottom time spectrum in Fig. 5.3 shows a kink at $\approx -20\,\text{ns}$. Monte Carlo studies (see red curve in bottom row of Fig. 5.3) show, that this structure is related to $pp \rightarrow pp\pi^+\pi^-$ events ,which happen to cause fake photons and thus an artificial time response. However, a narrower time window is not selected, because contributions from the signal channel $\eta \rightarrow \pi^+\pi^-\gamma$ (see green curve in the bottom row of Fig. 5.3) are situated below this kink.

---

[b] The Forward Trigger Hodoscope provides the time information for tracks in the Forward Detector. The Plastic Scintillator Barrel / calorimeter provide the time information for charged tracks in the Central Detector. The time information for neutral tracks in the Central Detector are given by the calorimeter only.

5.1.3 Event topology

After selecting the proton candidates and demanding time coincidences, all tracks within one event are combined to an event candidate. Table 5.1 summarises the requested track multiplicities which define the topology of an event candidate for a certain η decay. The event topology shown in the second line of Table 5.1 is used in the present analysis. If the requested multiplicities are not given, the event is rejected and not further processed in the analysis. Obviously, this condition allows the decays: $\eta \rightarrow \pi^+\pi^-\gamma$, $\eta \rightarrow \pi^+\pi^-\pi^0$ and $\eta \rightarrow e^+e^-\gamma$ to be reconstructed. Within a single event, the total number $N_{\eta\rightarrow\pi^+\pi^-\gamma}$ of all possible $\eta \rightarrow \pi^+\pi^-\gamma$ event combinations after reconstructing N_+ positive charged tracks, N_- negative charged tracks and N_γ neutral tracks in the Central Detector is given by:

Reaction	$N(FD)$	$(N_+ + N_-)(CD)$	$N_\gamma(CD)$
$\eta \rightarrow \pi^+\pi^-\pi^0$	$= 2$	≥ 2	≥ 2
$\eta \rightarrow \pi^+\pi^-\gamma$	$= 2$	≥ 2	≥ 1
$\eta \rightarrow e^+e^-\gamma$	$= 2$	≥ 2	≥ 1
$\eta \rightarrow \pi^+\pi^-e^+e^-$	$= 2$	≥ 4	–
$\eta \rightarrow e^+e^-e^+e^-$	$= 2$	≥ 4	–

Table 5.1: *The requested number $N(FD)$ of reconstructed charged tracks in the Forward Detector as well as the requested number of reconstructed charged $N_\pm(CD)$ and neutral $N_\gamma(CD)$ tracks in the Central Detector define event candidates for different η decays. The red coloured row indicates the requested event topology for the analysis of $\eta \rightarrow \pi^+\pi^-\gamma$ and $\eta \rightarrow \pi^+\pi^-\pi^0$.*

$$N_{\eta\rightarrow\pi^+\pi^-\gamma} = N_+(CD) \cdot N_-(CD) \cdot N_\gamma(CD) \tag{5.4}$$

If $N_\gamma \geq 2$, the number of all possible $\eta \rightarrow \pi^+\pi^-\pi^0$ event combinations is:

$$N_{\eta\rightarrow\pi^+\pi^-\pi^0} = N_+(CD) \cdot N_-(CD) \cdot \begin{pmatrix} N_\gamma \\ 2 \end{pmatrix} \tag{5.5}$$

The last factor in Eq. 5.5 is related to combinatorics. Fig. 5.4 shows the missing mass distribution, which has been calculated according to Eq. 4.3, after all basic analysis steps. The step at $0.4\,\mathrm{GeV/c^2}$ results from the preselection conditions which have been discussed in the previous chapter.

This spectrum shows a peak at the η mass $m_\eta = 0.548\,\mathrm{GeV/c^2}$, which corresponds to all η decays matching the topology shown in Table 5.1. The peak is on top of a huge background which is related to the multi-pion production reactions: $pp \rightarrow pp\pi^+\pi^-$, $pp \rightarrow pp\pi^+\pi^-\pi^0$ and $pp \rightarrow pp\pi^0\pi^0$. According to Monte Carlo simulation studies, the fraction of $pp \rightarrow pp\pi^+\pi^-$ events located in this background is about 69%. The remaining 31% of the background contain $pp \rightarrow pp\pi^+\pi^-\pi^0$ and $pp \rightarrow pp\pi^0\pi^0$ events. The latter production reaction might contribute to the background, because π^0 particles might decay into a photon and a lepton pair via a Dalitz decay with a branching ratio $\sim 1\%$. However, it is more likely, that a neutral pion decays into two photons and one of them interacts with the beam pipe and creates a dilepton (e^+e^-) pair via photo-conversion. In both cases, the final event topology meets the requirements listed in Table 5.1 and a $pp \rightarrow pp\pi^0\pi^0$ event is misinterpreted as an

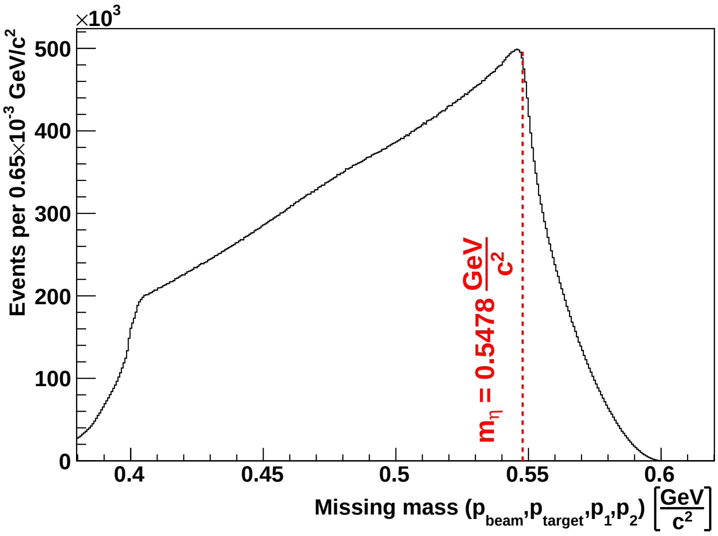

Figure 5.4: *Missing mass spectrum after selecting the proton candidates, demanding time coincidences and requesting the highlighted conditions in Table 5.1.*

$\eta \rightarrow \pi^+\pi^-\gamma$ event candidate. According to Monte Carlo simulation studies, the fraction of $pp \rightarrow pp\pi^0\pi^0$ events contributing to the background in Fig. 5.4 is below 0.1% and thus negligible.

The reaction $pp \rightarrow pp\pi^+\pi^-$ has the largest background contribution, due to its large production cross section (see Table 4.2) and wrongly reconstructed photons which lead to the same final state configuration as the decay $\eta \rightarrow \pi^+\pi^-\gamma$. The absolute reconstruction efficiencies for all analysis steps discussed so far (including the preselection conditions presented in Chapter 4) are listed in Appendix D.

In the following, two methods for performing the reaction specific analysis part (see bottom red box in Fig. 5.1) will be presented. Each of them is determined to reduce the multi-pion background and to distinguish between the different η decays inside the peak of Fig. 5.4. In a first approach, a purely cut based analysis chain including particle identification and simple kinematic considerations will be performed. The second approach is mainly based on a kinematic fit algorithm. The results of both approaches will finally be compared, in order to understand the influences of the kinematic fit and to check the consistency of the results.

5.2 Reaction specific analysis steps (1^{st} approach)

In order to investigate the influence of each analysis step, monitoring spectra are introduced. The first one is the missing mass spectrum which has already been discussed. This spectrum has a limited information content, because it only shows changes if event candidates are removed (assuming, that the calibration and particle identification are performed properly).

5.2.1 Monitoring spectra

It is also possible to reconstruct a particle via its N decay products. For the decay: $p \rightarrow \sum_i^N d_i$ of a particle p and its decay products d_i, each having a four momentum

$\mathbf{P}_{d_i}$, the invariant mass of the decay products can be calculated:

$$\text{Invariant mass } (d_1, .., d_N) = |\sum_i^N \mathbf{P}_{d_i}| \tag{5.6}$$

One might also calculate the invariant mass for a fraction of the decay particles (e.g. two photon invariant mass discussed in Chapter 3).

In case of the decay $\eta \rightarrow \pi^+\pi^-\gamma$, the invariant mass for all decay particles is given by:

$$\text{Invariant mass } (\pi^+, \pi^-, \gamma) = |\mathbf{P}_{\pi^+} + \mathbf{P}_{\pi^-} + \mathbf{P}_\gamma| \tag{5.7}$$

Due to energy and momentum conservation, the distribution of Eq. 5.7 should ideally be equal to the missing mass distribution. By definition, this spectrum is sensitive to the momenta of the decay particles.

5.2.1.1 Missing mass versus invariant mass

The top row of Fig. 5.5 shows the missing mass as function of the invariant mass (calculated according to Eq. 5.7) for Monte Carlo simulations (left) and data (right). Both distributions should ideally show a single point at (m_η, m_η) (see black, dashed lines in top row of Fig. 5.5). But resolution and reconstruction effects inside the detector as well as contributions from background events lead to a continuous distribution with maximum around (m_η, m_η). This effect is also observed in the invariant mass distributions (bottom row in Fig. 5.5). The enhancement towards low masses visible in the bottom left diagram is mainly caused by wrongly reconstructed, low

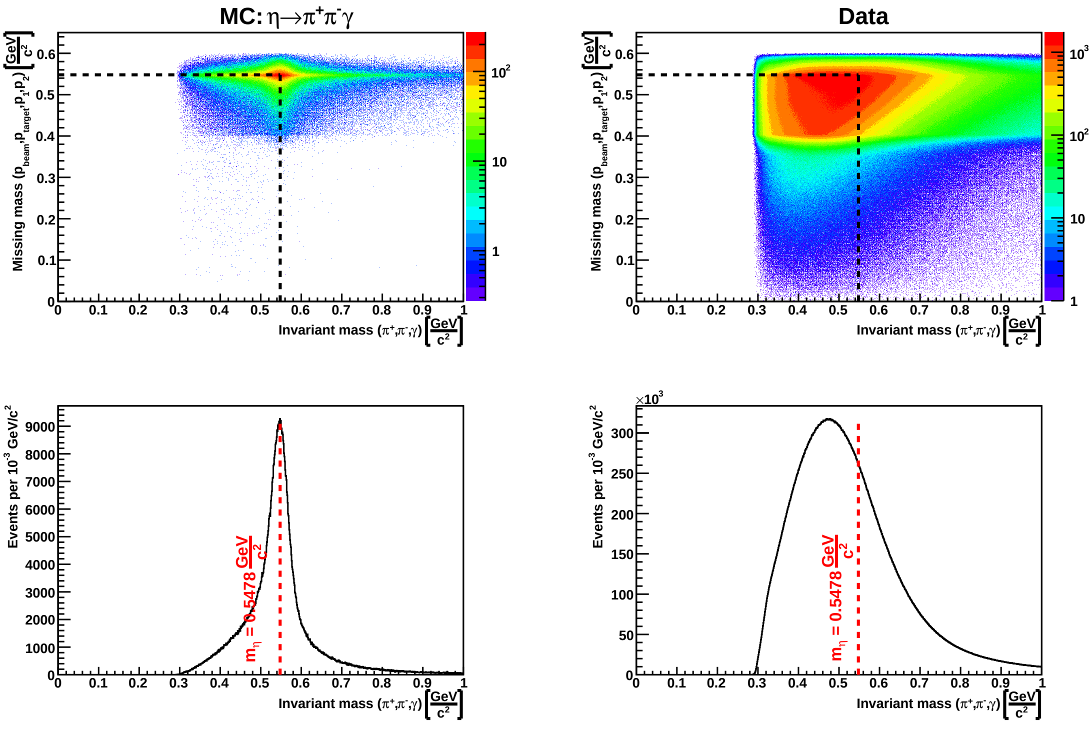

Figure 5.5: **Top:** *Missing mass as function of the invariant mass for Monte Carlo simulations of $\eta \rightarrow \pi^+\pi^-\gamma$ (left) and measured data (right).* **Bottom:** *Invariant mass distributions deduced from a one dimensional projection onto the x-axis of the spectra above. The black and red dashed lines indicate the η mass.*

energy photons which will be discussed later. Both spectra shown in the bottom row of Fig. 5.5 start at about $2 \cdot m_{\pi^\pm}$, because this is the kinematic lower limit in case of low energy photons. The invariant mass distribution deduced from the measured data is completely smeared out between 0.3 GeV/c^2 and 1 GeV/c^2, because of the contribution from other η decays and multi-pion production reactions. The rising step at 0.3 GeV/c^2 is caused by electrons which have been reconstructed as pions and thus lead to low invariant mass values. Background contributions stemming from $pp \to pp\pi^+\pi^-\pi^0$ and $\eta \to \pi^+\pi^-\pi^0$ events cause low invariant masses between 0.3 GeV/c^2 and 0.5 GeV/c^2, due to energy and momentum conservation. The remaining background is determined by the two charged pion production mechanism $pp \to pp\pi^+\pi^-$. All this leads to a widening of the $\eta \to \pi^+\pi^-\gamma$ invariant mass distribution and a maximum different from $m_\eta = 0.548\,\mathrm{GeV/c^2}$. The features of the missing mass spectra have been discussed in the previous section.

5.2.1.2 Energy and momentum balance

A more detailed insight into the decay kinematics is given by the missing energy E_{miss} and missing momentum P_{miss} of an event:

$$E_{miss} = E_{in} - E_{out} \tag{5.8}$$

$$P_{miss} = |\vec{P}_{in} - \vec{P}_{out}| \tag{5.9}$$

E_{in} and $\vec{P}_{in}$ are the sum energy and momentum of all incoming particles and E_{out} and $\vec{P}_{out}$ are the sum energy and momentum of all outgoing particles, respectively. A plot of the missing momentum as function of the missing energy is shown in Fig. 5.6. The benefit of this method is to check the energy and momentum balance

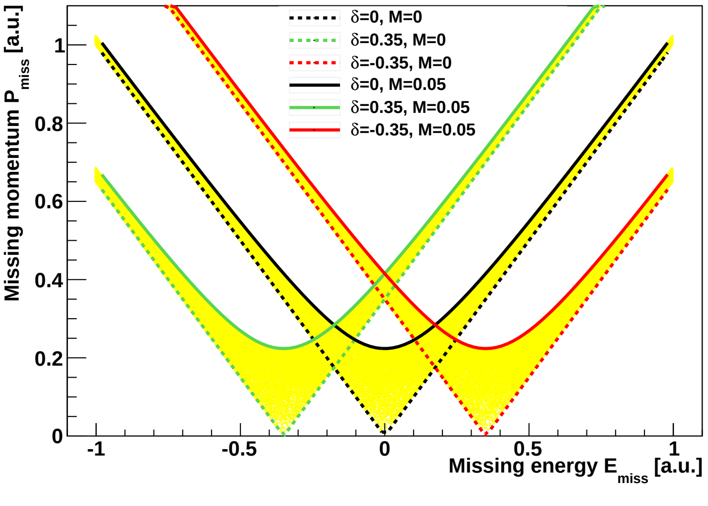

Figure 5.6: *Calculated missing momentum as a function of the missing energy for different parameters δ and M (see Eq. 5.10).*

for a certain reaction hypothesis (e.g. $\eta \to \pi^+\pi^-\gamma$), since P_{miss} and E_{miss} should be zero for the reaction of interest.

A correlation between P_{miss} and E_{miss} is found by two simple considerations: (i) Using $E^2 = P^2 + M^2$, the missing energy and momentum are connected via the missing mass M. (ii) The number of particles or particles masses within the current reaction do not match with those of the reaction of interest. This causes a constant shift of the missing energy, according to the energy of the additional / missing particles. This leads to the following parameterisation:

$$P_{miss} = \sqrt{(E_{miss} + \delta)^2 + M} \tag{5.10}$$

with a mass parameter M and shift parameter δ. The different scenarios shown in Fig. 5.6 can be explained by the following cases:

<u>Case 1:</u> Overall energy and momentum conservation: $P_{miss} = E_{miss} = M = \delta = 0$. All entries are localised at $(0, 0)$ in Fig. 5.6.

<u>Case 2:</u> The current reaction has a different topology (e.g. $\eta \rightarrow \pi^+\pi^-\pi^0$) or deviating particle masses (e.g. $\eta \rightarrow e^+e^-\gamma$). This causes a constant shift $\delta \neq 0$ on the x-axis. (see green and red curve in Fig. 5.6).

<u>Case 3:</u> Overall energy and momentum are balanced for massive particles only. Since photons have no rest mass, M is equal to zero which leads to $P_{miss} = E_{miss} \neq 0$. This case is indicated by the dashed lines in Fig. 5.6.

<u>Case 4:</u> No energy and momentum balance at all, leads to: $M \neq 0$, which is shown by the green, black and red solid curves in Fig. 5.6.

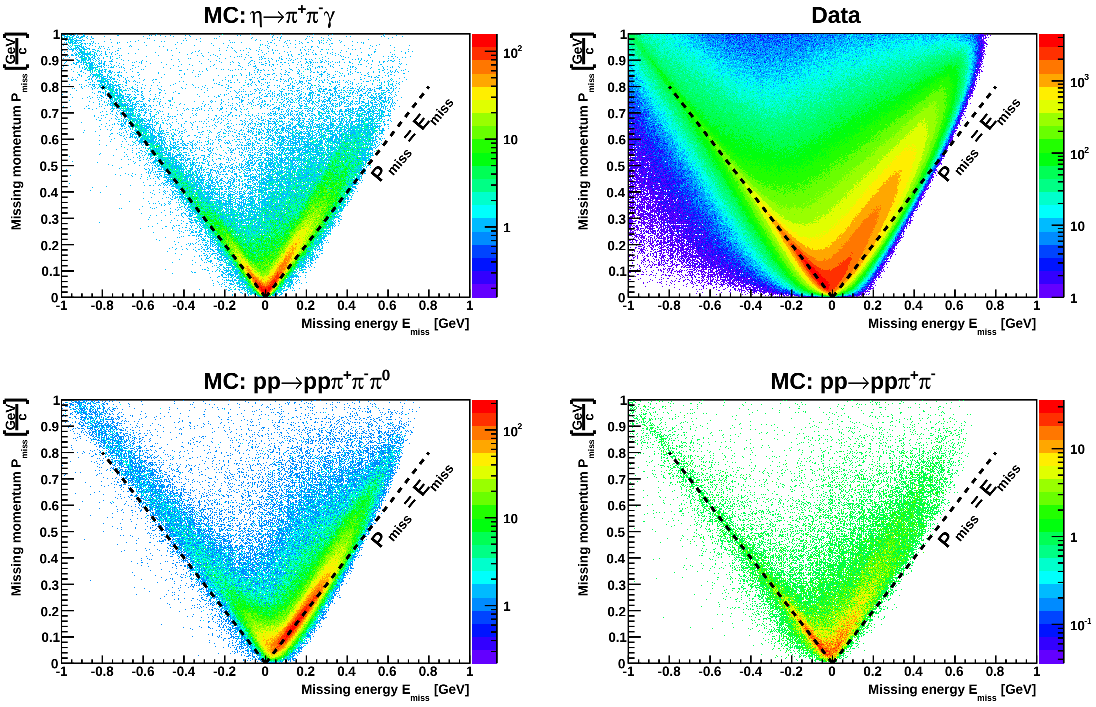

Figure 5.7: *Missing momentum plotted vs. missing energy for a Monte Carlo simulation of $\eta \rightarrow \pi^+\pi^-\gamma$ (top left), $pp \rightarrow pp\pi^+\pi^-\pi^0$ (bottom left), $pp \rightarrow pp\pi^+\pi^-$ (bottom right) and for measured data (top right). The black dashed lines in both plots indicate Case 2, where $P_{miss} = E_{miss} \neq 0$.*

The missing momentum and missing energy of the reaction: $\eta \rightarrow \pi^+\pi^-\gamma$ is plotted in Fig. 5.7 for a Monte Carlo simulation of $\eta \rightarrow \pi^+\pi^-\gamma$ (top left frame), measured data (top right frame) and multi-pion production reactions (bottom row).
For the simulated $\eta \rightarrow \pi^+\pi^-\gamma$ events, one would expect entries at the origin $(0, 0)$ only. But due to the detector properties (e.g. resolution, reconstruction efficiency)

and wrongly reconstructed particles, the values for P_{miss} and E_{miss} are smeared around the origin and located at non-zero values.

For the measured data not only $\eta \rightarrow \pi^+\pi^-\gamma$ events, but also all other reactions with the same event topology are present. This leads to continuous M and δ values and thus determines the distribution shown in Fig.5.7.

For $pp \rightarrow pp\pi^+\pi^-$ events, the left wing of the V-like structure is most populated, because an additional photon is requested which leads to negative missing energies. The opposite case is given for $pp \rightarrow pp\pi^+\pi^-\pi^0$ events, as one photon is missing in order to balance out energy and momentum. Thus, positive missing energies (i.e. the right wing of the V-like structure) are favoured and the whole distribution is shifted towards larger missing energies.

The energy and momentum balance spectra are directly correlated to the property of every reconstructed particle and thus allow to investigate the influence of each analysis step. Furthermore, all monitoring spectra are correlated with each other by the decay kinematics.

5.2.2 Identification of charged particles in the Central Detector: An excursion

The subdetector parts of the Central Detector have been discussed in Chapter 3. Charged particles are identified by inspecting their deposited energy in the Plastic Scintillator Barrel or Scintillator Electromagnetic Calorimeter as a function of their momentum, which has been reconstructed via the Mini Drift Chamber. Fig. 5.8 shows the particle identification plots which have already been presented in Chapter 3. The electrons that can be seen in those diagrams have different sources. The first sources are charged η decay channels like $\eta \rightarrow e^+e^-\gamma$ or $\eta \rightarrow \pi^+\pi^-e^+e^-$. The second source for electrons is conversion events in the beam pipe.

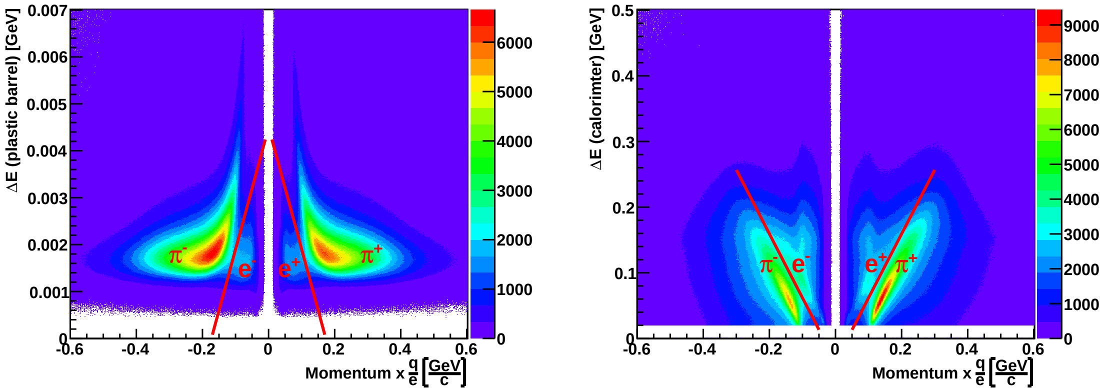

Figure 5.8: *Particle identification for charged tracks in the Central Detector obtained from measured data. The deposited energy of a charged track detected in the Plastic Scintillator Barrel (left) or in the calorimeter (right) is plotted as function of the reconstructed momentum times the particle charge. The red lines are drawn to visualise the different energy loss bands for pions and electrons.*

The top row of Fig. 5.9 shows two scenarios where electrons are produced. The first scenario is shown on the left: The electrons stem from an electric η decay (e.g. $\eta \rightarrow e^+e^-\gamma$) and thus, originate from the origin. Their curvature is caused by the solenoid field. This leads to a non-zero opening angle between the electron momenta at the beam pipe (see top left picture of Fig. 5.9). The second scenario shown on the right is related to conversion events: A photon originates from the beam-target interaction point and travels towards the beam pipe and interacts there via pair production with the beam pipe material. The resulting dilepton-pair has its origin at the beam pipe radius and hence an opening angle close to zero (see top right picture of Fig. 5.9). Conversion and non-conversion events can be monitored by the

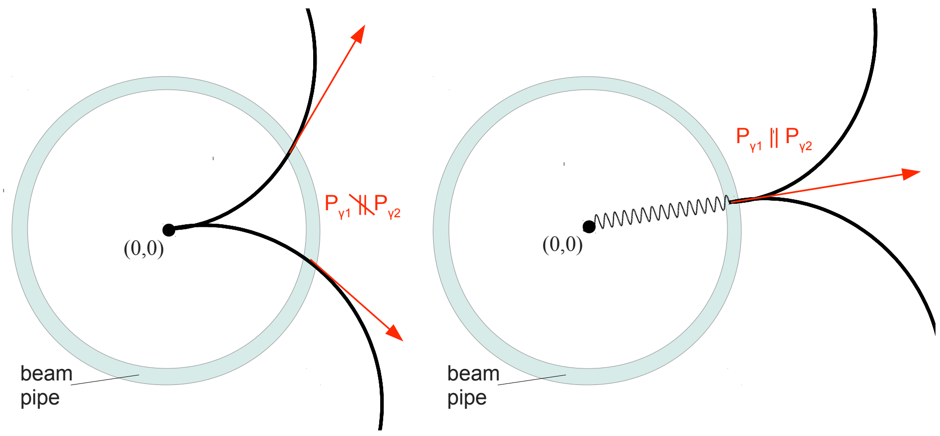

Electrons from Origin

Conversion Event

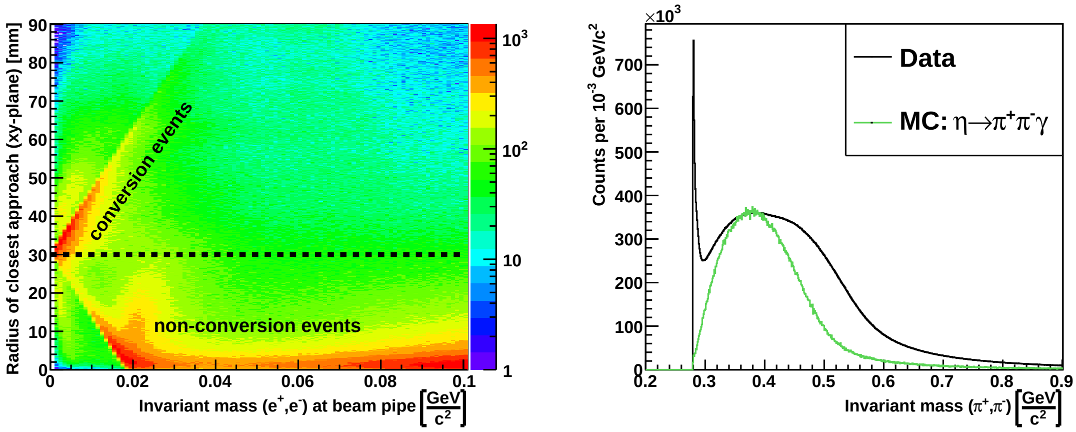

Figure 5.9: **Top:** *Schematic representation of a charged decay containing electrons (left picture) and a conversion event (right picture) [18].* **Bottom left:** *Radius of closest approach between the reconstructed charged tracks as a function of the invariant mass deduced from the two charged particles at the beam pipe region.* **Bottom right:** *Invariant mass distribution deduced from two charged tracks reconstructed in the Central Detector for data (black curve) and Monte Carlo simulations (green curve). The green curve has been scaled to the black curve, in order to allow for a better comparison.*

two dimensional spectrum shown in the bottom left frame of Fig. 5.9. In this diagram, the radius of closest distance (with respect to the origin) between the charged track curvatures in the xy-plane is plotted as a function of the invariant mass of the charged tracks at the beam pipe region. The invariant mass of the charged tracks corresponds to the opening angle of the particle momenta. The radius of closest approach should have its minimum at the origin for non-conversion events. For conversion electrons, the radius for the closest distance should be shifted to the beam pipe radius at $r = 30\,\mathrm{mm}$. This is exactly, what is observed by the two structures (separated by the black dashed line) in the bottom left picture of Fig. 5.9: The first structure is located at small invariant masses (small opening angles) and distances larger than 30 mm. Events with such a structure generally stem from conversion events. The second structure has large invariant masses (large opening angles) and distances near to the origin. This structure stems from electric decays. The reason why both structures have a finite enlargement and are not point-like, is related to the finite resolution of the Mini Drift Chamber.

The appearance of electrons within the data set can also be seen in the invariant mass spectrum obtained from two reconstructed charged tracks in the Central Detector. The bottom right diagram of Fig. 5.9 shows such a spectrum for data (black curve) and Monte Carlo simulations for $\eta \rightarrow \pi^+\pi^-\gamma$ (green curve). These distributions have been calculated according to Eq. 5.7. Hence, both spectra start at a minimum value: $2 \cdot m_{\pi^\pm} = 0.28\,\mathrm{GeV/c^2}$. The black curve shows a strong enhancement at this value, because of electrons which have been reconstructed as pions by assigning the improper mass. Charged pion pairs stemming from other reaction channels (e.g. $\eta \rightarrow \pi^+\pi^-\pi^0$ or $pp \rightarrow pp\pi^+\pi^-$) additionally contribute to the shape of the black curve.

Basically, a cut on the point of closest approach could be provided such, that all charged tracks with a closest distance larger than the beam pipe radius would be rejected. This would eliminate electrons stemming from conversion events, but not those originating from η or Dalitz decays. Thus, sufficient particle identification is needed to reject electron-like particle tracks, independent of their production mechanism.

5.2.3 Artificial neural networks

In order to perform particle identification for charged pions, the red lines shown in Fig. 5.8 could be used as a set of linear cuts. In doing so, all charged tracks with deposited energies situated above (under) the red lines in the left (right) picture of Fig. 5.8 are interpreted as charged pions. This method is quite simple and straight forward.

However, the deposited energies in the calorimeter for example are correlated to those in the Plastic Scintillator Barrel, because they depend on the initial kinetic energy of the detected particle. This has to be taken into account, when performing and optimising such a linear cut. The distinction between electrons and pions is a classification problem, i.e. two classes (in this case pions and electrons) which are characterised by a set of correlated variables (momentum and deposited energies) shall be separated.

This is the reason, why neural networks are used to distinguish between electrons and pions. Neural networks have become a helpful tool for solving classification problems [51, 52]. There are many network types available, which are assigned to the underlying problem. The neural network tested and used in this analysis is a multilayer perceptron, or a simple feed-forward-network, as shown in Fig. 5.10. Such a network is charecterised by its architecture [51, 52, 53]:

- Input layer I_i: Plug in of classification variables, such as particle properties. In this case the same variables which were used for the particle identification plots in Fig. 5.8, are also used for classification.
- Hidden layer H_j: Determines the networks behaviour. A feed-forward-network without any hidden layer might be described by a linear function and thus can solve linear separable problems only. If a more complex function for problem-solving is needed, the number of hidden layers has to be increased.
- Output layer O_1: Output of the discrimination variable, which varies continuously between 0 (for electrons) and 1 (for pions).

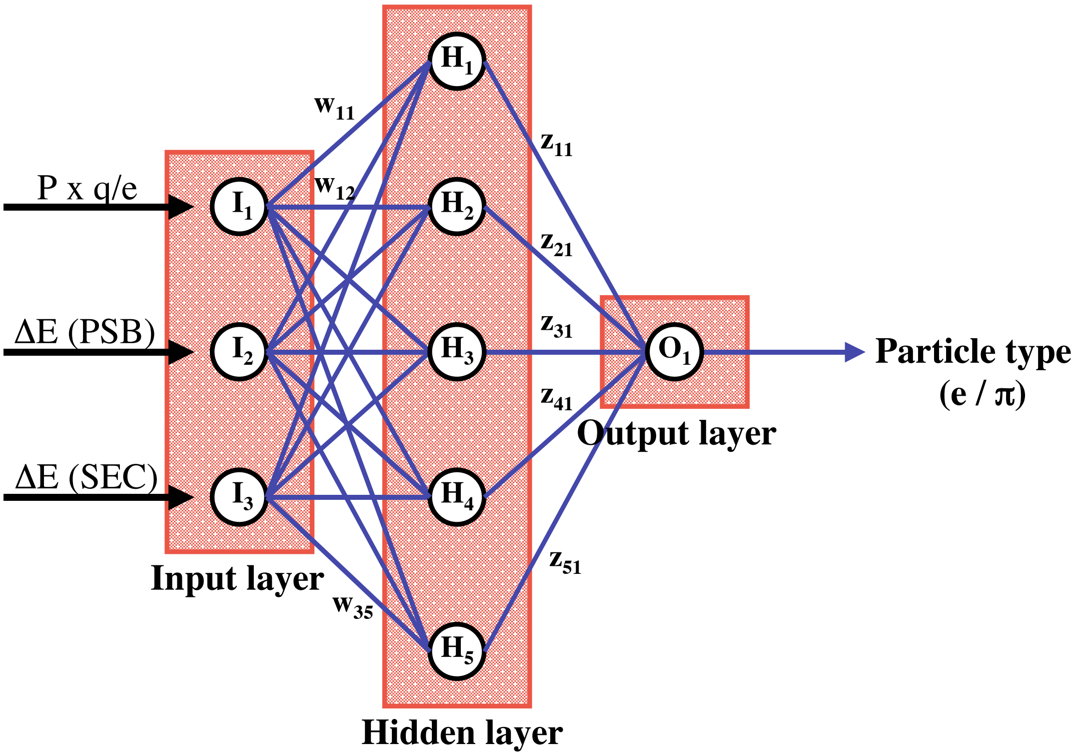

Figure 5.10: *A multilayer perceptron with one input, one hidden and one output layer. The architecture shown here is used for the particle identification problem.* $\Delta E(PSB)$ *denotes the deposited energy in the plastic barrel and* $\Delta E(SEC)$ *represents the deposited energy inside the calorimeter.*

Each layer of the network consists of a certain number of neurons (black circles in Fig. 5.10). The neurons are linked by weights (blue arrows in Fig. 5.10). The output of one neuron inside a layer is the input for all neurons in the following layers. The output of each neuron is characterised by an activation function f_{neuron}[c]. The final output O_1 of a neural network with one hidden layer as function of the input I_i is given by [53]:

$$O_1 = f_O\Big[\sum_{j=1}^{N_{\text{hidden}}} z_{j1} \cdot f_H\Big(\sum_{i=1}^{N_{\text{input}}} w_{ij} I_i\Big)\Big] \tag{5.11}$$

f_O and f_H are the activation functions used for neurons in the output and hidden layer respectively. The factors w_{ij} and z_{jk} are the weights between the neurons. The

---

[c] Which could be the identity, sigmoid or heavyside function. The function f_{neuron} for input and output neurons is in most cases the identity. [51, 52, 53]

number of neurons in the hidden layer is a free parameter and given by N_{hidden}. This number defines the performance and robustness of a neural network. The number of neurons N_{input} in the input layer is fixed by the number of input variables.

5.2.3.1 Training the network

The weights w_{ij} and z_{jk} are determined by training the neural network with a training data set, which has been obtained by analysing simulated single particle tracks for electrons and pions. The purpose of such a training sample is that each particle type (1 for pions, 0 for electrons) is known and associated to the classification variables. The ratio between electrons and pions in the training set has been set to one. In order to use the network for measured data, the detector resolution was adjusted according to the analysis of simulated single tracks (see Chapter 4).
The networks performance increases with the amount of provided information. Therefore, the kinematic ranges of electrons and pions have been included in the training data sample.
One half of the training data set is used as an unbiased test sample, in order to monitor the network response during the training phase [53]. The weights are iteratively refined by a back-propagation-algorithm which uses the output error between the network response O_1 and the known value O_{true}[d] for N training events:

$$\text{Error} = \frac{1}{2N^2} \cdot \sum_{a=1}^{N} (O_{1,a} - O_{true,a})^2 \qquad (5.12)$$

This value is propagated backwards through the network and each weight is updated by this error [51, 52, 53]. Afterwards, the training set is passed through the network again and a new output error is calculated. The weights are refined and the whole procedure starts again. The number of training iterations is another adjustable variable and is chosen such that the output error is minimal. In this analysis,

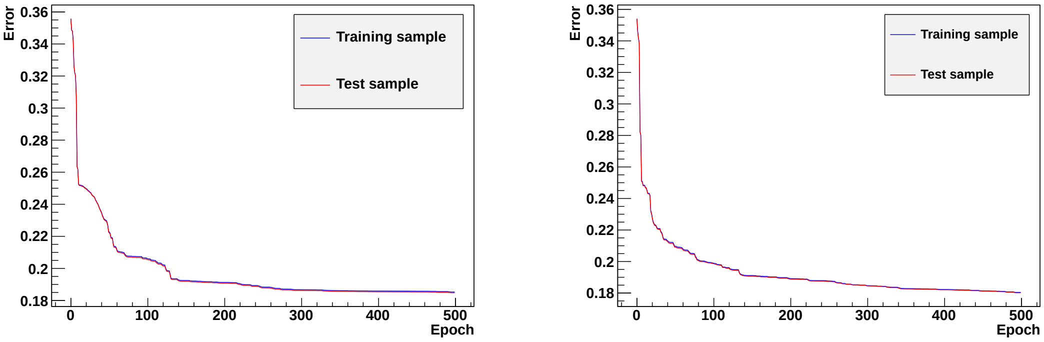

Figure 5.11: Error in Eq. 5.12 as a function of the training epoch (iteration) for negative (left) and positive (right) particles. The blue curve refers to the training data set, as the red one refers to the test sample.

two artificial neural networks with the architecture shown in Fig. 5.10 have been used. One for particles with positive charge and one network for negatively charged particles. Fig. 5.11 shows the development of the error in Eq. 5.12 during the training phase for the two networks. The blue curve represents the network response for the training data set. As mentioned above, the training of the network is supervised

---

[d] This value is 1 if the particle is a pion and 0 otherwise.

by a test sample, which is represented by the red curves in Fig. 5.11. The training of a neural network was successful, if the error decreases to a constant value with increasing training epoch. Additionally, the network response for the training and test sample have to converge to the same error. Otherwise the behaviour of the network would be unpredictable on input data, which might be different from the training sample. Fig. 5.11 shows, that the response curves for the two samples converge to the same error, which is nearly constant after 300 epochs. Thus, both neural networks are used in the following analysis.

5.2.3.2 Architecture and performance

The classification power of a network highly depends on its architecture, i.e. the number of hidden layers and the number of nodes $N_{\text{hidden},i}$ inside a hidden layer i. According to a theorem of Weierstrass [53], a multilayer perceptron with one hidden layer is able to approximate any continuous correlation function, if N_{hidden} is large enough. Alternatively, the same performance with a shorter training phase might be achieved with a smaller amount of neurons, but more hidden layers [53].
For this study, two types of networks have been tested: The first type has one hidden layer (i.e. $N_{\text{hidden},1} \neq 0$ and $N_{\text{hidden},2} = 0$) and the second type has two hidden layers (i.e. $N_{\text{hidden},1} \neq 0$ and $N_{\text{hidden},2} \neq 0$) respectively. The top left diagram of Fig. 5.12 shows the error of Eq. 5.12 for the classification of positive particles as function of the network architecture. All diagrams in Fig. 5.12 have been obtained after analysing a sample of simulated particle single tracks with 50% positrons (electrons) and 50% positive (negative) pions. The variation of the error with respect to the architecture is estimated by fitting a constant function (see red line in top left frame of Fig. 5.12). The reduced χ^2-value of that fit as well as the fit error suggests that the influence of the network architecture on solving this classification problem is negligible. According to that, a network with architecture (5 : 0) has been chosen for identifying positive and negative pions.
The response functions of such network types for different particles are shown in the top right of Fig. 5.12. Each of those functions is smoothly distributed over the whole range between zero and one with a maximum at zero or one. Some of those distributions show some additional structures and do not sharply end at zero or one. This is related to the fact that a trained network has a limited precision, which is defined by the classification problem (i.e. the input variables) itself.
The black line in the top right diagram of Fig. 5.12 indicates a cut on the output variable. This cut has been varied between zero and one in steps of 0.05. For each of those steps, the classification efficiency and purity for a certain particle type has been determined. The results of that study are shown in the bottom two diagrams of Fig. 5.12. The efficiency and purity for accepting/rejecting a particle type $p_T/\bar{p}_T$ (e.g. accepting positive pions and rejecting positrons) are defined as follows [54]:

$$\text{Efficiency} = \frac{N(p_T|O_1)}{N(p_T)} \tag{5.13}$$

$$\text{Purity} = \frac{N(p_T|O_1)}{N(p_T|O_1) + N(\bar{p}_T|O_1)} \tag{5.14}$$

$N(p_T|O_1)/N(\bar{p}_T|O_1)$ is the number of selected particles with type $p_T/\bar{p}_T$ after selecting a minimum output value O_1. The number of all particles with type p_T is given by $N(p_T)$. As shown in the top right plot of Fig. 5.12, all output functions have an overlap in a certain region (e.g. blue and red curve). Hence, a particle with type p_T

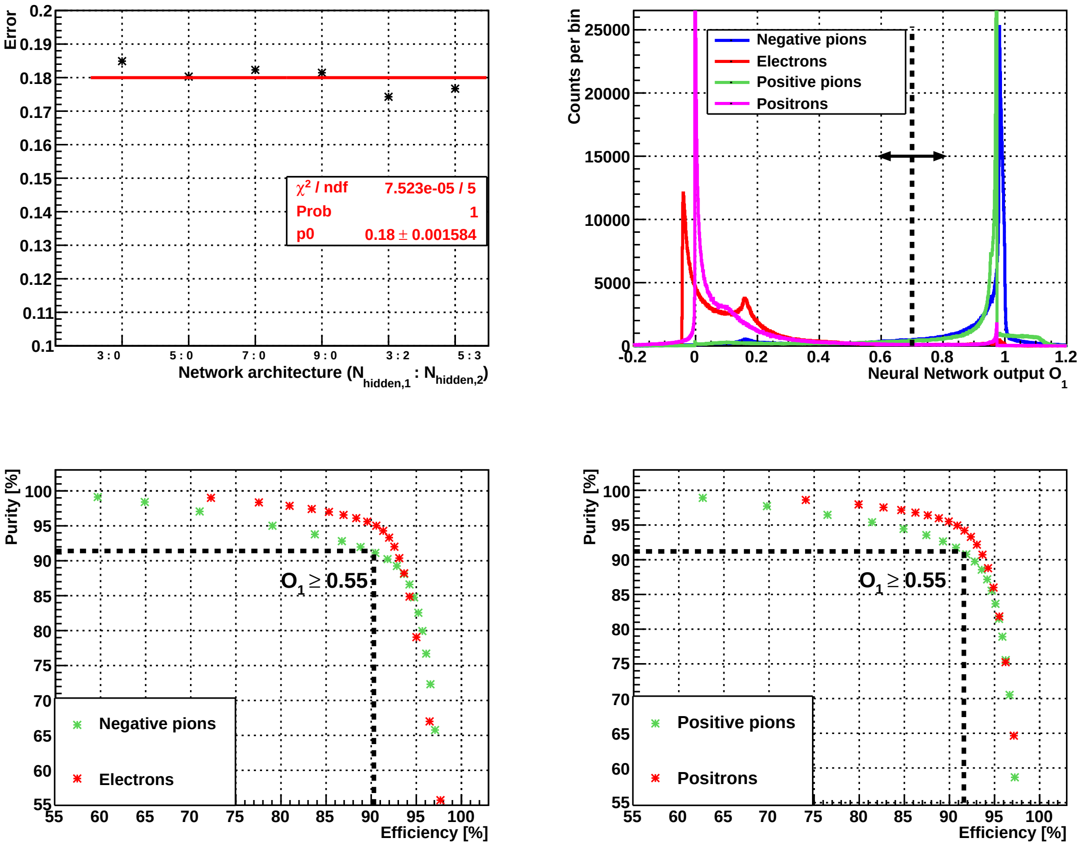

Figure 5.12: **Top left:** *Error for distinguishing between positive pions and positrons as function of the network architecture.* $N_{hidden,i}$ *is the number of neurons in the hidden layer* i*. The red line corresponds to a fit of a constant in order to estimate the deviation of the output error.* **Top right:** *Output of two neural networks (one for negative, one for positive particles) with one hidden layer and* 5 *neurons in it. The black dashed line indicates a cut on the output variable in order to determine the performance of the network.* **Bottom:** *Purity as function of efficiency for negative (left) and positive (right) particles. The black lines in both diagrams represent the purity/efficiency values, if charged tracks with* $O_1 \geq 0.55$ *are selected.*

might be wrongly identified as a particle with different type $\bar{p}_T$ (e.g. electrons are identified as negative pions or vice versa). The degree of misidentification, which depends on the selected minimum output variable O_1, is expressed by the purity. The efficiency for accepting positive pions is maximal, if the selected output O_1 is close to zero. But this leads to a small purity, because positrons are also located at this output region. In contrast, the purity is maximal, if the chosen O_1 is close to one, where positrons are very unlikely. In this case, the efficiency will be low.

The behavior of the purity as function of the efficiency indicates the performance of the neural network, which is also completely determined by the classification problem. The efficiency and purity would be 100% at the same time in case of an ideal classification. The bottom part of Fig. 5.12 shows that all performance curves asymptotical converge towards 100%.

For the recent analysis, charged tracks reconstructed in the Central Detector with $O_1 \geq 0.55$ have been selected as positive/negative pions. In both cases this selection corresponds to: Efficiency = Purity ≈ 91% (see black, dashed lines in bottom diagrams of Fig. 5.12). As mentioned before, the ratio between electrons and pions in the test data set is one, which is a bit unrealistic. A more realistic ratio (with a larger pion fraction) would shift the curves in the bottom diagram of Fig. 5.12 towards larger purity values, but not effect the efficiency. The top of Fig. 5.13 shows the particle identification plots after using neural networks for particle identification and demanding charged tracks with a neural network discrimination variable $O_1 \geq 0.55$. In both plots, the electron bands have disappeared and the pion bands remain. The structures which can be seen, are artefacts from the neural networks and have no physical meaning. The bottom left picture of Fig. 5.13 shows that nearly all electrons stemming from conversion decays have successfully been removed. Finally, the two pion invariant mass distribution for measured data (black curve in bottom right diagram of Fig. 5.13) shows a disappearance of the peak at low invariant masses. The green curve in that picture corresponds to simulated $\eta \rightarrow \pi^+\pi^-\gamma$ events after the same particle identification criteria. There is still a clear mismatch between the green and black curve, which is mainly related to contributions from direct pion production reactions with different kinematics. However, all four diagrams in Fig. 5.13 are correlated and provide the opportunity to cross check the influence of the particle identification. Based on these results, the neural network approach is used for the identification of pions.

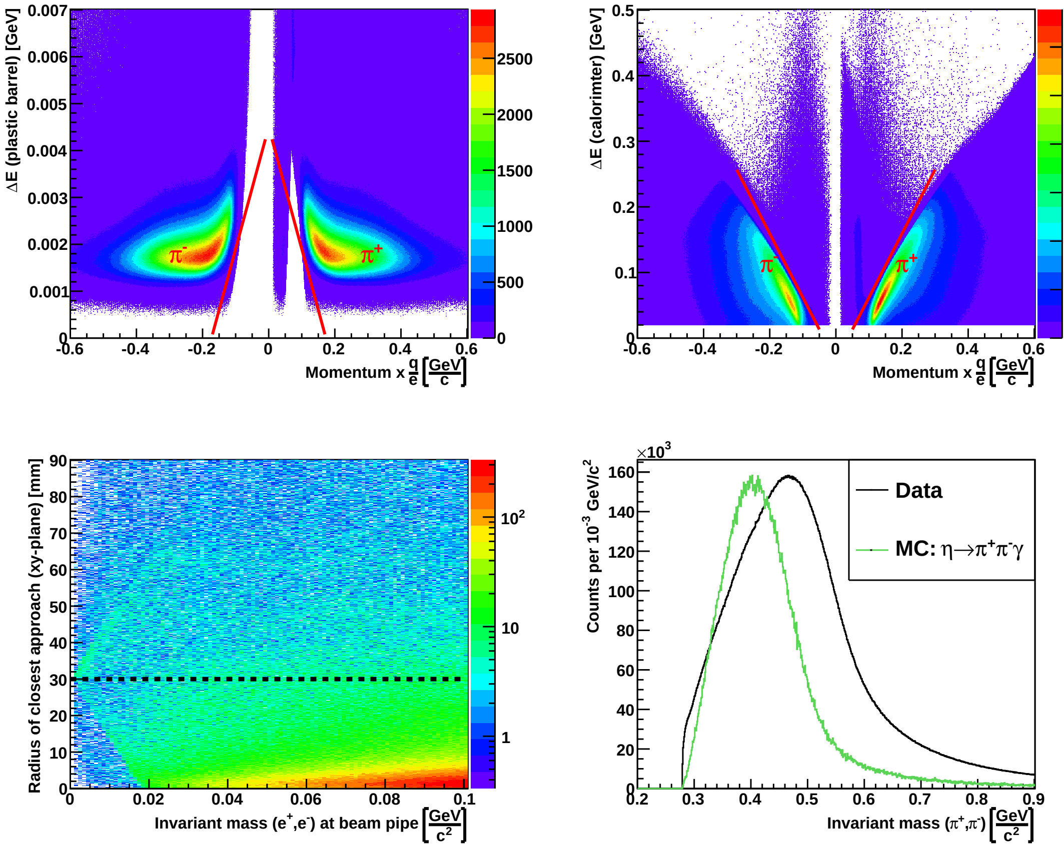

Figure 5.13: *Particle identification plots (top), radius of closest approach as function of the dilepton invariant mass at the beam pipe (bottom left) and two pion invariant mass (bottom right) after requesting two charged tracks reconstructed in the Central Detector with* $O_1 \geq 0.55$*. The red lines in the top row diagrams are drawn to visualise the positions of the energy loss bands for pions and electrons before particle identification (compare Fig. 5.8).*

Traditionally, neural networks are used for selecting a signal out of a dominating background. In this analysis pions are dominating, but the networks are used in the sense of an optimised classifier. The chosen architecture allows for a complex classification function and hence leads to a high identification performance, depending on a single discrimination variable.

5.2.4 Separating two and three pion final state events

After identifying pions, the squared missing mass according to Eq. 4.3 is calculated for the initial and charged final state particles. The corresponding distribution is shown in Fig. 5.14. According to energy and momentum conservation, the distribution should either peak at zero for reactions with one or no final state photons, or peak at $m_{\pi^0}^2 = 0.018\,\mathrm{GeV}^2/\mathrm{c}^4$ for reactions with two final state photons. Two enhancements at exactly those positions are visible in Fig. 5.14.

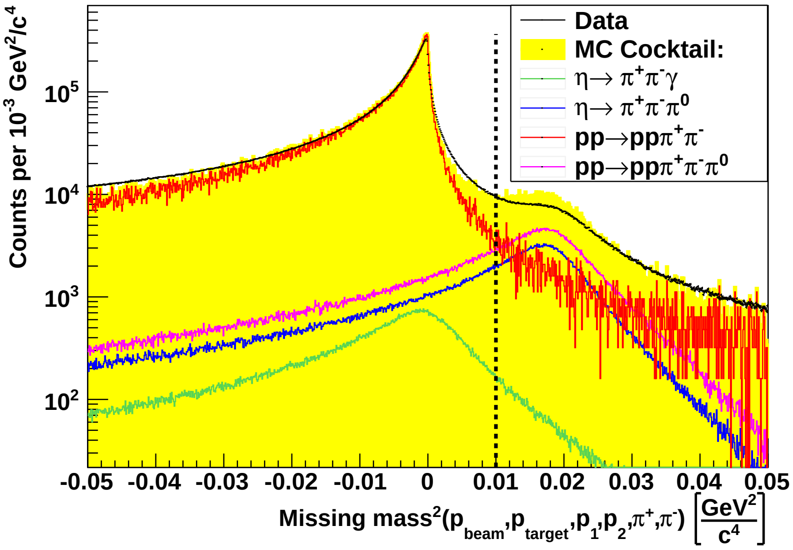

Figure 5.14: *Missing mass distribution deduced from the two initial state protons, two final state protons and two pions. The black, dashed line at* $0.01\,\mathrm{GeV}^2/\mathrm{c}^4$ *indicates a cut to separate between two and three pion final state reactions. Contributions from* $\eta \to e^+e^-\gamma$ *events are not shown here, because they are significantly suppressed by the particle identification discussed in the previous section (see also Fig. 5.27). The yellow shaded area represents the sum of the green, red, purple and blue curve. Each of those curves corresponds to a simulated reaction, which is listed in the inset box.*

The first maximum is dominated by $pp \to pp\pi^+\pi^-$ events (red curve), which is the main background contribution.

The second maximum at $m_{\pi^0}^2$ is determined by the three pion final state reactions $\eta \to \pi^+\pi^-\pi^0$ (blue curve) and $pp \to pp\pi^+\pi^-\pi^0$ (purple curve), which have a similar abundance. The shapes of the blue and purple curves are nearly identical, because the underlying reactions have the same final state configuration.

The signal channel $\eta \to \pi^+\pi^-\gamma$ (green curve in Fig. 5.14) is overwhelmed by the multi-pion-production reactions and the $\eta \to \pi^+\pi^-\pi^0$ decay. In order to separate between two and three pion final state reactions, a cut on the distribution in Fig. 5.14 has been introduced (see black, dashed line in Fig. 5.14). Events with a squared missing mass smaller than $0.01\,\mathrm{GeV}^2/\mathrm{c}^4$ are accepted as $\eta \to \pi^+\pi^-\gamma$ event candidates. All events with a larger missing mass are selected as $\eta \rightarrow \pi^+\pi^-\pi^0$ event candidates, respectively. For three pion final state reactions, the missing mass distribution shown in Fig. 5.14 should ideally be equivalent to the invariant mass distribution of two photons. Hence, the value of $0.01\,\mathrm{GeV}^2/\mathrm{c}^4$ has been chosen for separation, in order not to cut into the signal region of the two photon invariant mass distribution. In the next step, the single photon and π^0 candidates will be selected.

5.2.5 Identification of neutral particles in the Central Detector

The reconstruction of neutral particles in the Central Detector was discussed in Chapter 3. One problem which comes along with the reconstruction procedure is the appearance of so-called "split-offs". Fig. 5.15 shows a schematic drawing of the calorimeter which is hit by a particle. The incoming particle is reconstructed by a clustering algorithm which groups calorimeter elements with non-zero deposited energy. In case of a continuous and smooth energy spread over a group of elements (left side of Fig. 5.15) one single cluster will be returned by the clustering algorithm. But the detected particle might spread its energy inside the calorimeter in a non-continuous manner (right side of Fig. 5.15). In this case a primary cluster and an additional satellite will be returned. The satellite cluster is characterised by small energies and a close distance to the primary cluster. The additional cluster is called a split-off and identified as a neutral, low energy photon.

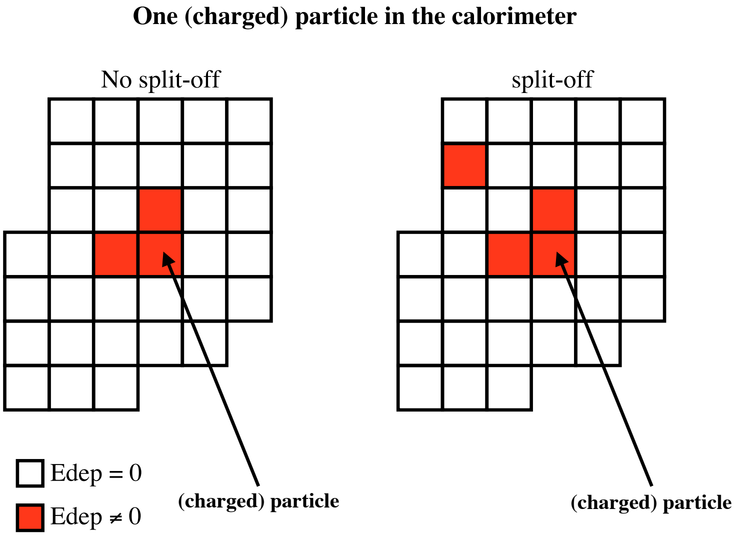

Figure 5.15: *Schematic representation of a neutral (charged) particle that enters the calorimeter. Each rectangle represents a detector element with (red rectangles) and without (white rectangles) deposited energy.* **Left:** *Reconstruction of a single cluster caused by the incoming particle.* **Right:** *Additional reconstruction of a satellite cluster (split-off).*

5.2.5.1 Selection of single photon candidates

The method presented in the following has been already applied and tested in the previous WASA analysis of $pd \rightarrow {}^3\mathrm{He}\eta[\eta \rightarrow \pi^+\pi^-\gamma]$ [7, 26]. Therefore, several aspects related to this analysis condition, which are discussed within this work, will be identical to those performed in [26]. The top left panel of Fig. 5.16 shows the

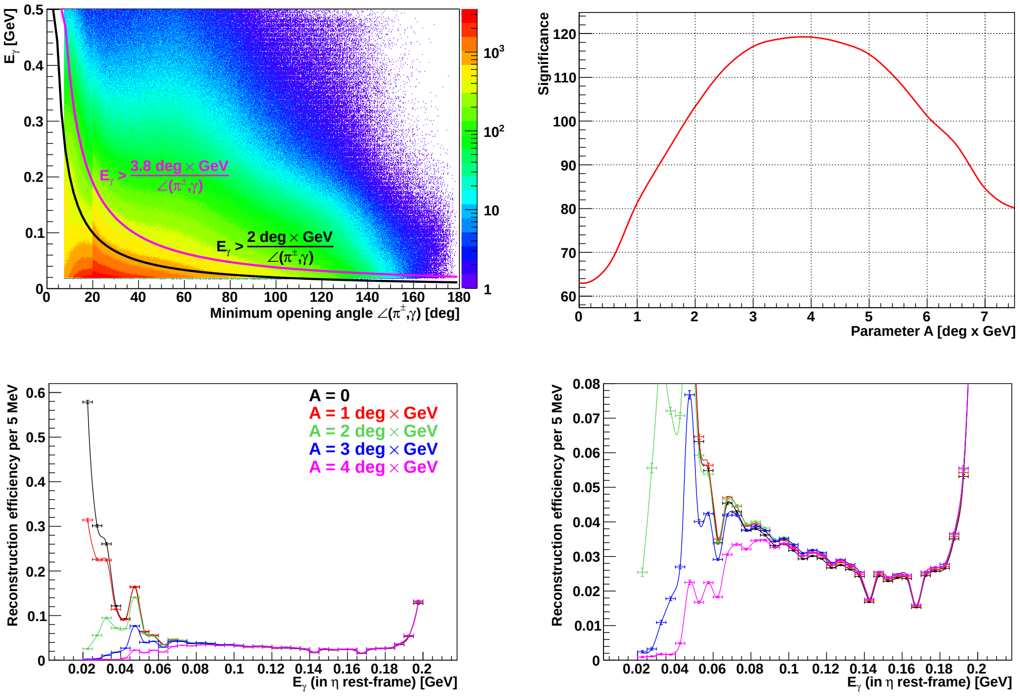

Figure 5.16: **Top left:** *Deposited energy of reconstructed photons as a function of the minimum opening angle between a reconstructed calorimeter cluster and the closest charged track entering the calorimeter. The black and purple hyperbolas indicate conditions to reject split-offs (see Eq. 5.15). All events with photon energies and opening angles below that curve are rejected.* **Top right:** *Significance of the signal (see Eq. 5.16) as function of the hyperbola parameter A. The significance has a maximum at* $A = 3.8\,deg \times \mathrm{GeV}$. **Bottom left:** *Reconstruction efficiency for* $\eta \rightarrow \pi^+\pi^-\gamma$ *as a function of the single photon energy in the* η *rest-frame for different hyperbola parameters A.* **Bottom right:** *Same plot with a zoom on small reconstruction efficiencies to visualise efficiency gaps.*

deposited energy of a photon candidate as function of the closest distance between a charged track entering the calorimeter and the reconstructed calorimeter cluster. The distance is expressed here as the minimum opening angle $\angle(\pi^\pm, \gamma)$ between a charged pion and the closest neutral track.

The photon energies have a lower limit of 20 MeV which corresponds to the calorimeter cluster threshold. The minimum opening angle starts at 7.5° due to the granularity of the crystals inside the calorimeter. The structure visible at $\angle(\pi^\pm, \gamma) \approx 20°$ is caused by $pp \rightarrow pp\pi^+\pi^-$ events, due to the track assignment discussed in Chapter 3: All charged tracks reconstructed in the Central Detector are checked for geometrical overlap between MDC and calorimeter clusters by the opening angle between them. As shown in Fig. 3.18, all calorimeter clusters with an overlap angle up to 20° are expected to stem from the same particle. Thus, minimum opening angles smaller than 20° can only be achieved by real or wrongly reconstructed photons. The latter is the case for $pp \rightarrow pp\pi^+\pi^-$. Due to the large production cross section of two charged pions (660 μb) compared to other pion production mechanisms, the fraction of split-off events is increased. This causes the structure at $\angle(\pi^\pm, \gamma) \approx 20°$ and the enhancement at small angles and low photon energies and thus exactly corresponds to the situation shown in the right picture of Fig. 5.15.

Finally, each $pp \rightarrow pp\pi^+\pi^-$ event which causes such a split-off photon, has the same final state configuration as $\eta \rightarrow \pi^+\pi^-\gamma$. In order to reject low energy satellite clusters at a close distance to the primary cluster, a hyperbolic cut as shown in Fig. 5.16 (left) has been introduced [26]:

$$E_\gamma > \frac{A}{\angle(\pi^\pm, \gamma)} \tag{5.15}$$

All events which do not fulfill this condition are rejected as split-off candidates.
The right side of Fig. 5.16 shows the significance as a function of the hyperbola parameter A. The significance is defined by [26]:

$$\text{Significance} = \frac{N_{sig}}{\sqrt{N_{sig} + N_{bkg}}} \tag{5.16}$$

N_{sig} denotes the number of signal events in the η-peak and N_{bkg} the number of entries in the remaining background. Both numbers have been obtained by fitting the two final state proton missing mass distribution, which will be discussed later in detail. The difference between Eq. 5.16 and the signal-to-background ratio $\frac{N_{sig}}{N_{bkg}}$ is, that the latter case is by definition sensitive to an improvement of the ratio between signal and background events. There is no information given, whether only background is reduced or signal events are removed too. In contrast, the significance takes both into account.
The top right picture of Fig. 5.16 shows that the largest significance is achieved for the hyperbola parameter $A = 3.8\,\text{deg} \times \text{GeV}$ (purple curve in top left plot of Fig. 5.16).
One issue, that comes along with this cut is the influence on the final photon energy distribution. For that purpose, the reconstruction efficiency for $\eta \to \pi^+\pi^-\gamma$ has been studied as a function of the photon energy in the η rest-frame for different values of the parameter A. The results are shown in the bottom part of Fig. 5.16. The efficiencies for all parameter values A are the same for photon energies larger than 0.08 GeV, but differ for smaller energies. Basically, each efficiency correction should compensate the influence of the corresponding parameter A. The bottom right picture of Fig. 5.16 shows that, at photon energies smaller than 0.05 GeV and $A > 2\,\text{deg} \times \text{GeV}$ the corresponding efficiencies are close to zero. This might lead to an overcorrection and thus causes an enhancement at small energies in the final E_γ distribution. Hence, the parameter A has been chosen to be $2\,\text{deg} \times \text{GeV}$ (black curve in top left plot of Fig. 5.16). According to Fig. 5.16, this value is reasonable to reject split-off events, but has no significant influence on the final photon energy distribution.

5.2.5.2 Selection of π^0 candidates

The identification of neutral pions is similar to the selection of single photons. Instead of investigating the single photon energy and the opening angle between the photon and a charged pion, the invariant mass of two photons (see Eq. 3.8) is determined. This distribution depends on the energy of the two photons and the opening angle between them. Thus, this distribution is also sensitive to split-offs. Fig. 5.17 shows the invariant mass distribution of two photons for measured data (black curve) and MC generated $\eta \to \pi^+\pi^-\pi^0$ events (green curve). Both curves show an enhancement at low invariant masses which correspond to split-offs and combinatorics. The enhancement in data is larger than in the simulation, because of rate effects inside the calorimeter. In order to select a π^0 candidate, a symmetric

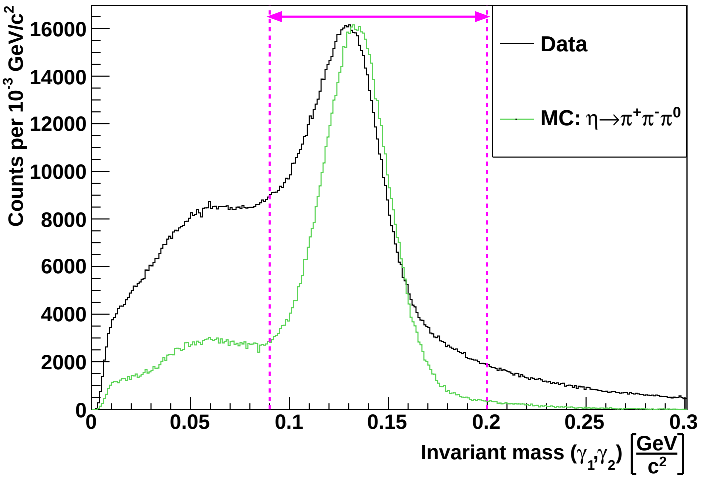

Figure 5.17: *Invariant mass distribution for two photons. The black curve is deduced from measured data and the green curve corresponds to Monte Carlo simulated* $\eta \rightarrow \pi^+\pi^-\pi^0$ *events and is scaled to the black curve with respect to the maximum intensity. The purple dashed lines indicate the window for selecting* π^0 *candidates.*

cut (see purple dashed lines in Fig. 5.17) around the π^0 mass is performed. Photon pairs are rejected, which do not fulfill the following condition:

$$0.09\frac{\text{GeV}}{c^2} \leq \text{Invariant mass } (\gamma_1, \gamma_2) \leq 0.2\frac{\text{GeV}}{c^2} \tag{5.17}$$

This selection window has been chosen such that the π^0 peak region is not effected significantly, but at the same time a considerable amount of combinatorical background is suppressed on the other hand (see green curve in Fig. 5.17).

5.3 Discussion of the first analysis approach

All analysis steps presented in the previous sections are evaluated by the monitoring spectra shown in Fig. 5.18 and Fig. 5.19. The background contributions in both missing mass spectra are described by the following function:

$$\text{background}(x) = \left(\sum_{i=0}^{4} a_i \cdot x^i\right) \times \left\{\sum_{j=1}^{2} \sigma_j \epsilon_j \cdot (\text{Missing mass})_j(x)\right\} \tag{5.18}$$

The function $(\text{Missing mass})_j(x)$ denotes the missing mass distribution of the multi-pion production reaction $pp \rightarrow pp\pi^+\pi^-\pi^0$ ($j = 1$) and $pp \rightarrow pp\pi^+\pi^-$ ($j = 2$). The factor $\sigma_j\epsilon_j$ is the product of the production cross section (see Chapter 4) and the reconstruction efficiency for $\eta \rightarrow \pi^+\pi^-\gamma$ and $\eta \rightarrow \pi^+\pi^-\pi^0$. The efficiencies are taken into account, in order to ensure sensitivity to the applied cuts and to obtain a realistic ratio between the remaining background contributions.
The kinematics of the simulated background reaction are solely determined by phase space which turned out to be improper to describe the shape of the measured background. This effect is corrected by the fourth order polynomial given in Eq. 5.18. If the simulated background matches the shape observed in data, the polynomial would be replaced by a constant factor.

The peak region of the missing mass spectra shown Fig. 5.18 and Fig. 5.19 are described by Monte Carlo simulated $pp \rightarrow pp\eta$ distributions without any additional corrections.

5.3.1 Reconstructing $\eta \rightarrow \pi^+\pi^-\gamma$ events

The final $\eta \rightarrow \pi^+\pi^-\gamma$ event candidates are obtained after particle identification, separation between two and three pion final states and suppression of split-offs. The corresponding two proton missing mass distribution is shown in the top right frame of Fig. 5.18. The black points refer to measured data which is fit by simulated signal and background events according to the procedure discussed in the previous section. The result of this fit is represented by the yellow coloured area (see the top right diagram in Fig. 5.18), which is the sum of the simulated signal and background. The individual contribution of each reaction (e.g. $\eta \rightarrow \pi^+\pi^-\gamma$ or $pp \rightarrow pp\pi^+\pi^-$) to the overall missing mass distribution is determined by the fit and indicated by a coloured curve (see inset box in top right frame of Fig. 5.18). In the following sections the overall fit of measured data with simulated signal and background events will be indicated by such a yellow shaded area.

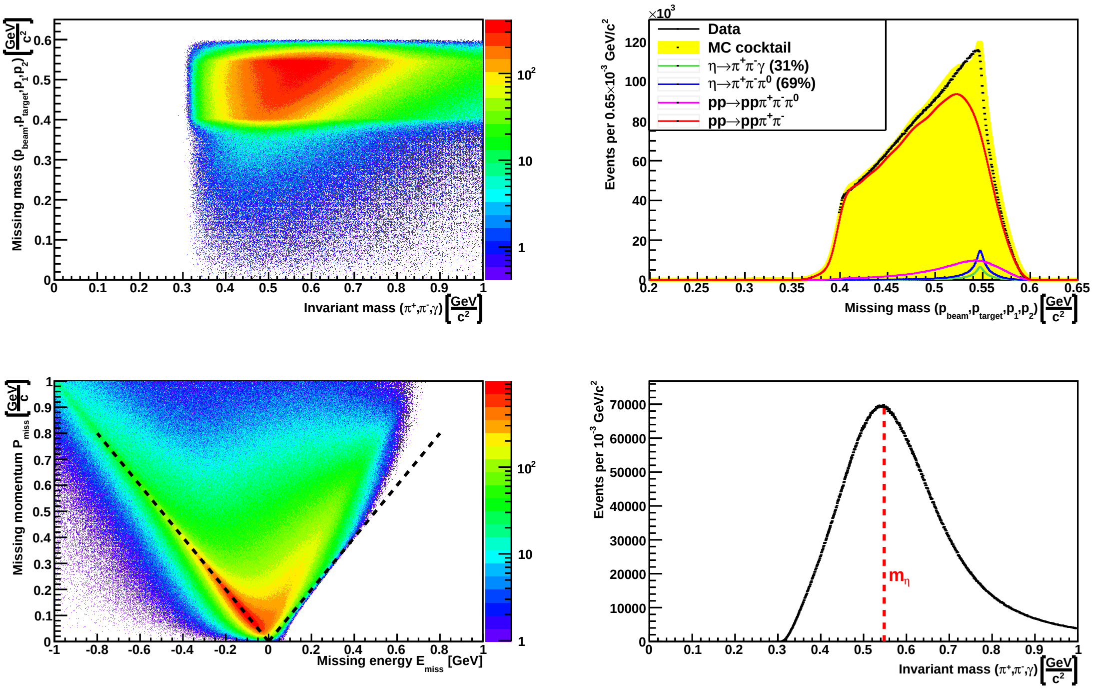

Figure 5.18: *Monitoring spectra for measured $\eta \rightarrow \pi^+\pi^-\gamma$ events after all analysis steps discussed in Sections 5.2.2 to 5.2.5.* **Top left:** *Two proton missing mass as a function of the invariant mass.* **Top right:** *Two proton missing mass. The range of the x-axis has been changed, in order to be sensitive to the peak region.* **Bottom left:** *Missing momentum versus missing energy.* **Bottom right:** *Invariant mass distribution deduced from the top left spectrum via a projection onto the x-axis. The red dashed line denotes the mass of the η meson.*

Due to the separation between two and three pion final states, background contributions from $pp \rightarrow pp\pi^+\pi^-\pi^0$ events (purple curve in top right frame of Fig. 5.18) are strongly suppressed compared to the remaining background which is completely determined by $pp \rightarrow pp\pi^+\pi^-$ events (red curve in top right frame of Fig. 5.18).

This effect can also be observed in the bottom left diagram of Fig. 5.18. Compared to the V-shaped distribution shown in Fig. 5.7, the left wing (dominated by $pp \rightarrow pp\pi^+\pi^-$ reactions) is now much more distinct than the right one (dominated by $pp \rightarrow pp\pi^+\pi^-\pi^0$ reactions). The maximum of the invariant mass distribution (bottom right diagram of Fig. 5.18) has been moved to the η mass for the same reason.
The rising step in Fig. 5.5 at invariant masses $\sim 2m_{\pi^\pm}$ has vanished, due to the rejection of electrons by the neural networks.
The properties of all spectra shown in Fig. 5.18 nicely reflect the provided analysis steps presented in Sections 5.2.2 to 5.2.5.

5.3.2 Reconstructing $\eta \rightarrow \pi^+\pi^-\pi^0$ events

The spectra for monitoring the reconstruction of $\eta \rightarrow \pi^+\pi^-\pi^0$ events (see Fig. 5.19) are obtained after particle identification, rejection of two pion final states (i.e. squared missing mass of protons and pions is $> 0.01\,\mathrm{GeV}^2/\mathrm{c}^4$) and an identification of π^0 candidates. Again, all monitoring spectra reflect the various analysis steps. Events stemming from $pp \rightarrow pp\pi^+\pi^-$ are suppressed due to the cut represented in Fig. 5.14 and the request of two photons. There is still a number of two pion production events (red line in the missing mass spectrum), which can be seen by the enhancement in the lower left corner of the momentum balance plot (bottom

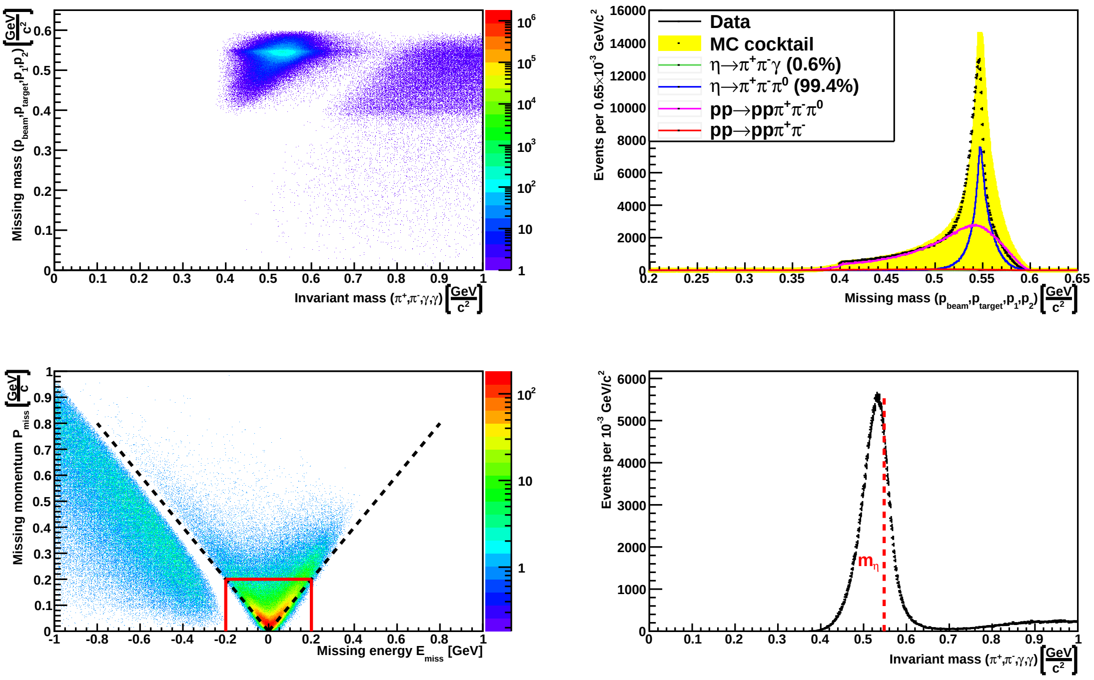

Figure 5.19: *Monitoring spectra for measured $\eta \rightarrow \pi^+\pi^-\pi^0$ events after all analysis steps discussed in Sections 5.2.2 to 5.2.5.* **Top left:** *Two proton missing mass as a function of the invariant mass.* **Top right:** *Two proton missing mass. The range of the x-axis has been changed, in order to be sensitive to the peak region.* **Bottom left:** *Missing momentum versus missing energy. The solid red lines indicate a hypothetical cut, which could be done, in order to force energy and momentum balance.* **Bottom right:** *Invariant mass distribution deduced from the top left spectrum via a projection onto the x-axis. The red dashed line denotes the mass of the η meson.*

left picture in Fig. 5.19). Two photons are missing for $pp \to pp\pi^+\pi^-$ in order to fulfill momentum conservation. Thus, large negative missing energies are populated. Those events are also responsible for the long tail visible on the right of the invariant mass distribution (bottom right corner of Fig. 5.19). In order to remove those events and to force energy and momentum balance a cut on the missing momentum and missing energy (indicated by the red box in the bottom left histogram of Fig. 5.19) could be performed. This would for sure remove most of the two pion production events and lead to a better momentum and energy conservation. The danger of such a cut is, that background reactions with similar event topology as the signal channel are not strongly effected by that cut and remain preferentially under the signal peak region.
The simulated η peak shown in the top right frame of Fig. 5.19 is wider than the distribution obtained from data. This effect is related to the energy smearing applied to the FRH-layers for simulated events, which has been discussed in Chapter 4.

All spectra shown in Fig. 5.18 and Fig. 5.19 show no significant contribution from $\eta \to e^+e^-\gamma$, because those events are suppressed to a negligible level (see Fig. 5.27) by the particle identification.
After applying this analysis chain, the reconstruction of $\eta \to \pi^+\pi^-\pi^0$ was quite successful, in the sense that a clear η-peak is visible in the missing mass spectrum. The signal-to-background ratio[e] is 0.59. Unfortunately, the channel $\eta \to \pi^+\pi^-\gamma$ could not be reconstructed as clearly. The corresponding missing mass spectrum shows no visible η-peak structure, because the background still dominates. The corresponding signal-to-background ratio is 0.05. Thus, a second approach using a kinematic fit will be introduced in the following.

5.4 Reaction specific analysis steps (2$^{\text{nd}}$ approach): The kinematic fit

A kinematic fit is a powerful tool to improve the resolution of all measured particle kinematic parameters under certain constraints like energy and momentum conservation. The kinematic fit used for this analysis is a least squares fit and allows to suppress background reactions which do not fulfil a given reaction hypothesis.

5.4.1 Least square

Assuming a reaction with N participating particles: 1+2 → 3+4+...+N, where each particle i is characterised by a set of k measured kinematic variables: $v_{i1}^{\text{meas}}, ..., v_{ik}^{\text{meas}}$, the following least squares Δ^2 is defined:

$$\Delta^2 \equiv \sum_{i=1}^{N} \sum_{j=1}^{k} \left(\frac{v_{ij}^{\text{fit}} - v_{ij}^{\text{meas}}}{\sigma_{ij}^{\text{meas}}} \right)^2 \tag{5.19}$$

The measured variables v_{ij}^{meas} are assumed to be Gaussian distributed around the initial (or true) value with a standard deviation $\sigma_{ij}^{\text{meas}}$. All detector properties, such as resolution, track reconstruction, detection inefficiencies, etc. are incorporated within $\sigma_{ij}^{\text{meas}}$. Those measurement errors are deduced from an error parameterisation,

---

[e] Here, this ratio is calculated by dividing the content of the total η-signal peak after background subtraction by the content of the subtracted background.

which will be discussed later. The values v_{ij}^{fit} in Eq. 5.19 are fit parameters, which are found by minimising Δ^2 for the given measurement errors $\sigma_{ij}^{\mathrm{meas}}$.

5.4.2 Constraints

For measured particles stemming from a certain reaction, the measured variables v_{ij}^{meas} are bound to constraints such as energy and momentum conservation. Those constraints also have to be fulfiled by the fitted variables v_{ij}^{fit}. Applying this to Eq. 5.19 leads to [55]:

$$\chi^2 = \Delta^2 + 2 \cdot \sum_{\mu} \lambda_\mu \cdot F_\mu(v_{11}^{\mathrm{fit}}, ..., v_{1k}^{\mathrm{fit}}, ..., v_{N1}^{\mathrm{fit}}, ..., v_{Nk}^{\mathrm{fit}}) \tag{5.20}$$

The constraints are summarised in the function F_μ. The intention is to minimise Δ^2 with respect to the set of imposed constraints by varying the parameters v_{ij}^{fit} for the given measurement errors $\sigma_{ij}^{\mathrm{meas}}$ (i.e. Eq. 5.20 has to be minimised). Mathematically, this is described by the Lagrangian formalism, i.e. the constraints are coupled via a Lagrange parameter to the function that has to be minimised. This is the reason why the constraint-function F_μ is coupled by the Lagrange parameter λ_μ to Δ^2.
Two pieces of information are available after the minimisation of Eq. 5.20: (i) The improved kinematic variables and (ii) The χ^2-value itself, which indicates how well a set of reconstructed particles fits to a certain reaction hypothesis.
The kinematics variables which are used in WASA to describe the measured particles are the kinetic energy E_{kin}, the polar angle θ and the azimuthal angle ϕ [55]. There is also the possibility to include constraints on the η mass, which is not done within this analysis. Such an additional constraint would make signal and background events with a mass near the η-meson indistinguishable.
In order to reconstruct $\eta \to \pi^+\pi^-\gamma$ and $\eta \to \pi^+\pi^-\pi^0$ events, a two reaction kinematic fit with the following hypothesis is used:

$$\text{reaction hypothesis 1:} \quad pp \to pp\pi^+\pi^-\gamma \tag{5.21}$$

$$\text{reaction hypothesis 2:} \quad pp \to pp\pi^+\pi^-\gamma\gamma \tag{5.22}$$

No constraint on the π^0 mass is used, because of the same reasons as mentioned before for the η mass. Additionally, it would not be possible to evaluate the improved photon energy resolution after kinematic fitting, because all fitted values would sharply peak at $m_{\pi^0} = 0.135\,\mathrm{GeV/c^2}$.

5.4.3 Error parameterisation

In order to assess χ^2, the errors $\sigma_{E_{kin}}^{\mathrm{meas}}$, $\sigma_{\theta}^{\mathrm{meas}}$ and $\sigma_{\phi}^{\mathrm{meas}}$ have to be determined. The WASA - detector is symmetric in ϕ, but has limitations in reconstructing the polar angle and particle momenta. Thus, the errors are taken to be functions of the reconstructed kinetic energy E_{kin} and the reconstructed θ angle (see Table 5.2). The error parameterisation is done by analysing simulated single particle tracks for protons, pions and photons.
The simulation of particle single tracks is performed in such a way, that the kinematic variables of the particles are homogeneously distributed over a specified energy and angular range. This range is defined by the geometrical detector acceptance on the one hand and the reaction specific phase space coverage on the other hand. However, the simulated particle single tracks are not biased by decay specific kinematics and

Error	Obtained from	E_{kin} step size	θ step size $(p, \pi^{\pm}, \gamma)$
$\sigma^{\text{meas}}_{E_{kin}}(E_{kin}, \theta)$	$\frac{E_{kin,true} - E_{kin,rec}}{E_{kin,rec}}$	50 MeV	$(1^\circ, 5^\circ, \text{crystal size})$
$\sigma^{\text{meas}}_{\theta}(E_{kin}, \theta)$	$\theta_{true} - \theta_{rec}$	50 MeV	$(1^\circ, 5^\circ, \text{crystal size})$
$\sigma^{\text{meas}}_{\phi}(E_{kin}, \theta)$	$\phi_{true} - \phi_{rec}$	50 MeV	$(1^\circ, 5^\circ, \text{crystal size})$

Table 5.2: *Measurement errors deduced from differential distributions, which are evaluated in steps of E_{kin} and θ.*

therefore allow to parameterise all areas of the detector with sufficient statistics. As discussed in Chapter 4, it is essential that the detector response for the simulations is properly adjusted to match the measured data. Otherwise, the estimated errors would not be appropriate and results obtained from the kinematic fit would not be comparable between measured and simulated data.
After analysing simulated single particle tracks, the errors are obtained by fitting error distributions, which are defined by the difference between true and reconstructed particle variables, in kinetic energy and θ steps (see Table 5.2). The step size in the polar angle θ depends on the particle type, but the kinetic energy steps are fixed to 50 MeV for all particles (see again Table 5.2). Fig. 5.20 shows examples

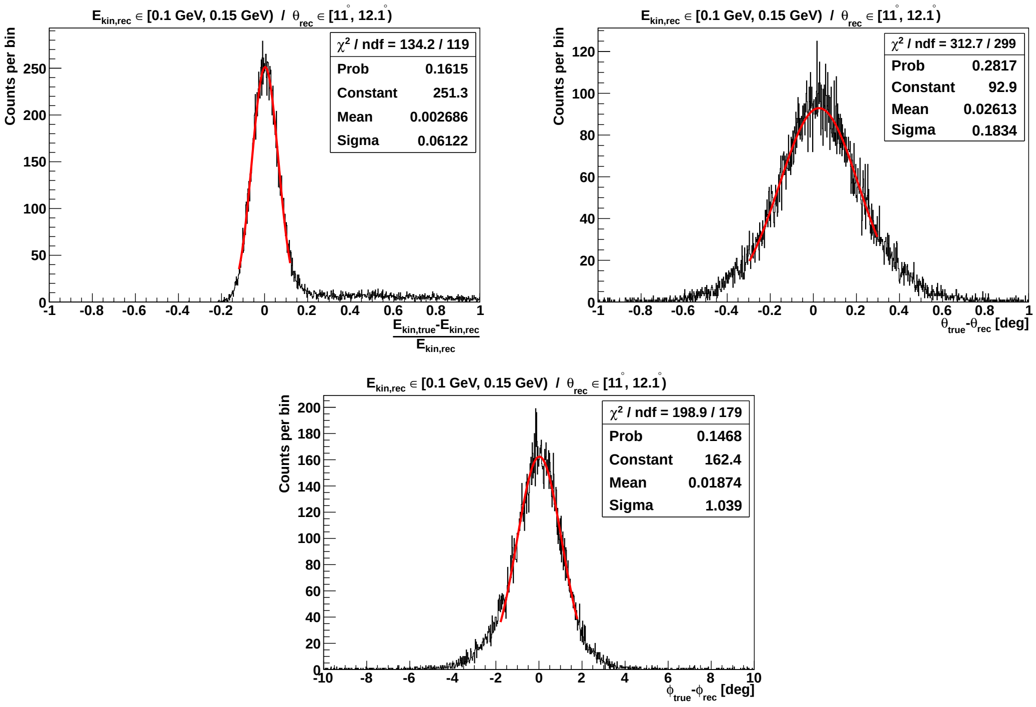

Figure 5.20: *Difference between true and reconstructed proton kinetic energy (top left), polar (top right) and the azimuthal angle (bottom). The distributions shown here are obtained for a proton kinetic energy range of:* $0.1\,\text{GeV} \leq \text{E}_{\text{kin,rec}} < 0.15\,\text{GeV}$ *and a polar angular range of:* $11^\circ \leq \theta_{rec} < 12.1^\circ$. *The red curves in each diagram represent Gaussian fits to the simulated distributions.*

of such distributions for protons in a certain kinetic energy and θ range. Each of those distributions is fit by a Gaussian function (see red curves in Fig. 5.20) and the resulting σ-parameter is assigned as measurement error to the corresponding E_{kin} and θ range. This procedure is repeated for all kinetic energy and polar angle ranges and for each particle type.

The particle reconstruction and detection is obviously embedded in the determined errors. The left diagram of Fig. 5.20 for example shows a tail towards positive $(E_{kin,true} - E_{kin,rec})/E_{kin,rec}$-values, which means that in this particular energy and θ range not all incoming proton energies are reconstructed properly. The $\phi_{true} - \phi_{rec}$ distribution shown on the right hand side of Fig. 5.20 is slightly asymmetric, because the azimuthal angle of particles reconstructed in the Forward Detector has to be corrected for influences from the solenoid field. This magnetic field correction depends on the reconstructed momentum (i.e. the kinetic energy) and the polar angle θ, which again are influenced by the detector properties. Gaussian functions are fit to the error distributions, because the least squares kinematic fit is based on the assumption, that the measured variables are Gaussian distributed. As shown in Fig. 5.20, not all error distributions are Gaussian for the reasons explained above. The Gaussian fits to all particle error distributions are performed in such a way that the tails of the distributions are excluded (see fits in Fig. 5.20). The impact of that will be discussed in the next section.

Table 5.3 shows the parameterised errors for all particles and their kinematic variables. All those plots show certain structures, which are related to the detector and reconstruction properties. The errors of the proton kinetic energies are nearly θ independent, because the detection surface of the five FRH layers increases with increasing θ which leads to a nearly full polar angular coverage. As mentioned

	Error of: E_{kin}	Error of: θ [°]	Error of: ϕ [°]
Protons	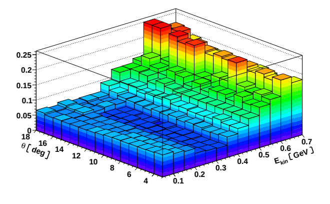	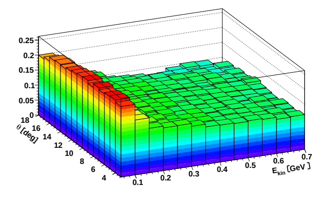	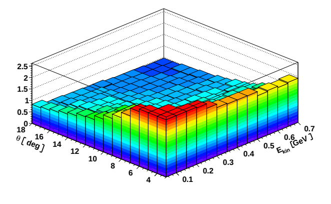
Pions	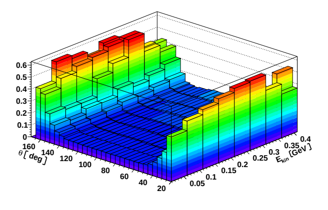	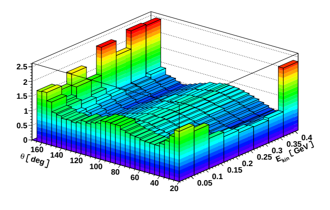	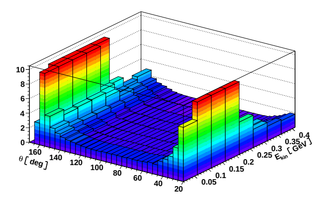
Photons	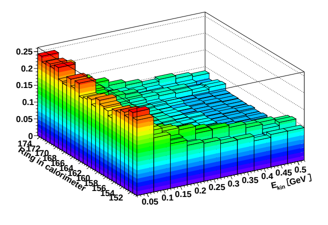	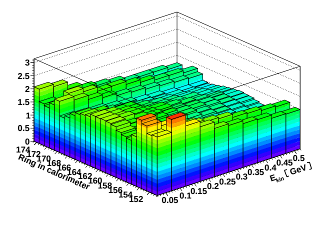	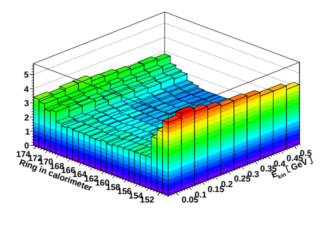

Table 5.3: *Error parameterisation plots of the* **kinetic energy (left)**, ***θ*** *(or* **ring in** *the* **calorimeter** *for photons)* **(centre)** *and* ***φ*** **(right)** *for* **protons (top row)**, **pions (centre row)** *and* **photons (bottom row)**. *The error values are plotted on the z-axis as function of the kinetic energy (x-axis) and the polar angle (or ring in the calorimeter for photons) (y-axis). The angular errors are given in degrees and the relative errors for the kinetic energies have no units.*

in Chapter 3, the maximum stopping power for protons in the FRH detector is $\sim 360\,\text{MeV}$. Protons with initial kinetic energies larger than this value will punch through the corresponding layer. Additionally, the possibility of hadronic interactions between the protons and the detector material increases with increasing kinetic energy which worsens the detector resolution. This effect can be seen in the error parameterisation plot for the proton kinetic energy: The error increases with increasing kinetic energies $> 350\,\text{MeV}$. The errors of the proton polar angle show an enhancement for kinetic energies $\leq 0.1\,\text{GeV}$, but is nearly independent of the polar angle and energy afterwards. The correlation between the error of the azimuthal angle, the polar angle and the kinetic energy (see right diagram in first row of Table 5.3) is related to the influence of the magnetic field, which has been mentioned above.

All parameterisation plots for the charged pions show an energy independent enhancement at polar angles: $20° \leq \theta < 50°$ and $140° \leq \theta < 170°$. This is related to the design of the Mini Drift Chamber (see Section 3.5.1). The number of drift wires which are used for track reconstruction, decreases at this angular range and thus leads to a poor momentum reconstruction. The error for measured pion θ angles additionally shows a maximum at $\theta = 90°$. This can be explained by the small pipe for the pellet target, which is situated at that angle and thus leads to reconstruction inefficiencies.

The photon kinematic variables are parameterised in kinetic energy and ring elements, which are numbered from 151 to 174 (see Section 3.5.3). This is related to the fact that the resolution of the polar angle is determined by the crystal size. All photon error parameterisation plots (see bottom line of Table 5.3) show the same behaviour as the diagrams presented in the second row. The reason for that is quite similar to the pion case: Crystals inside the rings 151-153 are located at the back part of the calorimeter, between the beam pipe entrance to the Central Detector and the liquid helium support structure. This leads to detection inefficiencies. The same reason holds for elements inside the rings 171-174. Those crystals are situated between the end of the central calorimeter part and the beam pipe exit. The error of the photon θ angles shows, like in case of the pions, a maximum at rings 163 and 164. This is again caused by the pellet target pipe, which enters the Central Detector at that point. As discussed in Chapter 3, the resolution of a scintillating calorimeter is given by: $\frac{\sigma(E)}{E} \sim \frac{1}{\sqrt{E}}$. This feature is the reason why the errors of all photon variables decrease with increasing kinetic energy.

A second piece of information, which is provided by the error parameterisation is the mean value μ from the Gaussian fits to the individual error distribution. Ideally, those values should be zero. Any deviation from that is again connected to detector and reconstruction properties. The obtained μ-values from the individual fits have been assigned to the corresponding E_{kin} and θ range, as it was done for the error parameterisation shown in Table 5.3. In the following, the mean values μ for each particle variable will be called offsets. Table 5.4 shows the offsets μ as function of E_{kin} and θ for all particle types.

The least squares kinematic fit is based on Gaussian error distributions, which are centred at zero. For that reason, the offsets shown in Table 5.4 are used to correct

	Offset of: E_{kin}	Offset of: θ [°]	Offset of: ϕ [°]
Protons	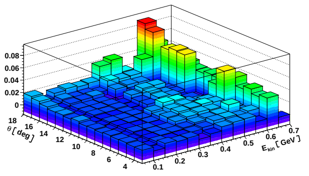	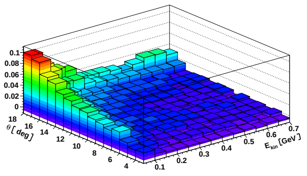	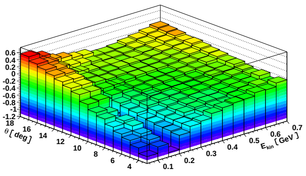
Pions	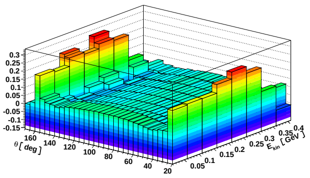	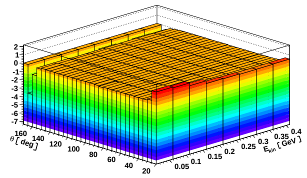	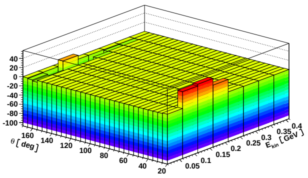
Photons	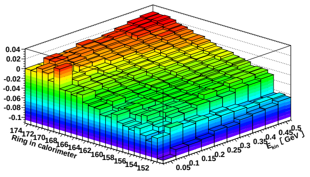	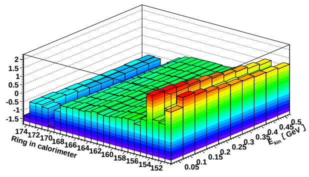	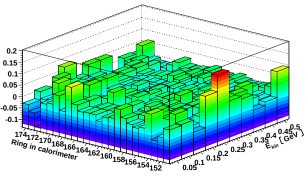

Table 5.4: *Offsets of the* **kinetic energy (left)**, $\boldsymbol{\theta}$ *(or* **ring in** *the* **calorimeter** *for photons)* **(centre)** *and* $\boldsymbol{\phi}$ **(right)** *for* **protons (top row)**, **pions (centre row)** *and* **photons (bottom row)**. *The offset values* μ *are plotted on the z-axis as function of the kinetic energy (x-axis) and the polar angle (y-axis). The angular offsets are given in degrees and the relative offsets for the kinetic energies have no units.*

the particle kinematic variables, before passing them towards the fit algorithm:[f]

$$
\begin{aligned}
E_{kin} &\rightarrow E_{kin} \cdot (1 + \mu_{E_{kin}}(E_{kin}, \theta)) && (5.23)\\
\theta &\rightarrow \theta + \mu_\theta(E_{kin}, \theta) && (5.24)\\
\phi &\rightarrow \phi + \mu_\phi(E_{kin}, \theta) && (5.25)
\end{aligned}
$$

5.4.4 Application and performance

After determining the measurement errors and correcting the kinematic variables by the offsets, the χ^2-values can be calculated for each combination of particles, which are assumed to stem either from $\eta \rightarrow \pi^+\pi^-\gamma$ or $\eta \rightarrow \pi^+\pi^-\pi^0$ decays. Fig. 5.21 a) and c) show the χ^2 distributions obtained from simulated $\eta \rightarrow \pi^+\pi^-\gamma$ and $\eta \rightarrow \pi^+\pi^-\pi^0$ events without the analysis specific cuts which have been discussed in Section 5.2. The red curve in each plot corresponds to the theoretically predicted χ^2-distribution $f(\chi^2, N)$:[g]

$$
f(\chi^2, N) = \frac{(\chi^2)^{\frac{N}{2}-1} \cdot e^{-\frac{\chi^2}{2}}}{2^{\frac{N}{2}} \cdot \Gamma\left(\frac{N}{2}\right)} \tag{5.26}
$$

The integer N represents the number of degrees of freedom, which is defined by the number of constraints and the number U of unknown variables. The request of energy and momentum conservation is fixed and already leads to four constraints.

---

[f] The offset values shown in Table 5.4 are discrete in E_{kin} and θ. In order to avoid discrete steps after correcting the kinematic variables with those offsets, a bilinear interpolation is additionally applied.

[g] The symbol $\Gamma(...)$ used here represents the Gamma function.

Thus, the number of degrees of freedom N is given by: $N = 4 - U + C_a$, as C_a represents the number of additional constraints (e.g. particle mass). In this analysis, all particle momenta are measured and no additional variable is fixed. This leads to: $N = 4 - 0 + 0 = 4$ degrees of freedom.

The obtained and theoretical χ^2-distributions in Fig. 5.21 a) and c) show deviations, which are related to the error distributions and the corresponding parameterisation (see Fig. 5.20). As discussed in the previous section, the error distributions are not Gaussian for the complete kinematic range, due to the detector and reconstruction properties. That means, they either have tails or have a non-Gaussian shape (see Fig. 5.20). However, these distributions are fit by Gaussian functions and existing tails (see Fig. 5.20) are excluded from the fit. This leads to errors, which are predominantly too small compared to the real width of the error distribution. As a consequence, the kinematic fit will return large χ^2 values, because the variation of the fit parameters during minimisation is limited by the assigned errors. This leads to the enhancement of the black distributions shown in Fig. 5.21 a) and c) towards large χ^2 values. Large errors, on the contrary, lead to small χ^2 values, because the fit parameters could be varied over a larger range in order to minimise the χ^2 function. In case of perfectly Gaussian shaped error distributions, the black curves in Fig. 5.21 a) and c) would be identical to the red ones.

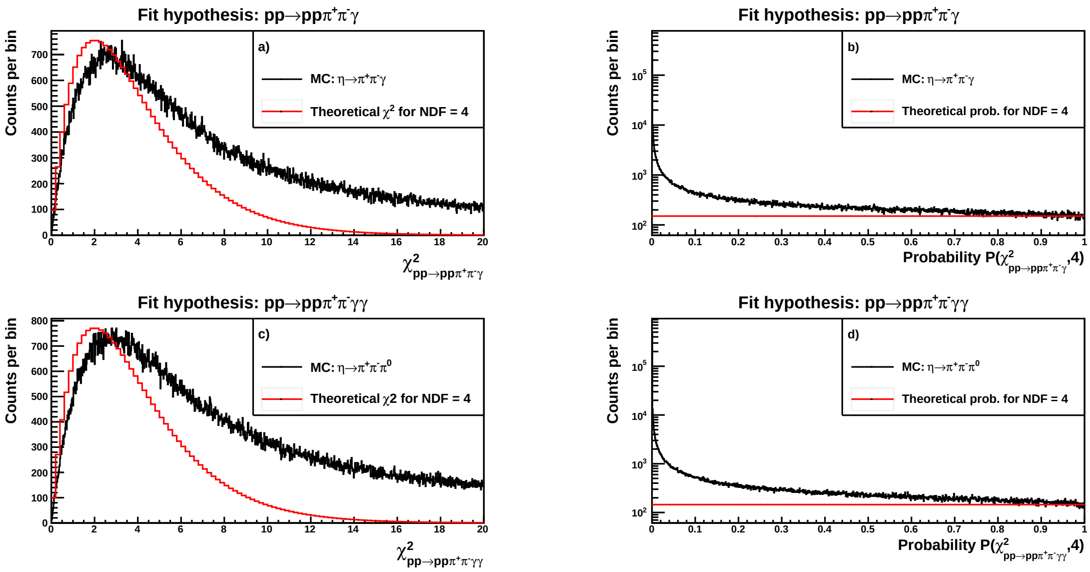

Figure 5.21: *Obtained χ^2 and probability distributions for the simulated reactions: $\eta \to \pi^+\pi^-\gamma$ (Fig.* **a)** *and* **b)***) and $\eta \to \pi^+\pi^-\pi^0$ (Fig.* **c)** *and* **d)***). Those plots are obtained after the basic cuts (e.g. proton identification, time correlations). The red curve in each diagram represents the theoretically predicted χ^2 / probability distribution for four degrees of freedom.*

5.4.4.1 The kinematic fit probability

Each χ^2-value is correlated to a fit probability $P(\chi^2, N)$ via the number of degrees of freedom N [55]:

$$P(\chi^2, N) = \frac{1}{\sqrt{2^N \cdot \Gamma\left(\frac{N}{2}\right)}} \cdot \int_{\chi^2}^{\infty} e^{-\frac{t}{2}} \cdot t^{\frac{N}{2}-1} dt \tag{5.27}$$

The plots of Eq 5.27 are shown in Fig. 5.21 b) and d). The red distributions again correspond to theoretical predictions. The deviations between the obtained and theoretical probabilities are directly related to those observed for the χ^2-distributions. Large χ^2-values lead to small probabilities and vice versa. Thus, the enhancement towards small probabilities of the black curves in Fig. 5.21 b) and d) stem from the enhancements seen in Fig. 5.21 a) and c).

The theoretical probability curves are uniformly distributed between zero and one, because they are based on errors correlated to pure Gaussian distributions.

Fig. 5.22 shows the probability distributions for the reaction hypotheses $pp \to pp\pi^+\pi^-\gamma$ (left) and $pp \to pp\pi^+\pi^-\gamma\gamma$ (right). Both distributions are obtained after particle identification in the Forward Detector and requesting time coincidences. It

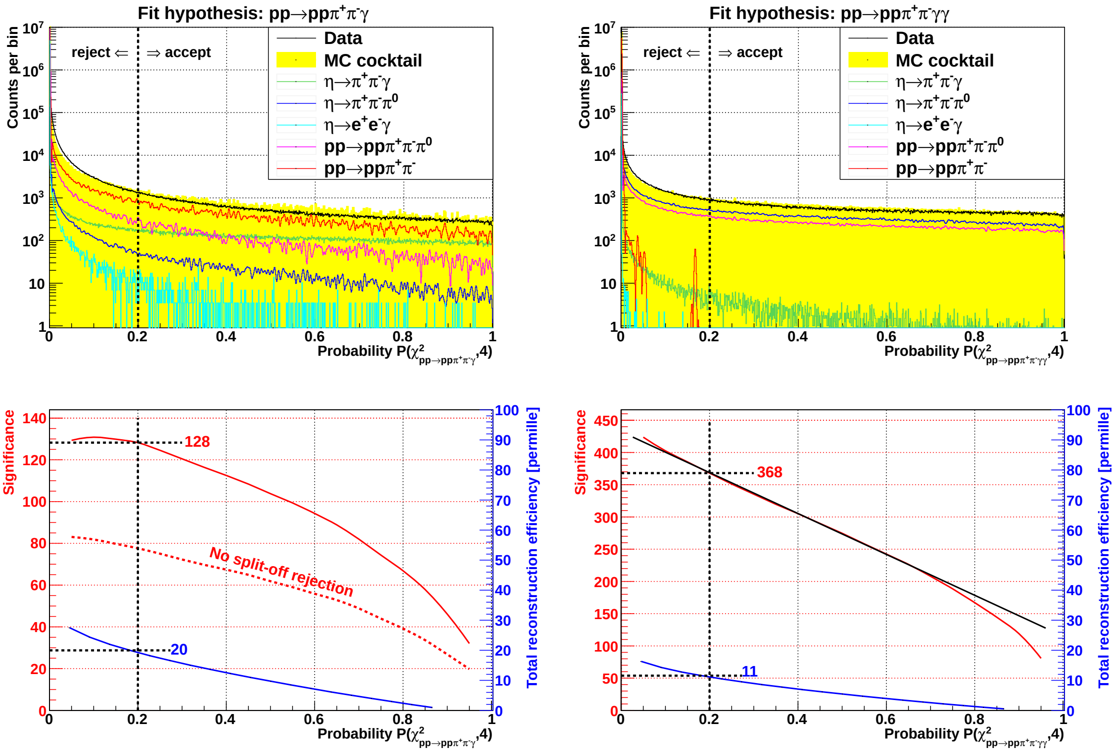

Figure 5.22: **Top:** *Kinematic fit probability $P(\chi^2, 4)$ for the reaction hypotheses $pp \to pp\pi^+\pi^-\gamma$ (left) and $pp \to pp\pi^+\pi^-\gamma\gamma$ (right). The black dashed lines indicate the event selection for probabilities larger than 20%.* **Bottom:** *Significance and efficiency for reconstructing $\eta \to \pi^+\pi^-\gamma$ events (left) and $\eta \to \pi^+\pi^-\pi^0$ events (right) as function of the corresponding kinematic fit probability. All histograms in the left column have been obtained after rejecting split-offs, except for the red dashed curve. The histograms shown in the right column have been filled after selecting a π^0 candidate. The dashed lines in each bottom plot refers to the cut drawn in the spectra above. The black solid line in the bottom right diagram is drawn to visualise the changing slope of the significance.*

turned out, that applying a kinematic fit only, is not sufficient to gain a manageable signal to background ratio for $\eta \rightarrow \pi^+\pi^-\gamma$, because of the large number of split-off events stemming from $pp \rightarrow pp\pi^+\pi^-$ reactions (compare dashed and solid red curves in bottom left frame of Fig. 5.22). Hence, a rejection of those events according to: $E_\gamma > \frac{2\,\mathrm{deg}\times\mathrm{GeV}}{\angle(\pi^\pm,\gamma)}$ has been additionally introduced (see Section 5.2.5).
For the analysis of three pion final state reactions π^0 candidates were selected via a cut on the invariant mass: $0.09\,\mathrm{GeV/c^2} \leq$ Invariant mass $(\gamma_1, \gamma_2) \leq 0.2\,\mathrm{GeV/c^2}$, as discussed in Section 5.2.5.
Background contributions are suppressed, by selecting events with a certain kinematic fit probability. All event candidates with a lower probability value are not expected to match the reaction hypothesis and thus rejected.
In order to chose a proper value, the significance has been studied as a function of the fit probability (see solid red curves in bottom row of Fig. 5.22). The significance has been calculated according to Eq. 5.16. In order to gain sensitivity, this equation was modified in such a way that the number of signal events N_{sig} of the corresponding η decay channel was corrected for the number of intruder events stemming from the other η decay. The number of intruder events on the other hand, was added to the calculated number of multi-pion background events.
The features of the solid red curves presented in the bottom row of Fig. 5.22 are directly correlated to the probability distributions shown above. The top left panel in Fig. 5.22 shows that for kinematic fit probabilities smaller than 20% the data signal is dominated by background events. For larger probabilities, contributions from three pion final state events (blue and purple curve) are continuously reduced. In contrast, the amount of two pion final states (red curve) is nearly constant. This leads to the falling slope of the significance for $P(\chi^2, 4) > 20\%$, because the variation of the total background content with respect to $P(\chi^2, 4)$ is smaller, than the variation of the signal content. The nearly constant significance plateau between 0% and 20% is caused by an opposite effect: The variation of the signal is small, compared to the reduction of background contributions.
The top right panel in Fig. 5.22 shows the probability distributions related to the analysis of $\eta \rightarrow \pi^+\pi^-\pi^0$ events. Here, the data signal is dominated by the three pion final state reactions, which have the same topology and thus, are influenced in the same way by the kinematic fit. This leads to a nearly linear dependency (compare the red and black lines in the bottom right plot of Fig. 5.22) between the significance and kinematic fit probability. The change in slope visible at $\sim 20\%$ and $\sim 65\%$ (compare again solid black and red lines) is related to the change of $\eta \rightarrow \pi^+\pi^-\gamma$ contributions to the background (see green curve in top right frame of Fig. 5.22). Therefore, the gradient of the red curve is influenced.
Both probability distributions in Fig. 5.22 show, that the majority of background events is located at probabilities $< 20\%$. This is in agreement with the calculated significance, which starts to be sensitive to the signal channel at $P(\chi^2, 4) \geq 20\%$. Hence, for both analyses, all particle combinations with kinematic fit probabilities ≥ 0.2 are accepted as possible event candidates. The corresponding efficiencies for selecting certain probabilities (including preselection, the basic analysis steps and the split-off rejection) are shown by the blue curves in the bottom row of Fig. 5.22.

5.4.4.2 Monitoring spectra after applying the kinematic fit

The results for reconstructing $\eta \rightarrow \pi^+\pi^-\gamma$ events via a selection on the kinematic fit probability and rejecting split-offs are shown in Fig. 5.23. The missing and invari-

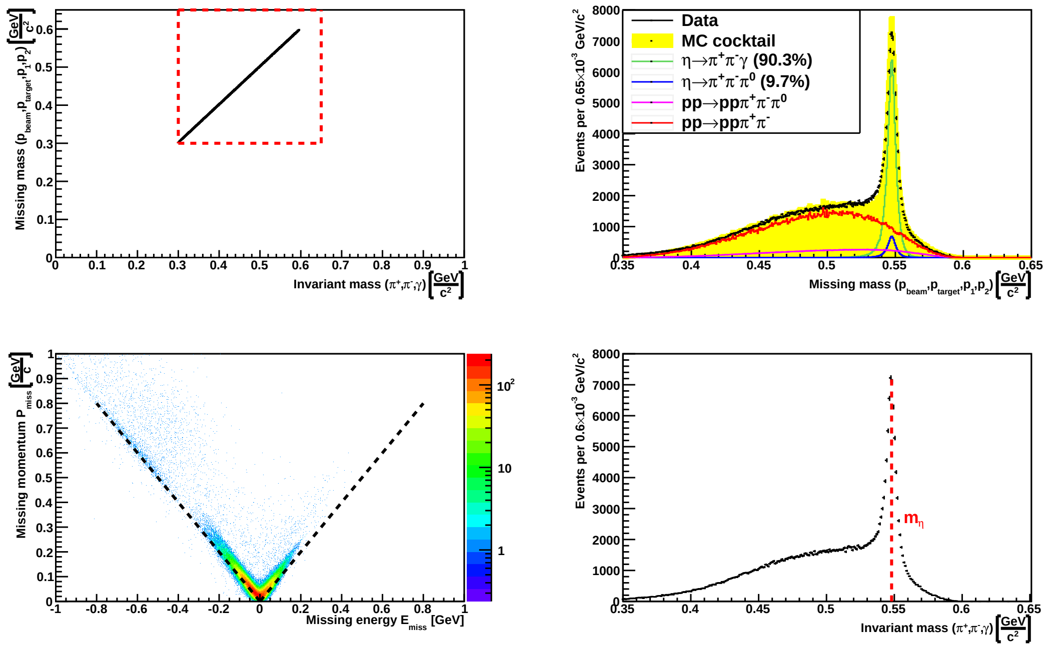

Figure 5.23: *Monitoring spectra for reconstructing $\eta \to \pi^+\pi^-\gamma$ events, under the conditions: $P(\chi^2_{pp\to pp\pi^+\pi^-\gamma}, 4) \geq 0.2$ and $E_\gamma > \frac{2\,\mathrm{deg}\times\mathrm{GeV}}{\angle(\pi^\pm,\gamma)}$.* **Top left:** *Two proton missing mass as function of the three decay particle invariant mass. Both quantities are obtained from the fitted particle momenta. The red dashed lines indicate the window from which the projections shown in the top and bottom right panels have been deduced.* **Top right:** *Two proton missing mass distribution.* **Bottom left:** *Missing momentum versus missing energy.* **Bottom right:** *Invariant mass distribution of the decay particles.*

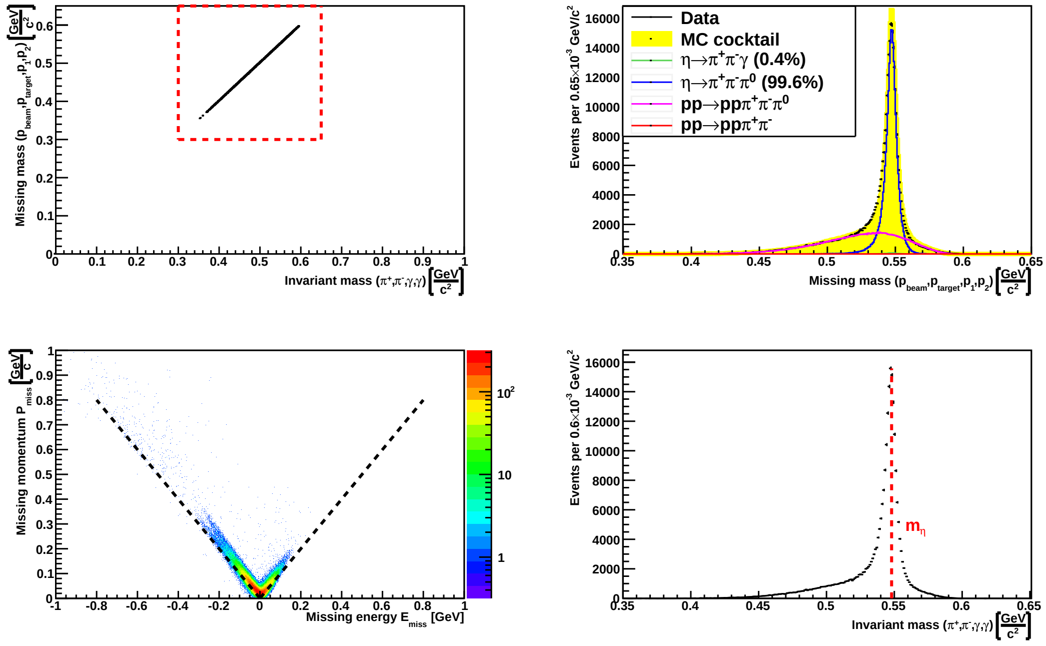

Figure 5.24: *Monitoring spectra for reconstructing $\eta \to \pi^+\pi^-\pi^0$ events, under the conditions: $P(\chi^2_{pp\to pp\pi^+\pi^-\gamma\gamma}, 4) \geq 0.2$ and $0.09\,\mathrm{GeV/c^2} \leq$ Invariant mass $(\gamma_1, \gamma_2) \leq 0.2\,\mathrm{GeV/c^2}$.* **Top left:** *Two proton missing mass as function of the three decay particles invariant mass. Both quantities are obtained from the fitted particle momenta. The red dashed lines indicate the window from which the projections shown in the top and bottom right panels have been deduced.* **Top right:** *Two proton missing mass distribution.* **Bottom left:** *Missing momentum versus missing energy.* **Bottom right:** *Invariant mass distribution of the decay particles.*

ant mass distributions have been calculated with the particle momenta which were refined by the kinematic fit.

The energy and momentum balance plot shown in the bottom left still refers to the reconstructed particle momenta. All diagrams nicely represent the observations made by the probability distribution studies: Background contributions are dominated by two pion production reactions (see red curve in the missing mass spectrum in Fig. 5.23), whereas three pion production events are suppressed (blue and purple curve in the missing mass plot). The signal-to-background ratio improved to 0.32, compared to the analysis chain discussed in Section 5.3.1. The top left plot in Fig. 5.23 shows a diagonal line, because the missing and invariant mass distributions are identical, which is also visible by comparing the top and bottom right histogram. This feature is related to the fact that the kinematic fit algorithm improves the resolution by enforcing energy and momentum conservation. Missing energy and missing momentum values are sharply distributed around zero (see bottom left diagram in Fig. 5.23), which indicates, that the fit algorithm is working properly and selecting events with the requested event topology and kinematics. The enhancement towards negative missing energies and non zero missing momenta is again caused by the large number of remaining $pp \to pp\pi^+\pi^-$ events. The monitoring spectra for analysing

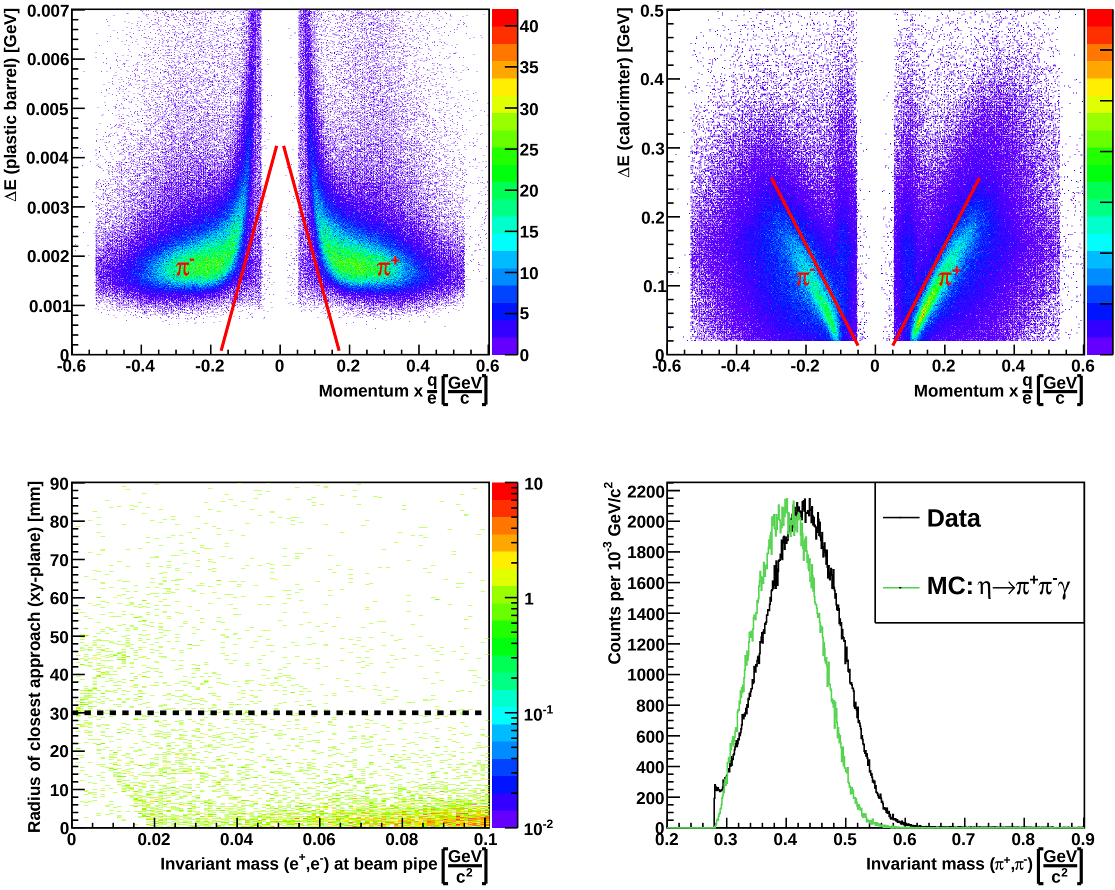

Figure 5.25: *Particle identification plots (top), radius of closest approach as a function of the dilepton invariant mass at the beam pipe (bottom left) and two pion invariant mass distribution for simulations (green) and measured (black) data (bottom right).The green curve is scaled to have the same height as the black one. All diagrams shown here are obtained after requesting:* $P(\chi^2_{pp\to pp\pi^+\pi^-\gamma}, 4) \geq 0.2$ *and* $E_\gamma > \frac{2\,\mathrm{deg}\times\mathrm{GeV}}{\angle(\pi^\pm,\gamma)}$.

$\eta \rightarrow \pi^+\pi^-\pi^0$ are plotted in Fig. 5.24. All events with less than three pions are drastically suppressed. Energy and momentum are balanced, which can be seen in the bottom left diagram of Fig. 5.24. The corresponding signal-to-background ratio is 1.43.

All monitoring spectra again indicate no contributions from $\eta \rightarrow e^+e^-\gamma$ reactions, because the kinematic fit suppresses them to a negligible level. The particle identification plots in Fig. 5.25 show clear energy loss bands related to charged pions without contributions from electrons (compare Fig. 5.8). The same holds for the two pion invariant mass and the dilepton mass near the beam pipe. Hence, an explicit particle identification for pions is not needed when the kinematic fit is applied. Electrons have a negligible mass compared to pions, thus they fail the energy and momentum balance constraint and do not pass the fit or are at least sufficiently suppressed due to the probability cut. The bottom right frame of Fig. 5.25 additionally shows that the measured (black curve) and simulated (green curve) dipion invariant mass distributions are more compatible in shape than presented in Fig. 5.9 or 5.13. This observation is again related to the features of the kinematic fit. A mismatch between the two curves still remains due to background events, which pass the probability cut. The left histogram in Fig. 5.26 shows the squared proton and pion missing mass distribution after the reconstruction of $\eta \rightarrow \pi^+\pi^-\gamma$ via the kinematic fit. The enhancement at $m^2_{\pi^0}$ has been removed, by suppressing three pion final states. The maximum at zero refers to events with no or one final state photon and is predominantly populated by $\eta \rightarrow \pi^+\pi^-\gamma$ and $pp \rightarrow pp\pi^+\pi^-$ events. The cut indicated by the black dashed line is not needed, because the requested kinematics are fulfiled via the fit algorithm.

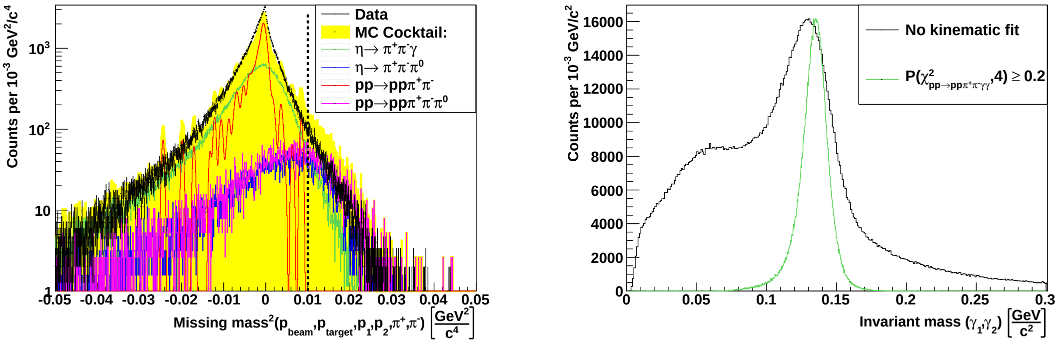

Figure 5.26: **Left:** *Missing mass distribution deduced from two protons and two pions, after requesting:* $P(\chi^2_{pp\rightarrow pp\pi^+\pi^-\gamma}, 4) \geq 0.2$ *and* $E_\gamma > \frac{2\,\mathrm{deg}\times\mathrm{GeV}}{\angle(\pi^\pm,\gamma)}$ *. The black, dashed line at* $0.01\,\mathrm{GeV}^2/\mathrm{c}^4$ *indicates the selection used in the first analysis approach.* **Right:** *Two photon invariant mass distribution deduced from data. The black curve corresponds to the analysis discussed in Sections 5.2.2 and 5.2.4. The green curve is obtained by using only a kinematic fit with the reaction hypothesis* $pp \rightarrow pp\pi^+\pi^-\gamma\gamma$ *as well as the* π^0 *selection presented in Section 5.3.2. The green curve is scaled to the black one for better comparison.*

The two photon invariant mass distribution after analysing $\eta \rightarrow \pi^+\pi^-\pi^0$ (green curve) is drawn in the right panel of Fig. 5.26. Based on the π^0 selection discussed in Section 5.3.2, one would expect that the green curve is limited between invariant masses $\geq 0.09\,\mathrm{GeV/c^2}$ and $\leq 0.2\,\mathrm{GeV/c^2}$. But due to the refinement of the photon variables by the kinematic fit, the obtained invariant mass values are smeared around these borders. For comparison, the invariant mass distribution (black curve in the right panel of Fig. 5.26) obtained after particle identification and suppression of two pion events is additionally drawn. The enhancement at low invariant masses (see black curve) is reduced by implementing the kinematic fit (see green curve), due to the suppression of combinatorial background, which does not pass the fit hypothesis. Additionally, the resolution is improved, because the available information of all measured particles is taken into account. The improvement of the photon energy resolution will be discussed in Chapter 6.

5.5 Intermediate conclusion

The analysis of $\eta \rightarrow \pi^+\pi^-\gamma$ and its reference channel $\eta \rightarrow \pi^+\pi^-\pi^0$ was performed by two independent approaches. The first one was based on particle identification, simple kinematic constraints (i.e. separation of two and three pion final state reactions) and the rejection of wrongly reconstructed photons inside the calorimeter. The corresponding relative[h] reconstruction efficiencies of each analysis condition are deduced from Monte Carlo simulated reactions and presented in Fig. 5.27. The acronym $\mathrm{MM}^2_{\pi^\pm}$ denotes the missing mass distribution shown in Fig. 5.14.

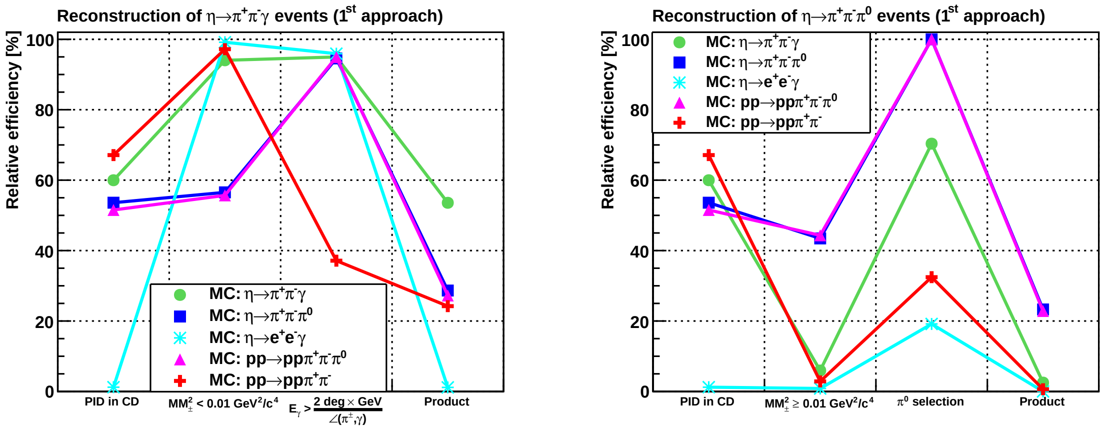

Figure 5.27: *Relative efficiencies for the reconstruction of $\eta \rightarrow \pi^+\pi^-\gamma$ (left) and $\eta \rightarrow \pi^+\pi^-\pi^0$ (right) events using the first analysis approach discussed in Sections 5.2.2 to 5.2.5. The efficiencies of the basic analysis steps (proton identification, time coincidences and event topology) as well as the preselection efficiencies are not included here.*

The particle identification acceptance via the neural networks is at lowest for the decay $\eta \rightarrow e^+e^-\gamma$, because electron like particles are rejected. The remaining reactions have different particle identification efficiencies due to the underlying kinematics (which are reaction dependant) of the pions. This also explains why the corresponding efficiencies are lower than calculated for the single particle tracks in Section 5.2.2.

Both diagrams in Fig. 5.27 show that the efficiencies of $\eta \rightarrow \pi^+\pi^-\pi^0$ and $pp \rightarrow pp\pi^+\pi^-\pi^0$ are nearly identical, which is again related to the common final state particle configuration.

The left side of Fig. 5.27 shows that all reactions with one or no photon in the final state are accepted by $> 90\%$ due to the cut on $\mathrm{MM}^2_{\pi^\pm}$, whereas reactions with two photons in the final state are rejected by $\approx 45\%$. This feature is directly correlated to the decay kinematics discussed in Section 5.2.4. As expected, the rejection of

---

[h] The efficiencies discussed here are given by the ratio between the number of events after and before applying the current analysis condition.

split-off candidates has the largest impact on $pp \to pp\pi^+\pi^-$ events (see red curve in left frame of Fig. 5.27). But due to the large abundance, those events still dominate the missing mass distribution shown in Fig. 5.18.

The relative efficiencies for reconstructing $\eta \to \pi^+\pi^-\pi^0$ events might be discussed in a similar way: Events stemming from $\eta \to e^+e^-\gamma$ are rejected due to the particle identification and the cut on the two pion missing mass distribution predominantly suppresses reactions with one or no photons in the final state. However, the efficiency for $\eta \to \pi^+\pi^-\pi^0$ and $pp \to pp\pi^+\pi^-\pi^0$ events after selecting $\mathrm{MM}^2_{\pi^\pm} \geq 0.01\,\mathrm{GeV}^2/\mathrm{c}^4$ is considerably small ($< 50\%$), because the corresponding two pion missing mass values (see blue and purple curves in Fig. 5.14) are also (strongly) populated in regions $< 0.01\,\mathrm{GeV}^2/\mathrm{c}^4$. The selection of a π^0 candidate further suppresses all decays with one photon at the most. The relative efficiency of $\eta \to \pi^+\pi^-\gamma$ after π^0 selection is quite large ($\approx 70\%$), because of the previous analysis condition: $\mathrm{MM}^2_{\pi^\pm} \geq 0.01\,\mathrm{GeV}^2/\mathrm{c}^4$. An additional fake photon leads to a possible π^0 candidate. The analysis steps presented in Fig. 5.27 were suitable for reconstructing $\eta \to \pi^+\pi^-\pi^0$ events, but failed for $\eta \to \pi^+\pi^-\gamma$, in the sense that it was not possible to reduce the large amount of two pion production events to a sufficient level (see missing mass plot in Fig. 5.18). Therefore, a kinematic fit algorithm has been applied, which uses the kinematic variables of all particles, including the reconstruction performance of the detector. This approach allowed the multi-pion background to be reduced to a manageable level (see the missing mass plots in Fig. 5.23 and 5.24 as well as the efficiencies in Fig. 5.28) and lead to a clear η signal for both decay channels. Investigation of the monitoring spectra and cross checks with the previous analysis chain showed consistency with respect to the reconstruction performance. Additionally, it was found that most of the analysis steps done within the first approach could be replaced by the kinematic fit (i.e. particle identification, separation between two and three pion final states).

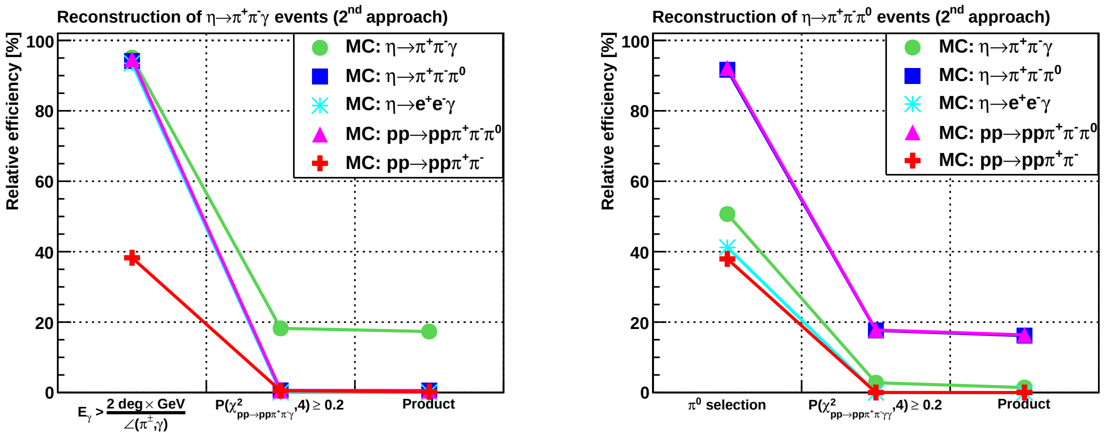

Figure 5.28: *Relative efficiencies for the reconstruction of $\eta \to \pi^+\pi^-\gamma$ (left) and $\eta \to \pi^+\pi^-\pi^0$ (right) events using the second analysis approach discussed in Section 5.4. The efficiencies of the basic analysis steps (proton identification, time coincidences and event topology) as well as the preselection efficiencies are not included here.*

The relative efficiencies of this analysis procedure are plotted in Fig. 5.28 and show similar features than presented in Fig. 5.27: Events stemming from $\eta \to \pi^+\pi^-\pi^0$ and $pp \to pp\pi^+\pi^-\pi^0$ have identical efficiencies due to the reasons explained above and the split-off rejection predominantly removes $pp \to pp\pi^+\pi^-$ events. The relative reconstruction efficiency for $\eta \to \pi^+\pi^-\gamma$ after selecting a π^0 candidate is smaller

than shown in Fig. 5.27, because of the missing cut on $\mathrm{MM}^2_{\pi^\pm}$. A similar conclusion can be drawn for the increased π^0 selection efficiency for $\eta \to e^+e^-\gamma$. The efficiency values for each analysis condition discussed in Figures 5.27 and 5.28 are listed in Appendix D. The last column in both figures represents the product of the efficiencies listed in the previous columns.
Fig. 5.28 clearly shows the reduction of background events due to the kinematic fit algorithm. However, using this method leads also to a considerably low acceptance for the signal channels. The reason for that can be easily seen in the top row of Fig. 5.22: Most of the signal events are located at small fit probabilities and therefore removed after requesting a minimum probability value of 0.2. As pointed out before, the benefit of this analysis method is the improved signal-to-background ratio which increased from 0.05 (first analysis approach) to 0.32 for $\eta \to \pi^+\pi^-\gamma$ and from 0.59 (first analysis approach) to 1.43 for $\eta \to \pi^+\pi^-\pi^0$, respectively.
According to that, the final analysis (schematically represented in Fig. 5.29) of $\eta \to \pi^+\pi^-\gamma$ and $\eta \to \pi^+\pi^-\pi^0$ includes, in addition to the basic analysis steps, the kinematic fit and the rejection of split-off events (see green highlighted box in Fig. 5.29). All results shown in the next chapter are based on this configuration.

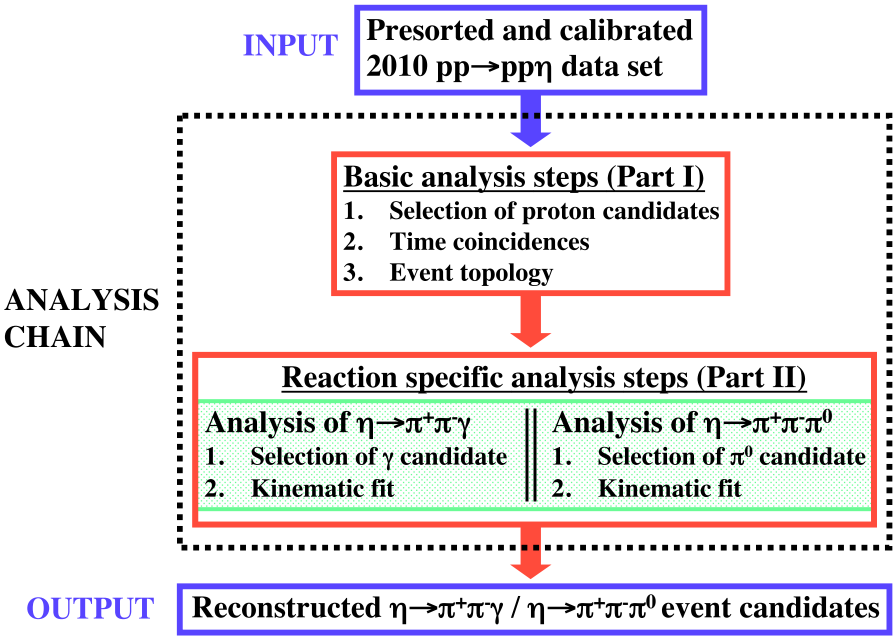

Figure 5.29: *Design of the final analysis module. The green box highlights the reaction specific analysis part, which has been described in Sections 5.2.5 and 5.4.*

5.6 Outlook: A possible 3^{rd} analysis approach

A third approach to this analysis could be the implementation of a multi-variable-analysis-tool, in order to improve the performance. The basic idea of such tools is to solve a classification problem, using a set of variables which might be correlated. The final output is one single variable, which is used as discriminator between signal and background events. Neural networks are one example for multi-variable-analysis-tools. There are many different types of tools implemented in the ROOT-software package [53]. Various tests showed that the most sufficient multi-variable-algorithm is provided by a boosted decision tree (see Fig. 5.30).

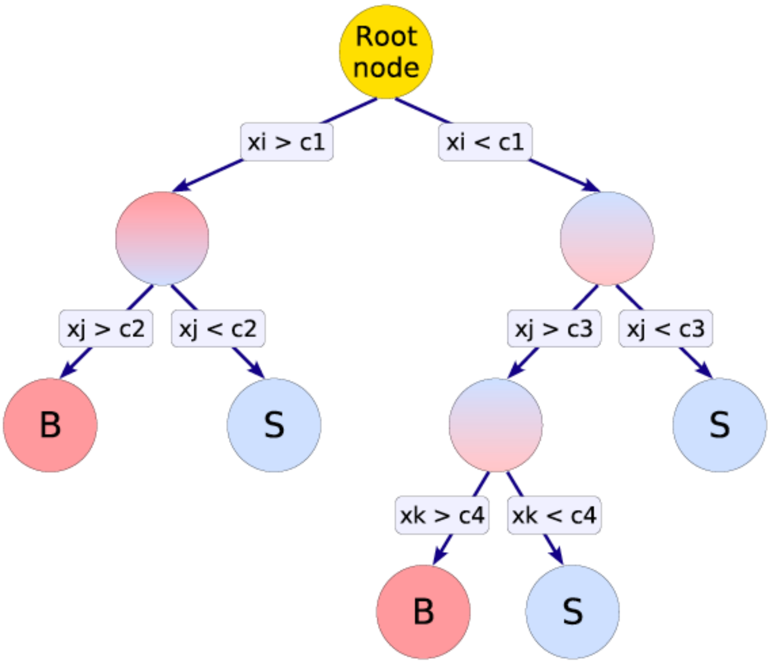

Figure 5.30: *Schematic representation of a decision tree [53]. The variables x are related to the classification parameters. The coefficients c are determined during the training of the decision tree.*

A boosted decision tree is quite similar to a neural network. Signal and background events are separated by a number of classification variables. Basically, such a tree consists of a set of linear cuts, which are performed in a certain order [53, 56] as indicated in Fig. 5.30.

A tree is built, by using a training data set, like it was done for the neural network. The initial training events define a Root node, which is divided into two sub-nodes (or branches) after a cut on the first variable x_i. The cut-parameter c_i is adjusted to achieve the maximum separation between signal and background events [53, 56]. The events in the two sub-nodes have to pass a second cut c_j, which is optimised again with respect to maximum separation. This leads to further nodes. Their events must pass a third cut and so on. The splitting procedure stops, if a minimum number of events is obtained. This number is specified by the user. The final nodes, or leaves, are called ”signal“ if the majority of events inside them are signal events. Otherwise the leaves are called ”background“.

The tree is supervised by a test sample. All events landing on a signal leaf are supposed to be signal and are counted with +1. Events landing on a background leave are counted with -1 [56]. The performance of this classification algorithm is improved by boosting: The identification error according to the training sample is calculated and the events are modified with weights (like those in the neural network case). A new tree is built with event weights. The misidentification is calculated again, which leads to updated weights and the procedure is repeated until the identification error is minimal. This leads to a forest with N decision trees. The classification, whether an event is more signal or background like, depends on the average score the event obtains from all trees in that forest. This number finally defines the discrimination variable D of that method [53, 56].

In order to improve the identification of $\eta \rightarrow \pi^+\pi^-\gamma$ events, a boosted decision tree with classification variables: (i) $P(\chi^2_{pp\rightarrow pp\pi^+\pi^-\gamma}, 4)$, (ii) minimum opening angle $\angle(\pi^\pm, \gamma)$ and (iii) E_γ was used. The tree was trained to separate between $\eta \rightarrow \pi^+\pi^-\gamma$ and $pp \rightarrow pp\pi^+\pi^-$ events. The three pion decay and production were not taken into account, because they are too similar with respect to the final state configuration. The left frame of Fig. 5.31 shows the output of the boosted decision tree for background (red) and signal events (green). The black line indicates a cut, which has been performed in the analysis in order to select signal events.

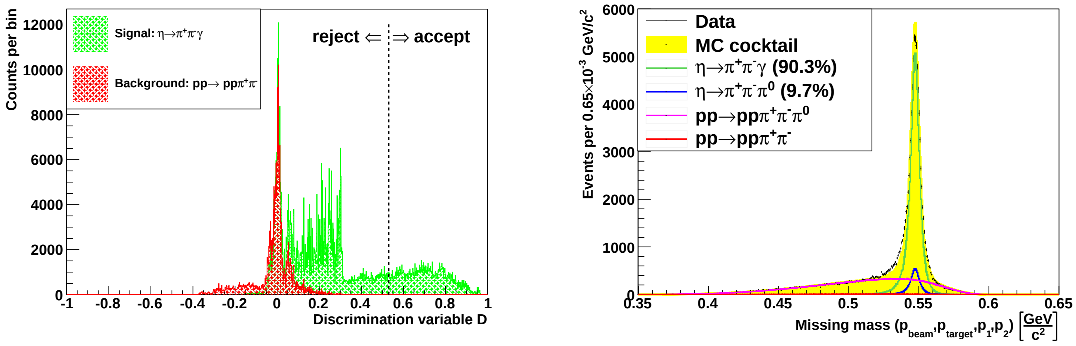

Figure 5.31: **Left:** *Discrimination variable D of a boosted decision tree for simulated background ($pp \rightarrow pp\pi^+\pi^-$) and signal ($\eta \rightarrow \pi^+\pi^-\gamma$) events. The black dashed line indicates a cut, which is used in the analysis to select signal events.* **Right:** *Missing mass for two protons after rejecting events with $D < 0.53$.*

The right frame of Fig. 5.31 shows the two proton missing mass after selecting events with $D \geq 0.53$. For better comparison, this cut has been chosen according to an reconstruction efficiency of 2%, which was also obtained for the analysis shown in Fig. 5.23. The number of two pion production events has been reduced drastically. The remaining background is determined by three pion final states only. The analysis conditions shown in Fig. 5.23 led to a signal to background ratio of 0.32 for reconstructing $\eta \rightarrow \pi^+\pi^-\gamma$ events. Using the approach presented in this section leads to a signal to background ratio of 1.43, which is nearly a factor five improvement. Additionally, the the number of discrimination variables has been decreased from two (kinematic fit probability $P(\chi^2, 4)$ and split-off rejection parameter A) to one.

Multi-variable-analysis-tools are predominantly used in cases, where the signal is highly dominated by background. However, in this third analysis approach, the tool was used to improve the event selection performance.

Nevertheless, such an approach is only applicable, if the systematics and the influence of each classification variable on the physical observables are understood (e.g. How does a variation of the kinematic fit probability effect the final result?). Additionally, it is again extremely necessary that simulation and data match. Otherwise, the output of the decision tree would be unpredictable. Thus, the implementation of a multi-variable-analysis is recommended as very last step in an analysis chain, when all systematic effects are (at least) understood. The discussion of those effects will be presented in the following chapter.

> *"Fall down seven times, get up eight times"*
>
> Bodhidharma

Chapter 6

Decay Observables of $\eta \to \pi^+\pi^-\gamma$

After reconstructing $\eta \to \pi^+\pi^-\gamma$ and $\eta \to \pi^+\pi^-\pi^0$ events, the physical observables (i.e. the relative branching ratio, the photon energy distribution and the pion-photon opening angle distribution) of $\eta \to \pi^+\pi^-\gamma$ shall be calculated. The results presented in this chapter are based on the following analysis conditions, which have been developed in the previous chapter:

Analysis of $\eta \to \pi^+\pi^-\gamma$:

i) Basic analysis steps (see Fig. 5.29)
ii) $E_\gamma > \frac{2\,\mathrm{deg}\times\mathrm{GeV}}{\angle(\pi^\pm,\gamma)}$
iii) $P(\chi^2_{pp\to pp\pi^+\pi^-\gamma}, 4) \geq 0.2$

Analysis of $\eta \to \pi^+\pi^-\pi^0$:

i) Basic analysis steps (see Fig. 5.29)
ii) $0.09\,\mathrm{GeV/c^2} \leq$ Invariant mass $(\gamma_1, \gamma_2) \leq 0.2\,\mathrm{GeV/c^2}$
iii) $P(\chi^2_{pp\to pp\pi^+\pi^-\gamma\gamma}, 4) \geq 0.2$

All observables are calculated after the kinematic fit (i.e. the fitted particle momenta are used). Finally, the systematic influences of different analysis conditions on the obtained results are investigated.

6.1 The relative branching ratio: $\frac{\Gamma(\eta\to\pi^+\pi^-\gamma)}{\Gamma(\eta\to\pi^+\pi^-\pi^0)}$

In order to determine the relative branching ratio $\frac{\Gamma(\eta\to\pi^+\pi^-\gamma)}{\Gamma(\eta\to\pi^+\pi^-\pi^0)}$, the number of expected $\eta \to \pi^+\pi^-\gamma$ events (N_1^{exp}) and the number of expected $\eta \to \pi^+\pi^-\pi^0$ events (N_2^{exp}) have to be calculated. They define the relative branching ratio in the following way:

$$\frac{\Gamma(\eta \to \pi^+\pi^-\gamma)}{\Gamma(\eta \to \pi^+\pi^-\pi^0)} = \frac{N_1^{exp}}{N_2^{exp}} \tag{6.1}$$

Suppose n different decays, which have been analysed within one analysis and the number of reconstructed events N_i^{rec} for each decay i has been determined. Furthermore, the reconstruction efficiency ϵ for each decay is obtained from Monte Carlo studies. This leads to:

$$\begin{pmatrix} N_1^{rec} \\ N_2^{rec} \\ \vdots \\ N_n^{rec} \end{pmatrix} = \begin{pmatrix} \epsilon_{11} & \epsilon_{12} & \cdots & \epsilon_{1n} \\ \epsilon_{21} & \epsilon_{22} & \cdots & \epsilon_{2n} \\ \vdots & \vdots & \ddots & \vdots \\ \epsilon_{n1} & \epsilon_{n2} & \cdots & \epsilon_{nn} \end{pmatrix} \cdot \begin{pmatrix} N_1^{exp} \\ N_2^{exp} \\ \vdots \\ N_n^{exp} \end{pmatrix} \tag{6.2}$$

N_i^{exp} is the number of expected events for decay i after efficiency correction. The efficiencies for reconstructing decay channel i as decay channel i are given by ϵ_{ii}. Reconstructing a different decay channel j as channel i is given by the efficiencies ϵ_{ij}. By inverting Eq. 6.2, the number of expected events N_i^{exp} for a decay channel i can be calculated by taking into account all other decay channels j which have been falsely reconstructed as channel i. According to Monte Carlo studies (see Fig. 5.28), there are only two reconstructed η decays ($\eta \to \pi^+\pi^-\gamma$ and $\eta \to \pi^+\pi^-\pi^0$) left after the analysis steps presented in the beginning of this chapter. This simplifies Eq. 6.2 to the following 2×2 matrix equation:

$$\begin{pmatrix} N_1^{exp} \\ N_2^{exp} \end{pmatrix} = \frac{1}{(\epsilon_{11}\epsilon_{22} - \epsilon_{12}\epsilon_{21})} \cdot \begin{pmatrix} \epsilon_{22} & -\epsilon_{12} \\ -\epsilon_{21} & \epsilon_{11} \end{pmatrix} \cdot \begin{pmatrix} N_1^{rec} \\ N_2^{rec} \end{pmatrix} \tag{6.3}$$

The number of reconstructed decay events N_i^{rec} is obtained after subtracting the multi-pion background from the missing mass spectra shown in Fig. 6.1 and calculating the integral of the remaining η peak signal. In order to be insensitive to background contributions outside the peak region, which might not have been completely removed by the background subtraction, the peak integral is determined for missing masses between 0.53 GeV/c^2 and 0.56 GeV/c^2. The resulting yields are $N_1^{rec} = (86.28 \pm 0.43) \cdot 10^3$ $\eta \to \pi^+\pi^-\gamma$ and $N_2^{rec} = (222.86 \pm 0.59) \cdot 10^3$ $\eta \to \pi^+\pi^-\pi^0$ events. Taking the reconstruction efficiencies[a] into account and using Eq. 6.3, the following result for the relative branching ratio is determined:

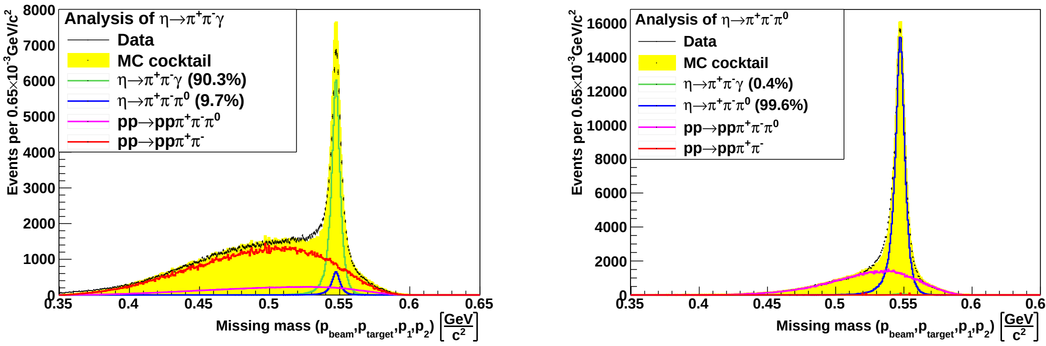

Figure 6.1: *Proton-proton missing mass distribution after the reconstruction of $\eta \to \pi^+\pi^-\gamma$ (left) and $\eta \to \pi^+\pi^-\pi^0$ (right) events via the analysis conditions presented in the beginning of this chapter. The missing mass distributions are obtained from the kinematically fitted proton momenta. Each distribution (black points) is fit by MC simulated reactions (see yellow shaded area and coloured curves).*

$$\underline{\underline{\frac{\Gamma(\eta \to \pi^+\pi^-\gamma)}{\Gamma(\eta \to \pi^+\pi^-\pi^0)} = 0.197 \pm 0.001_{\text{stat}}}} \tag{6.4}$$

The systematic uncertainties as well as an interpretation of this result will follow in later sections of this chapter.

---

[a] $\epsilon_{11} = 0.020$, $\epsilon_{12} = 0.41 \cdot 10^{-3}$, $\epsilon_{21} = 0.25 \cdot 10^{-3}$ and $\epsilon_{22} = 0.011$. The efficiencies presented here include the peak integration limits and are discussed in detail in Fig. 5.28 and Appendix D.

6.2 The E_γ distribution

The measured single photon energy distribution depends on the detector resolution of the calorimeter, which is improved by implementing a kinematic fit. The top left frame in Fig. 6.2 shows the fitted two photon invariant mass distribution as a function of the kinematic fit probability $P(\chi^2_{pp\to pp\pi^+\pi^-\gamma\gamma}, 4)$. A projection onto the y-axis of all data above the black line in Fig. 6.2 leads to an invariant mass distribution (top right frame in Fig. 6.2), which depends on a probability cut indicated by that line. The distribution is fit by a Novosibirsk function (green curve) in order to determine the photon energy resolution. The location of the black line is varied and the resolution is determined as a function of the minimum probability value as shown in the bottom frame of Fig. 6.2. Larger minimum fit probabilities lead to better resolution, because a large probability corresponds to a small χ^2-value. Using the kinematic fit improves the photon energy resolution by at least a factor ~ 2 [b], as indicated in the bottom plot in Fig. 6.2. The best achievable resolution is

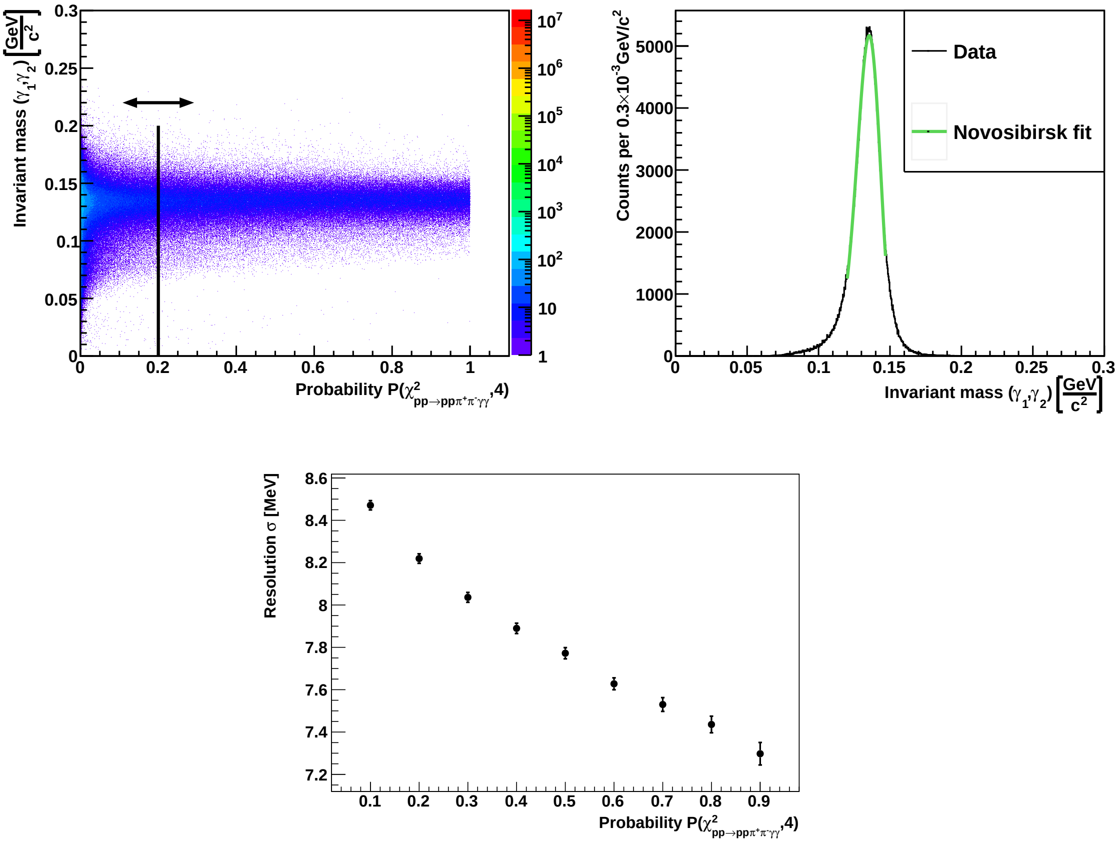

Figure 6.2: **Top left:** *Distribution of the two photon invariant mass versus the kinematic fit probability* $P(\chi^2_{pp\to pp\pi^+\pi^-\gamma\gamma}, 4)$*. The invariant mass is obtained from the photon variables returned by the kinematic fit. The black line indicates the minimum value accepted for the fit probability.* **Top right:** *Invariant mass distribution for* $P(\chi^2_{pp\to pp\pi^+\pi^-\gamma\gamma}, 4) \geq 0.2$*. The green curve represents a Novosibirsk function, which has been fit to the invariant mass distribution.* **Bottom:** *Photon energy resolution obtained from the fit shown in the top right frame as a function of the minimum kinematic fit probability. The error bars represent the uncertainties from the Novosibirsk fit.*

---

[b] The calorimeter resolution for the width of the $\pi^0 \to \gamma\gamma$ peak was determined in Chapter 4 to be 16 MeV.

$\approx 7.3\,\mathrm{MeV}$. This value defines a lower limit of sensitivity which will be important for the next step.

In order to understand the following procedure, some considerations need to be made. Using Eq. 6.2 leads to the number N_1^{exp} of expected $\eta \to \pi^+\pi^-\gamma$ events:

$$N_1^{exp} = \frac{1}{\epsilon_{11}} \cdot \left[N_1^{rec} - \epsilon_{12} \cdot N_2^{exp} \right] \tag{6.5}$$

All variables written here have the same meaning as defined in Section 6.1. The density of expected $\eta \to \pi^+\pi^-\gamma$ events with energy E_γ of the true single photon is given by $N_1^{exp}(E_\gamma)$, with: $N_1^{exp} = \int N_1^{exp}(E_\gamma)$. The same statements hold for: $N_1^{rec} = \int N_1^{rec}(E_\gamma)$ and $\epsilon_{11} = \int \epsilon_{11}(E_\gamma)$. Photons stemming from $\eta \to \pi^+\pi^-\pi^0$ decays have a different energy distribution, than photons related to $\eta \to \pi^+\pi^-\gamma$. According to that, N_2^{exp} and ϵ_{12} can not be investigated as a function of the photon energy E_γ, as it was done for N_1^{rec} or ϵ_{11}. However, there is a relative abundance of $\eta \to \pi^+\pi^-\pi^0$ events per photon energy due to misidentification, which shall be denoted as $R_2(E_\gamma)$[c]. According to Eq. 6.1, the decay width $\Gamma(\eta \to \pi^+\pi^-\gamma)$ is proportional to N_1^{exp}. Taking all this into account leads to the following relation:

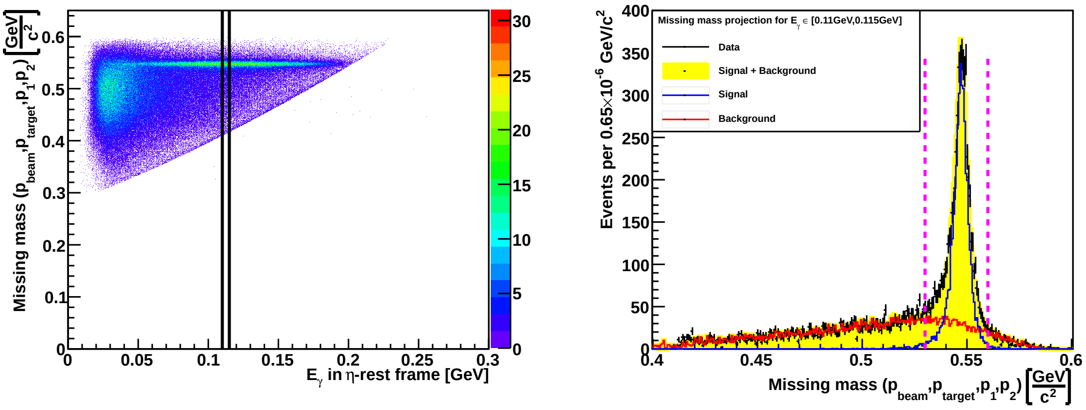

Figure 6.3: **Left:** *Proton-proton missing mass as a function of the photon energy distribution E_γ in the η rest frame, based on the analysis conditions presented in the beginning of this chapter. The black lines indicate as an example the range of $E_\gamma \in [0.11\,\mathrm{GeV}, 0.115\,\mathrm{GeV}]$ that has been selected to investigate the missing mass distribution presented in the right frame.* **Right:** *The data (black points) are described by MC simulations (yellow shaded area), using: $\eta \to \pi^+\pi^-\gamma$ for the signal region (blue curve) and $pp \to pp\pi^+\pi^- + pp \to pp\pi^+\pi^-\pi^0$ folded with a 4th order polynomial (red curve) for the background. The purple dashed lines at $0.53\,\mathrm{GeV/c^2}$ and $0.56\,\mathrm{GeV/c^2}$ indicate the integration window for the determination of the signal peak content.*

$$\frac{d\Gamma}{dE_\gamma} \propto N_1^{exp}(E_\gamma) = \frac{1}{\epsilon_{11}(E_\gamma)} \cdot \left[N_1^{rec}(E_\gamma) - R_2(E_\gamma) \cdot \epsilon_{12} \cdot N_2^{exp} \right] \tag{6.6}$$

This equation describes the single photon energy distribution and will be useful for the following steps. In order to reject photons related to $pp \to pp\pi^+\pi^-$ and

---

[c] The number of $\eta \to \pi^+\pi^-\pi^0$ events that have been falsely reconstructed as $\eta \to \pi^+\pi^-\gamma$ decays, at a given photon energy E_γ is given by $N_2(E_\gamma)$. This leads to the relative abundance $R_2(E_\gamma) = \frac{N_2(E_\gamma)}{\int N_2(E_\gamma)}$. By definition, this ratio is normalised to: $\int R_2(E_\gamma) = 1$. Furthermore, $R_2(E_\gamma)$ should not be mistaken with efficiency, because the effects of varying analysis conditions may cancel out to some extent.

$pp \to pp\pi^+\pi^-\pi^0$ decays, the missing mass deduced from the two protons is plotted vs. E_γ in the η rest-frame (see left side of Fig. 6.3). The sharp edge is related to the kinematic limit of E_γ. For each photon energy bin the missing mass spectrum is investigated and corrected for multi-pion background (see red curve on the right of Fig. 6.3). The bin size is chosen to be 5 MeV, which is narrower than the best resolution value given by the kinematic fit. This shall ensure sensitivity for the final energy distribution.

The number of reconstructed $\eta \to \pi^+\pi^-\gamma$ events inside the remaining signal peak is corrected by $\eta \to \pi^+\pi^-\pi^0$ events as well as for efficiency, according to Eq. 6.6. This procedure is repeated for all photon energy bins and leads to the distribution shown by the black points in Fig. 6.4. Using the model independent approach described in

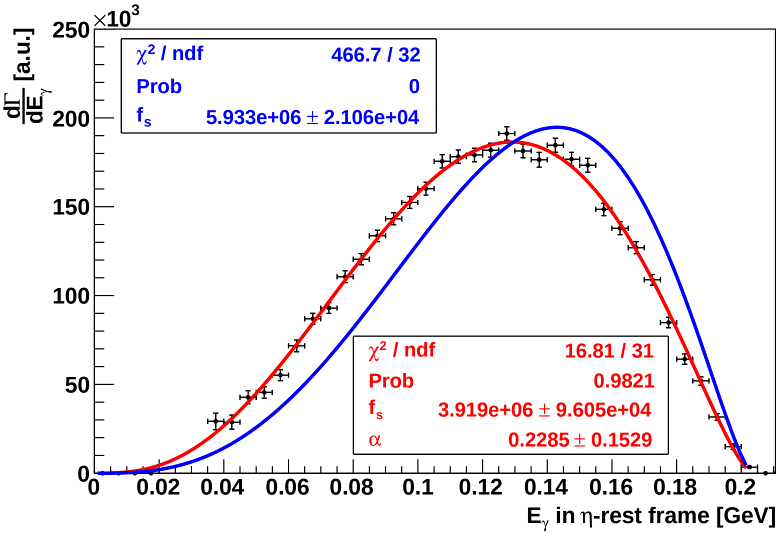

Figure 6.4: *Single photon energy distribution calculated from measured data (black points). The red curve corresponds to a fit of Eq. 2.29 to the measured data. The blue curve is obtained by using Eq. 2.28 to fit the measured energy distribution. The vertical error-bars of the measured distribution represent the statistical uncertainty. Horizontal bars refer to the bin width of 5 MeV. The fit parameter f_s is a scaling factor, which is implemented in Eq. 2.28 and 2.29.*

Eq. 2.29 to fit this distribution leads to the following α-parameter:

$$\underline{\underline{\alpha = (0.229 \pm 0.153_{\text{fit}})\,\text{GeV}^{-2}}} \tag{6.7}$$

The corresponding fitted distribution is presented by the red solid line in Fig. 6.4. Photon energies < 0.035 GeV have been omitted from fitting, because the missing mass spectra in the corresponding bin (see Appendix E) were clearly dominated by background and thus, did not allow for a clear determination of the eta signal content. Photon energies > 0.2 GeV where not taken into account, because they exceed the maximum kinematic limit of the decay $\eta \to \pi^+\pi^-\gamma$ (see Eq. 2.33).

The blue solid curve is related to a fit of Eq. 2.28, where no contributions from final state interactions are included.

Comparing the two fitted distributions (i.e. the blue and red curves in Fig. 6.4) clearly shows, that final state interactions have to be included, in order to describe the single photon energy distribution correctly. Both curves start at zero photon energy, which represents the kinematic lower limit of this decay (see again Eq. 2.33).

A further discussion and interpretation of the α-parameter will follow in the last section of this chapter.

6.3 The pion-photon opening angle distribution

The distribution of the opening angle between the positive charged pion and the single photon in the $\pi^+\pi^-$ rest-frame is obtained in the same way as described in the previous section. Fig. 6.5 shows the proton missing mass distribution as a function of the cosine of the opening angle between the positive pion and the photon. For each angular bin, the projection of the missing mass distribution is determined (see right frame in Fig. 6.5) and the background is subtracted. The remaining number of events in the peak is corrected with respect to Eq. 6.6. Fig. 6.6 shows the final results. Each curve is fit according to Eq. 2.34, which has been discussed in Chapter 2.

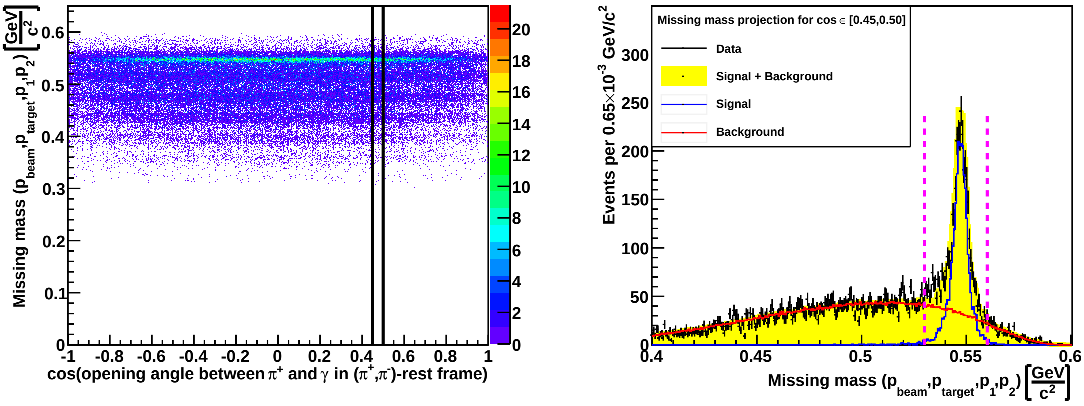

Figure 6.5: **Left:** *Proton-proton missing mass versus the cosine of the opening angle between the positive pion and single photon in the $\pi^+\pi^-$ rest frame, based on the analysis conditions presented in the beginning of this chapter. The black lines indicate the range of* $\cos\angle(\pi^+,\gamma) \in [0.45, 0.5]$ *that has been selected as an example to investigate the missing mass distribution presented in the right frame.* **Right:** *The data (black points) are described by MC simulations (yellow shaded area), using: $\eta \to \pi^+\pi^-\gamma$ for the signal region (blue curve) and $pp \to pp\pi^+\pi^- + pp \to pp\pi^+\pi^-\pi^0$ folded with a 4th order polynomial (red curve) for the background. The purple dashed lines indicate the region where the peak integral is calculated.*

In case of no D-wave contribution, the parameter β should be zero (blue curve in Fig. 6.6). A non-zero value for β would indicate a D-wave contribution, which is related to C-violation. The fit with $\beta \neq 0$ (red curve in Fig. 6.6) seems to describe the angular distributions best. The corresponding value is:

$$\underline{\underline{\beta = 0.350 \pm 0.054_{\text{fit}}}} \tag{6.8}$$

The data in Fig. 6.6 shows a fluctuation between $-0.4 \leq \cos\angle(\pi^+,\gamma) \leq 0.3$ as well as an enhancement for $0.45 \leq \cos\angle(\pi^+,\gamma) \leq 0.55$. Thus, an additional fit parameter might compensate for those effects rather than describing a physics observation. Points with $0.45 \leq \cos\angle(\pi^+,\gamma) \leq 0.55$ have been excluded from the fit.

The missing mass spectra related to those angular bins give no clear hints why an enhancement is observed within this region. A possible explanation could be given by

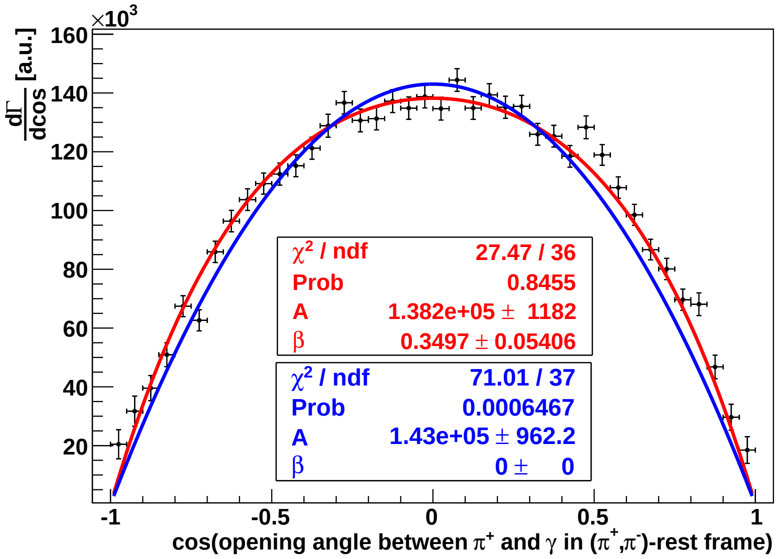

Figure 6.6: *Efficiency and background corrected opening angle distribution between the photon and the positive pion, measured in the dipion rest frame. The red and blue curves refer to a fit with Eq. 2.34, whereas the β-parameter was fixed to zero for the blue curve.*

the missing mass spectrum shown for the angular range $[0.45, 0.5]$ in Fig. 6.5. The left tail of the eta signal peak shows a shoulder between $0.53\,\mathrm{GeV/c^2}$ and $0.54\,\mathrm{GeV/c^2}$, which effects the peak content. The reasons for that shoulder are not yet clear and must be further investigated.

6.4 Addendum: Choosing the proper model

The efficiency correction used in Eq. 6.6 depends on the physics model, that is used as input for the simulation of $\eta \to \pi^+\pi^-\gamma$ events. Fig. 6.7 shows the measured energy (left) and angular (right) distribution after background subtraction, but without efficiency correction. The coloured curves represent generated events assuming that the kinematics of $\eta \to \pi^+\pi^-\gamma$ are distributed homogeneously over the phase space (red coloured distributions) or connected to the simplest matrix element (blue coloured distributions). A direct comparison shows, that the analysed measured data is in much better agreement with the distributions obtained by including the simplest matrix element.
The measured photon energy distribution is slightly shifted towards smaller energies, but is still in better agreement with the blue curve, than with the corresponding phase space distribution. The angular distribution related to the simplest matrix element is in clear agreement with the measured data. According to that, the simplest matrix element has been chosen to simulate the $\eta \to \pi^+\pi^-\gamma$ events. For a more detailed discussion see [26].

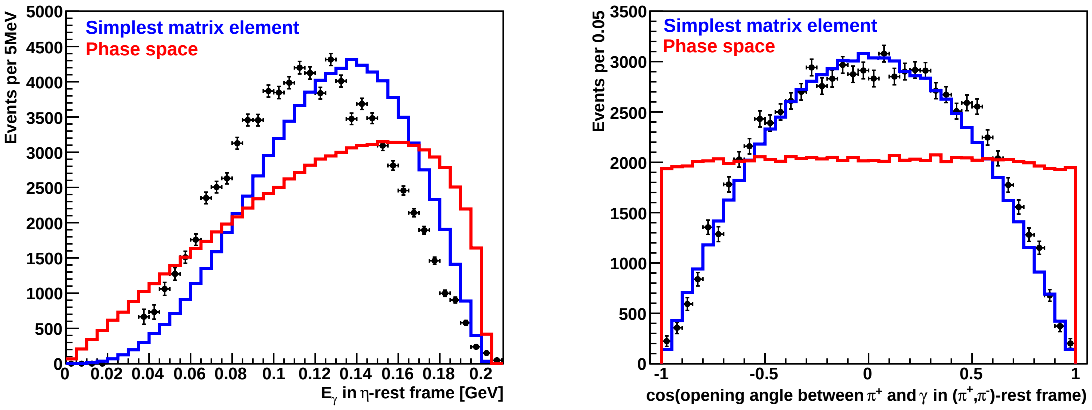

Figure 6.7: *Background corrected photon energy distribution (left) and angular (right) distribution without efficiency corrections. The solid curves represent the corresponding distributions obtained by assuming two different decay models for $\eta \rightarrow \pi^+\pi^-\gamma$. The blue coloured distributions correspond to the simplest matrix element discussed in Chapter 2. The red coloured curves are obtained by assuming a pure phase space distribution for $\eta \rightarrow \pi^+\pi^-\gamma$. The geometrical acceptance of the Central Detector of WASA is taken into account for the generated distributions. All curves are normalised to the measured data distributions.*

6.5 Dalitz Plot for $\eta \rightarrow \pi^+\pi^-\gamma$

As pointed out in Chapter 2, the photon energy distribution as well as the pion-photon opening angle distribution are visible in the Dalitz plot. The left panel of Fig. 6.8 shows the two proton missing mass as a function of the global bin number G_{bin}, which is parameterised by the Dalitz plot variables [14]:

$$G_{bin} \equiv \mathrm{FloorNint}\left[\frac{IM^2(\pi^+,\gamma)-\delta}{\delta}\right] + N_{bins} \cdot \mathrm{FloorNint}\left[\frac{IM^2(\pi^-,\gamma)-\delta}{\delta}\right] \tag{6.9}$$

$IM(\pi^\pm,\gamma)$ is the invariant mass of the positive / negative pion and the photon. The variable δ is defined as the ratio between the invariant mass range and the number of bins N_{bins} in the Dalitz plot. For this analysis, δ is chosen to be: $\delta = \frac{0.2\,\mathrm{GeV/c^2}}{25}$. The function FloorNint is the floor function, returning the integer of the argument. For each global bin, the missing mass projection is determined and processed in the same way as discussed in the previous two sections (i.e. background subtraction and acceptance correction). The resulting number of expected $\eta \rightarrow \pi^+\pi^-\gamma$ events is associated to G_{bin}, which is translated back to the corresponding bins within the Dalitz plot.

The result of this procedure is displayed in the right frame of Fig. 6.9. The left hand side shows the Dalitz plot without any background correction. The enhancement at low invariant masses is related to $pp \rightarrow pp\pi^+\pi^-$ events, which are connected to low energy photons. This enhancement is removed after background subtraction (see right panel). The horizontal and vertical lines in both diagrams represent the kinematic limit of the decay, which is given by: $m_\pi^2 \leq IM^2(\pi^\pm,\gamma) \leq (m_\eta - m_\pi)^2$. Low invariant masses $0.04\,\mathrm{GeV^2/c^4} \leq \mathrm{IM^2}(\pi^\pm,\gamma) < 0.08\,\mathrm{GeV^2/c^4}$ correspond to global bins $G_{bin} < 100$ in Fig. 6.8. Those regions are dominated by background contributions from multi-pion production. This causes zero entries in the right diagram of Fig. 6.9, because the signal is buried under this background and thus

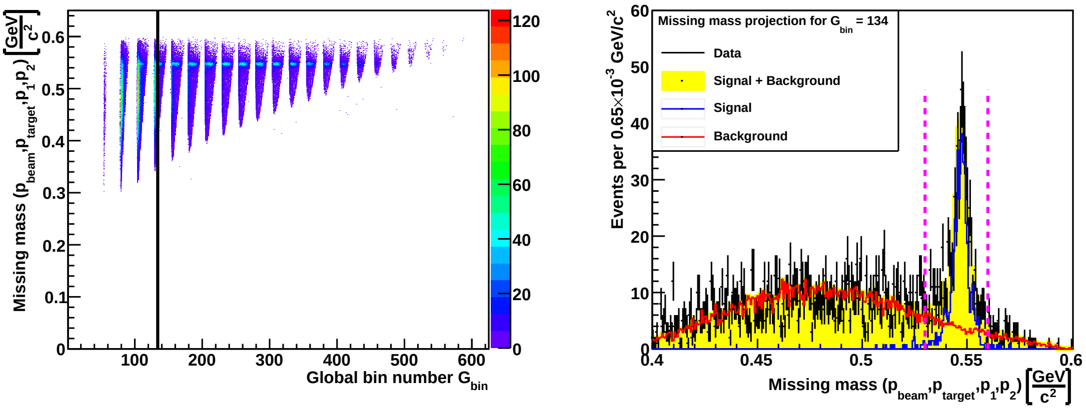

Figure 6.8: **Left:** *Two proton missing mass as function of the global bin number* G_{bin} *defined in Eq. 6.9, based on the analysis conditions presented in the beginning of this chapter. The black solid line indicates a projection of the missing mass for* $G_{bin} = 134$. **Right:** *Missing mass spectrum deduced from the projection shown in the left panel. The distribution is described by MC simulations (yellow shaded area), using:* $\eta \to \pi^+\pi^-\gamma$ *for the signal region (blue curve) and* $pp \to pp\pi^+\pi^- + pp \to pp\pi^+\pi^-\pi^0$ *folded with a 4th order polynomial (red curve). The purple dashed lines indicates the region, where the peak integral is calculated.*

removed after background subtraction. The diagonal represents the symmetry axis. A projection along the diagonal axis leads to the opening angle distribution discussed in the previous section. The population of the background corrected Dalitz plot at invariant masses $0.06\,\mathrm{GeV}^2/\mathrm{c}^4 \leq \mathrm{IM}^2(\pi^\pm,\gamma) < 0.12\,\mathrm{GeV}^2/\mathrm{c}^4$ corresponds to maxima visible in the photon energy and angular distribution.

In case of true C-violation phenomena, the Dalitz plot would show an asymmetry with respect to the diagonal line.

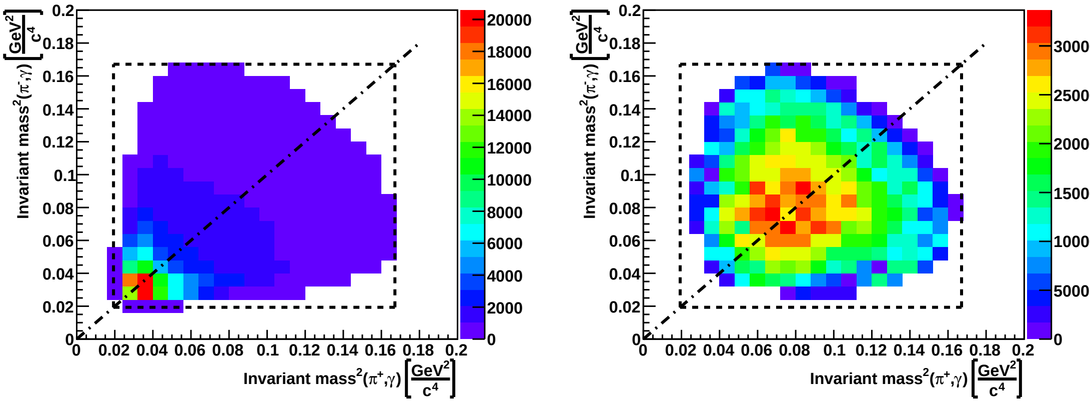

Figure 6.9: *Measured Dalitz plot of the decay* $\eta \to \pi^+\pi^-\gamma$. **Left:** *Without background subtraction.* **Right:** *With background subtraction and efficiency correction. The black, dashed box in each diagram represents the kinematical limit of the decay. The diagonal lines represent the symmetry axis.*

6.6 Investigation of systematic effects

The calculated observables discussed in the previous sections, are based on selection criteria applied within the analysis and thus may depend on underlying systematic effects. Those effects and the corresponding uncertainties will be discussed in the following subsections. The basic assumption for those investigations is, that influences related to one analysis parameter (e.g. the kinematic fit probability) are not correlated with the remaining parameters (e.g. the split-off rejection). Accordingly, the influence of each analysis condition on the final result is studied while fixing the remaining analysis parameters.

6.6.1 Uncertainties related to the kinematic fit

As presented in Chapter 5, the kinematic fit algorithm comprises all particle kinematic variables as well as the detector features and returns a single discrimination variable. Based on the selection of that variable, events are accepted or rejected and the particle kinematic variables are refined. This leads to a strong decisive power on the one hand, but may also cause large systematic effects on the other hand, especially if certain detector effects are described differently in simulated and measured data.

6.6.1.1 Pull distributions

The monitoring spectra discussed in Chapter 5 (e.g. energy and momentum balance) allow for a global investigation of the fit algorithm (i.e. whether energy and momentum conservation is given, or which particles are selected). A more detailed insight into the features of the fit are given by so called pull distributions, which are defined as follows:

$$\mathrm{Pull}(v_{ij}) = \frac{v_{ij}^{\mathrm{meas}} - v_{ij}^{\mathrm{fit}}}{\sqrt{(\sigma_{ij}^{\mathrm{meas}})^2 - (\sigma_{ij}^{\mathrm{fit}})^2}} \tag{6.10}$$

The variable v_{ij} represents the kinematic parameter j (i.e. E_{kin}, θ and ϕ) of a particle i. The errors of the measured variables are denoted by $\sigma_{ij}^{\mathrm{meas}}$ and the errors of the fit variables are represented by $\sigma_{ij}^{\mathrm{fit}}$, respectively. The fit errors are obtained in exactly the same way as the measurement errors: In a first step $v_{\mathrm{true}} - v_{\mathrm{fit}}$ distributions are determined in steps of kinetic energy and polar angle. The step size is the same one as used for the error parameterisation (see Chapter 5). Each distribution has been fit by a Gauss function and the obtained σ represents the error. The errors of the fit particle kinematic variables are presented in Table 6.1. The distributions show in which area (of the detector) and to what extent the error of each particle variable could be improved by the fit.

For the estimation of the fit errors, simulated $\eta \to \pi^+\pi^-\gamma$ events were analysed. These events have a defined phase space region, thus the distributions in the second and third row of Fig. 6.1 have zero entries in certain regions. Several enhancements due to low statistics are visible at the boarders of those regions.

The errors of the fit proton kinetic energies do not increase with kinetic energy, as observed for the measurement errors. The errors of the fit θ and ϕ proton angles are of the same order of magnitude as the corresponding errors for the reconstructed angles. Those variables are reconstructed with such precision, that they could not be improved by the kinematic fit.

The enhancements for reconstructed pion and photon variables at large and small

	Error of: E_{kin}	Error of: θ	Error of: ϕ
Protons	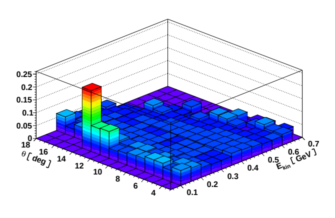	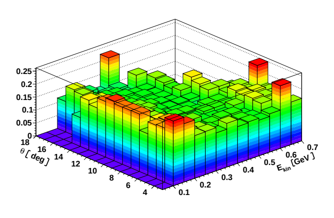	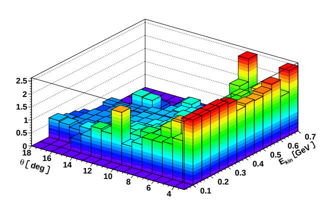
Pions	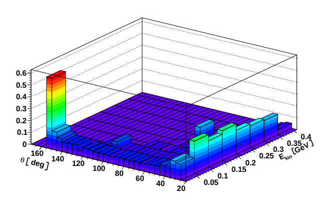	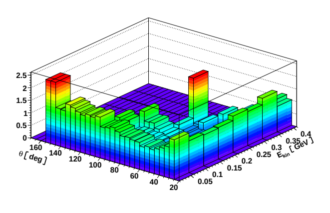	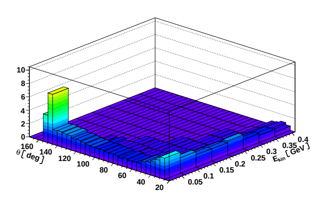
Photons	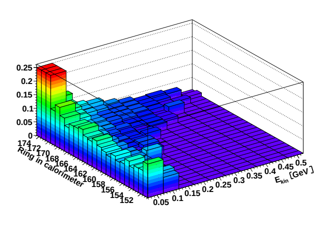	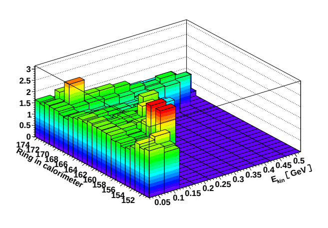	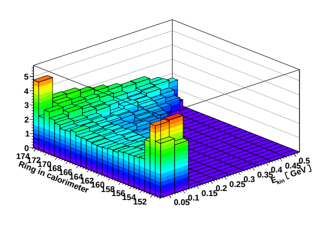

Table 6.1: *Errors of the fit particle kinematic variables:* **kinetic energy (left)**, ***θ*** *(or* **ring in** *the* **calorimeter** *for photons)* **(centre)** *and* ***ϕ*** **(right)** *for* **protons (top row)**, **pions (centre row)** *and* **photons (bottom row)**. *The error values are plotted on the z-axis as function of the kinetic energy (x-axis) and the polar angle (y-axis). The angular errors are given in degrees and the relative errors for the kinetic energies have no unit.*

θ angles (rings in calorimeter) are significantly reduced for the fitted variables (see second and third row in Table 6.1). Additionally, reconstruction inefficiencies at $\theta = 90^\circ$ (Ring $= 163, 164$) caused by the pellet target pipe are compensated by the fit algorithm. The trend of decreasing photon energy errors with increasing kinetic energies remains after refining the photon variables.

The errors of the fit and measured particle kinematic parameters are used to compute the pull distributions for simulated and measured data. In order to be able to compare the various pull distributions, both data sets were analysed under the same conditions, which have been introduced in the beginning of that chapter.

The underlying assumption for applying the kinematic fit is that all error distributions of the reconstructed variables are Gaussian and all variables are uncorrelated. According to that, the resulting error distributions of the fit variables should also be Gaussian. Thus, the distribution connected to Eq. 6.10 should also be Gaussian with $\sigma_{\text{Pull}} = 1$ and a mean value equal to zero. Any deviation from that is either related to systematic influences or to the error estimation. The χ^2-distribution obtained for $\eta \to \pi^+\pi^-\gamma$ was discussed in Chapter 5. Enhancements at large values are observed, due to underestimated measurement errors. This effects the fit particle variables as well as their errors and consequently the pull distributions, so that $\sigma_{\text{Pull}} \neq 1$. A non-zero mean value indicates that the error estimation is affected by systematic effects (e.g. calibration of a detector part). A comparison between the pulls obtained from simulated and measured data allows to investigate the influence of the kinematic fit algorithm on each of those data sets. Possible deviations might give a hint if reconstruction effects are described differently in simulations than in the measured data.

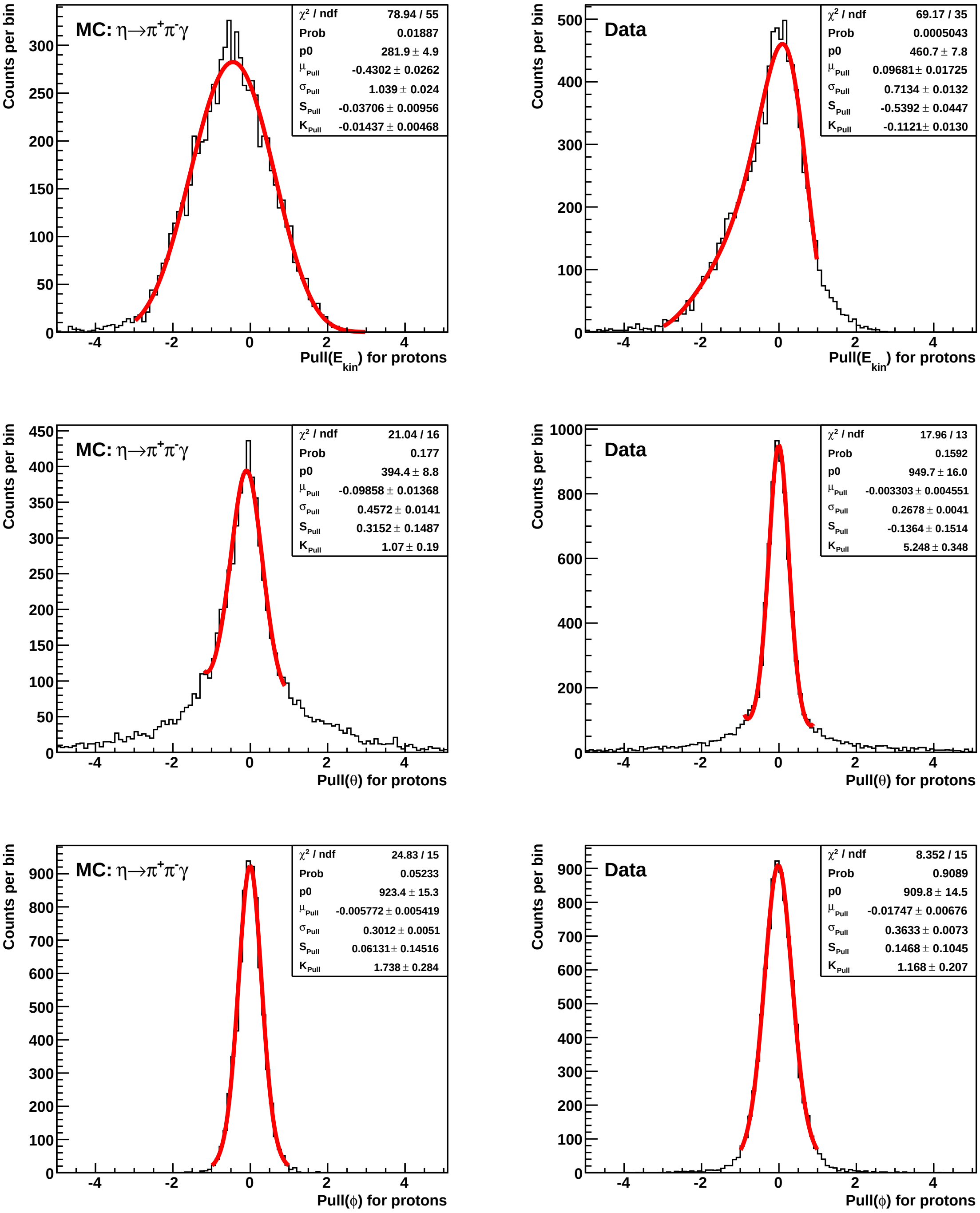

Figure 6.10: *Pull distributions for proton* **kinetic energies (top)**, $\boldsymbol{\theta}$ *angles* **(centre)** *and* $\boldsymbol{\phi}$ *angles* **(bottom)**. *The distributions are obtained for* **simulated** $\boldsymbol{\eta \rightarrow \pi^+\pi^-\gamma}$ *events* **(left column)** *and* **measured data (right column)**. *The red curves in each diagram represent fits of Eq. 6.11 to the distributions.*

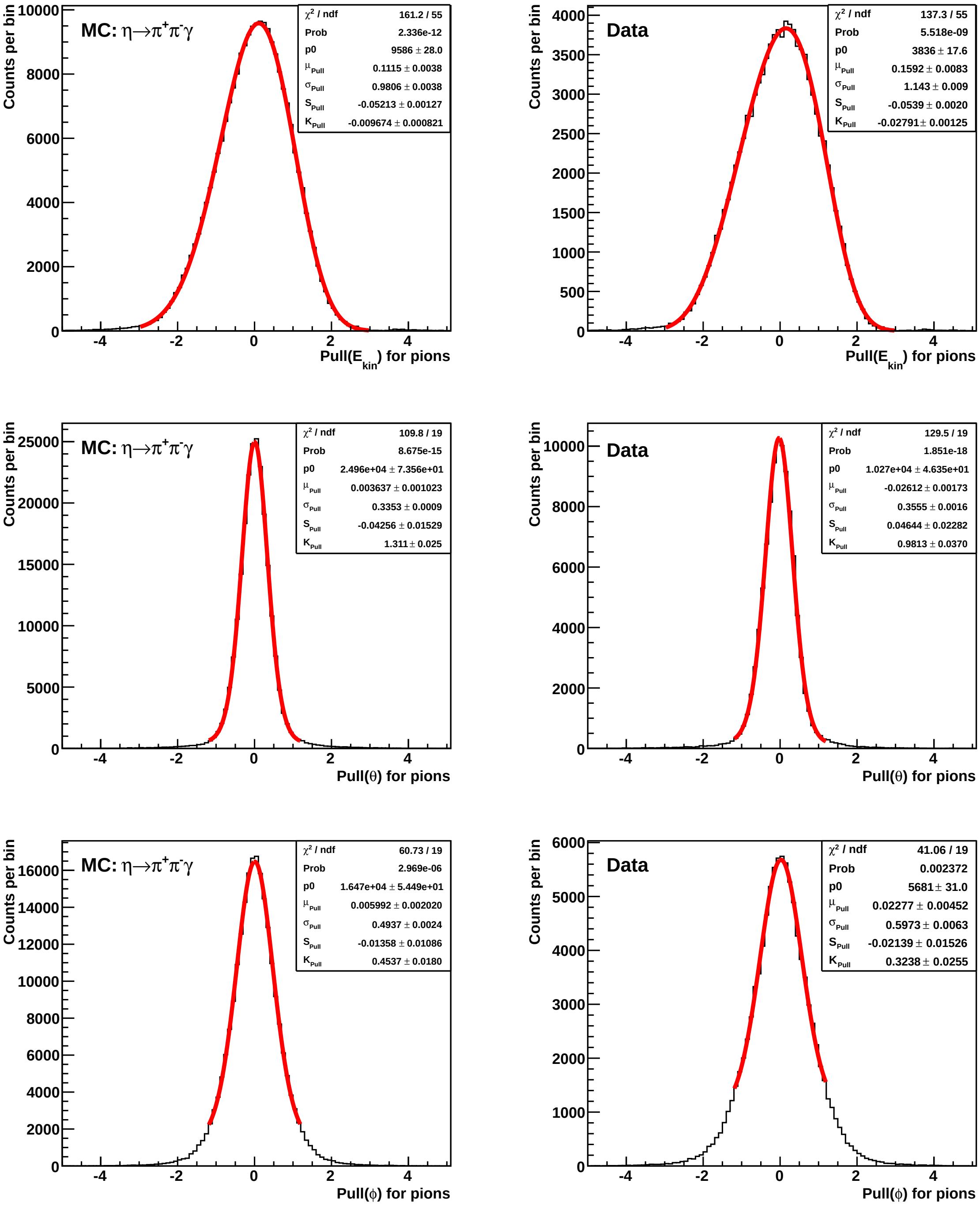

Figure 6.11: *Pull distributions for pion* **kinetic energies (top)**, $\boldsymbol{\theta}$ *angles* **(centre)** *and* $\boldsymbol{\phi}$ *angles* **(bottom)**. *The distributions are obtained for* **simulated** $\boldsymbol{\eta \to \pi^+\pi^-\gamma}$ *events* **(left column)** *and* **measured data (right column)**. *The red curves in each diagram represent fits of Eq. 6.11 to the distributions.*

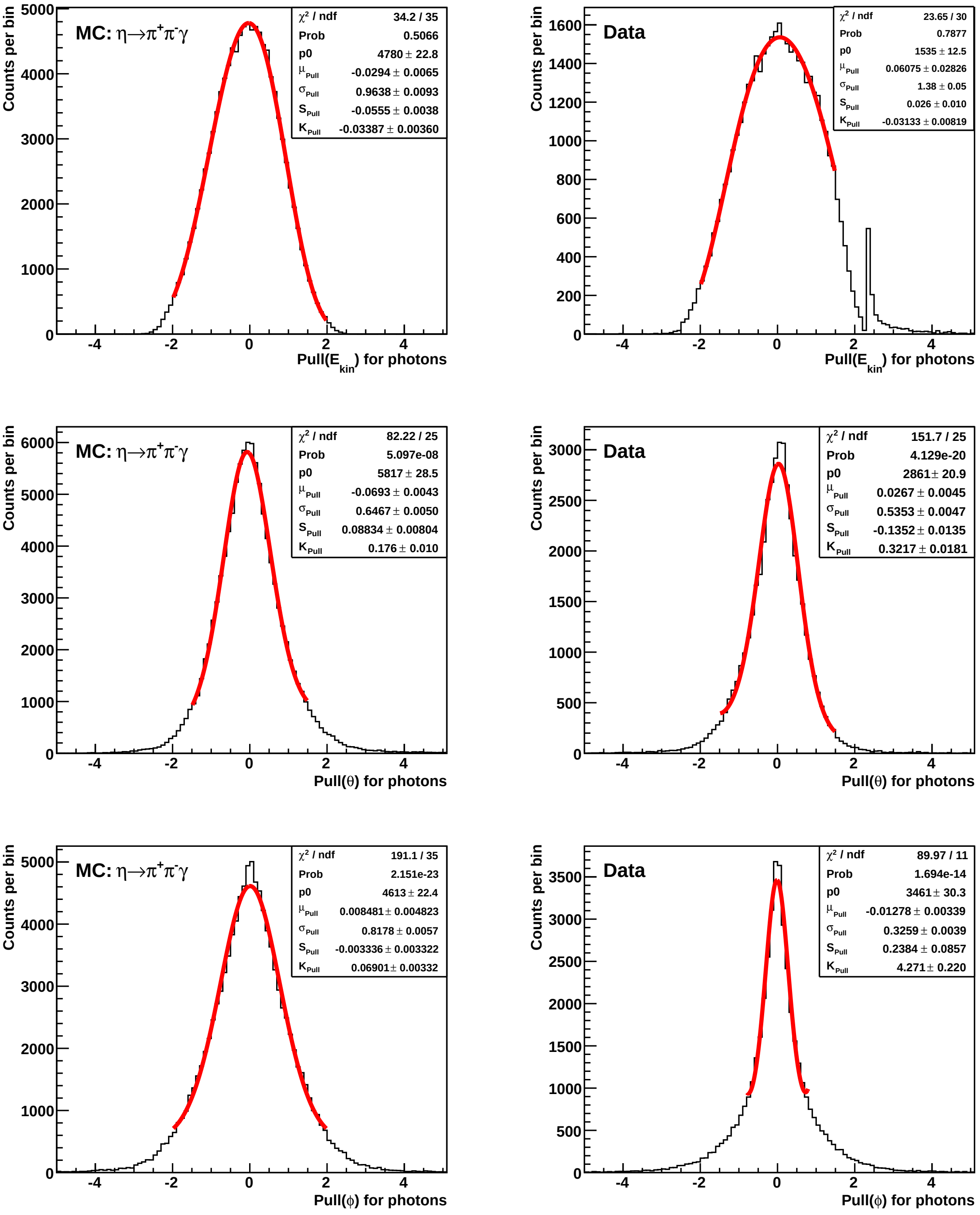

Figure 6.12: *Pull distributions for photon* **kinetic energies (top)**, $\boldsymbol{\theta}$ *angles* **(centre)** *and* $\boldsymbol{\phi}$ *angles* **(bottom)**. *The distributions are obtained for* **simulated** $\boldsymbol{\eta \to \pi^+\pi^-\gamma}$ *events* **(left column)** *and* **measured data (right column)**. *The red curves in each diagram represent fits of Eq. 6.11 to the distributions.*

Figures 6.10 to 6.12 show the pull distributions for all proton, pion and photon kinetic variables. Each of those distributions has been fit by the following function:

$$f_{\text{Pull}}(x) = p0 \cdot \exp\left[-\frac{1}{2\sigma^2_{\text{Pull}}} \cdot x^2 + \frac{\mu_{\text{Pull}}}{\sigma^2_{\text{Pull}}} \cdot x - \frac{1}{2} \cdot \left(\frac{\mu_{\text{Pull}}}{\sigma_{\text{Pull}}}\right)^2 + S_{\text{Pull}} \cdot x^3 + K_{\text{Pull}} \cdot x^4\right] \quad (6.11)$$

which is identical to a Gaussian function with mean μ_{Pull} and variance σ_{Pull}, if the parameters S_{Pull} and K_{Pull} are zero. The fit parameter S_{Pull} is related to the skewness of a distribution (i.e. the asymmetry), whereas the parameter K_{Pull} describes the kurtosis.

Not all pull distributions shown in Figures 6.10 to 6.12 stem from Gaussian distribution, because the corresponding values for S_{Pull} and K_{Pull} are different from zero (e.g. top left diagram in Fig. 6.10). The reasons for that are non-Gaussian error distributions (see Chapter 5) or correlations between the kinematic variables (e.g. between reconstructed proton azimuthal and proton polar angles, see also Chapter 5). A comparison of S_{Pull} and K_{Pull} between simulated and measured data allows to judge the deviation from a true Gaussian distribution within the two data sets.

The fit parameters μ_{Pull}, σ_{Pull}, K_{Pull} and S_{Pull} of the individual fits are summarised in Fig. 6.13. The parameters μ_{Pull} and σ_{Pull} are shown in the top panel. The kurtosis K_{Pull} and skewness S_{Pull} are presented in the bottom panel, respectively. Each particle type is represented by coloured data points. Ideally, all points shown in the top left diagram and bottom row of Fig. 6.13 should be located at $(0, 0)$ (indicated by vertical and horizontal dashed lines). All points at different coordinates have systematic effects within the error parameterisation. Points represented in the top right frame of Fig. 6.13 should be populated at $(1, 1)$ (see horizontal and vertical dashed lines), if the measured errors are estimated correctly.

If the simulated and measured particles are affected identically by the kinematic fit algorithm, all points presented in Fig. 6.13 should follow a diagonal line (see black, dashed diagonals). Any deviation from that line indicates that simulated and measured particle tracks are treated differently by the kinematic fit.

All pull distributions for the kinetic energies have a sigma larger than one (see full circles in the top right diagram of Fig. 6.13). The widths of the angular pull distributions are always distinctly smaller than one (compare rectangles and triangles in the top right diagram). The largest shift corresponding to μ_{Pull} is observed for simulated proton kinetic energies (see full circles in the top left diagram of Fig. 6.13). This might be related to the θ dependent energy smearing for simulated events, as discussed in Chapter 4. The largest deviation between the σ-values obtained for simulated and measured data is found for photon ϕ angles and photon kinetic energies.

The bottom row of Fig. 6.13 shows that the pull distributions for all particle kinetic energies have a nearly vanishing kurtosis whereas all angular pull distributions have a kurtosis larger than zero. A positive kurtosis in Eq. 6.11 leads to a Gaussian distribution with extended tails which represents the shape of the angular pull distributions presented in Fig. 6.10 to 6.12. The largest values for K_{Pull} are obtained for the measured proton θ and photon ϕ angles. This indicates a difference in shape between the corresponding measured and simulated pull distributions.

The skewness S_{Pull} is different from zero for most of the pull distributions. Additionally, the majority of the points displayed in the bottom right diagram of Fig. 6.13 does not follow a diagonal line which again indicates an incompatible shape of the simulated and measured pull distributions. The results presented in Fig. 6.13 show that the largest deviations from the diagonal lines (in all four diagrams) are related to

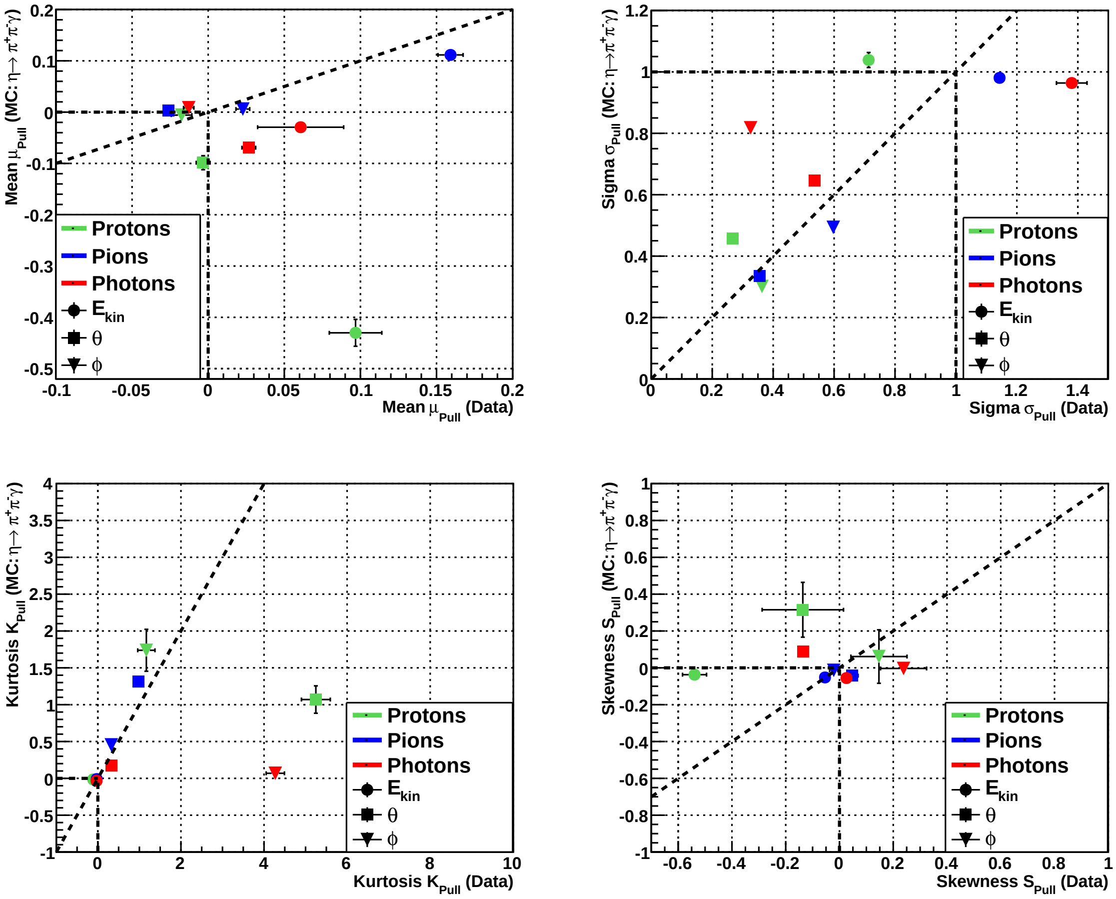

__Figure 6.13:__ Mean value (top left diagram), sigma value (top right diagram), kurtosis (bottom left diagram) and skewness (bottom right diagram) deduced from a fit of Eq. 6.11 to the pull distributions calculated from simulated $\eta \rightarrow \pi^+\pi^-\gamma$ events as function of the corresponding values deduced from measured data. The kinematic variables of protons / pions / photons are represented by green / blue / red points, respectively. The kinetic energy / θ angle / ϕ angle of each particle is represented by a circle / rectangle / triangle, respectively. The fit error of each value is represented by the error bar of the symbol. The black dashed diagonals in each diagram are drawn in order to visualise the deviation between measured and simulated data. The horizontal and vertical dashed lines represent the fit parameters, which are expected in case of Gaussian distributed pull values.

the proton and photon kinematic variables. This leads to the conclusion that the error parameterisation still has to be tuned (even) further and the differences in reconstructing measured and simulated particle tracks (i.e. the deviation from the diagonal line) need to be carefully evaluated. However, those results do not allow to judge how and to what extent those differences effect the systematic behaviour of the kinematic fit on each data set. Therefore, the cut on the kinematic fit probability for selecting $\eta \rightarrow \pi^+\pi^-\gamma$ events will be varied to study the corresponding effect on the observables. This procedure will be discussed in the following section.

6.6.1.2 Correlation between the relative branching ratio and the kinematic fit probability

Systematic effects induced by the kinematic fit are investigated by varying the cut on the fit probabilities: $P(\chi^2_{pp\to pp\pi^+\pi^-\gamma}, 4)$ / $P(\chi^2_{pp\to pp\pi^+\pi^-\gamma\gamma}, 4)$. The parameter A for rejecting split-offs as well as the selection of a π^0 candidate are not changed in this study. The results are displayed in Fig. 6.14. The minimum probability $P(\chi^2_{pp\to pp\pi^+\pi^-\gamma}, 4)$ was increased between 5% and 95% in steps of 0.05. The corresponding branching ratio was calculated according to Eq. 6.3.
In order to demonstrate the impact of a θ independent energy resolution of the various FRH layers on the systematic uncertainties, a test sample containing $\sim$ 25% of the 2010 $pp\eta$ data set has been analysed. For this data sample the energy resolution was set constant for each FRH layer and the corresponding results are presented in the top left frame and second row of Fig. 6.14. The relative branching ratio decreases linearly with increasing minimum probability from 0.23 at maximum and 0.16 at minimum. This corresponds to a total variation of $\sim$ 30%, which already indicates a significant influence of the kinematic fit on the final result.
Ideally, a varying cut on the kinematic fit probability should have no effect on the final result, because the corresponding reconstruction efficiencies (obtained from simulated data) are taken into account by Eq. 6.3. A large probability cut for instance leads to a small number of accepted events, which is compensated by the corresponding efficiency. This only works, if the detector response is described in the same way for the simulated and measured data set. According to the results shown in the left frame of Fig. 6.14, the reconstruction efficiency for $\eta \to \pi^+\pi^-\gamma$ seems to decrease insufficiently in simulations with increasing probability. Therefore, the influence of the probability cut could not be compensated.
The centre left diagram in Fig. 6.14 shows the number of expected $\eta \to \pi^+\pi^-\gamma$ events as a function of the different kinematic fit probability for different reaction hypothesis. The red data points are obtained by selecting events with $P(\chi^2_{pp\to pp\pi^+\pi^-\gamma\gamma}, 4) \geq 0.2$ and varying the cut on $P(\chi^2_{pp\to pp\pi^+\pi^-\gamma}, 4)$ in steps of 0.05. The number of expected events deduced from different cuts on $P(\chi^2_{pp\to pp\pi^+\pi^-\gamma\gamma}, 4)$ and a fixed cut $P(\chi^2_{pp\to pp\pi^+\pi^-\gamma}, 4) \geq 0.2$ are represented by the blue data points, repsectively. The same correlation studies are made for the number of expected $\eta \to \pi^+\pi^-\pi^0$ events, which are presented in the right frame of the second row in Fig. 6.14. According to Eq. 6.2 the number of expected events for a decay channel i are connected to a different channel j via the non-diagonal matrix elements. Hence it is assumed, that the number of expected $\eta \to \pi^+\pi^-\gamma$ / $\eta \to \pi^+\pi^-\pi^0$ events also varies for different cuts on $P(\chi^2_{pp\to pp\pi^+\pi^-\gamma\gamma}, 4)$ / $P(\chi^2_{pp\to pp\pi^+\pi^-\gamma}, 4)$. However, Fig. 6.14 shows that the number of expected $\eta \to \pi^+\pi^-\pi^0$ events is not effected by different cuts on $P(\chi^2_{pp\to pp\pi^+\pi^-\gamma}, 4)$ (see red data points in right frame of the second row). This is because the efficiency for reconstructing an $\eta \to \pi^+\pi^-\gamma$ event as an $\eta \to \pi^+\pi^-\pi^0$ event candidate is negligible (also see Fig. 6.1). Thus, the number of expected $\eta \to \pi^+\pi^-\pi^0$ events only depends on the variation of $P(\chi^2_{pp\to pp\pi^+\pi^-\gamma\gamma}, 4)$. The variation of the number of expected $\eta \to \pi^+\pi^-\gamma$ events varies for different cuts on $P(\chi^2_{pp\to pp\pi^+\pi^-\gamma\gamma}, 4)$ within the statistical errors (represented by the error bars in Fig. 6.14). According to that, effects on the relative branching ratio by varying either $P(\chi^2_{pp\to pp\pi^+\pi^-\gamma\gamma}, 4)$ or $P(\chi^2_{pp\to pp\pi^+\pi^-\gamma}, 4)$ can be investigated separately.
The second row of Fig. 6.14 represents the same effect, which is shown in the top left diagram: The number of expected events for both channels decreases with increasing fit probability, because the efficiency is underestimated. Thus, the relative

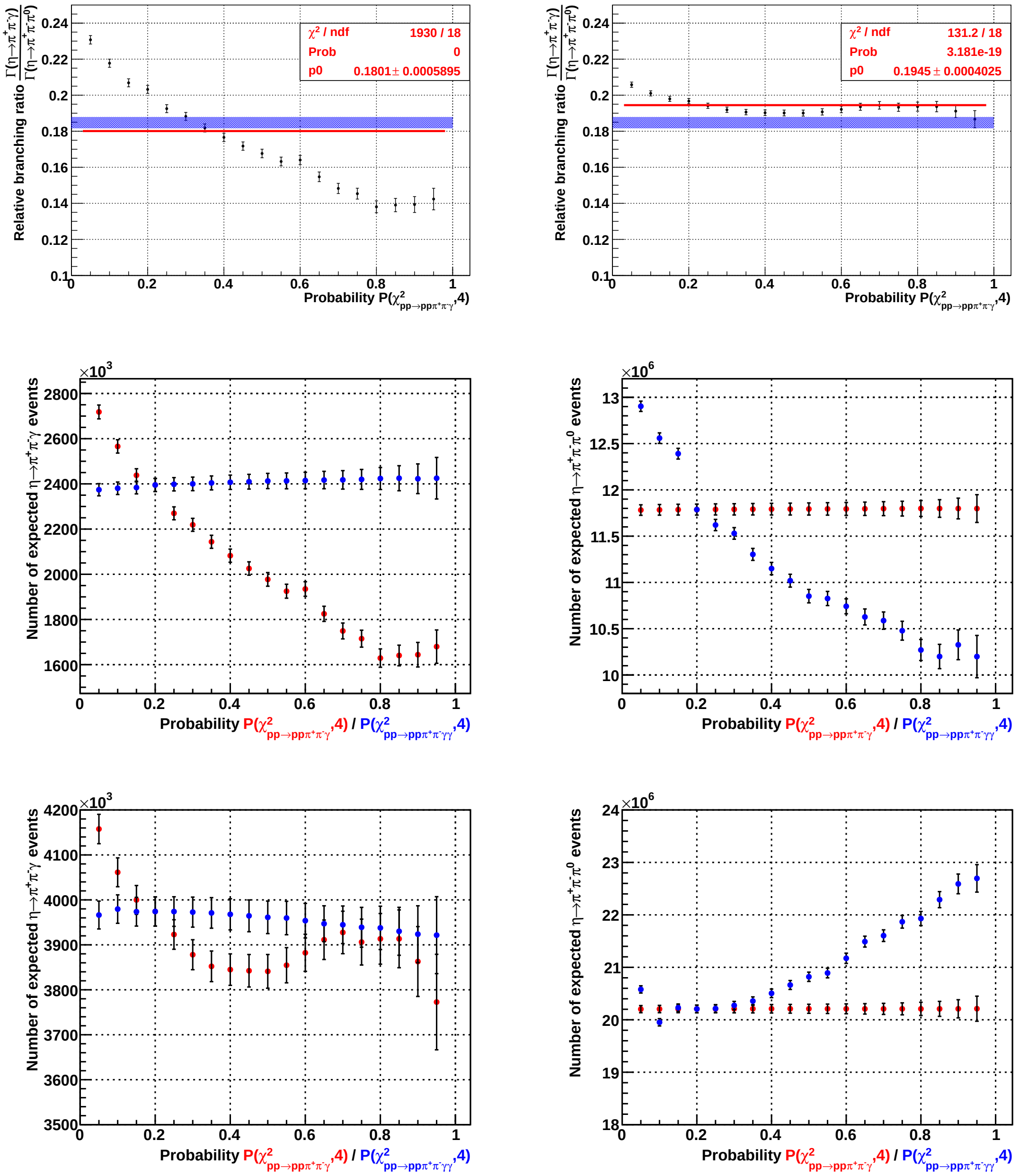

Figure 6.14: **Top:** *Relative branching ratio* $\frac{\Gamma(\eta\to\pi^+\pi^-\gamma)}{\Gamma(\eta\to\pi^+\pi^-\pi^0)}$ *as a function of the minimum kinematic fit probability. The results are obtained without (left frame) and with (right frame)* θ *dependent energy smearing of the FRH scintillators for simulated data. The red lines in each diagram refer to a fit of a constant function. The PDG - value [10] for the relative branching ratio:* 0.1847 ± 0.0003 *is represented by a blue bar.* **Centre:** *Number of expected* $\eta \to \pi^+\pi^-\gamma$ *(left frame) and* $\eta \to \pi^+\pi^-\pi^0$ *(right frame) events as function of the selected fit probabilities* $P(\chi^2_{pp\to pp\pi^+\pi^-\gamma}, 4)$ *(red) and* $P(\chi^2_{pp\to pp\pi^+\pi^-\gamma\gamma}, 4)$ *(blue).* θ *dependent energy resolution for the FRH scintillators was not applied here.* **Bottom:** *Same plots as shown in the centre row, but* θ *dependent FRH energy resolution is included. The error bars in both plots represent the statistical uncertainties.*

branching ratio, which is the ratio of both numbers, shows a similar pattern. The situation changes, if a θ dependent resolution of the FRH modules is applied for simulated protons. The corresponding results are shown in the top right frame and bottom row of Fig. 6.14, after analysing ∼ 42% of the 2010 $pp\eta$ data set. The variation of the individual data points is significantly smaller than presented in

the left frame in Fig. 6.14. The remaining periodical fluctuation is directly connected to the correlation between the number of expected $\eta \rightarrow \pi^+\pi^-\gamma$ events and $P(\chi^2_{pp\rightarrow pp\pi^+\pi^-\gamma}, 4)$ (see red points in bottom left diagram of Fig. 6.14). The number of expected $\eta \rightarrow \pi^+\pi^-\pi^0$ events does not depend on the choice of $P(\chi^2_{pp\rightarrow pp\pi^+\pi^-\gamma}, 4)$ (see red points in bottom right frame of Fig. 6.14) and has therefore no influence on the pattern shown in the top right panel of Fig. 6.14.
In order to have a measure for the correlation between the relative branching ratio and the kinematic fit probability $P(\chi^2_{pp\rightarrow pp\pi^+\pi^-\gamma}, 4)$, a constant function was fit to the data points shown in the top row of Fig. 6.14. The results of the fit are represented by the red lines in each diagram. Any other function would not be adequate, since the results are expected to be independent from choosing a certain fit probability. The reduced χ^2-values are (in both cases) much larger than one and thus indicate, that the pattern is not in agreement with a constant function. Therefore, the errors of the fit parameter (see inset boxes in top row of Fig. 6.14) do not reflect the disagreement between the red lines and the measured distributions. This observation comes about because the least squares fit errors are estimated within the variation of the χ^2-value between χ^2 and $\chi^2 + 1$. For large χ^2-values (i.e. $\chi^2 >> \mathrm{ndf}^{\mathrm{d}}$) this procedure becomes insensitive to the variation of the fit parameters and thus leads to underestimated fit errors (see case 1 in Appendix G). Therefore, the standard deviation σ between the data points y_i in the top diagrams of Fig. 6.14 and the fit parameter $p0$ is calculated:

$$\sigma^2 = \frac{1}{\mathrm{ndf}} \cdot \sum_i (y_i - p0)^2 \tag{6.12}$$

Accordingly, the uncertainty σ_{kFit1} introduced by the kinematic fit with reaction hypothesis $pp \rightarrow pp\pi^+\pi^-\gamma$ and with a constant FRH energy resolution reads as $\sigma_{kFit1} = 0.030$. This value is in agreement with the maximum differences between the data points presented in the top left panel of Fig. 6.14 and the fitted red line. Including a θ dependent energy resolution reduces the uncertainty to $\sigma_{kFit1} = 0.005$. Unfortunately, the number of expected $\eta \rightarrow \pi^+\pi^-\pi^0$ events shows, even after introducing the θ dependent FRH energy resolution, a strong correlation with respect to varying values of $P(\chi^2_{pp\rightarrow pp\pi^+\pi^-\gamma\gamma}, 4)$ (see blue data points in bottom right panel of Fig. 6.14). For probabilities $\leq 30\%$, the variation is nearly zero, but increases linearly for larger probability values. Naively, a similar dependence between the number of expected events and the chosen fit probability would be expected for both decay channels, since the reconstruction of protons and their implementation in the kinematic fit algorithm is identical. The only difference is the number of photons requested by the reaction hypothesis, which might indicate that neutral particles are described differently in the measured and simulated data set. This would be in agreement with the observations made in Fig. 6.13. However, at this stage it is unclear, why the two decay channels are affected differently with respect to different fit probabilities. This is another issue, which has to be checked carefully in the future.
The influence of choosing a different minimum probability $P(\chi^2_{pp\rightarrow pp\pi^+\pi^-\gamma\gamma}, 4)$ on the relative branching ratio is studied by fixing the selection of $P(\chi^2_{pp\rightarrow pp\pi^+\pi^-\gamma}, 4)$ to $P(\chi^2_{pp\rightarrow pp\pi^+\pi^-\gamma}, 4) \geq 0.2$ and varying $P(\chi^2_{pp\rightarrow pp\pi^+\pi^-\gamma\gamma}, 4)$ in steps of 0.05. The results of this study are displayed in Fig. 6.15 excluding (left) and including (right) an angle dependent resolution of the FRH scintillators. The corresponding uncertainties are

---

[d] The acronym ndf denotes the number of degrees of freedom.

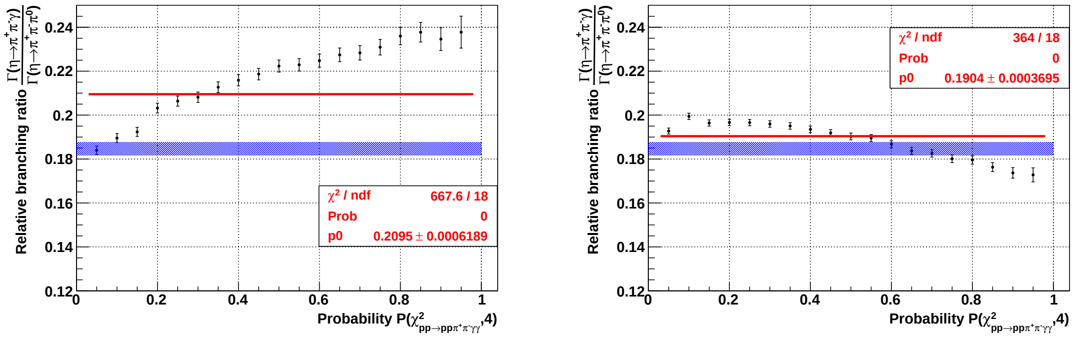

Figure 6.15: *Relative branching ratio* $\frac{\Gamma(\eta\to\pi^+\pi^-\gamma)}{\Gamma(\eta\to\pi^+\pi^-\pi^0)}$ *for* $P(\chi^2_{pp\to pp\pi^+\pi^-\gamma},4) \geq 0.2$ *as a function of different cuts on* $P(\chi^2_{pp\to pp\pi^+\pi^-\gamma\gamma},4)$. **Left:** *Without* θ *dependent FRH resolution correction and* **Right:** *With* θ *dependent FRH resolution correction. The PDG-value for the relative branching ratio is represented by the blue box. The error bars of each point represent the statistical error. The red lines represent a fit of a constant function to the data points.*

calculated according to Eq. 6.12, because of the reasons discussed above. This leads to $\sigma_{kFit2} = 0.019$ for a constant FRH energy resolution and $\sigma_{kFit2} = 0.009$ if the resolution is angle dependent.

Finally, the total uncertainty introduced by the kinematic fit is obtained by: $\sigma_{kFit} = \sqrt{\sigma^2_{kFit1} + \sigma^2_{kFit2}}$. This leads to $\sigma_{kFit} = 0.036$ if the FRH energy smearing is angle independent. If the simulated energy resolution of the FRH is made angle dependent, the total uncertainty is: $\sigma_{kFit} = 0.010$, which is nearly a factor of four improvement, compared to the previous case.

This result, as well as the distribution shown in the top right frame of Fig. 6.14 lead to the conclusion that the effect of a θ dependent energy resolution of each FRH module either has to be implemented in the simulated data set, or significantly reduced within the measured data. Otherwise, the kinematic fit algorithm treats simulated and measured protons differently and the obtained efficiencies are inadequate. In the following, all presented results include the θ dependent FRH energy resolution within the simulated data set.

6.6.1.3 Correlation between the E_γ-distribution and the kinematic fit probability

The effect of choosing different minimum probabilities $P(\chi^2_{pp\to\pi^+\pi^-\gamma},4)$ and $P(\chi^2_{pp\to\pi^+\pi^-\gamma\gamma},4)$ on the photon energy distribution is studied in the same way as discussed above. The results are shown in Fig. 6.16. All diagrams displayed in the top row are obtained for a fixed selection of $P(\chi^2_{pp\to pp\pi^+\pi^-\gamma\gamma},4) \geq 0.2$ and a varying cut on $P(\chi^2_{pp\to pp\pi^+\pi^-\gamma},4)$. Diagrams in the bottom row correspond to a fixed $P(\chi^2_{pp\to pp\pi^+\pi^-\gamma},4) \geq 0.2$ and a varying $P(\chi^2_{pp\to pp\pi^+\pi^-\gamma\gamma},4)$. The left column of Fig. 6.16 shows the photon energy distributions for different probability cuts. The corresponding α parameters and their fit errors (according to Eq. 2.29) are presented in the right column.

The various cuts on the fit probability were performed in steps of 0.1, as the two extreme scenarios $P \geq 0.1$ and $P \geq 0.9$ are represented by red / blue markers in the diagrams shown in the left panel of Fig.6.16. The distributions plotted there have negative entries for energies $E_\gamma < 0.035\,\text{GeV}$ because a clear detection of an

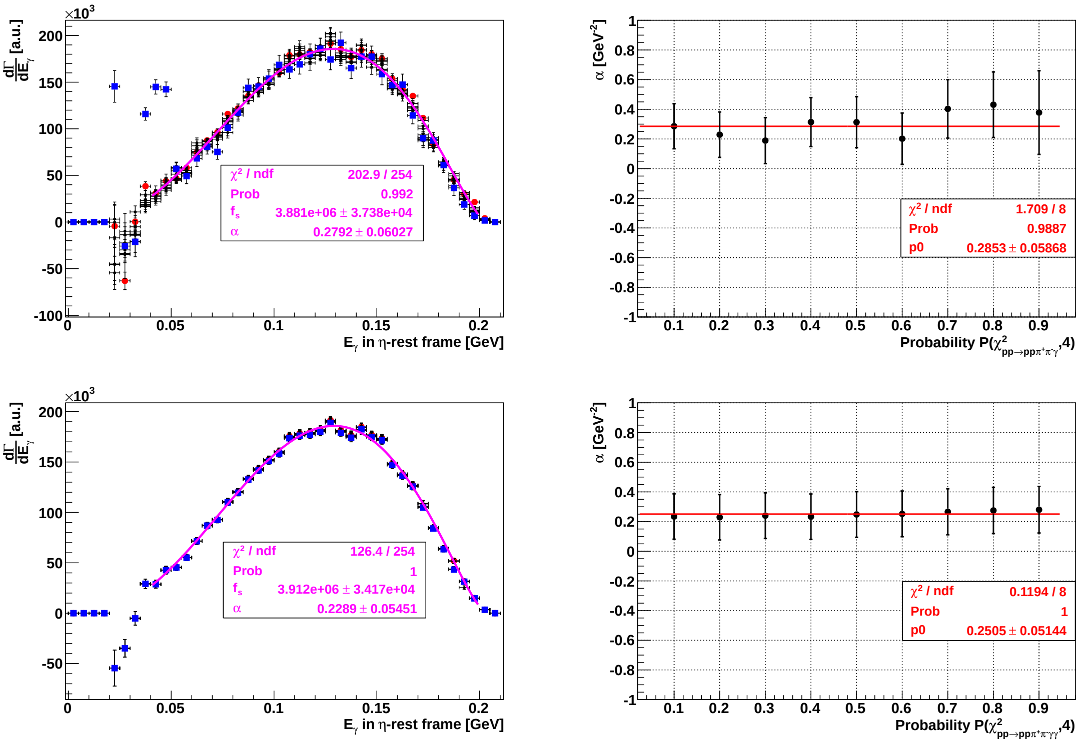

Figure 6.16: **Left:** *E_γ-distribution in the η-rest frame for different cuts on $P(\chi^2_{pp\to pp\pi^+\pi^-\gamma},4)$ and $P(\chi^2_{pp\to pp\pi^+\pi^-\gamma\gamma},4) \geq 20\%$ (top), different cuts on $P(\chi^2_{pp\to pp\pi^+\pi^-\gamma\gamma},4)$ and $P(\chi^2_{pp\to pp\pi^+\pi^-\gamma},4) \geq 20\%$ (bottom). The extreme case $P \geq 0.1$ is indicated by red spherical markers and $P \geq 0.9$ is represented by blue rectangular markers respectively. The bottom left diagram shows no red marker, because they are superposed by the blue data points. Statistical errors are represented by the error bars. The purple solid lines correspond to a simultaneous fit of Eq. 2.29 to all E_γ-distributions, except the one indicated by the blue rectangular markers shown in the top left panel.* **Right:** *Each distribution in the left frame was fit by Eq. 2.29 and the α parameter is plotted as function of the corresponding cut on the fit probability. Here, the error bars correspond to the parameter error, obtained from each individual fit. The red line refers to a constant function, which was fit to the data points. The fit results are shown in the rectangular box.*

eta signal in the corresponding missing mass projection bin is not possible due to large background contributions. Therefore, all distributions shown in the left panel of Fig. 6.16 have been fit by Eq. 2.29 without considering photon energies $E_\gamma < 0.035\,\mathrm{GeV}$[e]. The data points shown in the top left diagram of Fig. 6.16 show a uniform pattern and thus stem from a common distribution. This observation is confirmed by the purple solid line, which represents a simultaneous fit of all E_γ-distribution (except the blue coloured one) with Eq. 2.29.

The blue coloured data points show a clear deviation from this uniform pattern. They correspond to a probability cut $P(\chi^2_{pp\to pp\pi^+\pi^-\gamma},4) \geq 0.9$ and therefore suffer from insufficient statistics in the corresponding missing mass spectra.

The α-values deduced from each of the E_γ-distributions are presented as a function of the kinematic fit probability $P(\chi^2_{pp\to pp\pi^+\pi^-\gamma},4)$ in the right column of Fig. 6.16. The error bar of each point comprises the uncertainty related to the background correction of the individual missing mass spectrum as well as the statistical error of the

---

[e] For $P(\chi^2_{pp\to pp\pi^+\pi^-\gamma},4) \geq 0.9$, the left fit boundary was changed to 0.06 GeV because of negative or an unreasonably large number of entries.

η-peak content. Within those errors, the α-parameters follow a constant pattern with respect to $P(\chi^2_{pp\rightarrow pp\pi^+\pi^-\gamma}, 4)$. This observation is approved by a reduced χ^2 value, obtained from fitting a constant function (see red line in top right diagram) to those points. One striking feature of the top right correlation diagram in Fig. 6.16 is, that the average α-value changes abruptly from $\approx 0.28\,\mathrm{GeV}^{-2}$ to $\approx 0.4\,\mathrm{GeV}^{-2}$ for kinematic fit probabilities larger than 60 %.

One hint for the explanation for that effect is given by the error bars which increase with increasing fit probability. Choosing larger kinematic fit probabilities leads to larger statistical fluctuations within the individual photon energy distribution and thus increases the fit error of α. In order to get a better insight into this problem, the measured photon energy distribution related to $P(\chi^2_{pp\rightarrow pp\pi^+\pi^-\gamma}, 4) \geq 0.8$ has been fit by Eq. 2.29 with two different α-parameters. The results of that study are shown in Fig. 6.17. The solid red curve is obtained by fitting Eg. 2.29 to the data points without any constraints on α. The black dashed curve is deduced from a fit with a fixed α-value of $0.229\,\mathrm{GeV}^{-2}$, which was determined in Section 6.2 for kinematic fit probabilities $P(\chi^2_{pp\rightarrow pp\pi^+\pi^-\gamma}, 4) \geq 0.2$. Both fit curves overlap and refer to similar reduced χ^2 values. Thus, neither of the two presented α-parameters is preferable. This leads to the conclusion that the enhancement shown in the top right diagram of Fig. 6.16 at probabilities $> 60\%$ is rather connected to the statistical fluctuations within the corresponding E_γ-distribution than to a systematic effect caused by the kinematic fit. Therefore, using Eq. 6.12 to estimate the kinematic fit related uncertainty σ_{kFit1} would be inappropriate in this case, because the individual error of the individual α-parameter has to be taken into account.

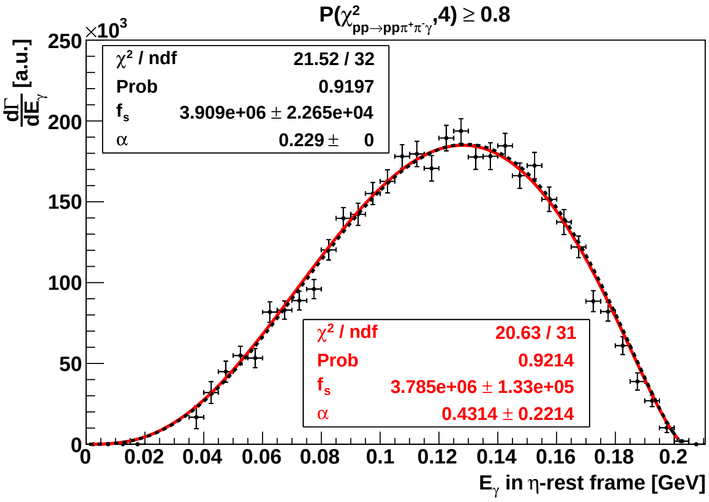

Figure 6.17: *Photon energy distribution obtained for choosing events with* $P(\chi^2_{pp\rightarrow pp\pi^+\pi^-\gamma}, 4) \geq 0.8$. *The solid red and black dashed curves correspond to a fit of Eq. 2.29 to the data points for* α *being a free parameter (red curve) and being fixed to* $0.229\,\mathrm{GeV}^{-2}$ *(black dashed curve).*

Thus, the uncertainty related to varying the kinematic fit probability is given by the parameter error $\pm 0.059\,\mathrm{GeV}^{-2}$ of $p0$ displayed in the top right diagram of Fig. 6.16. Another issue, related to the scenario shown in Fig. 6.17 is the sensitivity of the shape of the photon energy distribution to different α values. The black dashed and red solid curve are hard to distinguish by eye, even though the corresponding α values are different. According to that, the shape of the photon energy distribution predicted by Eq. 2.29 has a certain insensitivity to different α parameters.

The bottom row of Fig. 6.16 shows the correlation between the photon energy distribution and the probability $P(\chi^2_{pp\to pp\pi^+\pi^-\gamma\gamma}, 4)$. Varying the probability has an influence on the number of expected $\eta \to \pi^+\pi^-\pi^0$ events (see previous section), which is used to correct the photon energy distribution for background contributions from those events. As shown in the previous section, the number of expected $\eta \to \pi^+\pi^-\pi^0$ events increases with increasing fit probability $P(\chi^2_{pp\to pp\pi^+\pi^-\gamma\gamma}, 4)$. Thus, a correlation between the photon energy distribution and $P(\chi^2_{pp\to pp\pi^+\pi^-\gamma\gamma}, 4)$ is expected.

However, the bottom row of Fig. 6.16 shows a negligible correlation: All photon energy distributions related to different values for $P(\chi^2_{pp\to pp\pi^+\pi^-\gamma\gamma}, 4)$ have the same shape and thus, only the distribution related to the blue data points is visible. Hence, the α-parameter is insensitive to the correction of $\eta \to \pi^+\pi^-\pi^0$ events. This statement is supported by the considerably small χ^2-value. Additionally, the error bars show no significant variation with respect to $P(\chi^2_{pp\to pp\pi^+\pi^-\gamma\gamma}, 4)$ and are $\sim 0.153\,\mathrm{GeV}^{-2}$.

These observations correspond to case 2 discussed in Appendix G and thus the parameter error of $p0$ (see box in bottom right diagram of Fig. 6.16) can not be taken to estimate the uncertainty related to varying $P(\chi^2_{pp\to pp\pi^+\pi^-\gamma\gamma}, 4)$. Thus, Eq. 6.12 is used instead in order to decouple the (constant) α fit errors from fluctuations caused by different cuts on $P(\chi^2_{pp\to pp\pi^+\pi^-\gamma\gamma}, 4)$. This leads to $\sigma_{kFit2} = 0.019\,\mathrm{GeV}^{-2}$ and the total systematic error for α related to the kinematic fit is given by $\sigma_{kFit} = \sqrt{0.059^2 + 0.019^2}\,\mathrm{GeV}^{-2} = 0.062\,\mathrm{GeV}^{-2}$.

All photon energy distributions shown in the left panel have been fit simultaneously by Eq. 2.29 (see purple curves in top and bottom diagram) in order to have a cross check for the error estimation method displayed in the right column of Fig. 6.16. The results of both multiple fits are in good agreement with the parameters extracted from fitting a constant function to the different α parameters. This indicates that both approaches are valid for estimating the systematic uncertainty. The benefit of the method presented in the right column is that the dependence between the individual α parameter and the kinematic fit probability can be investigated separately. Additionally, possible correlations between the α fit error and analysis cuts can be studied. However, to judge the final result or uncertainty each α value should always be investigated in combination with the associated E_γ distribution.

6.6.1.4 Correlation between the (π^+, γ) opening angle and the kinematic fit probability

The systematic uncertainties for the opening angle between a charged pion and the single photon are studied as discussed in the previous section. Fig. 6.18 summarises the angular distributions and their corresponding β-values (determined according to Eq. 2.34) as a function of different kinematic fit cuts. All distributions presented in the left column show an enhancement for angles $0.45 \leq \cos\angle(\pi^+, \gamma) \leq 0.55$, which was already observed in Fig. 6.6. Therefore, this region is not included when determining the β-value.

The results are similar to those obtained in the previous section: The angular distributions related to different probabilities $P(\chi^2_{pp\to pp\pi^+\pi^-\gamma}, 4)$ follow a uniform slope (see purple solid curve in top left frame of Fig. 6.18). The effect of different $P(\chi^2_{pp\to pp\pi^+\pi^-\gamma\gamma}, 4)$ values is not visible in the bottom left diagram because all distributions overlap. The corresponding β-parameters follow a constant pattern with respect to different selections of $P(\chi^2_{pp\to pp\pi^+\pi^-\gamma}, 4)$ or $P(\chi^2_{pp\to pp\pi^+\pi^-\gamma\gamma}, 4)$. The un-

certainty of β related to selecting different probabilities $P(\chi^2_{pp\to pp\pi^+\pi^-\gamma}, 4)$ is given by the error 0.021 of $p0$, displayed in the top right panel of Fig. 6.18. The error of each data point depends on the chosen probability, because of the correlated statistical fluctuations. Hence, the individual errors have to be taken into account for the final error determination. Additionally, the reduced χ^2-value of ~ 0.16 indicates a reasonable error estimation by the fit.
The individual errors of β with respect to different probabilities $P(\chi^2_{pp\to pp\pi^+\pi^-\gamma\gamma}, 4)$ (see bottom line of Fig. 6.18) are constant ~ 0.054. Taking Eq. G.7 into account leads to 0.018, which is identical to the error shown in the box in the bottom right diagram of Fig. 6.18. The uncertainty estimated via fitting a constant function is not adequate because only the fit error of Eq. 2.34 is incorporated within this value. Thus, the error on β related to $P(\chi^2_{pp\to pp\pi^+\pi^-\gamma\gamma}, 4)$ is estimated via Eq. 6.12 to be $\sigma_{kFit2} = 0.012$ and the total uncertainty is given by $\sigma_{kFit} = 0.024$.
The solid purple curves presented in the left column correspond again to a multiple fit of Eq. 2.34 to all opening angle distributions. The fit results are in agreement with the values deduced from fitting a constant to the individual β-values (see red inserts in the right panel of Fig. 6.18).

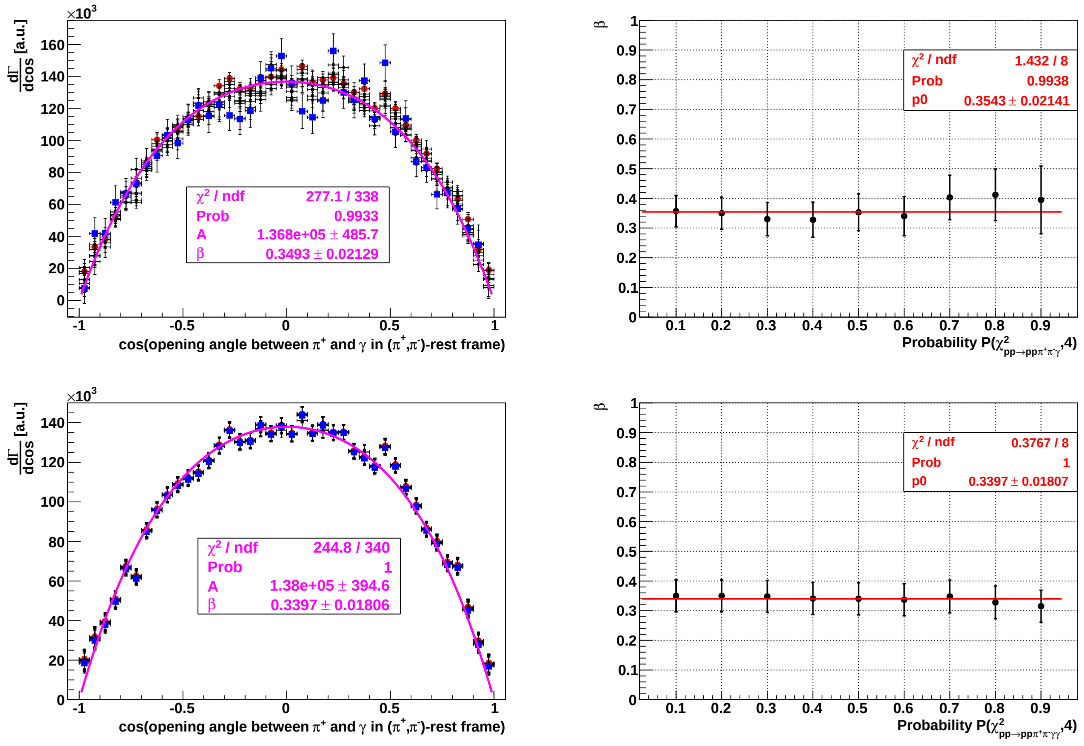

Figure 6.18: **Left:** *Opening angle distribution between the positive pion and the single photon in the (π^+, π^-)-rest frame for: different cuts on $P(\chi^2_{pp\to pp\pi^+\pi^-\gamma}, 4)$ and $P(\chi^2_{pp\to pp\pi^+\pi^-\gamma\gamma} \geq 20\%$ (top), different cuts on $P(\chi^2_{pp\to pp\pi^+\pi^-\gamma\gamma}, 4)$ and $P(\chi^2_{pp\to pp\pi^+\pi^-\gamma} \geq 20\%$ (bottom). The extreme case $P \geq 0.1$ is indicated by red spherical markers and $P \geq 0.9$ is represented by blue rectangular markers. Statistical errors are represented by the error bars. All distributions have been fit at once by Eq. 2.34, which is represented by the purple solid line.* **Right:** *Each distribution in the left frame was fit by Eq. 2.34 and the β parameter is plotted as function of the corresponding cut on the fit probability. Here, the error bars correspond to the parameter error from each individual fit. The red line refers to a constant function, which was fit to the data points.*

6.6.2 Uncertainties related to the split-off rejection

As mentioned in Chapter 5, the parameter A can not be increased to any value, because at some point the efficiency correction fails and the shape of the photon energy distribution will change. Fig. 6.19 shows the reconstruction efficiency of $\eta \to \pi^+\pi^-\gamma$ as a function of the photon energy (top row) and the pion-photon opening angle (bottom row). The green, blue and red points correspond to $P(\chi^2_{pp\to pp\pi^+\pi^-\gamma}, 4) \geq 0.2$, $P(\chi^2_{pp\to pp\pi^+\pi^-\gamma}, 4) \geq 0.5$ and $P(\chi^2_{pp\to pp\pi^+\pi^-\gamma}, 4) \geq 0.9$, respectively. The left column of Fig. 6.19 is obtained for accepting photons with $E_\gamma > \frac{2\,\text{deg}\times\text{GeV}}{\angle(\pi^\pm,\gamma)}$. The right column corresponds to reconstructed events with $E_\gamma > \frac{4\,\text{deg}\times\text{GeV}}{\angle(\pi^\pm,\gamma)}$. The opening angle efficiency presented in the bottom row shows no values ≤ 0, thus there are no efficiency gaps for the analysis parameters presented here.

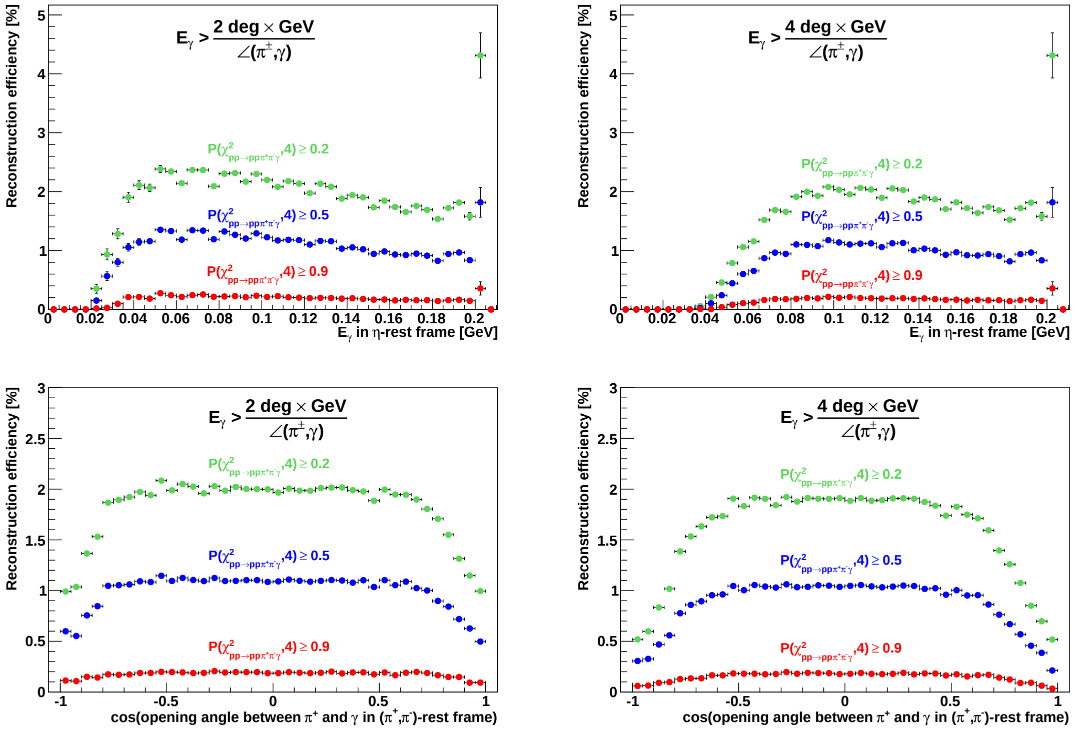

Figure 6.19: *Reconstruction efficiency of $\eta \to \pi^+\pi^-\gamma$ obtained from Monte Carlo simulations as function of the photon energy E_γ in the η-rest frame (top row) and the opening angle between the positive pion and photon in the dipion rest frame (bottom row). The coloured markers represent different cuts on the minimum probability $P(\chi^2_{pp\to pp\pi^+\pi^-\gamma}, 4)$. The diagrams shown in the left column correspond to the split-off rejection condition $E_\gamma > \frac{2\,\text{deg}\times\text{GeV}}{\angle(\pi^\pm,\gamma)}$ and the right column is obtained for $E_\gamma > \frac{4\,\text{deg}\times\text{GeV}}{\angle(\pi^\pm,\gamma)}$.*

By definition of the split-off rejection condition, the reconstruction efficiency as a function of the photon energy is directly correlated to the split-off rejection parameter A. Comparing the two diagrams displayed in the top row of Fig. 6.19 shows that no regions with zero efficiency occur for $A = 2\,\text{deg} \times \text{GeV}$ and different kinematic fit probabilities. The large efficiencies visible at $E_\gamma \sim 0.2\,\text{GeV}$ are because this is the kinematical limit. Bins with zero efficiency occur at $E_\gamma < 0.02\text{GeV}$ because deposited hits with energy smaller than 20 MeV inside the calorimeter are rejected (see Chapter 3).

Choosing photons via $A = 4\,\text{deg} \times \text{GeV}$ leads to regions with zero efficiency for $E_\gamma \leq 0.0375\,\text{GeV}$. This energy range can not be recovered in the final spectrum.

Larger values of A (not shown here) lead to bins with zero efficiency at even larger photon energies and thus influence the shape of the final distribution. However, since photon energies $< 0.035\,\text{GeV}$ are rejected from fitting Eq. 2.29 to the photon energy distribution (see Section 6.2), the value $A = 4\,\text{deg} \times \text{GeV}$ was considered to be the maximum limit of the split-off rejection parameter. If A is chosen to be too small the multiple-pion background is not rejected sufficiently. This situation is presented in Fig. 6.20. The diagrams displayed in the left column present the two proton missing mass as a function of E_γ (top frame) or the pion-photon opening angle (bottom frame). The split-off rejection parameter was set to $A = 1\,\text{deg} \times \text{GeV}$, without changing the conditions on the kinematic fit probability.

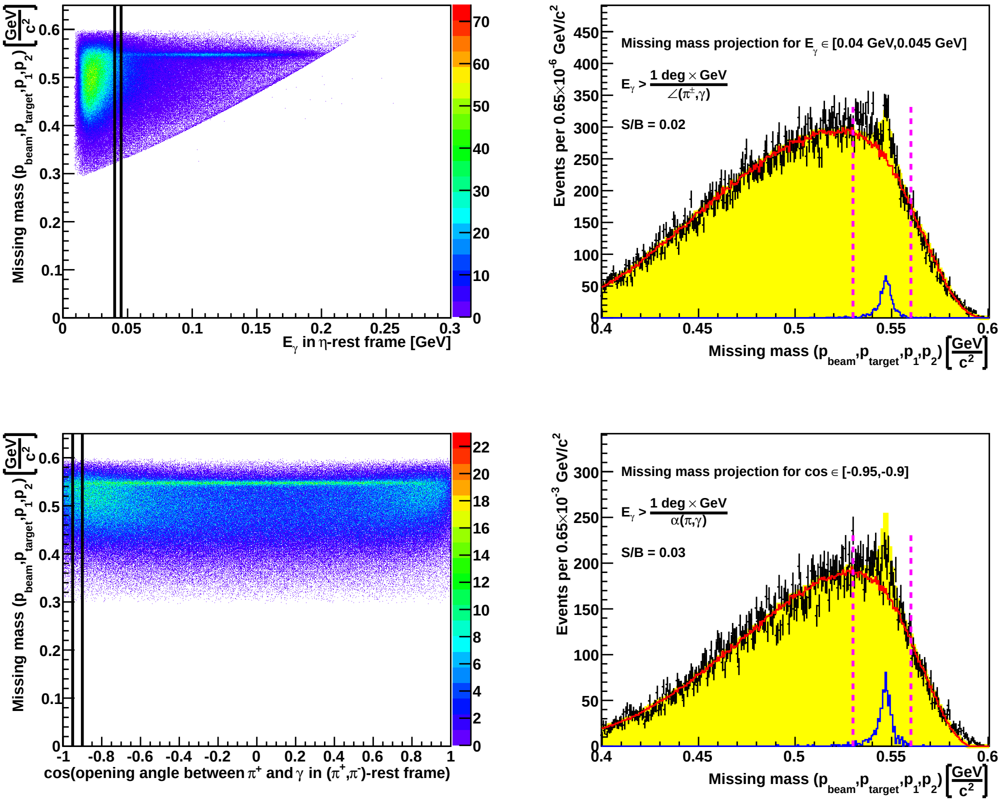

Figure 6.20: **Left:** *Two proton missing mass distribution as a function of the single photon energy (top) or the pion-photon opening angle (bottom). Both diagrams are obtained for* $P(\chi^2_{pp\to pp\pi^+\pi^-\gamma}, 4) \geq 0.2$, $P(\chi^2_{pp\to pp\pi^+\pi^-\gamma\gamma}, 4) \geq 0.2$ *and* $A = 1\,\text{deg} \times \text{GeV}$. *The black lines in each diagram represent a projection window for the two proton missing mass distribution.* **Right:** *Proton-proton missing mass distribution (top / bottom) deduced from the projection shown in the (top / bottom) left frame. Each distribution is described by MC simulations (yellow shaded area), using:* $\eta \to \pi^+\pi^-\gamma$ *(blue curve) for the signal region and* $pp \to pp\pi^+\pi^- + pp \to pp\pi^+\pi^-\pi^0$ *folded with a 4th order polynomial (red curve) for the background. The purple dashed lines are drawn to visualise the signal region. The acronym S/B denotes the signal to background ratio.*

The top left diagram in Fig. 6.20 shows a strong population of background events at energies $E_\gamma \leq 0.05\,\text{GeV}$, compared to Fig. 6.3. This leads to difficulties in subtracting the background and determining of the eta peak content (see top right diagram in Fig. 6.20 and compare to the corresponding spectrum shown in Appendix E), which effects the final E_γ-distribution. The same conclusions might be drawn for the diagrams presented in the bottom row of Fig. 6.20. Comparing those to Fig. 6.5

shows, that using $A = 1\,\text{deg} \times \text{GeV}$ for split-off rejection is not efficient enough to reject background contributions at $\cos[\angle(\pi^+,\gamma)] < -0.8$ and $\cos[\angle(\pi^+,\gamma)] > 0.8$. Those observations will be important for the following discussions.

The influence of different split-off rejection conditions $E_\gamma > \frac{A}{\angle(\pi^\pm,\gamma)}$ on the final results is investigated, by varying the parameter A. For that purpose, both minimum fit probabilities are fixed to $P(\chi^2_{pp\to pp\pi^+\pi^-\gamma}, 4) \geq 0.2$ and $P(\chi^2_{pp\to pp\pi^+\pi^-\gamma\gamma}, 4) \geq 0.2$.

6.6.2.1 Correlation between the relative branching ratio and A

The influence of different A-values on the relative branching ratio is investigated in the same manner as done in the previous section. In order to visualise the effect of choosing different values for A, the split-off rejection parameter A is increased from $1\,\text{deg} \times \text{GeV}$ to $6\,\text{deg} \times \text{GeV}$. For each value, the relative branching ratio has been calculated. The corresponding result is displayed in Fig. 6.21. The relative branching ratio decreases with increasing A-parameter, indicating a strong correlation. Ratios with $A > 4\,\text{deg} \times \text{GeV}$ were not considered for the constant line fit because of the reasons explained above.

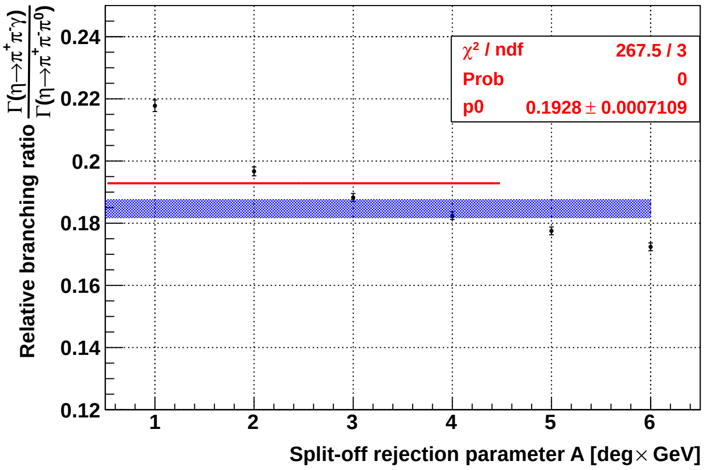

Figure 6.21: **Left:** *Relative branching ratio as a function of the split-off rejection parameter. The statistical uncertainties of each point are represented by the error bars. The red line represents a fit with a constant to the various points, excluding* $A > 4\,\text{deg} \times \text{GeV}$.

The resulting uncertainty is estimated according to Eq. 6.12, due to the large reduced χ^2 value. The corresponding error is $\sigma_A = 0.016$. This value does not change significantly, if the ratio with $A = 4\,\text{deg} \times \text{GeV}$ is also omitted, because of the large branching ratio value at $A = 1\,\text{deg} \times \text{GeV}$.

A more detailed insight into this problem is given by the investigation of the differential distributions, which are discussed in the following two sections.

6.6.2.2 Correlation between the E_γ-distribution and A

The dependence between the single photon energy distribution and the split-off rejection parameter A is presented in the left panel of Fig. 6.22. The red and blue data points highlight the extreme cases $A = 1\,\text{deg} \times \text{GeV}$ and A= $6\,\text{deg} \times \text{GeV}$, whereas the green points refer to $A = 4\,\text{deg} \times \text{GeV}$. Only photon energies $\lesssim 0.1\,\text{GeV}$ are affected by a variation of A, which is in agreement to the observation made during

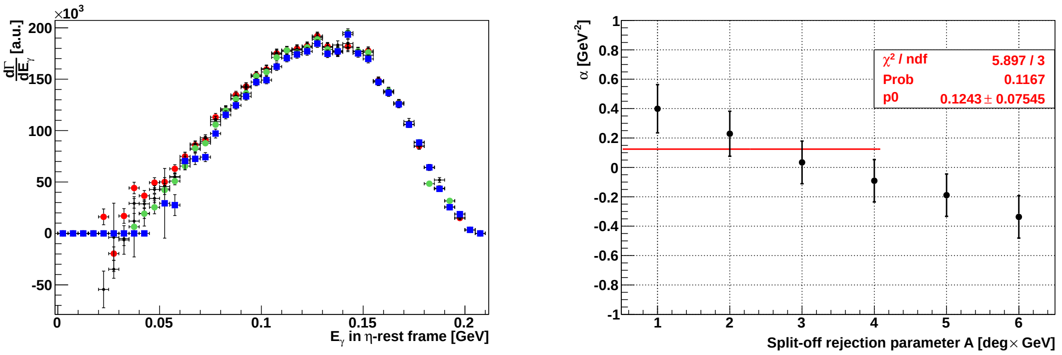

Figure 6.22: **Left:** *E_γ-distributions for different values of the parameter A. The red, green and blue points represent the values: $A = 1\,\mathrm{deg} \times \mathrm{GeV}$, $A = 4\,\mathrm{deg} \times \mathrm{GeV}$ and $A = 6\,\mathrm{deg} \times \mathrm{GeV}$.* **Right:** *$\alpha$-values and errors obtained from fitting Eq. 2.29 to the distributions shown in the left frame. A constant fit is performed to those values with $A \leq 4\,\mathrm{deg} \times \mathrm{GeV}$.*

the study of efficiency gaps. Low statistics at photon energies $< 0.035\,\mathrm{GeV}$ cause negative y-values or strong fluctuations for $A \geq 5\,\mathrm{deg} \times \mathrm{GeV}$. This effect is visible by comparing the red, blue and green data points in the left frame of Fig. 6.22. The left tail of the energy distribution seems to be shifted to higher energies when A is increased and thus effects the final α-value shown in the right diagram in Fig. 6.22. The different values do not follow a constant pattern with respect to a changing A. This leads to a reduced χ^2 value of ~ 2, obtained by fitting a constant function (see red line in right diagram of Fig. 6.22). The uncertainty predicted by the error of $p0$ is $0.076\,\mathrm{GeV}^{-2}$, which is in the order of the error of $\sigma_{kFit} = 0.062\,\mathrm{GeV}^{-2}$. This is unreasonable because the fluctuations of α with respect to different kinematic fit probabilities (see right hand side of Fig. 6.16) are much smaller than presented in the right panel of Fig. 6.22. Thus, the uncertainty is estimated by Eq. 6.12 and reads as $\sigma_A = 0.217\,\mathrm{GeV}^{-2}$.

The distribution presented by the red markers (see left panel of Fig. 6.22) corresponds to $A = 1\,\mathrm{deg} \times \mathrm{GeV}$. The fluctuations visible at photon energies $< 0.05\,\mathrm{GeV}$ are caused by background contributions from $pp \rightarrow pp\pi^+\pi^-$, which have been shown in Fig. 6.20. For the reasons discussed above, photon energies $< 0.05\,\mathrm{GeV}$ were not taken into account for fitting Eq. 2.29 to the red marker points.

6.6.2.3 Correlation between the (π^+, γ) opening angle and A

Finally, the opening angle distribution between π^+ and γ in the dipion rest frame is investigated for A-values between $1\,\mathrm{deg} \times \mathrm{GeV}$ and $6\,\mathrm{deg} \times \mathrm{GeV}$. The results are presented in Fig. 6.23.

Angles with $0.45 \leq \cos[\angle(\pi^+, \gamma)] \leq 0.55$ are not considered for determining the β-parameter. All data points shown in the left frame of Fig. 6.23 follow a uniform pattern, except the red labeled data points. Those values correspond to events with $E_\gamma > \frac{1\,\mathrm{deg} \times \mathrm{GeV}}{\angle(\pi^\pm, \gamma)}$. The reason for the enhancements visible at $\cos[\angle(\pi^+, \gamma)] < -0.5$ and $\cos[\angle(\pi^+, \gamma)] > 0.5$ are the strong population of $pp \rightarrow pp\pi^+\pi^-$ events which can not be completely corrected by the background subtraction routine. The whole distribution does not allow for a reasonable fit by Eq. 2.34, because the additional β-parameter compensates the large fluctuations rather than describing a physics related effect. Thus, the corresponding angular distribution has only been fit in the

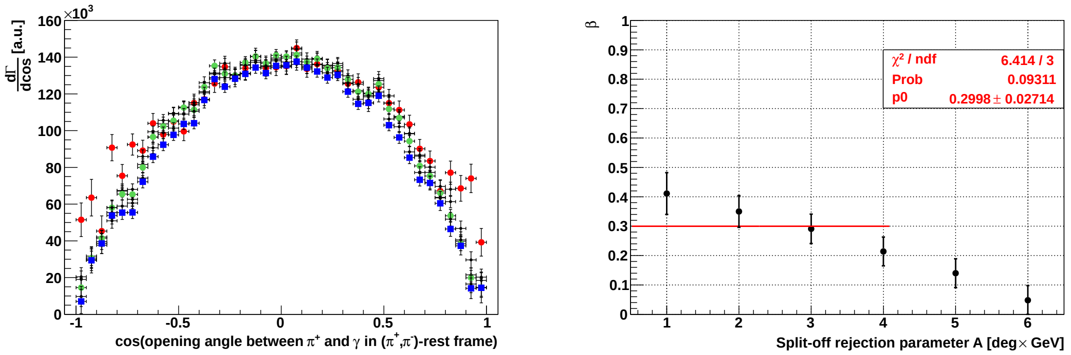

Figure 6.23: **Left:** *Distribution of the cosine of the pion-photon opening angle for different split-off rejection conditions. The scenarios* $A = 1\,\mathrm{deg} \times \mathrm{GeV}$ *and* $A = 6\,\mathrm{deg} \times \mathrm{GeV}$ *are highlighted by red and blue markers.* **Right:** *Obtained* β*-values and errors, from fitting the distributions in the left frame using Eq. 2.34. Split-off rejection parameters with* $A > 4\,\mathrm{deg} \times \mathrm{GeV}$ *were not taken into account for fitting a constant function (red line) to the various* β*-values.*

range $[-0.8, 0.8]$ (According to the observations made in Fig. 6.20.). The resulting uncertainty is given by Eq. 6.12 to be $\sigma_A = 0.086$.

6.6.3 Luminosity effects

As discussed in Section 3.2, the interaction rate between the beam and target protons is correlated to the adjusted pellet rate and beam intensity. This effects the reconstruction efficiency within the calorimeter [18].
It was pointed out in Chapter 3 that pulses stemming from the calorimeter crystals are about several μs long. Thus, the capability of the calorimeter to distinguish between two signals that hit the detector within a certain time window, is limited. This effects both, the track reconstruction and the reconstruction inefficiencies on the other hand, due to pileup effects and detector dead time.
To first order, this effect scales with the number of photons [18]. Accordingly channels with different number of photons might have a different reconstruction efficiency, depending on the instantaneous luminosity.

6.6.3.1 Correlation between relative branching ratio and different luminosities

The top left panel of Fig. 6.24 shows the distribution of the pellet rate (black distribution), obtained for the 2010 $pp\eta$ data. The luminosities achieved during the experiment are monitored via elastic pp scattering events, which are counted by "trigger 17" (see blue distribution in left diagram of Fig. 6.24). The ratio of those rates $\frac{\text{Trigger 17 rate}}{\text{Pellet rate}}$ is proportional to the instantaneous luminosity[f]. The most probable value for the pellet rate is achieved at $\sim 7.5\,\mathrm{kHz}$ and $\sim 330\,\mathrm{kHz}$ for trigger 17. This corresponds to a luminosity of $\approx 3 \cdot 10^{31}\,\mathrm{cm}^{-2}\mathrm{s}^{-1}$. The top right frame of Fig. 6.24 shows the missing mass distribution after reconstructing $\eta \to \pi^+\pi^-\gamma$ events as function of the ratio between the pellet and trigger 17 rate. The maximum rate is found for a ratio of 40. For each luminosity interval i on the x-axis with

$$10 \cdot i \leq \frac{\text{Trigger 17 rate}}{\text{Pellet rate}} \leq 10 \cdot (i+1) \tag{6.13}$$

---

[f] For a detailed description see [18].

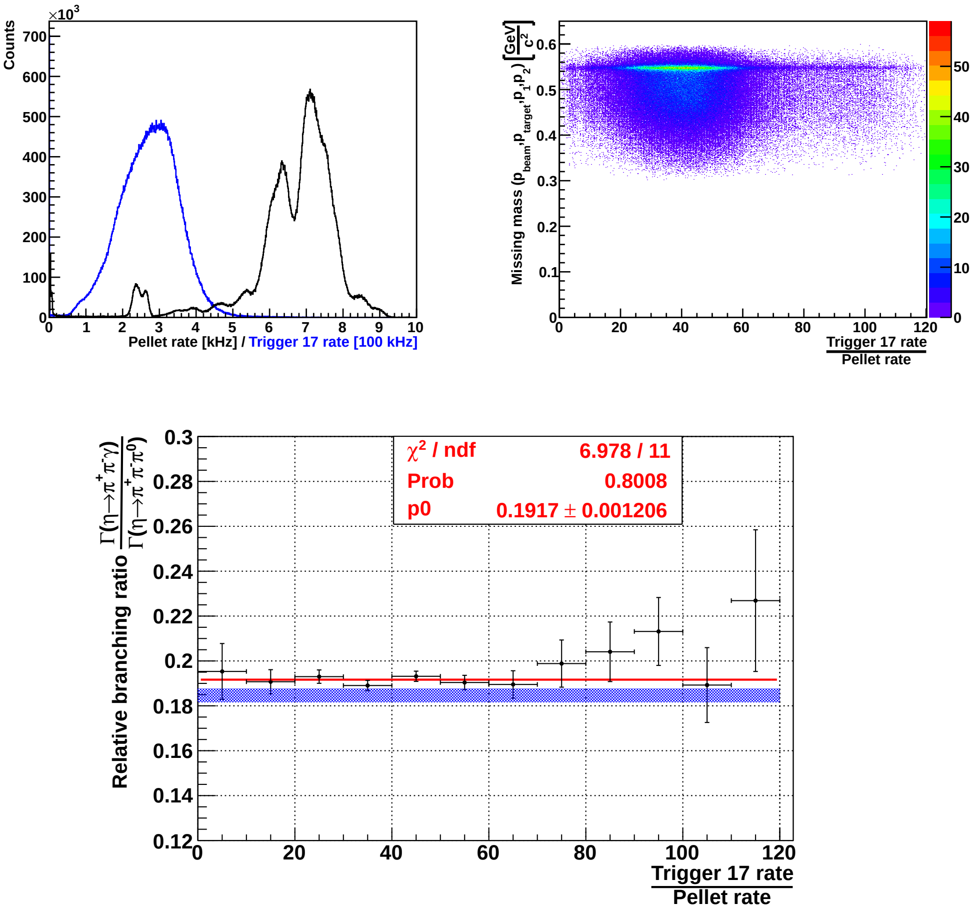

Figure 6.24: **Top left:** *Pellet and trigger 17 rate. The dominant rates are* $\sim 7.5\,\mathrm{kHz}$ *for the pellet counter and* $\sim 330\,\mathrm{kHz}$ *for the trigger 17 counter.* **Top right:** *Two proton missing mass after requesting:* $P(\chi^2_{pp\to pp\pi^+\pi^-\gamma}, 4) \geq 0.2$ *and* $E_\gamma > \frac{2\,\mathrm{deg}\times\mathrm{GeV}}{\angle(\pi^\pm,\gamma)}$ *as function of the ratio between the pellet and trigger 17 rates, which is proportional to the instantaneous luminosity.* **Bottom:** *Relative branching ratio* $\frac{\Gamma(\eta\to\pi^+\pi^-\gamma)}{\Gamma(\eta\to\pi^+\pi^-\pi^0)}$ *for different luminosity intervals. The red line represents a fit with a constant function and the blue bar corresponds the PDG-value for the relative branching ratio [10]. Horizontal error bars represent the width of the luminosity range and vertical error bars correspond to the statistical uncertainty.*

the projection of the missing mass is computed and the number of expected $\eta \to \pi^+\pi^-\gamma$ is determined. The same procedure is repeated to determine the number of expected $\eta \to \pi^+\pi^-\pi^0$ events as a function of luminosity. The corresponding relative branching ratio is calculated and plotted versus the luminosity interval, which is shown in the bottom line of Fig. 6.24. The statistical uncertainties shown in that diagram are correlated to the of different luminosities (see right panel of Fig. 6.24). Thus, the error bars increase for larger luminosities and have to be taken into account for the error estimation. The reduced χ^2 obtained from fitting a constant function to the data points in Fig. 6.24 is 0.63 and thus supports the hypothesis that the relative branching ratio is constant with respect to different luminosity intervals. The uncertainty caused by varying the luminosity is given by the error of $p0$ and reads as $\sigma_{lum} = 0.001$.

6.6.3.2 Correlation between the E_γ-distribution and different luminosities

The procedure discussed in the previous section was repeated for the photon energy distribution and the corresponding α-value was determined. The width of the luminosity intervals chosen here is different than presented in Eq. 6.13, in order to provide sufficient statistics for the individual photon energy distribution. The three luminosity ranges are presented in the left frame of Fig. 6.25. The sum of the three distributions shown there is equal to the overall photon energy distribution presented in Fig. 6.4. The distribution indicated by green markers (see left panel of Fig. 6.25) has the largest number of entries because the corresponding luminosity range is mostly populated (compare top right panel of Fig. 6.24).

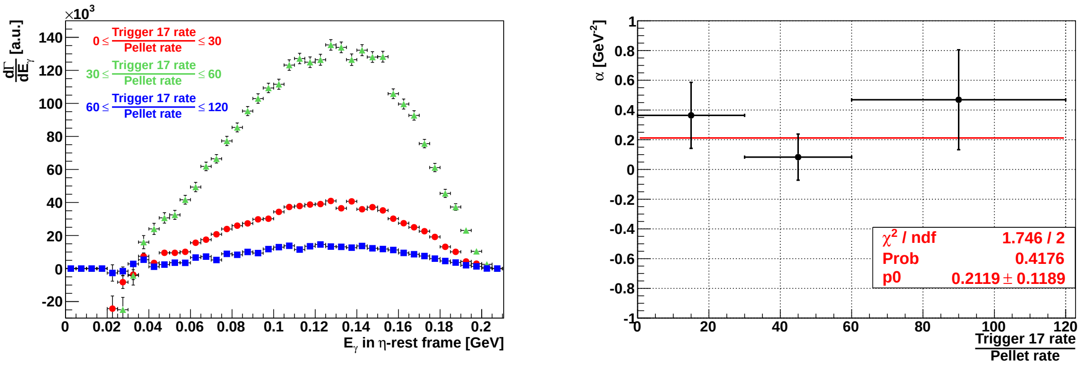

Figure 6.25: **Left:** *Photon energy distribution for three different luminosity intervals. The luminosity ranges* $0 \leq \frac{\textit{Trigger 17 rate}}{\textit{Pellet rate}} \leq 30$, $30 \leq \frac{\textit{Trigger 17 rate}}{\textit{Pellet rate}} \leq 60$ *and* $60 \leq \frac{\textit{Trigger 17 rate}}{\textit{Pellet rate}} \leq 120$ *are represented by red, green and blue coloured markers respectively.* **Right:** *α parameter deduced from the spectra shown in the left panel. Horizontal error bars correspond to the luminosity range and vertical error bars represent the fit error of each α value. A constant function is fit to all data points, as indicated by the red line.*

The α value obtained for each luminosity range as well as the corresponding fit error are shown in the right panel of Fig. 6.25. The distribution of the data points is in agreement with a constant function, as indicated by the reduced χ^2-value. The uncertainty is given by the error of $p0$: $\sigma_{lum} = 0.119\,\text{GeV}^{-2}$.

6.6.3.3 Correlation between the (π^+, γ) opening angle and different luminosities

The pion-photon opening angle distribution is studied for the same three different luminosity ranges, that were discussed in the previous section. The results are displayed in Fig. 6.26 and the individual β-values show (within the errors) a constant pattern with respect to different luminosity ranges. The corresponding uncertainty related to the fit shown in the right panel of Fig. 6.26 is given by: $\sigma_{lum} = 0.048$.

As presented in the previous section, the angular distribution obtained for luminosity ranges $30 \leq \frac{\text{Trigger 17 rate}}{\text{Pellet rate}} \leq 60$ (see green markers in left panel of Fig. 6.26) has the largest integral.

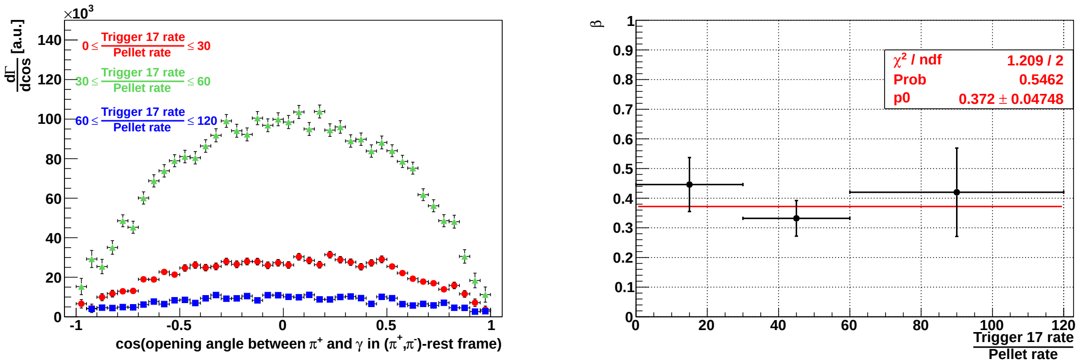

Figure 6.26: **Left:** *Opening angle distribution between the positive charged pion and the photon for the three different luminosity intervals:* $0 \leq \frac{\text{Trigger 17 rate}}{\text{Pellet rate}} \leq 30$ *(red markers),* $30 \leq \frac{\text{Trigger 17 rate}}{\text{Pellet rate}} \leq 60$ *(green markers) and* $60 \leq \frac{\text{Trigger 17 rate}}{\text{Pellet rate}} \leq 120$ *(blue markers). The sum of all three distributions is equal to the overall opening angle distribution shown in Fig. 6.6.* **Right:** β *parameter obtained from the spectra shown in the left panel and Eq. 2.34. Horizontal error bars correspond to the luminosity range and vertical error bars represent the fit error of each* β *value. A constant function (see red line) is fit to all data points.*

6.6.4 Determination of the η-peak content

The last issue which shall be discussed within the study of systematic uncertainties is the determination of the η-peak content after background subtraction. For that purpose, four different scenarios have been investigated:

1.) The η-signal peak obtained from measured data (after background subtraction) might be different from the simulated signal due to different implementations of detector effects (e.g. the θ dependent FRH energy resolution). Therefore, the η-peak content is determined from the simulated $\eta \to \pi^+\pi^-\gamma$ missing mass distribution, in order to test for any inconsistency.

2.) The fourth order polynomial in Eq. 5.18 is replaced by a third order polynomial, in order to check the sensitivity of the results with respect to the background determination.

3.) The integration range: $[0.53\,\text{GeV/c}^2, 0.56\,\text{GeV/c}^2]$ for determining the content of the η-peak is changed to: $[0.48\,\text{GeV/c}^2, 0.61\,\text{GeV/c}^2]$. A poor fit of the background outside the peak region would lead to enhancements after background subtraction. Therefore, increasing the integration window allows to check for the background subtraction performance, which effects the final η-peak content.

4.) Same issue as discussed in 3.), but the integration window covers the missing mass range: $[0.4\,\text{GeV/c}^2, 0.65\,\text{GeV/c}^2]$.

The results for those analysis conditions are displayed in Figures 6.27 and 6.28. The various coloured differential distributions shown in the left column of Fig. 6.28 follow a common pattern, except the photon energy distribution indicated by purple marker points. This plot is obtained by using Eq. 5.18 with a third order polynomial. Entries within the range $E_\gamma \in [0.1\,\text{GeV}, 0.15\,\text{GeV}]$ seem to be enhanced for scenario 2 compared to the other distributions. However, a fit (which is not displayed here) showed, that this distribution is in agreement with the shape predicted by Eq. 2.29

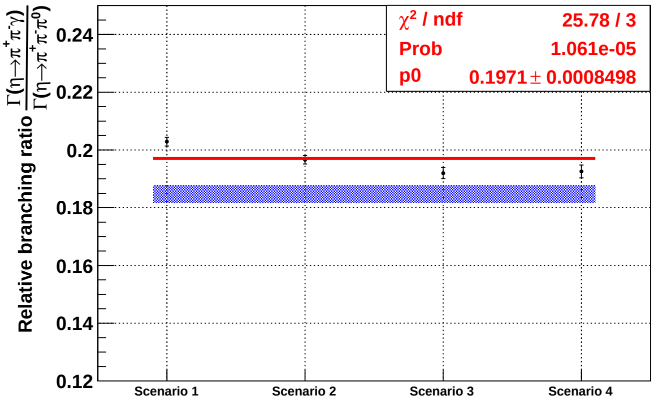

__Figure 6.27:__ Relative branching ratio as a function of four different analysis conditions described in the text. The blue coloured box represents the PDG-value for the relative branching ratio [10].

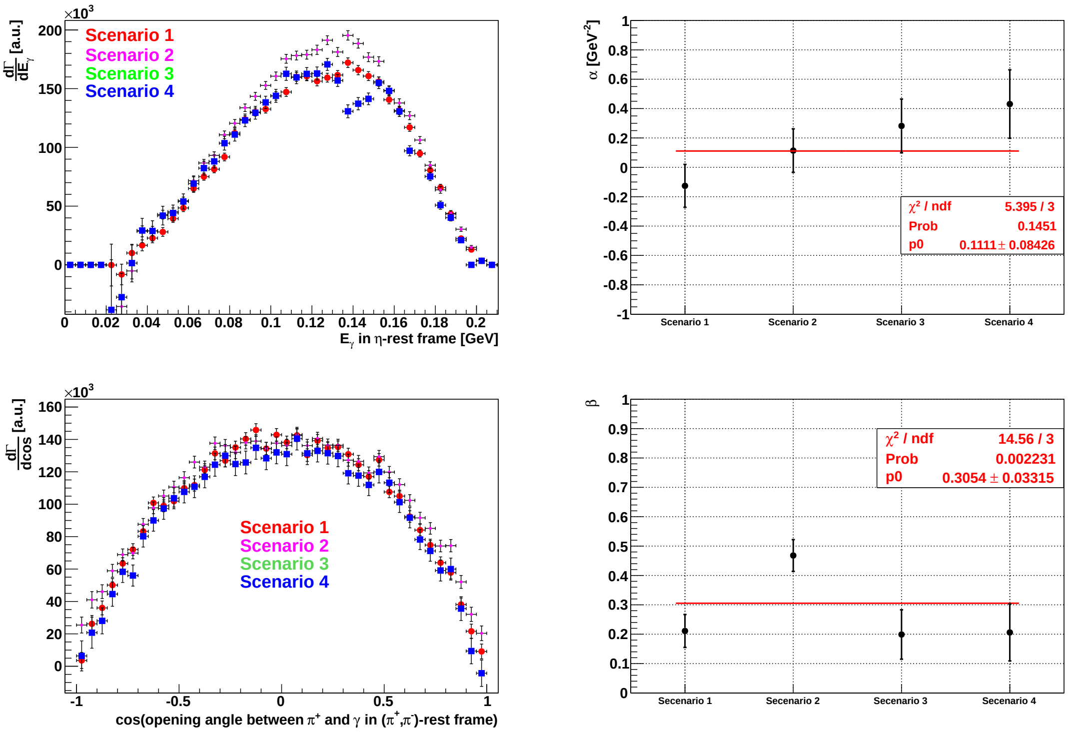

__Figure 6.28:__ E_γ-distribution and α-parameter (top row) and pion-photon opening angle distribution and β (bottom row) as a function of the four different analysis conditions mentioned in the text.

with $\alpha = (0.114 \pm 0.146)\,\mathrm{GeV}^{-2}$. The E_γ-distribution representing scenario 4 (blue data points in top left frame of Fig. 6.28 shows non-reasonable structures for energies between 0.12 GeV and 0.15 GeV. This is related to the description of the background within this energy region (see corresponding spectra in Appendix E). Negative entries occur and are taken into account due to the large integration window. This results into reduced bin contents as shown in the top left diagram of Fig. 6.28. Those entries are not taken into account for fitting Eq. 2.29.

The systematic errors are calculated according to Eq. 6.12 for the cases shown in

Fig. 6.27 and the second row of Fig. 6.28. The error of α for varying the η-peak content is given by the error shown in the right panel of Fig. 6.28.

6.6.5 Summary of the investigated systematic effects

All observables and the systematic uncertainties corresponding to different analysis conditions are listed in Table 6.2. The largest uncertainty of the relative branching ratio and α is provided by the split-off rejection condition and thus dominates the total systematic error.

Observable	Uncertainty related to:				**Total error**
	σ_{kFit}	σ_A	σ_{lum}	σ_{peak}	$\boldsymbol{\sigma_{sys}}$
$\boldsymbol{\frac{\Gamma(\eta \to \pi^+\pi^-\gamma)}{\Gamma(\eta \to \pi^+\pi^-\pi^0)}}$	0.010	0.016	0.001	0.005	**0.020**
$\boldsymbol{\alpha}$ **[GeV^{-2}]**	0.062	0.217	0.119	0.084	**0.269**
$\boldsymbol{\beta}$	0.024	0.086	0.048	0.137	**0.170**

Table 6.2: *Summary of all uncertainties for the determined observables of $\eta \to \pi^+\pi^-\gamma$. The total error σ_{sys} represents the quadratic sum of all errors presented in the second, third, fourth and fifth column: $\sigma_{sys} = \sqrt{\sigma_{kFit}^2 + \sigma_A^2 + \sigma_{lum}^2 + \sigma_{peak}^2}$*

The relative branching ratio has the total systematic error of 0.020. This observation is not surprising because the relative branching ratio is related to the overall missing mass spectra of the reconstructed $\eta \to \pi^+\pi^-\gamma$ and $\eta \to \pi^+\pi^-\pi^0$ events. Those distributions are only sensitive to the reduction of event candidates and thus have a certain robustness with respect to changing analysis conditions.

The situation is completely different for α and β. These observables are deduced from distributions, which are directly connected to the kinematics of the decay particles and thus show a higher sensitivity. This also explains the large error for α and β caused by varying the split-off rejection parameter A. By definition, the split-off suppression condition removes photons depending on their energy and opening angle with respect to charged tracks. Depending on the choice of A, a cut into the signal region of $\eta \to \pi^+\pi^-\gamma$ is performed, which finally influences the distributions of the kinematic variables of this decay. However, this analysis method is essential for the suppression of dominating background contributions stemming from $pp \to pp\pi^+\pi^-$ events. Future studies will deal with an optimisation of that analysis tool, in order to decrease the corresponding systematic uncertainty.

Changing the luminosity has the largest impact on α, because the high rates predominantly influence the performance of the calorimeter, which is used to reconstruct photons.

The systematic errors estimated for α within this work are of the same order as the corresponding errors determined in [7]. Though, uncertainties related to varying the kinematic fit probability are found to be smaller within this analysis.

The largest systematical uncertainty for β is related to the determination of the η-peak content, which has to be investigated further.

6.7 Summary and discussion of the results

After calculating the decay related observables for $\eta \to \pi^+\pi^-\gamma$ and estimating the analysis dependent uncertainties, the obtained results are discussed and compared to previous measurements.

6.7.1 Result for the relative branching ratio $\frac{\Gamma(\eta\to\pi^+\pi^-\gamma)}{\Gamma(\eta\to\pi^+\pi^-\pi^0)}$

Using the ratio determined in Eq. 6.4 and the systematic uncertainties listed in Table 6.2, leads to the final result displayed in Fig. 6.29. The results obtained from theoretical predictions and previous measurements, which have already been discussed in Chapter 2, are shown for comparison again.

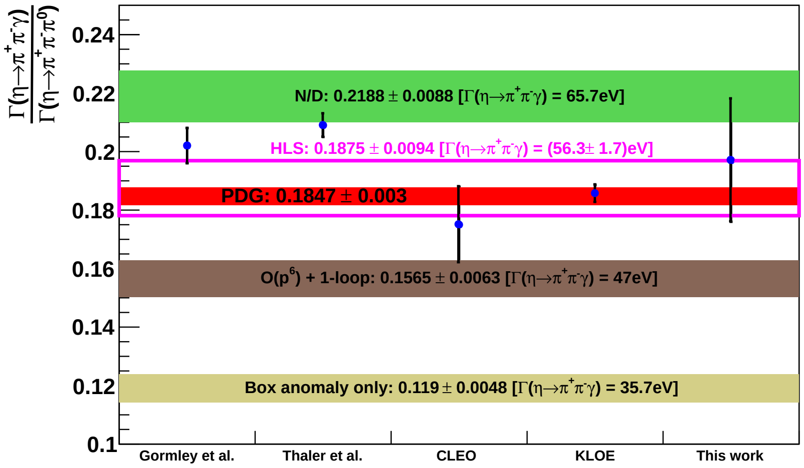

Figure 6.29: *Summary of the measured (blue markers with error bars) and theoretical predicted (coloured boxes) relative branching ratios. The error bars of each point represent the sum of the statistical and systematical errors.*

The absolute value of the relative branching ratio determined here is in agreement with the ratio obtained from Gormley et al.[g]. However, the large error bars (which are dominated by the systematic error) do not exclude any of the previous results shown in Fig. 6.29 and thus none of them is clearly rejected by the recent measurement.

From a theoretical point of view, the branching ratio found within this work supports the pion-pion interaction model implementing Hidden Local Symmetries or using a N/D structure, which matches vector meson dominance and one-loop chiral corrections at once. The HLS model is also confirmed by the KLOE result (see Fig. 6.29), whereas the N/D structure model is only in agreement with the current result due to the large systematical error. The theoretically predicted branching ratio including pion loop corrections and higher order momenta ($O(p^6)$+1-loop) is

---

[g] If the error of the Gormley et al. result is taken into account.

rejected by the current result. The relative branching ratio predicted by considering the box anomaly term only (i.e. no final state interactions are included) is presented by the yellow coloured box in Fig. 6.29. All measured data points show a clear deviation from this value and therefore indicate that final state interactions have to be included in the description of the decay $\eta \to \pi^+\pi^-\gamma$.

6.7.2 Result for the α-value

Fig. 6.30 summarises the α values determined in previous measurements (also see Chapter 2) as well as the α-parameter found within this work. The coloured bars represent the α-values and their corresponding errors deduced from different theoretical approaches, which include final state interactions between the pions. The α value for describing the photon energy distribution related to the box anomaly term only is $-1.7\,\mathrm{GeV}^{-2}$ which is not presented in Fig. 6.30. The α-values presented by

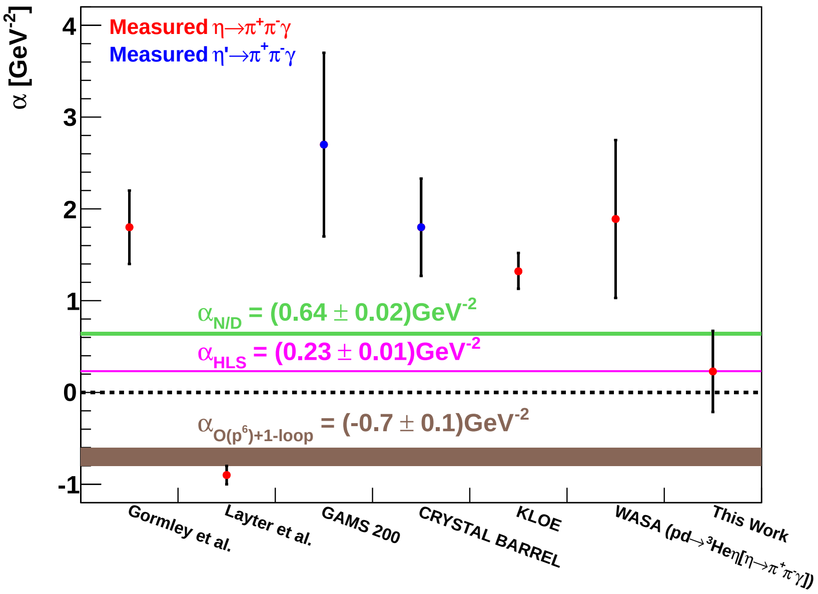

Figure 6.30: *Summary of the measured (red and blue points) and theoretical predicted (coloured bars) α-values. The black dashed line corresponds to $\alpha = 0$. The error bars of all measured values include the statistical, systematical and the theoretical error of* $0.02\,\mathrm{GeV}^{-2}$ *[7], whereas the width of the coloured bars represents the error of the corresponding theoretical α-value.*

the KLOE and WASA-at-COSY collaborations are larger than one and in agreement to each other within the error bars. The σ-distance n between the α-value found within this work and previous measurements is calculated according to:

$$n = \frac{|\alpha_{\text{previous}} - \alpha_{\text{this work}}|}{\sigma_{\text{previous}} + \sigma_{\text{this work}}} \tag{6.14}$$

where σ_{previous} / $\sigma_{\text{this work}}$ correspond to the error bars of α_{previous} / $\alpha_{\text{this work}}$ presented in Fig. 6.30. The benefit of Eq. 6.14 is that the σ-distance does not depend on the choice of one particular error of α (i.e. $n\sigma$ can either be read as $n\sigma_{\text{this work}}$ or $n\sigma_{\text{previous}}$).

Accordingly, the α-value found within this work is $\sim 1.3\sigma$ away from the previous

WASA-at-COSY result and $\sim 1.7\sigma$ away from the KLOE result. Furthermore, the tendency towards α-values $> 1\,\mathrm{GeV}^{-2}$ [h], which is indicated in Fig. 6.30, is not reproduced by the recent α-parameter.
However, the result obtained within this thesis is in agreement with $\alpha_{\mathrm{HLS}} = 0.23\,\mathrm{GeV}^{-2}$ and therefore supports the HLS model. Due to the large (systematic) error the current α-value does not exclude $\alpha = 0$ and $\alpha_{N/D} = 0.64\,\mathrm{GeV}^{-2}$. The same observations were made for the current value of the relative branching ratio discussed in the previous section. Thus, both measured decay observables of $\eta \rightarrow \pi^+\pi^-\gamma$ (i.e. the E_γ-distribution and the relative branching ratio) are consistent with respect to each other.
As pointed out in Chapter 2, each α-parameter is related to a different physical interpretation: For $\alpha = 0$ the pion-pion interaction would be solely described by the pion vector form factor (see Eq. 2.29). This factor is universal and applicable on every reaction including interacting pions. A non-zero value for α on the contrary indicates a reaction specific contribution from pion-pion interactions, which is described by different theoretical models. Assuming a non-zero α-parameter for the recent measurement, the pion-pion-interaction, which contributes to the box anomaly term would be described by a vector meson dominance model, which incorporates hidden local symmetries or an N/D structure.

6.7.2.1 Comparison with the previous WASA-at-COSY result

Another important issue within the recent discussion is a direct comparison of the photon energy distribution obtained from the two different WASA-at-COSY data sets. Fig. 6.31 shows a comparison between the E_γ-distribution based on the $pp \rightarrow pp\eta[\eta \rightarrow \pi^+\pi^-\gamma]$ (blue points) data set and the previous WASA-at-COSY

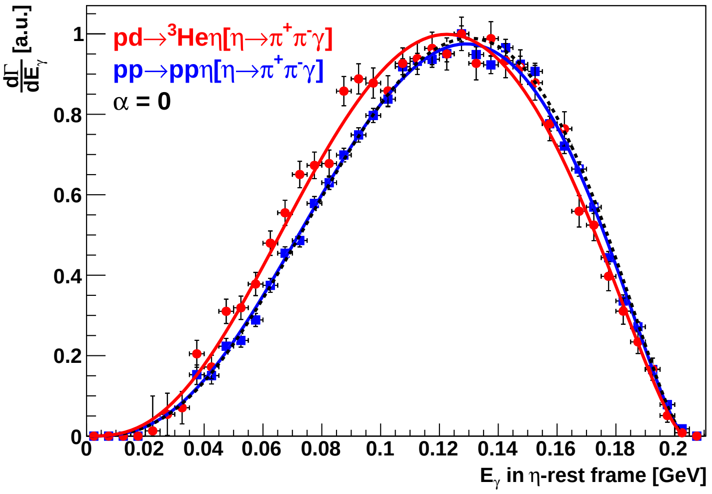

Figure 6.31: *Photon energy distribution obtained from the* $pd \rightarrow {}^3\mathrm{He}\eta[\eta \rightarrow \pi^+\pi^-\gamma]$. *(red solid circles - values taken from [7]) and* $pp \rightarrow pp\eta[\eta \rightarrow \pi^+\pi^-\gamma]$ *(blue solid rectangles) data set. Both distributions are scaled to the same height. The red and blue solid curves represent Eq. 2.29 with* $\alpha = 1.89\,\mathrm{GeV}^{-2}$ *and* $\alpha = 0.229\,\mathrm{GeV}^{-2}$*, respectively. The black dashed curve corresponds to a fit of Eq. 2.29 to both measured distributions at once with a fixed parameter* $\alpha = 0$.

---

[h] The results of the CRYSTAL BARREL and the GAMS200 collaborations are not taken into consideration for this discussion because their α values correspond to the reaction $\eta' \rightarrow \pi^+\pi^-\gamma$.

measurement (red points), using the $pd \to {}^3\mathrm{He}\eta[\eta \to \pi^+\pi^-\gamma]$ reaction. The red distribution is shifted towards smaller photon energies with respect to the blue one. The largest deviation between the two distributions is located at photon energies $E_\gamma < 0.1\,\mathrm{GeV}$. For photon energies $< 0.035\,\mathrm{GeV}$ the blue coloured distribution has zero entries, as explained in Section 6.2. A simultaneous fit of Eq. 2.29 with fixed $\alpha = 0$ to both data sets (black dashed line in Fig. 6.31) shows that the result gained within this work is rather in agreement with $\alpha = 0$ than with the previous WASA-at-COSY result.

6.7.2.2 Sensitivity study

The following study is related to item ii) in Section 2.6 and deals with the sensitivity of the photon energy distribution E_γ with respect to different α-values which has also been mentioned in Section 6.6.1.3. The corresponding results are displayed in Fig. 6.32. The variation of α with respect to the shape of the E_γ-distribution is investigated in the following way: In a first step the photon energy distribution is calculated for α-values which are increased in steps of $0.05\,\mathrm{GeV}^{-2}$ between $-2\,\mathrm{GeV}^{-2}$ and $3\,\mathrm{GeV}^{-2}$ (see black points in top frame of Fig. 6.32). The number of bins as well as the bin width (5 MeV) of this distribution are chosen to be the same as for the two distributions shown in Fig. 6.31. The statistical error in each photon energy bin is set to zero (see black points in top frame of Fig. 6.32), because an ideal E_γ-distribution with sufficiently large statistics[i] in each energy bin is assumed. The black points shown in the top frame of Fig. 6.32 represent such a distribution with $\alpha = 0.2\,\mathrm{GeV}^{-2}$. The height is scaled to the height of the measured distribution shown in Fig. 6.4. For each α-value the corresponding E_γ-distribution is fit by Eq. 2.28, Eq. 2.29 with $\alpha = 0$ and Eq. 2.29 with $\alpha = 1.89\,\mathrm{GeV}^{-2}$, respectively

The bottom frame of Fig. 6.32 shows the probability of each of the three fits as a function of the corresponding α-value (blue solid, red solid and black dashed lines). Each probability distribution has a plateau at one with a certain width which is directly connected to the bin width and the statistical error of the calculated E_γ-distribution. According to the red solid curve shown in the bottom panel of Fig. 6.32, E_γ-distributions with a bin width of 5 MeV and α-values between $-0.4\,\mathrm{GeV}^{-2}$ and $0.4\,\mathrm{GeV}^{-2}$ are compatible with a photon energy distribution described by Eq. 2.29 with $\alpha = 0$. This feature explains the situation shown in Fig. 6.17 and moreover indicates the maximum achievable sensitivity of α with respect to an E_γ-distribution with negligible statistical fluctuations (i.e. the total available $pp\eta$ data set is analysed) and a bin width of 5 MeV.

Assuming that sufficiently large statistics are provided, the sensitivity can be increased (i.e the width of the plateau is decreased) if the width of each photon energy bin is decreased. But a smaller bin width is connected to less entries in each bin and might cause statistical fluctuations due to background subtraction. Therefore, the E_γ bin width can be increased as long as the statistical error of the bin content does not increase significantly. Otherwise, the sensitivity is not improved by a smaller bin width.

The same conclusions can be drawn for the blue solid and black dashed curves presented in Fig. 6.32. The blue curve shows that the shape of an E_γ-distribution provided by the simplest matrix element can be described by the model independent approach with $\alpha = -1.7\,\mathrm{GeV}^{-2}$.

Using a bin width of 5 MeV and assuming sufficient statistics, the photon energy

---

[i] This condition can be realised by analysing the total 2010, 2012 and 2008 $pp\eta$ data set.

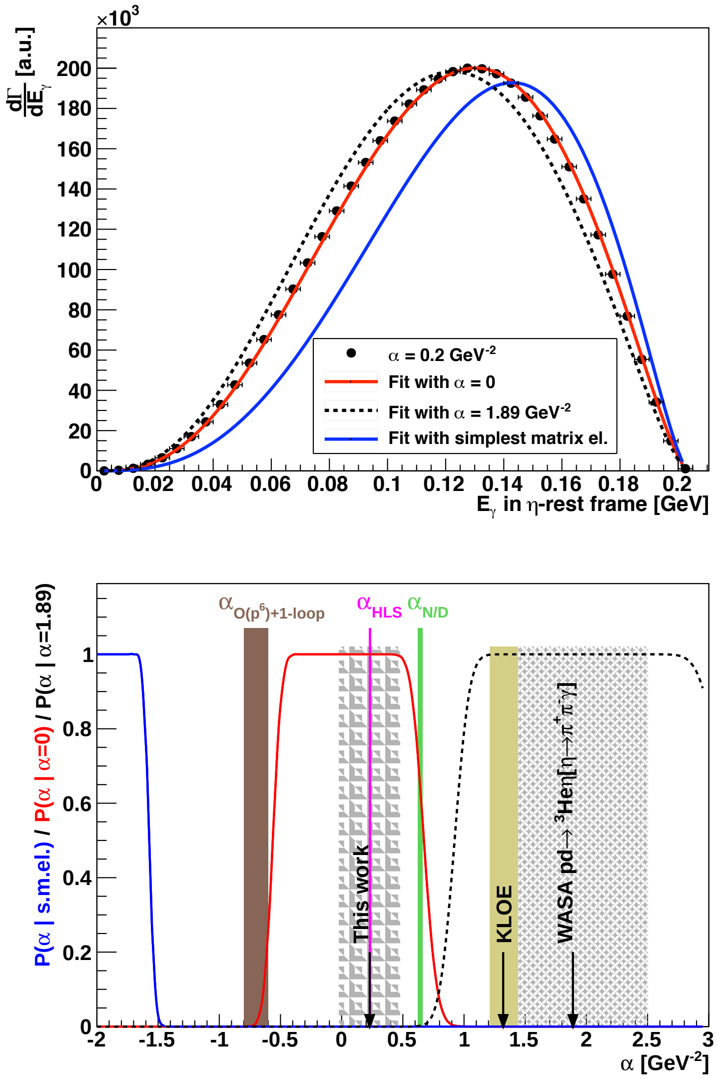

Figure 6.32: **Top:** *Calculated photon energy distribution (black points) for* $\alpha = 0.2\,\mathrm{GeV}^{-2}$*. The horizontal error bars represent the chosen energy bin width of* 5 MeV*. The calculated distribution is fit by Eq. 2.28 (blue curve) and Eq. 2.29 for* $\alpha = 0$ *(red curve) and* $\alpha = 1.89\,\mathrm{GeV}^{-2}$ *(black, dashed curve), respectively.* **Bottom:** *Probabilities for fitting Eq. 2.28 (blue curve), Eq. 2.29 with* $\alpha = 0$ *(red curve) and* $\alpha = 1.89\,\mathrm{GeV}^{-2}$ *(black, dashed curve) to the calculated* E_γ*-distributions obtained for different* α*-values (see x-axis). The coloured boxes represent the theoretical as well as the experimental values for* α *which have been discussed in the previous section. The statistical errors of each measured value is not included, because negligible statistical fluctuations in each energy bin are assumed. The black arrows point to the* α*-values measured by KLOE, WASA-at-COSY and within this thesis.*

distributions previously measured by KLOE and WASA-at-COSY are compatible in shape according to the black dashed curve.

However, comparing all three probability curves indicates that the maximum achievable sensitivity of α is sufficient to clearly distinguish between photon energy distributions related to the simplest matrix element and dipion final state interactions described by $\alpha = 0$ or $\alpha = 1.89\,\mathrm{GeV}^{-2}$. Furthermore, E_γ-distributions predicted by the N/D or the pion-1-loop model can be separated from those described by the pion vector form factor only. Unfortunately, a clear distinction between the HLS model and $\alpha = 0$ is not possible within this maximum sensitivity (see solid red curve and purple box in the bottom panel of Fig. 6.32). The results shown in Fig. 6.32 are consistent with those displayed in Fig. 6.30: The α-value found in this work clearly rejects the previous WASA-at-COSY and KLOE result but is in agreement with an E_γ-distribution predicted by the pion vector form factor or the HLS model. The N/D model is not confirmed in Fig. 6.32, because the statistical error of α is not taken into account.

According to the results presented in this section the remaining $pp\eta$ data have to be analysed in order to improve the sensitivity of α with respect to the measured photon energy distribution and to make a clear statement of the underlying model to describe the dipion final state interactions.

6.7.2.3 Cross check with the $s_{\pi\pi}$-distribution

As pointed out in Chapter 2, the squared two pion invariant mass distribution $s_{\pi\pi}$ is sensitive to contributions from final state interactions between the charged pions in $\eta \to \pi^+\pi^-\gamma$ and related to the E_γ-distribution via Eq. 2.32. Thus, both distributions should be described by the same α-parameter with respect to Eq. 2.29.

Fig. 6.33 shows the $s_{\pi\pi}$-distribution obtained after background subtraction and efficiency correction. The background subtraction is performed in the same way as presented in Section 6.2, i.e. the two proton missing mass distribution is corrected for background in $s_{\pi\pi}$-bins. The width of each $s_{\pi\pi}$-bin is directly correlated via Eq. 2.32 to the bin width of the E_γ-distribution[j] and thus determined to be: 5.5 MeV^2. The remaining entries after background subtraction are corrected for efficiency according to Eq. 6.6, using the proper $s_{\pi\pi}$-distribution generated by Pluto. The final distribution shown in Fig. 6.33 is kinematically limited according to Eq. 2.31. However, mass values larger than 0.26 GeV^2 are not observed [k] in Fig. 6.33 due to the lack of

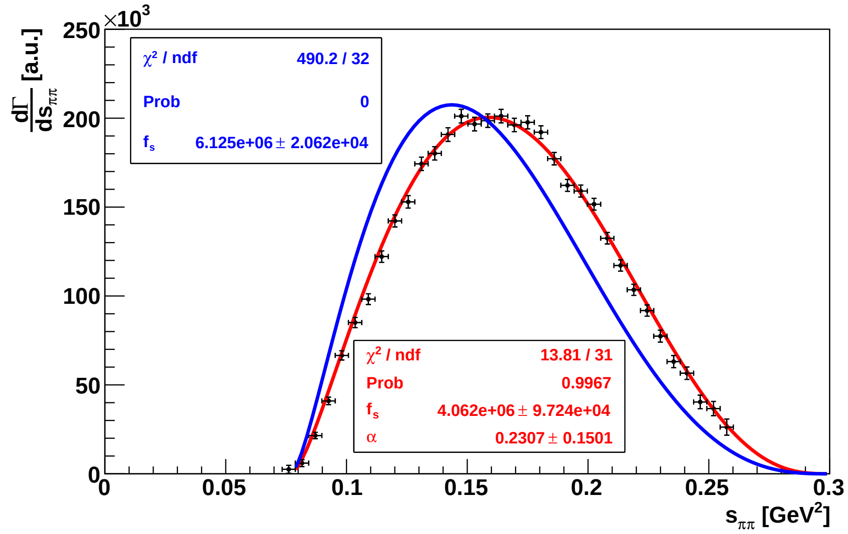

Figure 6.33: *Two pion invariant mass squared distribution $s_{\pi\pi}$ for $\eta \to \pi^+\pi^-\gamma$ after background subtraction and efficiency correction. The blue curve represents a fit of Eq. 2.28 and the red curve corresponds to a fit of Eq. 2.29, respectively. The measured as well as the fitted distributions are kinematically limited according to Eq. 2.31.*

---

[j] Using: $5\,\mathrm{MeV} = \{\mathrm{E}_\gamma(\mathrm{bin\ i+1}) - \mathrm{E}_\gamma(\mathrm{bin\ i})\} \overset{\mathrm{Eq.\ 2.32}}{=} \frac{1}{2\mathrm{m}_\eta} \cdot \{\mathrm{s}_{\pi\pi}(\mathrm{bin\ i}) - \mathrm{s}_{\pi\pi}(\mathrm{bin\ i+1})\}$.

[k] This invariant mass region corresponds to photon energies $E_\gamma < 0.035$ GeV in Fig. 6.4, which could not be determined for similar reasons.

statistics in the corresponding missing mass spectra. Fitting Eq. 2.28 (blue curve in Fig. 6.33) and Eq. 2.29 (red curve in Fig. 6.33) to the measured $s_{\pi\pi}$-distribution shows again, that two pion final state interactions have to be taken into account, in order to describe the decay $\eta \to \pi^+\pi^-\gamma$.
The corresponding α-value (see red inset box in Fig. 6.33) is, within the fit-error, in good agreement with the α-parameter obtained from the E_γ-distribution presented in Section 6.2. Thus, both results are consistent and show, that the E_γ- and the $s_{\pi\pi}$-distribution equally describe contributions from two pion final state interactions. Additionally, the simultaneous investigation of both distributions allows to cross check the obtained α-parameter, which was done in this section.

6.7.3 Result for the β-value

Fig. 6.34 shows the β-parameter determined within this work in comparison with results obtained in previous measurements. The current result is (according to

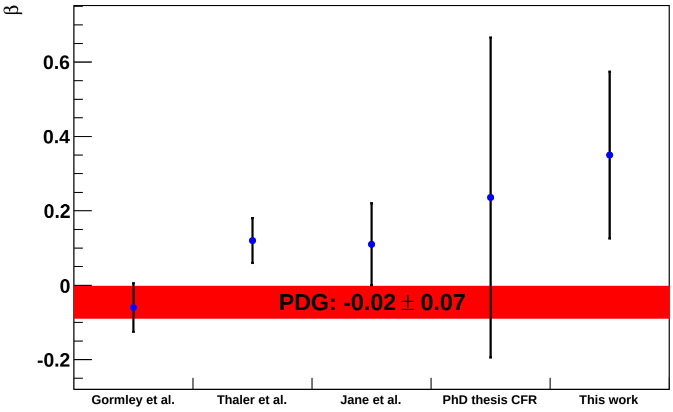

Figure 6.34: *Summary of measured β values. The red solid box represents the PDG-value [10] for β.*

Eq. 6.14) $\sim 1.3\sigma$ away from the PDG-value. Considering the fluctuations and shape of the distribution shown in Fig. 6.6, the β-value is rather compensating these features than being related to a C-violating process.
Thus, deviations from $\beta = 0$ could not be proven beyond doubt within this work.

6.7.4 Discussion

The questions posted in Section 2.6 can be answered in the following way:

i) The relative branching ratio found within this work does not allow for a clear statement about a trend towards values $\gtrsim 0.2$ (Gormley and Thaler results) or < 0.19 (CLEO and KLOE results). Both values are confirmed within the large error bars.

ii) The α-parameter obtained from measuring $pd \to {}^3\mathrm{He}\eta[\eta \to \pi^+\pi^-\gamma]$ is not confirmed within this work by 1.3σ. The α value found here is in clear agreement with the theoretical prediction given by the HLS-model (see Fig. 6.30).

However, predictions made by the N/D-structure-model and $\alpha = 0$ are not excluded due to the large systematic error. Further studies (see Sections 6.7.2.1 and 6.7.2.2) showed, that a clear distinction between $\alpha = 0$ and $\alpha \neq 0$ with respect to the shape of the E_γ-distribution is not possible within this work.

iii) The relative branching ratio and the E_γ-distribution were determined independently from each other within this work. **Both** decay observables are (within the given errors) consistent with the theoretical models presented in Section 2.4.3, except for the pion-1-loop-model (see item c) in Section 2.4.3).

However, the fact, that the β-parameter is not in agreement with zero within the error bars weakens the statements made in *ii*). The pion-photon opening angle distribution and the E_γ distribution are obtained from the Dalitz-plot and therefore are not independent variables. A change in the shape of one of the two distributions leads to a change in shape of the other one. If it turns out, that the angular distribution will change as a result of more detailed systematic studies, it is expected that the photon energy distribution will change as well. How strong the impact of that change on the final α-parameter will be can not be predicted.
The underlying statistics for all distributions shown here is based on 77904 ± 532 reconstructed $\eta \rightarrow \pi^+\pi^-\gamma$ events after subtracting multi-pion background and contributions from $\eta \rightarrow \pi^+\pi^-\pi^0$ [1]. This is about five times more statistics than in the previous WASA-at-COSY experiment [7]. According to that, one would naively expect a factor $\sqrt{5} \approx 2.2$ improvement within the statistical error of α. The corresponding statistical error found in the recent analysis is $0.153\,\mathrm{GeV}^{-2}$, which is a factor of ~ 1.6 better and quite in agreement with the expected improvement. The underlying statistics for the KLOE results is about a factor three larger [6].
As pointed out at the beginning of this chapter, the recent results are obtained for analysing 42% of the 2010 $pp\eta$ data set. Due to the large (and dominating) systematical uncertainties, this portion of analysed data is sufficient for the aims presented in Section 2.6, i.e. more analysed data decreases the statistical error, but does not effect the systematical uncertainties. However, the remaining $pp\eta$ data (i.e. the remaining part of the 2010 data set plus the complete 2012 data set) have to be analysed, as discussed in the following section.

6.8 Future aspects and plans

The major issue for future investigations is a more detailed study of systematic effects, aiming for a reduction of the systematic errors. Additionally, the sensitivity of α with respect to the E_γ distribution has to be increased in order to distinguish between the various pion-pion interaction models. Therefore, the remaining $pp\eta$ data set has to be analysed, in order to increase the statistics in low populated experimental conditions (e.g. low / high luminosity ranges which could no be investigated within this work). Increasing statistics might also allow for a better description of the E_γ-distribution in the range of $E_\gamma < 0.035\,\mathrm{GeV}$.
Another important topic will be the understanding (and maybe correction) of the θ dependent energy resolution of the Forward Range Hodoscope (FRH) layers. As it was pointed out in Section 6.6.1.2, this dependency leads to a large systematic

---

[1] The number of reconstructed $\eta \rightarrow \pi^+\pi^-\gamma$ events presented in Section 6.1 includes contributions from $\eta \rightarrow \pi^+\pi^-\pi^0$ events.

uncertainty with respect to changing the kinematic fit probability. This investigation is also connected to the study of the correlation between the relative branching ratio and a varying probability $P(\chi^2_{pp\rightarrow pp\pi^+\pi^-\gamma\gamma}, 4)$.
According to Table 6.2, one of the largest uncertainties on all observables is provided by the split-off rejection condition. This analysis method has to be investigated in more detail and might be refined, in order to reduce the corresponding uncertainty. The efficiency obtained for reconstructing $\eta \rightarrow \pi^+\pi^-\gamma$ events is $\sim 2\%$, which was sufficient for rejecting a large amount of background and to determine the observables of $\eta \rightarrow \pi^+\pi^-\gamma$. On the other hand, a large fraction of the signal is lost because of the chosen minimum kinematic fit probability. Most of the signal events are located at fit probabilities < 0.2, where the largest population of background events is found too (see left panel of Fig. 5.22). However, this acceptance will be optimised in order to profit from the large statistics within the $pp\eta$ data set.
Finally, the obtained result on α has to be validated, which is directly connected with finding the reason for the non-zero β-parameter. All those studies will happen in the framework of a common $pp\eta$ analysis module, which allows to access all charged η decays. Studying decays with a similar topology (e.g. $\eta \rightarrow e^+e^-\gamma$) or a common underlying reaction (e.g. $\eta \rightarrow \pi^+\pi^-\gamma^*, \gamma^* \rightarrow e^+e^-$) allows for systematic cross checks and investigation of the various analysis conditions from different point of views.

Chapter 7

Summary and Outlook

The decay $\eta \to \pi^+\pi^-\gamma$ was analysed within this work with respect to the determination of the relative branching ratio $\frac{\Gamma(\eta\to\pi^+\pi^-\gamma)}{\Gamma(\eta\to\pi^+\pi^-\pi^0)}$ and the single photon energy distribution E_γ. Both observables allow to study contributions from charged pion final state interactions, which dominate the box anomaly term beyond the chiral limit. The E_γ-distribution was fit by a model independent approach using one parameter (α) to describe the shape and therefore contributions from final state interactions [4]. A reaction independent description of the pion-pion interactions by the pion vector form factor is realised by $\alpha = 0$, whereas any reaction specific interaction processes are related to $\alpha \neq 0$.
The η-mesons were produced in the reaction $pp \to pp\eta$ at 1.4 GeV beam kinetic energy, using the COSY accelerator and the reaction $pp \to pp\eta[\eta \to \pi^+\pi^-\gamma]$ was measured with the WASA detector. The data were taken in three different run periods in 2008, 2010 and 2012. The analysis of $\eta \to \pi^+\pi^-\gamma$ performed in this work is restricted to 42% of the data set acquired in 2010.
This data set was preselected in order to reduce contributions from multi-pion production reactions and to decrease the average file size per run. Therefore, a threshold of 0.4 GeV/c^2 was applied on the proton-proton missing mass and at least one pair of oppositely charged particles in the Central Detector was requested. The resulting data subset is suitable for the investigation of all charged η decay channels. Detector resolutions were adjusted in the simulated data with respect to the resolutions obtained for the measured data. A calorimeter ring wise energy calibration was applied for the reconstruction of simulated neutral tracks which allowed for a consistent description of the $\pi^0 \to \gamma\gamma$ and $\eta \to \gamma\gamma$ invariant mass distribution.
The relative branching ratio $\frac{\Gamma(\eta\to\pi^+\pi^-\gamma)}{\Gamma(\eta\to\pi^+\pi^-\pi^0)}$ was determined by analysing the decay channels $\eta \to \pi^+\pi^-\gamma$ and $\eta \to \pi^+\pi^-\pi^0$ simultaneously. Additionally, the analysis of $\eta \to \pi^+\pi^-\pi^0$ was used to correct for background contributions stemming from this channel and to monitor the calorimeter calibration and photon energy resolution via the decay $\pi^0 \to \gamma\gamma$. Background contributions stemming from multi-pion production reactions, which are a competing process to the η production, were suppressed by implementing a least squares kinematic fit algorithm. In doing so, a minimum kinematic fit probability of 20% was selected for the reconstruction of $\eta \to \pi^+\pi^-\gamma$ and $\eta \to \pi^+\pi^-\pi^0$ events. In addition to that, falsely reconstructed low energy photons with a distance close to charged tracks in the Central Detector were rejected. The latter condition is important for the analysis of $\eta \to \pi^+\pi^-\gamma$, because the corresponding measured signal is dominated by the background reaction $pp \to pp\pi^+\pi^-$ which has in combination with a falsely reconstructed photon the same final state configuration.

The final analysis of $\eta \to \pi^+\pi^-\gamma$ led to 77904±532 reconstructed $\eta \to \pi^+\pi^-\gamma$ events after background subtraction and correcting for contributions from $\eta \to \pi^+\pi^-\pi^0$. This number is about a factor of five larger than obtained in the previous WASA-at-COSY result [7].
The relative branching ratio determined in this work was found to be:

$$\boldsymbol{\frac{\Gamma(\eta \to \pi^+\pi^-\gamma)}{\Gamma(\eta \to \pi^+\pi^-\pi^0)} = 0.197 \pm 0.001_{stat} \pm 0.02_{sys}} \tag{7.1}$$

which is in agreement with all results obtained from previous experiments [5, 6, 10, 19, 20], due to the large systematical error. The result presented in Eq. 7.1 is in agreement with the theoretical value predicted by the HLS-model [2], which includes vector meson dominance terms in addition to the Wess-Zumino-Witten Lagrangian. According to this model, dipion final state interactions are basically described by $\gamma - V[V \to \pi^+\pi^-]$ transitions [2]. This model is also confirmed by the measured branching ratio from the KLOE collaboration [6].
Due to the error in Eq. 7.1, the recent value for the relative branching ratio is also consistent with the theoretical model described in Ref. [1], which describes pion-pion interactions in a way that contributions from vector meson dominance as well as pion loop corrections are included.
The single photon energy distribution E_γ, which was determined in this work, is described by the model-independent approach [4] presented in Eq. 2.29:

$$\boldsymbol{\alpha = (0.229 \pm 0.153_{stat} \pm 0.269_{sys} \pm 0.02_{theor})\,\mathrm{GeV}^{-2}} \tag{7.2}$$

This value is, like the relative branching ratio in Eq. 7.1, consistent with the HLS-model, but does not exclude the α-value obtained according to Ref. [1]. The α-parameter presented in Eq. 7.2 is, within the errors, also in agreement with $\alpha = 0$. This value corresponds to a description of dipion final state interactions based on the pion vector form factor, which does (unlike the models in Ref. [1,2]) not depend on the underlying decay.
Previous measurements of α performed by the KLOE- [6] and WASA-at-COSY collaboration [7] are in agreement for $\alpha \gtrsim 1\,\mathrm{GeV}^{-2}$ and therefore do not support any theoretical model presented in Ref. [1, 2, 3]. Those measured results are not confirmed within 1.7σ and 1.3σ by the current result.
Eq. 7.2 was additionally cross checked by determining the two pion invariant mass squared distribution $s_{\pi\pi}$ (see Section 6.7.2.3), which is directly connected to the dipion final state interactions. The corresponding α-value is, within the statistical error, in excellent agreement with Eq. 7.2.
The results found within this work show clearly, that a description of the decay $\eta \to \pi^+\pi^-\gamma$ by the box anomaly term without including dipion final state interactions is not possible. Furthermore, they are consistent with respect to each other in the sense that both results support the same theoretical models.
Detailed systematic studies showed that the largest contribution to the systematical error of the relative branching ratio and α is related to the rejection of low energy photons in the calorimeter. Systematic effects related to the selection of a minimum kinematic fit probability were reduced by a factor ~ 4 by implementing a polar angle dependent energy resolution of each layer within the Forward Range Hodoscope (FRH) of WASA.
Future plans for the analysis of $\eta \to \pi^+\pi^-\gamma$ deal with the analysis of the remaining 2010, 2012 and 2008 $pp\eta$ data sets which allows for a more detailed investigation of

systematic effects. This will decrease the statistical error, but also might increase the systematic uncertainty. The rejection condition of low energy photons as well as the investigation of the angular dependence of the FRH resolution will be a major part of ongoing systematic studies. All these aspects aim for an optimisation of the analysis of $\eta \to \pi^+\pi^-\gamma$ and a validation or refinement of the current results for the relative branching ratio and α. The outcome of this procedure will (hopefully) be a closer insight into the dynamics of the anomalous decay $\eta \to \pi^+\pi^-\gamma$.

Appendix A

Preselection statistics

The file size of each data run (numbered from 16304 to 22015) within the 2010 $pp\eta$ data set is presented in Fig. A.1. The black crosses refer to the initial file size without applying any preselection condition. The file size per run obtained after requesting the conditions discussed in Section 4.4.2 and after file compression are indicated by red crosses respectively. The run numbers from 18181 to 18756 are missing, because they correspond to the $pp \to pp\pi^0$ calorimeter calibration runs. The average file size per run is $\sim 21\,\text{GB}$ before and $\sim 1.9\,\text{GB}$ after the preselection.

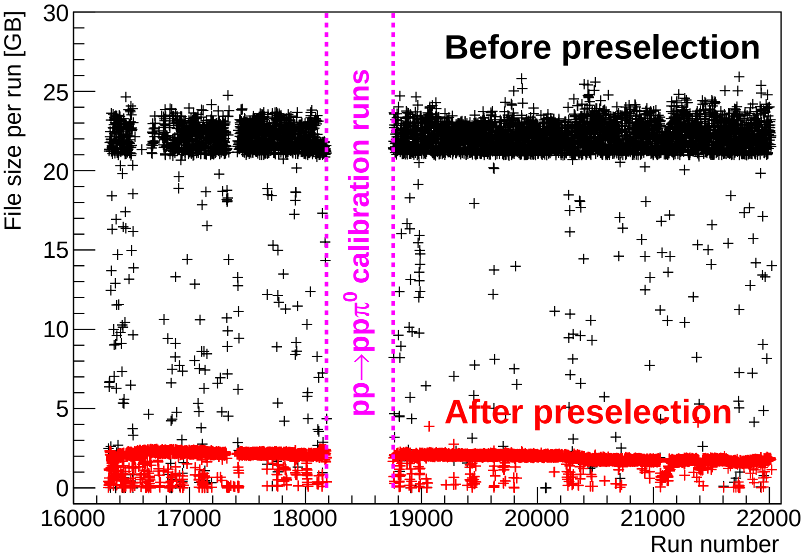

Figure A.1: *File size per run as a function of the individual run number of the 2010 $pp\eta$ data set. Black (red) crosses represent the file size per run before (after) preselection.*

Appendix B

Adjusting the simulated FRH / SE energy resolution

The simulated energy resolutions were matched with respect to measured data, as discussed in Chapter 4. Table B.1 summarises the two parameters (a and b), that have been used in Eq. 4.6 for performing a ring wise calibration of the simulated photon energy. The global correction factor in Eq. 4.6 is given by: $f_{glob} = 1.037$. The

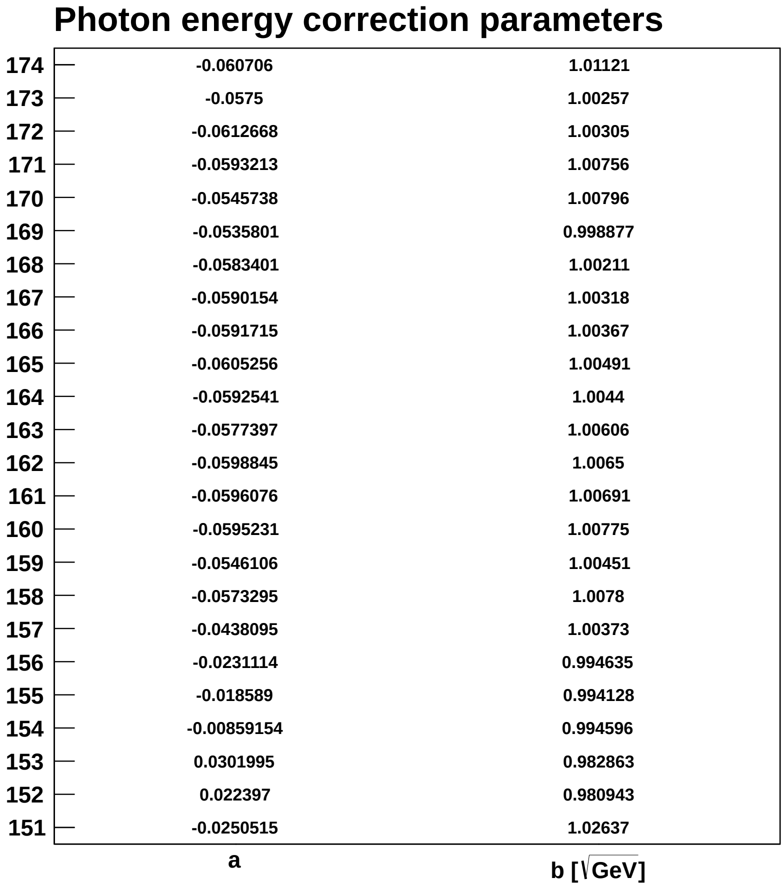

Photon energy correction parameters

	a	b [$\sqrt{\text{GeV}}$]
174	-0.060706	1.01121
173	-0.0575	1.00257
172	-0.0612668	1.00305
171	-0.0593213	1.00756
170	-0.0545738	1.00796
169	-0.0535801	0.998877
168	-0.0583401	1.00211
167	-0.0590154	1.00318
166	-0.0591715	1.00367
165	-0.0605256	1.00491
164	-0.0592541	1.0044
163	-0.0577397	1.00606
162	-0.0598845	1.0065
161	-0.0596076	1.00691
160	-0.0595231	1.00775
159	-0.0546106	1.00451
158	-0.0573295	1.0078
157	-0.0438095	1.00373
156	-0.0231114	0.994635
155	-0.018589	0.994128
154	-0.00859154	0.994596
153	0.0301995	0.982863
152	0.022397	0.980943
151	-0.0250515	1.02637

Table B.1: *Parameter $a(i)$ and $b(i)$ of Eq. 4.6 as a function of the ring number i within the calorimeter.*

resolution of each layer within the Forward Range Hodoscope (FRH) was made angle dependent for the simulated data, according to the description in Section 4.5.2. The difference between the measured and simulated resolution is presented in Table B.2. The simulated resolutions $\bar{\sigma}^2_{MC}$ were obtained for a relative Gaussian smearing of 0.015 (see also Section 4.5.2). Finally, $\Delta\sigma(\mathrm{FRH}i,\theta)$ is used for smearing the simulated FRH resolution again, according to step 5 in Section 4.5.2.

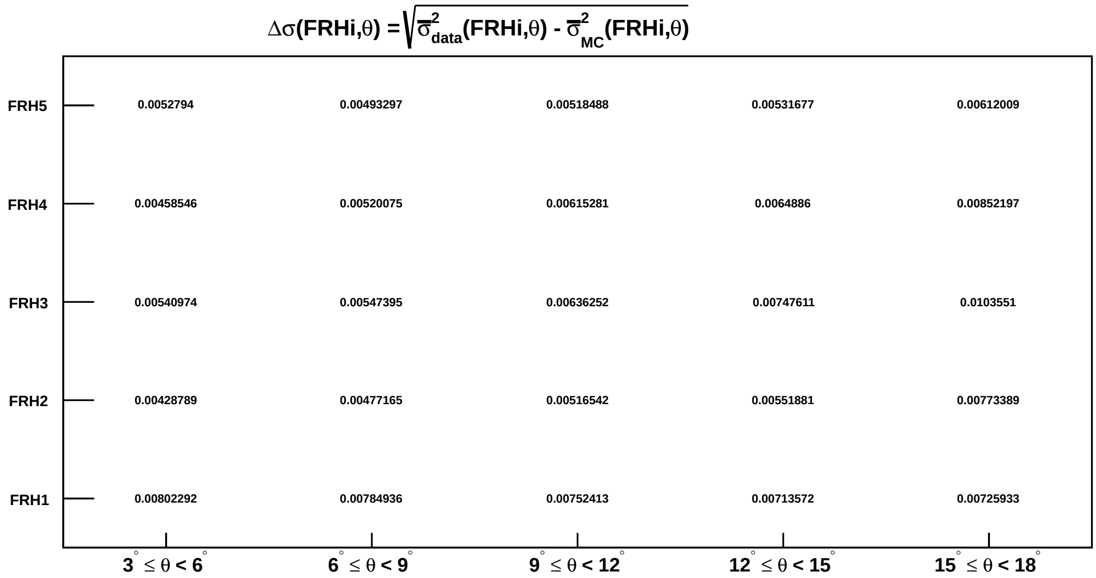

$$\Delta\sigma(\mathrm{FRHi},\theta) = \sqrt{\bar{\sigma}^2_{data}(\mathrm{FRHi},\theta) - \bar{\sigma}^2_{MC}(\mathrm{FRHi},\theta)}$$

	$3^\circ \leq \theta < 6^\circ$	$6^\circ \leq \theta < 9^\circ$	$9^\circ \leq \theta < 12^\circ$	$12^\circ \leq \theta < 15^\circ$	$15^\circ \leq \theta < 18^\circ$
FRH5	0.0052794	0.00493297	0.00518488	0.00531677	0.00612009
FRH4	0.00458546	0.00520075	0.00615281	0.0064886	0.00852197
FRH3	0.00540974	0.00547395	0.00636252	0.00747611	0.0103551
FRH2	0.00428789	0.00477165	0.00516542	0.00551881	0.00773389
FRH1	0.00802292	0.00784936	0.00752413	0.00713572	0.00725933

Table B.2: *Difference $\Delta\sigma(FRHi,\theta)$ between measured and simulated resolution as function of different FRH layers and θ ranges.*

Appendix C

Error parameterisation

The values of the error of each reconstructed particle variable are listed below. They correspond to the spectra shown in Section 5.4.3.

C.1 Errors of reconstructed proton variables

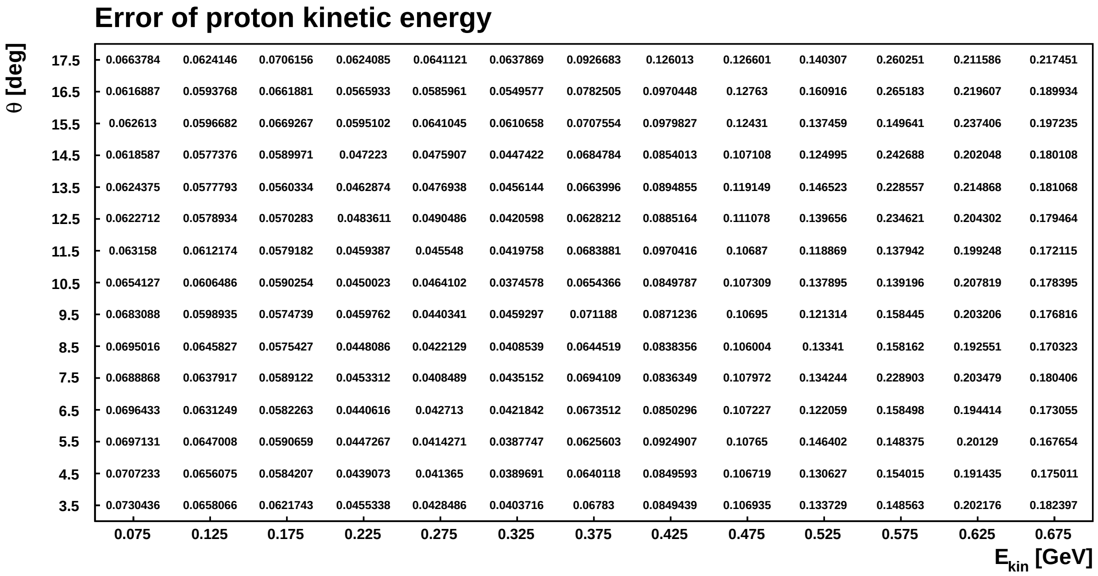

Error of proton kinetic energy

θ [deg] \ E_{kin} [GeV]	0.075	0.125	0.175	0.225	0.275	0.325	0.375	0.425	0.475	0.525	0.575	0.625	0.675
17.5	0.0663784	0.0624146	0.0706156	0.0624085	0.0641121	0.0637869	0.0926683	0.126013	0.126601	0.140307	0.260251	0.211586	0.217451
16.5	0.0616887	0.0593768	0.0661881	0.0565933	0.0585961	0.0549577	0.0782505	0.0970448	0.12763	0.160916	0.265183	0.219607	0.189934
15.5	0.062613	0.0596682	0.0669267	0.0595102	0.0641045	0.0610658	0.0707554	0.0979827	0.12431	0.137459	0.149641	0.237406	0.197235
14.5	0.0618587	0.0577376	0.0589971	0.047223	0.0475907	0.0447422	0.0684784	0.0854013	0.107108	0.124995	0.242688	0.202048	0.180108
13.5	0.0624375	0.0577793	0.0560334	0.0462874	0.0476938	0.0456144	0.0663996	0.0894855	0.119149	0.146523	0.228557	0.214868	0.181068
12.5	0.0622712	0.0578934	0.0570283	0.0483611	0.0490486	0.0420598	0.0628212	0.0885164	0.111078	0.139656	0.234621	0.204302	0.179464
11.5	0.063158	0.0612174	0.0579182	0.0459387	0.045548	0.0419758	0.0683881	0.0970416	0.10687	0.118869	0.137942	0.199248	0.172115
10.5	0.0654127	0.0606486	0.0590254	0.0450023	0.0464102	0.0374578	0.0654366	0.0849787	0.107309	0.137895	0.139196	0.207819	0.178395
9.5	0.0683088	0.0598935	0.0574739	0.0459762	0.0440341	0.0459297	0.071188	0.0871236	0.10695	0.121314	0.158445	0.203206	0.176816
8.5	0.0695016	0.0645827	0.0575427	0.0448086	0.0422129	0.0408539	0.0644519	0.0838356	0.106004	0.13341	0.158162	0.192551	0.170323
7.5	0.0688868	0.0637917	0.0589122	0.0453312	0.0408489	0.0435152	0.0694109	0.0836349	0.107972	0.134244	0.228903	0.203479	0.180406
6.5	0.0696433	0.0631249	0.0582263	0.0440616	0.042713	0.0421842	0.0673512	0.0850296	0.107227	0.122059	0.158498	0.194414	0.173055
5.5	0.0697131	0.0647008	0.0590659	0.0447267	0.0414271	0.0387747	0.0625603	0.0924907	0.10765	0.146402	0.148375	0.20129	0.167654
4.5	0.0707233	0.0656075	0.0584207	0.0439073	0.041365	0.0389691	0.0640118	0.0849593	0.106719	0.130627	0.154015	0.191435	0.175011
3.5	0.0730436	0.0658066	0.0621743	0.0455338	0.0428486	0.0403716	0.06783	0.0849439	0.106935	0.133729	0.148563	0.202176	0.182397

Error of proton θ angle [deg]

θ [deg]	0.075	0.125	0.175	0.225	0.275	0.325	0.375	0.425	0.475	0.525	0.575	0.625	0.675
17.5	0.200061	0.140297	0.121886	0.120304	0.0879475	0.0841204	0.0839543	0.0783732	0.0750832	0.0926802	0.100166	0.0982176	0.084273
16.5	0.207656	0.160784	0.133744	0.129727	0.109968	0.105629	0.102293	0.0964078	0.0976307	0.0983616	0.093533	0.0907012	0.10084
15.5	0.220779	0.165811	0.138488	0.123859	0.121937	0.115027	0.109263	0.112074	0.103902	0.101052	0.105587	0.0979729	0.0964772
14.5	0.224185	0.175286	0.137903	0.126478	0.121855	0.122136	0.114353	0.112223	0.115786	0.112581	0.108564	0.0994561	0.106065
13.5	0.221849	0.173758	0.147932	0.13153	0.125563	0.125081	0.119267	0.117581	0.111317	0.116085	0.118375	0.109138	0.102476
12.5	0.22733	0.178404	0.141103	0.131353	0.131095	0.125251	0.120405	0.117551	0.113466	0.107635	0.117988	0.108277	0.107889
11.5	0.231991	0.183356	0.144439	0.137275	0.130828	0.122768	0.123901	0.115348	0.116427	0.10908	0.113206	0.111814	0.118366
10.5	0.236785	0.182684	0.142429	0.137482	0.123831	0.128936	0.123359	0.121091	0.119441	0.115896	0.114378	0.113329	0.109548
9.5	0.238567	0.173887	0.143062	0.138442	0.129896	0.127485	0.124904	0.118459	0.114876	0.116443	0.11295	0.111553	0.107265
8.5	0.229645	0.17376	0.143972	0.141388	0.132538	0.128903	0.11967	0.121464	0.113876	0.117211	0.111218	0.111651	0.10396
7.5	0.242139	0.182888	0.146155	0.139033	0.133756	0.124975	0.124309	0.118523	0.11629	0.119818	0.10871	0.117816	0.102718
6.5	0.235936	0.187384	0.147672	0.134493	0.137242	0.124904	0.125042	0.121456	0.115505	0.121187	0.114406	0.113983	0.114031
5.5	0.240615	0.184734	0.143771	0.141772	0.13118	0.128016	0.125084	0.119118	0.123373	0.119849	0.115431	0.109515	0.111506
4.5	0.24362	0.181496	0.151989	0.137645	0.133753	0.129217	0.127302	0.119951	0.120132	0.119202	0.115376	0.11897	0.108951
3.5	0.235218	0.182925	0.148281	0.142396	0.143025	0.133706	0.12446	0.12313	0.121249	0.123618	0.120827	0.113889	0.115888

E_{kin} [GeV]

Error of proton ϕ angle [deg]

θ [deg]	0.075	0.125	0.175	0.225	0.275	0.325	0.375	0.425	0.475	0.525	0.575	0.625	0.675
17.5	0.831299	0.66241	0.668327	0.632417	0.625318	0.603844	0.605693	0.540146	0.513113	0.509962	0.497614	0.461717	0.463501
16.5	0.880859	0.695165	0.718615	0.660462	0.645619	0.641797	0.573358	0.540249	0.538715	0.51374	0.495925	0.490669	0.466864
15.5	0.947303	0.76916	0.791981	0.718815	0.70869	0.688595	0.602812	0.582066	0.57676	0.539577	0.505975	0.486858	0.524296
14.5	1.02668	0.831742	0.86612	0.801558	0.758204	0.715892	0.627117	0.595524	0.569399	0.563118	0.543887	0.514489	0.531965
13.5	1.10875	0.853788	0.894454	0.820172	0.781827	0.747804	0.656493	0.634903	0.606856	0.591085	0.603382	0.545203	0.572633
12.5	1.22387	0.951841	1.01249	0.918024	0.84759	0.767512	0.721992	0.664165	0.651044	0.644343	0.619903	0.612314	0.577823
11.5	1.25444	1.03903	1.09509	0.968129	0.900782	0.809188	0.765787	0.687002	0.700717	0.676882	0.680938	0.637527	0.655005
10.5	1.43189	1.15693	1.34937	1.09927	0.963887	0.848259	0.819904	0.749907	0.7349	0.710009	0.748313	0.70759	0.688839
9.5	1.61743	1.52588	1.52281	1.15971	1.00627	0.914355	0.848315	0.825077	0.841103	0.819023	0.793276	0.747743	0.797603
8.5	1.80876	1.6228	1.55116	1.26334	1.09738	0.993151	0.922518	0.913459	0.898073	0.85909	0.817309	0.855215	0.84491
7.5	2.04502	1.63228	1.6769	1.34515	1.17581	1.08316	1.04666	1.03595	0.968906	0.937302	0.992588	0.987195	0.940182
6.5	2.38423	1.85604	1.81282	1.4717	1.31037	1.26682	1.15469	1.12613	1.13303	1.13138	1.0708	1.06437	1.11418
5.5	2.70715	2.12979	1.96647	1.71075	1.52861	1.40957	1.38021	1.30799	1.28414	1.23111	1.27466	1.29486	1.20877
4.5	3.36131	2.58715	2.2422	2.05189	1.82626	1.75949	1.61343	1.58777	1.52645	1.62034	1.46967	1.53277	1.50533
3.5	4.46498	3.1607	2.70557	2.46302	2.26438	2.11532	2.08421	2.08049	2.07534	1.89867	1.94296	1.88511	1.92948

E_{kin} [GeV]

C.2 Errors of reconstructed pion variables

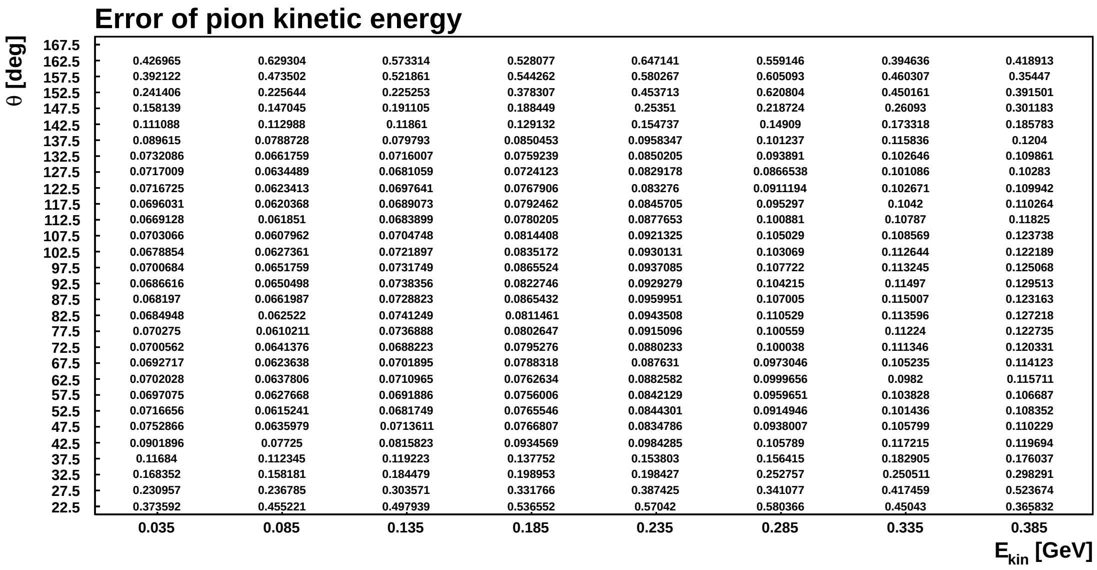

Error of pion kinetic energy

	0.035	0.085	0.135	0.185	0.235	0.285	0.335	0.385
167.5								
162.5	0.426965	0.629304	0.573314	0.528077	0.647141	0.559146	0.394636	0.418913
157.5	0.392122	0.473502	0.521861	0.544262	0.580267	0.605093	0.460307	0.35447
152.5	0.241406	0.225644	0.225253	0.378307	0.453713	0.620804	0.450161	0.391501
147.5	0.158139	0.147045	0.191105	0.188449	0.25351	0.218724	0.26093	0.301183
142.5	0.111088	0.112988	0.11861	0.129132	0.154737	0.14909	0.173318	0.185783
137.5	0.089615	0.0788728	0.079793	0.0850453	0.0958347	0.101237	0.115836	0.1204
132.5	0.0732086	0.0661759	0.0716007	0.0759239	0.0850205	0.093891	0.102646	0.109861
127.5	0.0717009	0.0634489	0.0681059	0.0724123	0.0829178	0.0866538	0.101086	0.10283
122.5	0.0716725	0.0623413	0.0697641	0.0767906	0.083276	0.0911194	0.102671	0.109942
117.5	0.0696031	0.0620368	0.0689073	0.0792462	0.0845705	0.095297	0.1042	0.110264
112.5	0.0669128	0.061851	0.0683899	0.0780205	0.0877653	0.100881	0.10787	0.11825
107.5	0.0703066	0.0607962	0.0704748	0.0814408	0.0921325	0.105029	0.108569	0.123738
102.5	0.0678854	0.0627361	0.0721897	0.0835172	0.0930131	0.103069	0.112644	0.122189
97.5	0.0700684	0.0651759	0.0731749	0.0865524	0.0937085	0.107722	0.113245	0.125068
92.5	0.0686616	0.0650498	0.0738356	0.0822746	0.0929279	0.104215	0.11497	0.129513
87.5	0.068197	0.0661987	0.0728823	0.0865432	0.0959951	0.107005	0.115007	0.123163
82.5	0.0684948	0.062522	0.0741249	0.0811461	0.0943508	0.110529	0.113596	0.127218
77.5	0.070275	0.0610211	0.0736888	0.0802647	0.0915096	0.100559	0.11224	0.122735
72.5	0.0700562	0.0641376	0.0688223	0.0795276	0.0880233	0.100038	0.111346	0.120331
67.5	0.0692717	0.0623638	0.0701895	0.0788318	0.087631	0.0973046	0.105235	0.114123
62.5	0.0702028	0.0637806	0.0710965	0.0762634	0.0882582	0.0999656	0.0982	0.115711
57.5	0.0697075	0.0627668	0.0691886	0.0756006	0.0842129	0.0959651	0.103828	0.106687
52.5	0.0716656	0.0615241	0.0681749	0.0765546	0.0844301	0.0914946	0.101436	0.108352
47.5	0.0752866	0.0635979	0.0713611	0.0766807	0.0834786	0.0938007	0.105799	0.110229
42.5	0.0901896	0.07725	0.0815823	0.0934569	0.0984285	0.105789	0.117215	0.119694
37.5	0.11684	0.112345	0.119223	0.137752	0.153803	0.156415	0.182905	0.176037
32.5	0.168352	0.158181	0.184479	0.198953	0.198427	0.252757	0.250511	0.298291
27.5	0.230957	0.236785	0.303571	0.331766	0.387425	0.341077	0.417459	0.523674
22.5	0.373592	0.455221	0.497939	0.536552	0.57042	0.580366	0.45043	0.365832

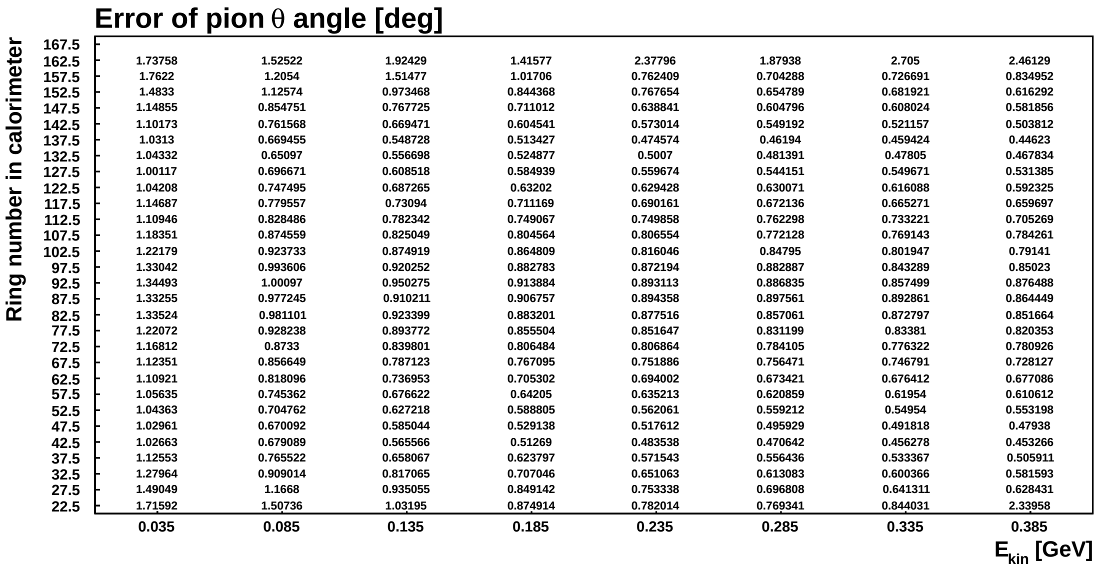

Error of pion θ angle [deg]

	0.035	0.085	0.135	0.185	0.235	0.285	0.335	0.385
167.5								
162.5	1.73758	1.52522	1.92429	1.41577	2.37796	1.87938	2.705	2.46129
157.5	1.7622	1.2054	1.51477	1.01706	0.762409	0.704288	0.726691	0.834952
152.5	1.4833	1.12574	0.973468	0.844368	0.767654	0.654789	0.681921	0.616292
147.5	1.14855	0.854751	0.767725	0.711012	0.638841	0.604796	0.608024	0.581856
142.5	1.10173	0.761568	0.669471	0.604541	0.573014	0.549192	0.521157	0.503812
137.5	1.0313	0.669455	0.548728	0.513427	0.474574	0.46194	0.459424	0.44623
132.5	1.04332	0.65097	0.556698	0.524877	0.5007	0.481391	0.47805	0.467834
127.5	1.00117	0.696671	0.608518	0.584939	0.559674	0.544151	0.549671	0.531385
122.5	1.04208	0.747495	0.687265	0.63202	0.629428	0.630071	0.616088	0.592325
117.5	1.14687	0.779557	0.73094	0.711169	0.690161	0.672136	0.665271	0.659697
112.5	1.10946	0.828486	0.782342	0.749067	0.749858	0.762298	0.733221	0.705269
107.5	1.18351	0.874559	0.825049	0.804564	0.806554	0.772128	0.769143	0.784261
102.5	1.22179	0.923733	0.874919	0.864809	0.816046	0.84795	0.801947	0.79141
97.5	1.33042	0.993606	0.920252	0.882783	0.872194	0.882887	0.843289	0.85023
92.5	1.34493	1.00097	0.950275	0.913884	0.893113	0.886835	0.857499	0.876488
87.5	1.33255	0.977245	0.910211	0.906757	0.894358	0.897561	0.892861	0.864449
82.5	1.33524	0.981101	0.923399	0.883201	0.877516	0.857061	0.872797	0.851664
77.5	1.22072	0.928238	0.893772	0.855504	0.851647	0.831199	0.83381	0.820353
72.5	1.16812	0.8733	0.839801	0.806484	0.806864	0.784105	0.776322	0.780926
67.5	1.12351	0.856649	0.787123	0.767095	0.751886	0.756471	0.746791	0.728127
62.5	1.10921	0.818096	0.736953	0.705302	0.694002	0.673421	0.676412	0.677086
57.5	1.05635	0.745362	0.676622	0.64205	0.635213	0.620859	0.61954	0.610612
52.5	1.04363	0.704762	0.627218	0.588805	0.562061	0.559212	0.54954	0.553198
47.5	1.02961	0.670092	0.585044	0.529138	0.517612	0.495929	0.491818	0.47938
42.5	1.02663	0.679089	0.565566	0.51269	0.483538	0.470642	0.456278	0.453266
37.5	1.12553	0.765522	0.658067	0.623797	0.571543	0.556436	0.533367	0.505911
32.5	1.27964	0.909014	0.817065	0.707046	0.651063	0.613083	0.600366	0.581593
27.5	1.49049	1.1668	0.935055	0.849142	0.753338	0.696808	0.641311	0.628431
22.5	1.71592	1.50736	1.03195	0.874914	0.782014	0.769341	0.844031	2.33958

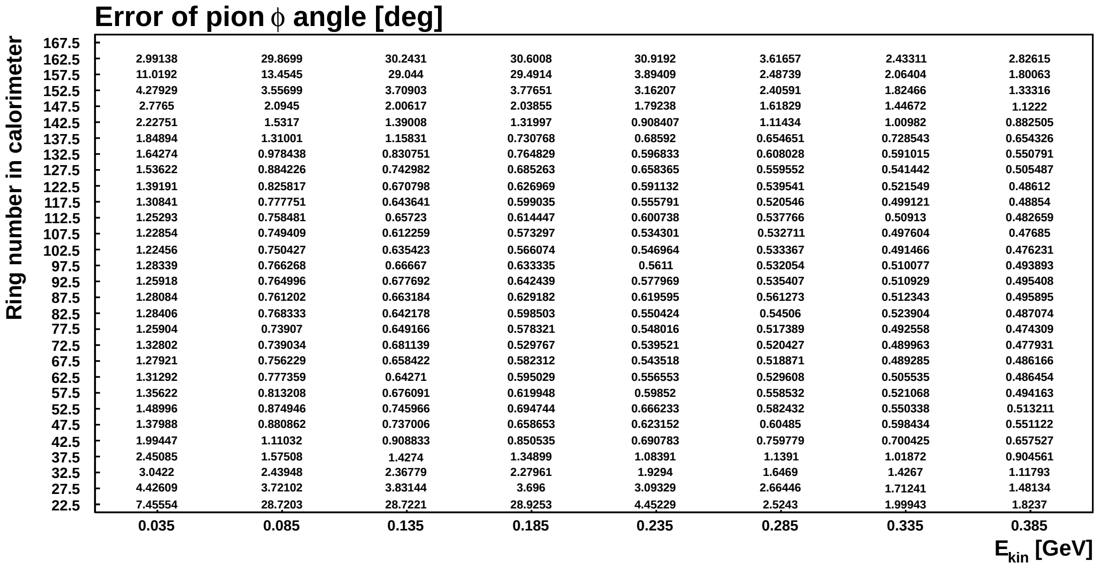

Error of pion ϕ angle [deg]

Ring number in calorimeter	0.035	0.085	0.135	0.185	0.235	0.285	0.335	0.385
167.5								
162.5	2.99138	29.8699	30.2431	30.6008	30.9192	3.61657	2.43311	2.82615
157.5	11.0192	13.4545	29.044	29.4914	3.89409	2.48739	2.06404	1.80063
152.5	4.27929	3.55699	3.70903	3.77651	3.16207	2.40591	1.82466	1.33316
147.5	2.7765	2.0945	2.00617	2.03855	1.79238	1.61829	1.44672	1.1222
142.5	2.22751	1.5317	1.39008	1.31997	0.908407	1.11434	1.00982	0.882505
137.5	1.84894	1.31001	1.15831	0.730768	0.68592	0.654651	0.728543	0.654326
132.5	1.64274	0.978438	0.830751	0.764829	0.596833	0.608028	0.591015	0.550791
127.5	1.53622	0.884226	0.742982	0.685263	0.658365	0.559552	0.541442	0.505487
122.5	1.39191	0.825817	0.670798	0.626969	0.591132	0.539541	0.521549	0.48612
117.5	1.30841	0.777751	0.643641	0.599035	0.555791	0.520546	0.499121	0.48854
112.5	1.25293	0.758481	0.65723	0.614447	0.600738	0.537766	0.50913	0.482659
107.5	1.22854	0.749409	0.612259	0.573297	0.534301	0.532711	0.497604	0.47685
102.5	1.22456	0.750427	0.635423	0.566074	0.546964	0.533367	0.491466	0.476231
97.5	1.28339	0.766268	0.66667	0.633335	0.5611	0.532054	0.510077	0.493893
92.5	1.25918	0.764996	0.677692	0.642439	0.577969	0.535407	0.510929	0.495408
87.5	1.28084	0.761202	0.663184	0.629182	0.619595	0.561273	0.512343	0.495895
82.5	1.28406	0.768333	0.642178	0.598503	0.550424	0.54506	0.523904	0.487074
77.5	1.25904	0.73907	0.649166	0.578321	0.548016	0.517389	0.492558	0.474309
72.5	1.32802	0.739034	0.681139	0.529767	0.539521	0.520427	0.489963	0.477931
67.5	1.27921	0.756229	0.658422	0.582312	0.543518	0.518871	0.489285	0.486166
62.5	1.31292	0.777359	0.64271	0.595029	0.556553	0.529608	0.505535	0.486454
57.5	1.35622	0.813208	0.676091	0.619948	0.59852	0.558532	0.521068	0.494163
52.5	1.48996	0.874946	0.745966	0.694744	0.666233	0.582432	0.550338	0.513211
47.5	1.37988	0.880862	0.737006	0.658653	0.623152	0.60485	0.598434	0.551122
42.5	1.99447	1.11032	0.908833	0.850535	0.690783	0.759779	0.700425	0.657527
37.5	2.45085	1.57508	1.4274	1.34899	1.08391	1.1391	1.01872	0.904561
32.5	3.0422	2.43948	2.36779	2.27961	1.9294	1.6469	1.4267	1.11793
27.5	4.42609	3.72102	3.83144	3.696	3.09329	2.66446	1.71241	1.48134
22.5	7.45554	28.7203	28.7221	28.9253	4.45229	2.5243	1.99943	1.8237

E_{kin} [GeV]

C.3 Errors of reconstructed photon variables

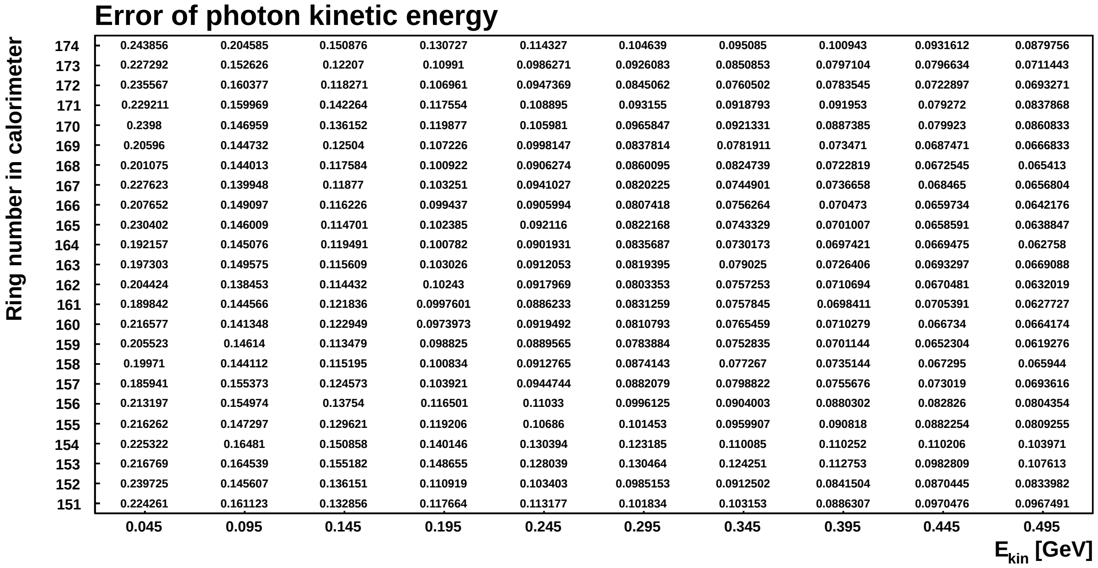

Error of photon kinetic energy

Ring number in calorimeter	0.045	0.095	0.145	0.195	0.245	0.295	0.345	0.395	0.445	0.495
174	0.243856	0.204585	0.150876	0.130727	0.114327	0.104639	0.095085	0.100943	0.0931612	0.0879756
173	0.227292	0.152626	0.12207	0.10991	0.0986271	0.0926083	0.0850853	0.0797104	0.0796634	0.0711443
172	0.235567	0.160377	0.118271	0.106961	0.0947369	0.0845062	0.0760502	0.0783545	0.0722897	0.0693271
171	0.229211	0.159969	0.142264	0.117554	0.108895	0.093155	0.0918793	0.091953	0.079272	0.0837868
170	0.2398	0.146959	0.136152	0.119877	0.105981	0.0965847	0.0921331	0.0887385	0.079923	0.0860833
169	0.20596	0.144732	0.12504	0.107226	0.0998147	0.0837814	0.0781911	0.073471	0.0687471	0.0666833
168	0.201075	0.144013	0.117584	0.100922	0.0906274	0.0860095	0.0824739	0.0722819	0.0672545	0.065413
167	0.227623	0.139948	0.11877	0.103251	0.0941027	0.0820225	0.0744901	0.0736658	0.068465	0.0656804
166	0.207652	0.149097	0.116226	0.099437	0.0905994	0.0807418	0.0756264	0.070473	0.0659734	0.0642176
165	0.230402	0.146009	0.114701	0.102385	0.092116	0.0822168	0.0743329	0.0701007	0.0658591	0.0638847
164	0.192157	0.145076	0.119491	0.100782	0.0901931	0.0835687	0.0730173	0.0697421	0.0669475	0.062758
163	0.197303	0.149575	0.115609	0.103026	0.0912053	0.0819395	0.079025	0.0726406	0.0693297	0.0669088
162	0.204424	0.138453	0.114432	0.10243	0.0917969	0.0803353	0.0757253	0.0710694	0.0670481	0.0632019
161	0.189842	0.144566	0.121836	0.0997601	0.0886233	0.0831259	0.0757845	0.0698411	0.0705391	0.0627727
160	0.216577	0.141348	0.122949	0.0973973	0.0919492	0.0810793	0.0765459	0.0710279	0.066734	0.0664174
159	0.205523	0.14614	0.113479	0.098825	0.0889565	0.0783884	0.0752835	0.0701144	0.0652304	0.0619276
158	0.19971	0.144112	0.115195	0.100834	0.0912765	0.0874143	0.077267	0.0735144	0.067295	0.065944
157	0.185941	0.155373	0.124573	0.103921	0.0944744	0.0882079	0.0798822	0.0755676	0.073019	0.0693616
156	0.213197	0.154974	0.13754	0.116501	0.11033	0.0996125	0.0904003	0.0880302	0.082826	0.0804354
155	0.216262	0.147297	0.129621	0.119206	0.10686	0.101453	0.0959907	0.090818	0.0882254	0.0809255
154	0.225322	0.16481	0.150858	0.140146	0.130394	0.123185	0.110085	0.110252	0.110206	0.103971
153	0.216769	0.164539	0.155182	0.148655	0.128039	0.130464	0.124251	0.112753	0.0982809	0.107613
152	0.239725	0.145607	0.136151	0.110919	0.103403	0.0985153	0.0912502	0.0841504	0.0870445	0.0833982
151	0.224261	0.161123	0.132856	0.117664	0.113177	0.101834	0.103153	0.0886307	0.0970476	0.0967491

E_{kin} [GeV]

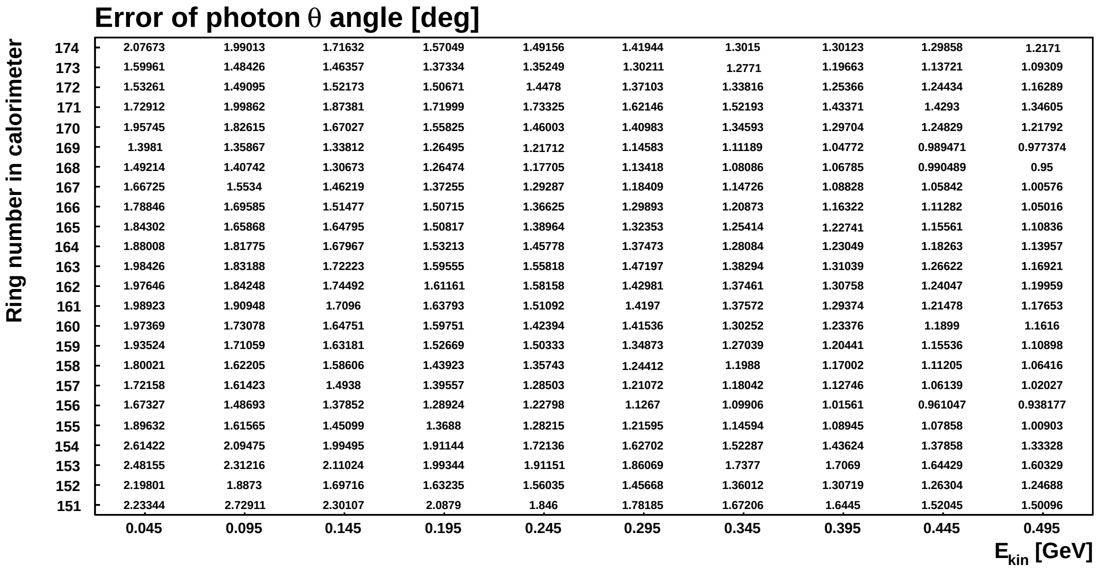

Error of photon θ angle [deg]

Ring number in calorimeter	0.045	0.095	0.145	0.195	0.245	0.295	0.345	0.395	0.445	0.495
174	2.07673	1.99013	1.71632	1.57049	1.49156	1.41944	1.3015	1.30123	1.29858	1.2171
173	1.59961	1.48426	1.46357	1.37334	1.35249	1.30211	1.2771	1.19663	1.13721	1.09309
172	1.53261	1.49095	1.52173	1.50671	1.4478	1.37103	1.33816	1.25366	1.24434	1.16289
171	1.72912	1.99862	1.87381	1.71999	1.73325	1.62146	1.52193	1.43371	1.4293	1.34605
170	1.95745	1.82615	1.67027	1.55825	1.46003	1.40983	1.34593	1.29704	1.24829	1.21792
169	1.3981	1.35867	1.33812	1.26495	1.21712	1.14583	1.11189	1.04772	0.989471	0.977374
168	1.49214	1.40742	1.30673	1.26474	1.17705	1.13418	1.08086	1.06785	0.990489	0.95
167	1.66725	1.5534	1.46219	1.37255	1.29287	1.18409	1.14726	1.08828	1.05842	1.00576
166	1.78846	1.69585	1.51477	1.50715	1.36625	1.29893	1.20873	1.16322	1.11282	1.05016
165	1.84302	1.65868	1.64795	1.50817	1.38964	1.32353	1.25414	1.22741	1.15561	1.10836
164	1.88008	1.81775	1.67967	1.53213	1.45778	1.37473	1.28084	1.23049	1.18263	1.13957
163	1.98426	1.83188	1.72223	1.59555	1.55818	1.47197	1.38294	1.31039	1.26622	1.16921
162	1.97646	1.84248	1.74492	1.61161	1.58158	1.42981	1.37461	1.30758	1.24047	1.19959
161	1.98923	1.90948	1.7096	1.63793	1.51092	1.4197	1.37572	1.29374	1.21478	1.17653
160	1.97369	1.73078	1.64751	1.59751	1.42394	1.41536	1.30252	1.23376	1.1899	1.1616
159	1.93524	1.71059	1.63181	1.52669	1.50333	1.34873	1.27039	1.20441	1.15536	1.10898
158	1.80021	1.62205	1.58606	1.43923	1.35743	1.24412	1.1988	1.17002	1.11205	1.06416
157	1.72158	1.61423	1.4938	1.39557	1.28503	1.21072	1.18042	1.12746	1.06139	1.02027
156	1.67327	1.48693	1.37852	1.28924	1.22798	1.1267	1.09906	1.01561	0.961047	0.938177
155	1.89632	1.61565	1.45099	1.3688	1.28215	1.21595	1.14594	1.08945	1.07858	1.00903
154	2.61422	2.09475	1.99495	1.91144	1.72136	1.62702	1.52287	1.43624	1.37858	1.33328
153	2.48155	2.31216	2.11024	1.99344	1.91151	1.86069	1.7377	1.7069	1.64429	1.60329
152	2.19801	1.8873	1.69716	1.63235	1.56035	1.45668	1.36012	1.30719	1.26304	1.24688
151	2.23344	2.72911	2.30107	2.0879	1.846	1.78185	1.67206	1.6445	1.52045	1.50096

E_{kin} [GeV]

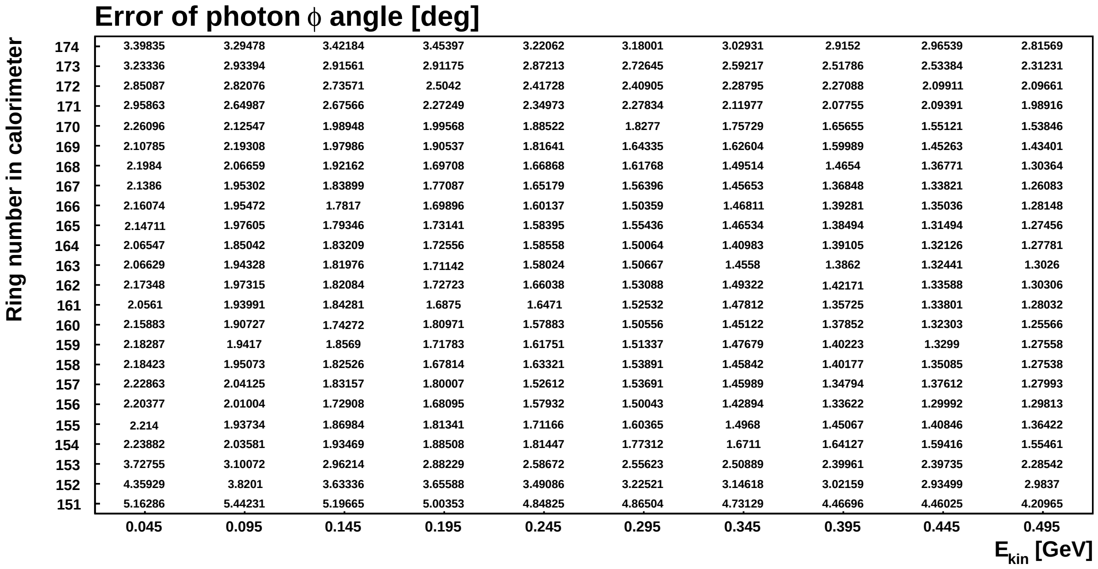

Error of photon ϕ angle [deg]

Ring number in calorimeter	0.045	0.095	0.145	0.195	0.245	0.295	0.345	0.395	0.445	0.495
174	3.39835	3.29478	3.42184	3.45397	3.22062	3.18001	3.02931	2.9152	2.96539	2.81569
173	3.23336	2.93394	2.91561	2.91175	2.87213	2.72645	2.59217	2.51786	2.53384	2.31231
172	2.85087	2.82076	2.73571	2.5042	2.41728	2.40905	2.28795	2.27088	2.09911	2.09661
171	2.95863	2.64987	2.67566	2.27249	2.34973	2.27834	2.11977	2.07755	2.09391	1.98916
170	2.26096	2.12547	1.98948	1.99568	1.88522	1.8277	1.75729	1.65655	1.55121	1.53846
169	2.10785	2.19308	1.97986	1.90537	1.81641	1.64335	1.62604	1.59989	1.45263	1.43401
168	2.1984	2.06659	1.92162	1.69708	1.66868	1.61768	1.49514	1.4654	1.36771	1.30364
167	2.1386	1.95302	1.83899	1.77087	1.65179	1.56396	1.45653	1.36848	1.33821	1.26083
166	2.16074	1.95472	1.7817	1.69896	1.60137	1.50359	1.46811	1.39281	1.35036	1.28148
165	2.14711	1.97605	1.79346	1.73141	1.58395	1.55436	1.46534	1.38494	1.31494	1.27456
164	2.06547	1.85042	1.83209	1.72556	1.58558	1.50064	1.40983	1.39105	1.32126	1.27781
163	2.06629	1.94328	1.81976	1.71142	1.58024	1.50667	1.4558	1.3862	1.32441	1.3026
162	2.17348	1.97315	1.82084	1.72723	1.66038	1.53088	1.49322	1.42171	1.33588	1.30306
161	2.0561	1.93991	1.84281	1.6875	1.6471	1.52532	1.47812	1.35725	1.33801	1.28032
160	2.15883	1.90727	1.74272	1.80971	1.57883	1.50556	1.45122	1.37852	1.32303	1.25566
159	2.18287	1.9417	1.8569	1.71783	1.61751	1.51337	1.47679	1.40223	1.3299	1.27558
158	2.18423	1.95073	1.82526	1.67814	1.63321	1.53891	1.45842	1.40177	1.35085	1.27538
157	2.22863	2.04125	1.83157	1.80007	1.52612	1.53691	1.45989	1.34794	1.37612	1.27993
156	2.20377	2.01004	1.72908	1.68095	1.57932	1.50043	1.42894	1.33622	1.29992	1.29813
155	2.214	1.93734	1.86984	1.81341	1.71166	1.60365	1.4968	1.45067	1.40846	1.36422
154	2.23882	2.03581	1.93469	1.88508	1.81447	1.77312	1.6711	1.64127	1.59416	1.55461
153	3.72755	3.10072	2.96214	2.88229	2.58672	2.55623	2.50889	2.39961	2.39735	2.28542
152	4.35929	3.8201	3.63336	3.65588	3.49086	3.22521	3.14618	3.02159	2.93499	2.9837
151	5.16286	5.44231	5.19665	5.00353	4.84825	4.86504	4.73129	4.46696	4.46025	4.20965

E_{kin} [GeV]

The offsets (with respect to the Gaussian distribution of true minus reconstructed particle variable) of all particle variables are presented in the following. The values correspond to the spectra discussed in Section 5.4.3

C.4 Offsets of reconstructed proton variables

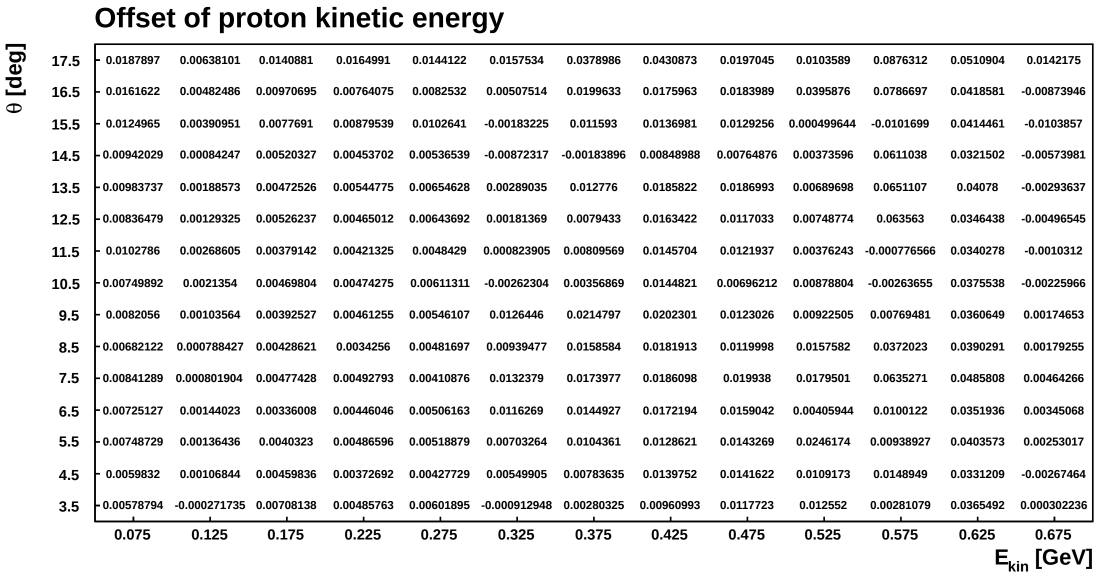

Offset of proton kinetic energy

θ [deg] \ E_{kin} [GeV]	0.075	0.125	0.175	0.225	0.275	0.325	0.375	0.425	0.475	0.525	0.575	0.625	0.675
17.5	0.0187897	0.00638101	0.0140881	0.0164991	0.0144122	0.0157534	0.0378986	0.0430873	0.0197045	0.0103589	0.0876312	0.0510904	0.0142175
16.5	0.0161622	0.00482486	0.00970695	0.00764075	0.0082532	0.00507514	0.0199633	0.0175963	0.0183989	0.0395876	0.0786697	0.0418581	-0.00873946
15.5	0.0124965	0.00390951	0.0077691	0.00879539	0.0102641	-0.00183225	0.011593	0.0136981	0.0129256	0.000499644	-0.0101699	0.0414461	-0.0103857
14.5	0.00942029	0.00084247	0.00520327	0.00453702	0.00536539	-0.00872317	-0.00183896	0.00848988	0.00764876	0.00373596	0.0611038	0.0321502	-0.00573981
13.5	0.00983737	0.00188573	0.00472526	0.00544775	0.00654628	0.00289035	0.012776	0.0185822	0.0186993	0.00689698	0.0651107	0.04078	-0.00293637
12.5	0.00836479	0.00129325	0.00526237	0.00465012	0.00643692	0.00181369	0.0079433	0.0163422	0.0117033	0.00748774	0.063563	0.0346438	-0.00496545
11.5	0.0102786	0.00268605	0.00379142	0.00421325	0.0048429	0.000823905	0.00809569	0.0145704	0.0121937	0.00376243	-0.000776566	0.0340278	-0.0010312
10.5	0.00749892	0.0021354	0.00469804	0.00474275	0.00611311	-0.00262304	0.00356869	0.0144821	0.00696212	0.00878804	-0.00263655	0.0375538	-0.00225966
9.5	0.0082056	0.00103564	0.00392527	0.00461255	0.00546107	0.0126446	0.0214797	0.0202301	0.0123026	0.00922505	0.00769481	0.0360649	0.00174653
8.5	0.00682122	0.000788427	0.00428621	0.0034256	0.00481697	0.00939477	0.0158584	0.0181913	0.0119998	0.0157582	0.0372023	0.0390291	0.00179255
7.5	0.00841289	0.000801904	0.00477428	0.00492793	0.00410876	0.0132379	0.0173977	0.0186098	0.019938	0.0179501	0.0635271	0.0485808	0.00464266
6.5	0.00725127	0.00144023	0.00336008	0.00446046	0.00506163	0.0116269	0.0144927	0.0172194	0.0159042	0.00405944	0.0100122	0.0351936	0.00345068
5.5	0.00748729	0.00136436	0.0040323	0.00486596	0.00518879	0.00703264	0.0104361	0.0128621	0.0143269	0.0246174	0.00938927	0.0403573	0.00253017
4.5	0.0059832	0.00106844	0.00459836	0.00372692	0.00427729	0.00549905	0.00783635	0.0139752	0.0141622	0.0109173	0.0148949	0.0331209	-0.00267464
3.5	0.00578794	-0.000271735	0.00708138	0.00485763	0.00601895	-0.000912948	0.00280325	0.00960993	0.0117723	0.012552	0.00281079	0.0365492	0.000302236

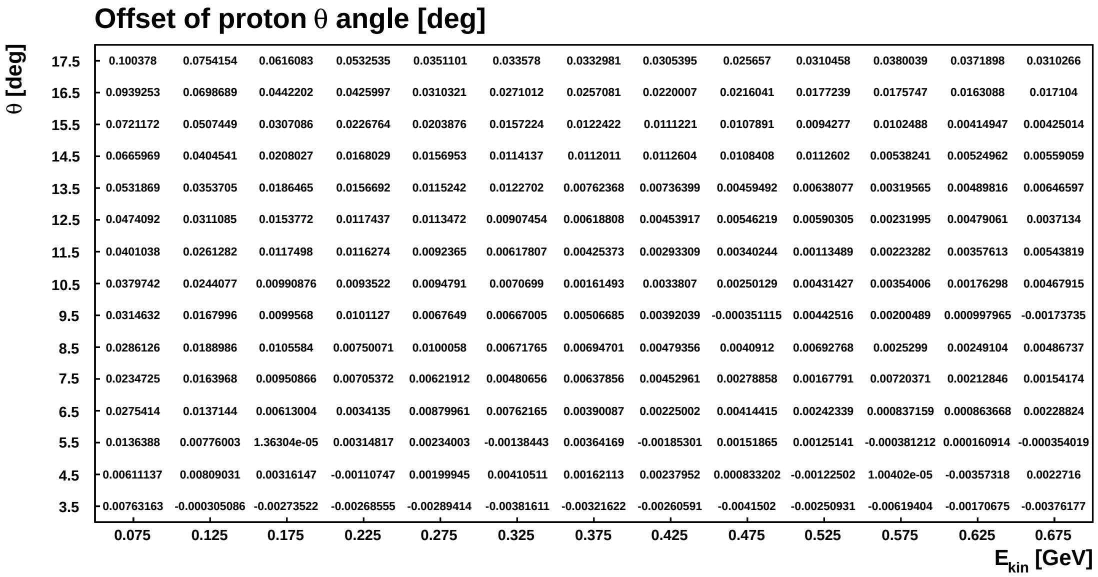

Offset of proton θ angle [deg]

θ [deg] \ E_{kin} [GeV]	0.075	0.125	0.175	0.225	0.275	0.325	0.375	0.425	0.475	0.525	0.575	0.625	0.675
17.5	0.100378	0.0754154	0.0616083	0.0532535	0.0351101	0.033578	0.0332981	0.0305395	0.025657	0.0310458	0.0380039	0.0371898	0.0310266
16.5	0.0939253	0.0698689	0.0442202	0.0425997	0.0310321	0.0271012	0.0257081	0.0220007	0.0216041	0.0177239	0.0175747	0.0163088	0.017104
15.5	0.0721172	0.0507449	0.0307086	0.0226764	0.0203876	0.0157224	0.0122422	0.0111221	0.0107891	0.0094277	0.0102488	0.00414947	0.00425014
14.5	0.0665969	0.0404541	0.0208027	0.0168029	0.0156953	0.0114137	0.0112011	0.0112604	0.0108408	0.0112602	0.00538241	0.00524962	0.00559059
13.5	0.0531869	0.0353705	0.0186465	0.0156692	0.0115242	0.0122702	0.00762368	0.00736399	0.00459492	0.00638077	0.00319565	0.00489816	0.00646597
12.5	0.0474092	0.0311085	0.0153772	0.0117437	0.0113472	0.00907454	0.00618808	0.00453917	0.00546219	0.00590305	0.00231995	0.00479061	0.0037134
11.5	0.0401038	0.0261282	0.0117498	0.0116274	0.0092365	0.00617807	0.00425373	0.00293309	0.00340244	0.00113489	0.00223282	0.00357613	0.00543819
10.5	0.0379742	0.0244077	0.00990876	0.0093522	0.0094791	0.0070699	0.00161493	0.0033807	0.00250129	0.00431427	0.00354006	0.00176298	0.00467915
9.5	0.0314632	0.0167996	0.0099568	0.0101127	0.0067649	0.00667005	0.00506685	0.00392039	-0.000351115	0.00442516	0.00200489	0.000997965	-0.00173735
8.5	0.0286126	0.0188986	0.0105584	0.00750071	0.0100058	0.00671765	0.00694701	0.00479356	0.0040912	0.00692768	0.0025299	0.00249104	0.00486737
7.5	0.0234725	0.0163968	0.00950866	0.00705372	0.00621912	0.00480656	0.00637856	0.00452961	0.00278858	0.00167791	0.00720371	0.00212846	0.00154174
6.5	0.0275414	0.0137144	0.00613004	0.0034135	0.00879961	0.00762165	0.00390087	0.00225002	0.00414415	0.00242339	0.000837159	0.000863668	0.00228824
5.5	0.0136388	0.00776003	1.36304e-05	0.00314817	0.00234003	-0.00138443	0.00364169	-0.00185301	0.00151865	0.00125141	-0.000381212	0.000160914	-0.000354019
4.5	0.00611137	0.00809031	0.00316147	-0.00110747	0.00199945	0.00410511	0.00162113	0.00237952	0.000833202	-0.00122502	1.00402e-05	-0.00357318	0.0022716
3.5	0.00763163	-0.000305086	-0.00273522	-0.00268555	-0.00289414	-0.00381611	-0.00321622	-0.00260591	-0.0041502	-0.00250931	-0.00619404	-0.00170675	-0.00376177

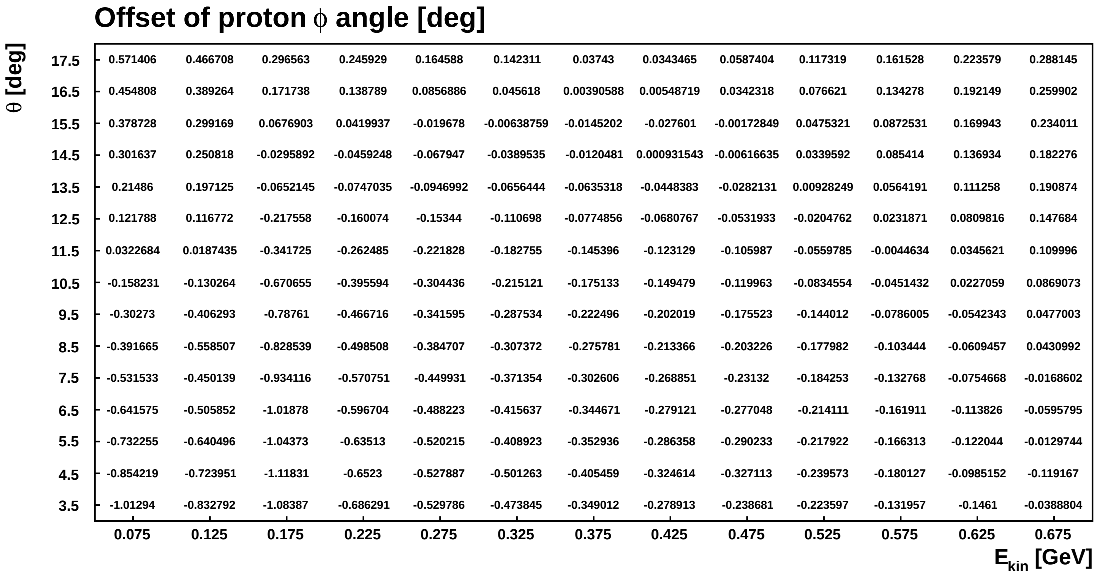

θ [deg]	0.075	0.125	0.175	0.225	0.275	0.325	0.375	0.425	0.475	0.525	0.575	0.625	0.675
17.5	0.571406	0.466708	0.296563	0.245929	0.164588	0.142311	0.03743	0.0343465	0.0587404	0.117319	0.161528	0.223579	0.288145
16.5	0.454808	0.389264	0.171738	0.138789	0.0856886	0.045618	0.00390588	0.00548719	0.0342318	0.076621	0.134278	0.192149	0.259902
15.5	0.378728	0.299169	0.0676903	0.0419937	-0.019678	-0.00638759	-0.0145202	-0.027601	-0.00172849	0.0475321	0.0872531	0.169943	0.234011
14.5	0.301637	0.250818	-0.0295892	-0.0459248	-0.067947	-0.0389535	-0.0120481	0.000931543	-0.00616635	0.0339592	0.085414	0.136934	0.182276
13.5	0.21486	0.197125	-0.0652145	-0.0747035	-0.0946992	-0.0656444	-0.0635318	-0.0448383	-0.0282131	0.00928249	0.0564191	0.111258	0.190874
12.5	0.121788	0.116772	-0.217558	-0.160074	-0.15344	-0.110698	-0.0774856	-0.0680767	-0.0531933	-0.0204762	0.0231871	0.0809816	0.147684
11.5	0.0322684	0.0187435	-0.341725	-0.262485	-0.221828	-0.182755	-0.145396	-0.123129	-0.105987	-0.0559785	-0.0044634	0.0345621	0.109996
10.5	-0.158231	-0.130264	-0.670655	-0.395594	-0.304436	-0.215121	-0.175133	-0.149479	-0.119963	-0.0834554	-0.0451432	0.0227059	0.0869073
9.5	-0.30273	-0.406293	-0.78761	-0.466716	-0.341595	-0.287534	-0.222496	-0.202019	-0.175523	-0.144012	-0.0786005	-0.0542343	0.0477003
8.5	-0.391665	-0.558507	-0.828539	-0.498508	-0.384707	-0.307372	-0.275781	-0.213366	-0.203226	-0.177982	-0.103444	-0.0609457	0.0430992
7.5	-0.531533	-0.450139	-0.934116	-0.570751	-0.449931	-0.371354	-0.302606	-0.268851	-0.23132	-0.184253	-0.132768	-0.0754668	-0.0168602
6.5	-0.641575	-0.505852	-1.01878	-0.596704	-0.488223	-0.415637	-0.344671	-0.279121	-0.277048	-0.214111	-0.161911	-0.113826	-0.0595795
5.5	-0.732255	-0.640496	-1.04373	-0.63513	-0.520215	-0.408923	-0.352936	-0.286358	-0.290233	-0.217922	-0.166313	-0.122044	-0.0129744
4.5	-0.854219	-0.723951	-1.11831	-0.6523	-0.527887	-0.501263	-0.405459	-0.324614	-0.327113	-0.239573	-0.180127	-0.0985152	-0.119167
3.5	-1.01294	-0.832792	-1.08387	-0.686291	-0.529786	-0.473845	-0.349012	-0.278913	-0.238681	-0.223597	-0.131957	-0.1461	-0.0388804

C.5 Offsets of reconstructed pion variables

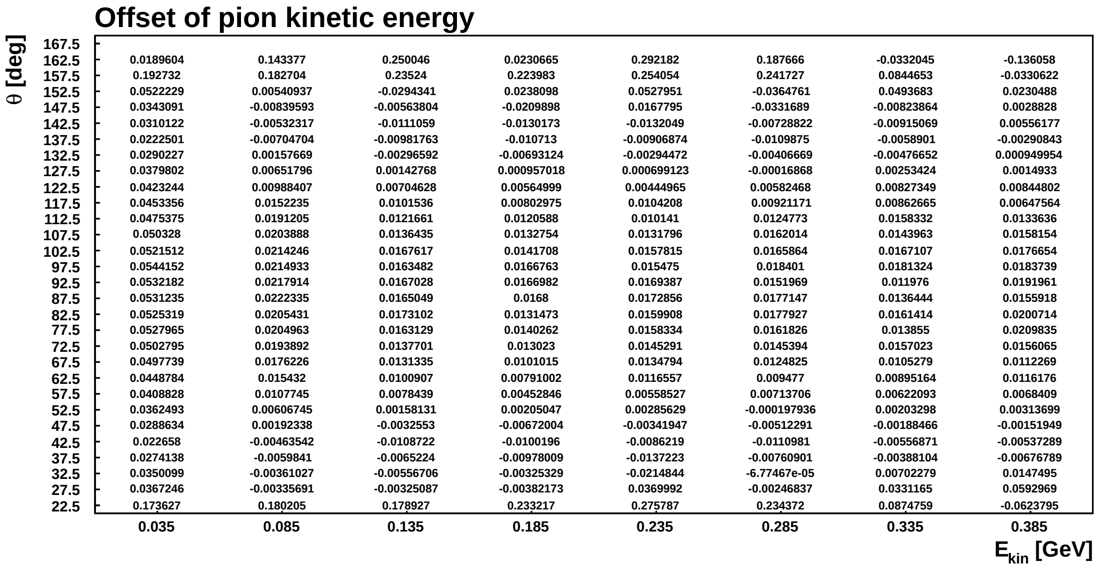

θ [deg]	0.035	0.085	0.135	0.185	0.235	0.285	0.335	0.385
167.5								
162.5	0.0189604	0.143377	0.250046	0.0230665	0.292182	0.187666	-0.0332045	-0.136058
157.5	0.192732	0.182704	0.23524	0.223983	0.254054	0.241727	0.0844653	-0.0330622
152.5	0.0522229	0.00540937	-0.0294341	0.0238098	0.0527951	-0.0364761	0.0493683	0.0230488
147.5	0.0343091	-0.00839593	-0.00563804	-0.0209898	0.0167795	-0.0331689	-0.00823864	0.0028828
142.5	0.0310122	-0.00532317	-0.0111059	-0.0130173	-0.0132049	-0.00728822	-0.00915069	0.00556177
137.5	0.0222501	-0.00704704	-0.00981763	-0.010713	-0.00906874	-0.0109875	-0.0058901	-0.00290843
132.5	0.0290227	0.00157669	-0.00296592	-0.00693124	-0.00294472	-0.00406669	-0.00476652	0.000949954
127.5	0.0379802	0.00651796	0.00142768	0.000957018	0.000699123	-0.00016868	0.00253424	0.0014933
122.5	0.0423244	0.00988407	0.00704628	0.00564999	0.00444965	0.00582468	0.00827349	0.00844802
117.5	0.0453356	0.0152235	0.0101536	0.00802975	0.0104208	0.00921171	0.00862665	0.00647564
112.5	0.0475375	0.0191205	0.0121661	0.0120588	0.010141	0.0124773	0.0158332	0.0133636
107.5	0.050328	0.0203888	0.0136435	0.0132754	0.0131796	0.0162014	0.0143963	0.0158154
102.5	0.0521512	0.0214246	0.0167617	0.0141708	0.0157815	0.0165864	0.0167107	0.0176654
97.5	0.0544152	0.0214933	0.0163482	0.0166763	0.015475	0.018401	0.0181324	0.0183739
92.5	0.0532182	0.0217914	0.0167028	0.0166982	0.0169387	0.0151969	0.011976	0.0191961
87.5	0.0531235	0.0222335	0.0165049	0.0168	0.0172856	0.0177147	0.0136444	0.0155918
82.5	0.0525319	0.0205431	0.0173102	0.0131473	0.0159908	0.0177927	0.0161414	0.0200714
77.5	0.0527965	0.0204963	0.0163129	0.0140262	0.0158334	0.0161826	0.013855	0.0209835
72.5	0.0502795	0.0193892	0.0137701	0.013023	0.0145291	0.0145394	0.0157023	0.0156065
67.5	0.0497739	0.0176226	0.0131335	0.0101015	0.0134794	0.0124825	0.0105279	0.0112269
62.5	0.0448784	0.015432	0.0100907	0.00791002	0.0116557	0.009477	0.00895164	0.0116176
57.5	0.0408828	0.0107745	0.0078439	0.00452846	0.00558527	0.00713706	0.00622093	0.0068409
52.5	0.0362493	0.00606745	0.00158131	0.00205047	0.00285629	-0.000197936	0.00203298	0.00313699
47.5	0.0288634	0.00192338	-0.0032553	-0.00672004	-0.00341947	-0.00512291	-0.00188466	-0.00151949
42.5	0.022658	-0.00463542	-0.0108722	-0.0100196	-0.0086219	-0.0110981	-0.00556871	-0.00537289
37.5	0.0274138	-0.0059841	-0.0065224	-0.00978009	-0.0137223	-0.00760901	-0.00388104	-0.00676789
32.5	0.0350099	-0.00361027	-0.00556706	-0.00325329	-0.0214844	-6.77467e-05	0.00702279	0.0147495
27.5	0.0367246	-0.00335691	-0.00325087	-0.00382173	0.0369992	-0.00246837	0.0331165	0.0592969
22.5	0.173627	0.180205	0.178927	0.233217	0.275787	0.234372	0.0874759	-0.0623795

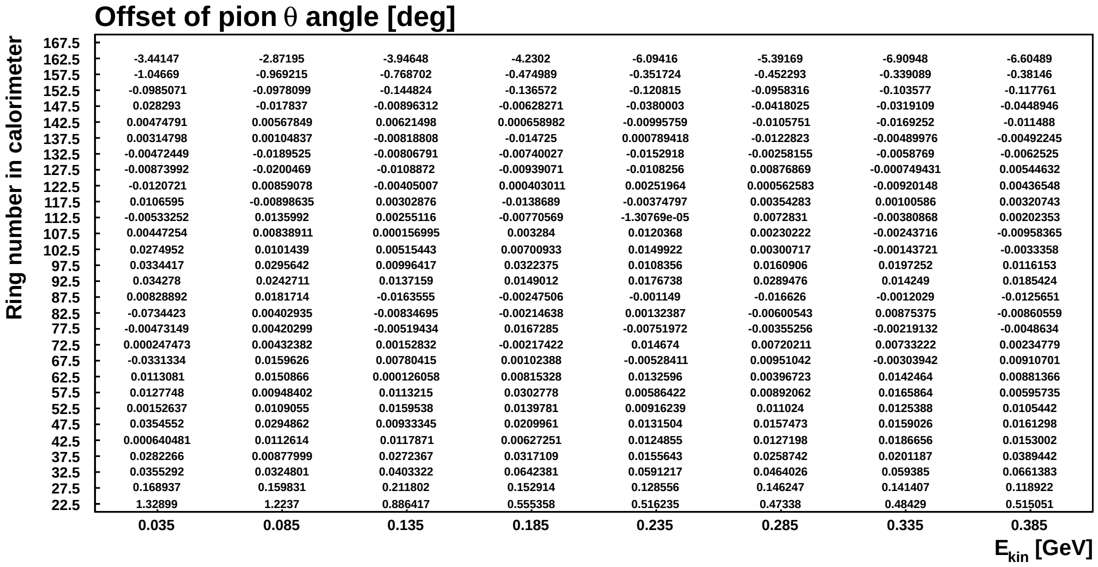

Offset of pion θ angle [deg]

Ring number in calorimeter	0.035	0.085	0.135	0.185	0.235	0.285	0.335	0.385
167.5								
162.5	-3.44147	-2.87195	-3.94648	-4.2302	-6.09416	-5.39169	-6.90948	-6.60489
157.5	-1.04669	-0.969215	-0.768702	-0.474989	-0.351724	-0.452293	-0.339089	-0.38146
152.5	-0.0985071	-0.0978099	-0.144824	-0.136572	-0.120815	-0.0958316	-0.103577	-0.117761
147.5	0.028293	-0.017837	-0.00896312	-0.00628271	-0.0380003	-0.0418025	-0.0319109	-0.0448946
142.5	0.00474791	0.00567849	0.00621498	0.000658982	-0.00995759	-0.0105751	-0.0169252	-0.011488
137.5	0.00314798	0.00104837	-0.00818808	-0.014725	0.000789418	-0.0122823	-0.00489976	-0.00492245
132.5	-0.00472449	-0.0189525	-0.00806791	-0.00740027	-0.0152918	-0.00258155	-0.0058769	-0.0062525
127.5	-0.00873992	-0.0200469	-0.0108872	-0.00939071	-0.0108256	0.00876869	-0.000749431	0.00544632
122.5	-0.0120721	0.00859078	-0.00405007	0.000403011	0.00251964	0.000562583	-0.00920148	0.00436548
117.5	0.0106595	-0.00898635	0.00302876	-0.0138689	-0.00374797	0.00354283	0.00100586	0.00320743
112.5	-0.00533252	0.0135992	0.00255116	-0.00770569	-1.30769e-05	0.0072831	-0.00380868	0.00202353
107.5	0.00447254	0.00838911	0.000156995	0.003284	0.0120368	0.00230222	-0.00243716	-0.00958365
102.5	0.0274952	0.0101439	0.00515443	0.00700933	0.0149922	0.00300717	-0.00143721	-0.0033358
97.5	0.0334417	0.0295642	0.00996417	0.0322375	0.0108356	0.0160906	0.0197252	0.0116153
92.5	0.034278	0.0242711	0.0137159	0.0149012	0.0176738	0.0289476	0.014249	0.0185424
87.5	0.00828892	0.0181714	-0.0163555	-0.00247506	-0.001149	-0.016626	-0.0012029	-0.0125651
82.5	-0.0734423	0.00402935	-0.00834695	-0.00214638	0.00132387	-0.00600543	0.00875375	-0.00860559
77.5	-0.00473149	0.00420299	-0.00519434	0.0167285	-0.00751972	-0.00355256	-0.00219132	-0.0048634
72.5	0.000247473	0.00432382	0.00152832	-0.00217422	0.014674	0.00720211	0.00733222	0.00234779
67.5	-0.0331334	0.0159626	0.00780415	0.00102388	-0.00528411	0.00951042	-0.00303942	0.00910701
62.5	0.0113081	0.0150866	0.000126058	0.00815328	0.0132596	0.00396723	0.0142464	0.00881366
57.5	0.0127748	0.00948402	0.0113215	0.0302778	0.00586422	0.00892062	0.0165864	0.00595735
52.5	0.00152637	0.0109055	0.0159538	0.0139781	0.00916239	0.011024	0.0125388	0.0105442
47.5	0.0354552	0.0294862	0.00933345	0.0209961	0.0131504	0.0157473	0.0159026	0.0161298
42.5	0.000640481	0.0112614	0.0117871	0.00627251	0.0124855	0.0127198	0.0186656	0.0153002
37.5	0.0282266	0.00877999	0.0272367	0.0317109	0.0155643	0.0258742	0.0201187	0.0389442
32.5	0.0355292	0.0324801	0.0403322	0.0642381	0.0591217	0.0464026	0.059385	0.0661383
27.5	0.168937	0.159831	0.211802	0.152914	0.128556	0.146247	0.141407	0.118922
22.5	1.32899	1.2237	0.886417	0.555358	0.516235	0.47338	0.48429	0.515051

E_{kin} [GeV]

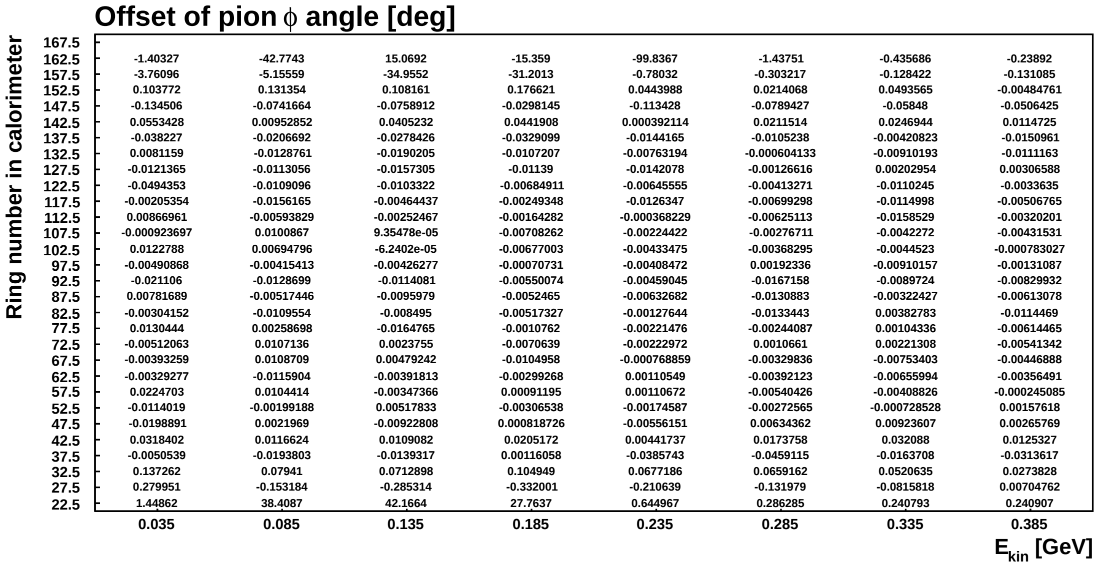

Offset of pion ϕ angle [deg]

Ring number in calorimeter	0.035	0.085	0.135	0.185	0.235	0.285	0.335	0.385
167.5								
162.5	-1.40327	-42.7743	15.0692	-15.359	-99.8367	-1.43751	-0.435686	-0.23892
157.5	-3.76096	-5.15559	-34.9552	-31.2013	-0.78032	-0.303217	-0.128422	-0.131085
152.5	0.103772	0.131354	0.108161	0.176621	0.0443988	0.0214068	0.0493565	-0.00484761
147.5	-0.134506	-0.0741664	-0.0758912	-0.0298145	-0.113428	-0.0789427	-0.05848	-0.0506425
142.5	0.0553428	0.00952852	0.0405232	0.0441908	0.000392114	0.0211514	0.0246944	0.0114725
137.5	-0.038227	-0.0206692	-0.0278426	-0.0329099	-0.0144165	-0.0105238	-0.00420823	-0.0150961
132.5	0.0081159	-0.0128761	-0.0190205	-0.0107207	-0.00763194	-0.000604133	-0.00910193	-0.0111163
127.5	-0.0121365	-0.0113056	-0.0157305	-0.01139	-0.0142078	-0.00126616	0.00202954	0.00306588
122.5	-0.0494353	-0.0109096	-0.0103322	-0.00684911	-0.00645555	-0.00413271	-0.0110245	-0.0033635
117.5	-0.00205354	-0.0156165	-0.00464437	-0.00249348	-0.0126347	-0.00699298	-0.0114998	-0.00506765
112.5	0.00866961	-0.00593829	-0.00252467	-0.00164282	-0.000368229	-0.00625113	-0.0158529	-0.00320201
107.5	-0.000923697	0.0100867	9.35478e-05	-0.00708262	-0.00224422	-0.00276711	-0.0042272	-0.00431531
102.5	0.0122788	0.00694796	-6.2402e-05	-0.00677003	-0.00433475	-0.00368295	-0.0044523	-0.000783027
97.5	-0.00490868	-0.00415413	-0.00426277	-0.00070731	-0.00408472	0.00192336	-0.00910157	-0.00131087
92.5	-0.021106	-0.0128699	-0.0114081	-0.00550074	-0.00459045	-0.0167158	-0.0089724	-0.00829932
87.5	0.00781689	-0.00517446	-0.0095979	-0.0052465	-0.00632682	-0.0130883	-0.00322427	-0.00613078
82.5	-0.00304152	-0.0109554	-0.008495	-0.00517327	-0.00127644	-0.0133443	0.00382783	-0.0114469
77.5	0.0130444	0.00258698	-0.0164765	-0.0010762	-0.00221476	-0.00244087	0.00104336	-0.00614465
72.5	-0.00512063	0.0107136	0.0023755	-0.0070639	-0.00222972	0.0010661	0.00221308	-0.00541342
67.5	-0.00393259	0.0108709	0.00479242	-0.0104958	-0.000768859	-0.00329836	-0.00753403	-0.00446888
62.5	-0.00329277	-0.0115904	-0.00391813	-0.00299268	0.00110549	-0.00392123	-0.00655994	-0.00356491
57.5	0.0224703	0.0104414	-0.00347366	0.00091195	0.00110672	-0.00540426	-0.00408826	-0.000245085
52.5	-0.0114019	-0.00199188	0.00517833	-0.00306538	-0.00174587	-0.00272565	-0.000728528	0.00157618
47.5	-0.0198891	0.0021969	-0.00922808	0.000818726	-0.00556151	0.00634362	0.00923607	0.00265769
42.5	0.0318402	0.0116624	0.0109082	0.0205172	0.00441737	0.0173758	0.032088	0.0125327
37.5	-0.0050539	-0.0193803	-0.0139317	0.00116058	-0.0385743	-0.0459115	-0.0163708	-0.0313617
32.5	0.137262	0.07941	0.0712898	0.104949	0.0677186	0.0659162	0.0520635	0.0273828
27.5	0.279951	-0.153184	-0.285314	-0.332001	-0.210639	-0.131979	-0.0815818	0.00704762
22.5	1.44862	38.4087	42.1664	27.7637	0.644967	0.286285	0.240793	0.240907

E_{kin} [GeV]

C.6 Offsets of reconstructed photon variables

Offset of photon kinetic energy

Ring number in calorimeter	0.045	0.095	0.145	0.195	0.245	0.295	0.345	0.395	0.445	0.495
174	0.000355877	0.000371352	0.00707476	0.00884249	0.0152492	0.0117507	0.0145289	0.0195439	0.0244555	0.0272662
173	-5.81293e-05	0.016822	0.0105869	0.01208	0.0133303	0.0144518	0.0175932	0.0207687	0.0243127	0.0258329
172	0.00947163	0.0153933	0.0101459	0.0135498	0.010877	0.0128367	0.0122701	0.020377	0.0228182	0.0270007
171	0.00405783	0.00927019	0.00921737	0.00546102	0.00741203	0.00964868	0.00917094	0.0183259	0.0192798	0.0236202
170	-0.0097846	-0.008929	0.00455816	0.00354927	0.00136625	0.00487174	0.0091686	0.0127966	0.0139678	0.0179898
169	0.0198377	-0.00722614	-0.00382316	-0.00637297	0.00130828	0.00222342	0.00585024	0.00851017	0.0143394	0.0162343
168	-0.0205655	-0.0100192	-0.0152254	-0.00677211	-0.00717344	-0.00305969	0.000811205	0.00471772	0.0100166	0.0124703
167	-0.0202387	-0.018482	-0.0162017	-0.0160385	-0.01069	-0.0072662	-0.00372882	0.00297718	0.00516824	0.00723632
166	-0.0254207	-0.0180527	-0.0172447	-0.0170596	-0.0142258	-0.0095299	-0.00813741	-0.00229505	0.000828975	0.00743478
165	-0.0192834	-0.0278122	-0.0231033	-0.0210642	-0.0158684	-0.012079	-0.00840294	-0.00625686	-0.00189558	0.00315748
164	-0.0342011	-0.029854	-0.0286434	-0.0255135	-0.0237772	-0.0172156	-0.0117158	-0.0095324	-0.00520475	-0.000870344
163	-0.0374403	-0.033082	-0.0296093	-0.030325	-0.0260151	-0.0217773	-0.0168219	-0.0119565	-0.0104367	-0.00514149
162	-0.0386077	-0.0313122	-0.0337115	-0.032572	-0.0251896	-0.0240543	-0.0166856	-0.0148403	-0.0113959	-0.00781395
161	-0.0488801	-0.0428492	-0.0397851	-0.0338522	-0.0278231	-0.0262058	-0.0213745	-0.0184144	-0.01544	-0.00824855
160	-0.0484182	-0.0405825	-0.038347	-0.0380502	-0.0340801	-0.0296793	-0.024823	-0.0207281	-0.0155529	-0.0126716
159	-0.0396223	-0.0365975	-0.0371274	-0.0350808	-0.0335331	-0.0318816	-0.0255328	-0.0227871	-0.0199004	-0.0146317
158	-0.0536531	-0.0449817	-0.0459632	-0.037079	-0.0363588	-0.0314952	-0.0277374	-0.0252589	-0.0203328	-0.0169895
157	-0.0574324	-0.0441268	-0.0393916	-0.0437879	-0.0378289	-0.0358163	-0.0324958	-0.0283333	-0.0230279	-0.023822
156	-0.0615919	-0.0402324	-0.0471006	-0.0401162	-0.0362904	-0.0339454	-0.0301455	-0.0279346	-0.0249401	-0.0220886
155	-0.0534033	-0.0496698	-0.0390665	-0.0393315	-0.0385598	-0.0295231	-0.0312036	-0.0242769	-0.0240199	-0.0230367
154	-0.0651006	-0.0560858	-0.0462596	-0.0452557	-0.0384509	-0.0406507	-0.0391309	-0.031791	-0.0333478	-0.0293959
153	-0.0740664	-0.0665269	-0.0603142	-0.0580621	-0.0642243	-0.0591841	-0.0630272	-0.0656832	-0.0673245	-0.0661185
152	-0.0632404	-0.0506143	-0.0593296	-0.0558275	-0.0632434	-0.0618045	-0.0625119	-0.0653187	-0.0624238	-0.0629916
151	-0.105093	-0.0920404	-0.0915791	-0.0891331	-0.0809556	-0.0833072	-0.0760658	-0.0731193	-0.071385	-0.0655473

E_{kin} [GeV]

Offset of photon θ angle [deg]

Ring number in calorimeter	0.045	0.095	0.145	0.195	0.245	0.295	0.345	0.395	0.445	0.495
174	-1.32928	-1.42916	-1.34051	-1.34259	-1.34702	-1.33477	-1.32352	-1.36137	-1.28746	-1.28612
173	-0.425003	-0.421789	-0.503672	-0.500667	-0.534289	-0.564552	-0.563023	-0.588018	-0.560319	-0.578985
172	-0.400585	-0.383693	-0.445162	-0.542146	-0.585645	-0.614498	-0.604677	-0.594919	-0.598656	-0.607694
171	-0.524181	-0.965352	-1.21423	-1.33617	-1.34125	-1.34721	-1.28826	-1.27523	-1.25295	-1.21125
170	-1.55292	-1.64748	-1.61853	-1.62244	-1.58761	-1.55452	-1.50184	-1.45082	-1.37168	-1.34066
169	-0.525548	-0.565269	-0.610384	-0.630454	-0.612825	-0.609873	-0.608182	-0.592696	-0.567312	-0.537705
168	-0.14547	-0.173684	-0.225382	-0.237966	-0.234009	-0.271291	-0.265042	-0.25531	-0.268881	-0.249166
167	-0.127028	-0.129498	-0.110585	-0.121349	-0.116583	-0.13713	-0.0924033	-0.0865129	-0.0750224	-0.0903724
166	-0.067767	-0.121457	-0.101332	-0.0853392	-0.0849129	-0.0500564	-0.0386191	-0.0288369	-0.00691536	-0.0321417
165	-0.114863	-0.080676	-0.102678	-0.0802436	-0.058635	-0.0512016	-0.0336786	-0.0337608	-0.0230078	-0.0225008
164	-0.0496681	-0.0340885	-0.039862	-0.0112537	-0.0274532	-0.01717	-0.0303537	-0.00489625	0.0016156	-0.00296078
163	0.0347936	0.0554803	0.0293232	0.045212	0.059181	0.0384562	0.0235398	0.0436755	0.0239965	0.00725681
162	-0.0382887	-0.00964136	-0.0331689	-0.00964592	-0.000531094	0.0054614	0.00505557	0.0128522	-0.00945088	0.00145015
161	-0.0415089	-0.0360285	-0.0246352	-0.0487968	-0.0479183	-0.0375068	-0.0378934	-0.0334337	-0.0250742	-0.0357758
160	0.0214781	0.0208152	0.0279221	0.0326625	0.0123762	0.00531446	-0.0129825	0.00664569	0.00869347	0.00657335
159	0.0842104	0.123797	0.130688	0.119272	0.104359	0.0965327	0.0694891	0.0753203	0.0733828	0.0811532
158	0.142084	0.156551	0.166747	0.126414	0.124624	0.114075	0.0974165	0.101955	0.108123	0.100182
157	0.144069	0.130987	0.092068	0.106425	0.0887663	0.101932	0.102522	0.0814357	0.0955508	0.0697093
156	-0.0497392	-0.0230489	-0.0467845	-0.0110637	-0.0405915	-0.0370833	-0.030629	-0.0561357	-0.0448303	-0.0670244
155	0.344939	0.354914	0.284326	0.264493	0.265378	0.234102	0.211628	0.210221	0.173638	0.131393
154	1.9295	1.88507	1.79309	1.66759	1.56384	1.45896	1.34178	1.25487	1.14873	1.06097
153	0.510595	0.86727	0.977986	1.05889	1.01893	1.00278	0.962385	0.889634	0.808048	0.723561
152	0.402171	0.498333	0.547764	0.641236	0.628454	0.641929	0.629829	0.600969	0.605956	0.626585
151	1.22943	1.8104	1.65477	1.5155	1.39699	1.34583	1.31243	1.24529	1.21139	1.13923

E_{kin} [GeV]

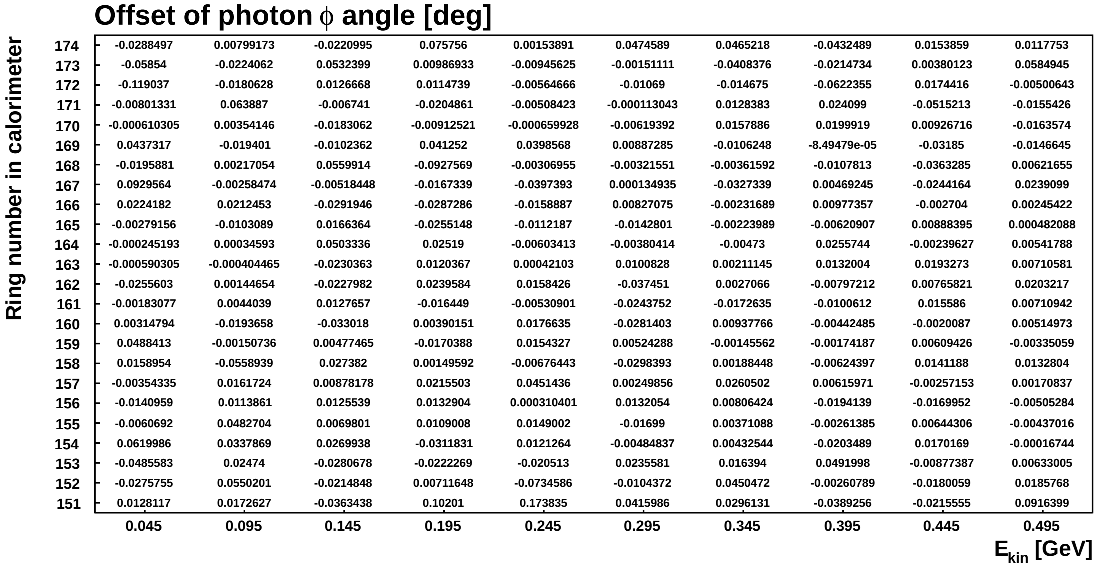

Offset of photon ϕ angle [deg]

Ring number in calorimeter / E_{kin} [GeV]	0.045	0.095	0.145	0.195	0.245	0.295	0.345	0.395	0.445	0.495
174	-0.0288497	0.00799173	-0.0220995	0.075756	0.00153891	0.0474589	0.0465218	-0.0432489	0.0153859	0.0117753
173	-0.05854	-0.0224062	0.0532399	0.00986933	-0.00945625	-0.00151111	-0.0408376	-0.0214734	0.00380123	0.0584945
172	-0.119037	-0.0180628	0.0126668	0.0114739	-0.00564666	-0.01069	-0.014675	-0.0622355	0.0174416	-0.00500643
171	-0.00801331	0.063887	-0.006741	-0.0204861	-0.00508423	-0.000113043	0.0128383	0.024099	-0.0515213	-0.0155426
170	-0.000610305	0.00354146	-0.0183062	-0.00912521	-0.000659928	-0.00619392	0.0157886	0.0199919	0.00926716	-0.0163574
169	0.0437317	-0.019401	-0.0102362	0.041252	0.0398568	0.00887285	-0.0106248	-8.49479e-05	-0.03185	-0.0146645
168	-0.0195881	0.00217054	0.0559914	-0.0927569	-0.00306955	-0.00321551	-0.00361592	-0.0107813	-0.0363285	0.00621655
167	0.0929564	-0.00258474	-0.00518448	-0.0167339	-0.0397393	0.000134935	-0.0327339	0.00469245	-0.0244164	0.0239099
166	0.0224182	0.0212453	-0.0291946	-0.0287286	-0.0158887	0.00827075	-0.00231689	0.00977357	-0.002704	0.00245422
165	-0.00279156	-0.0103089	0.0166364	-0.0255148	-0.0112187	-0.0142801	-0.00223989	-0.00620907	0.00888395	0.000482088
164	-0.000245193	0.00034593	0.0503336	0.02519	-0.00603413	-0.00380414	-0.00473	0.0255744	-0.00239627	0.00541788
163	-0.000590305	-0.000404465	-0.0230363	0.0120367	0.00042103	0.0100828	0.00211145	0.0132004	0.0193273	0.00710581
162	-0.0255603	0.00144654	-0.0227982	0.0239584	0.0158426	-0.037451	0.0027066	-0.00797212	0.00765821	0.0203217
161	-0.00183077	0.0044039	0.0127657	-0.016449	-0.00530901	-0.0243752	-0.0172635	-0.0100612	0.015586	0.00710942
160	0.00314794	-0.0193658	-0.033018	0.00390151	0.0176635	-0.0281403	0.00937766	-0.00442485	-0.0020087	0.00514973
159	0.0488413	-0.00150736	0.00477465	-0.0170388	0.0154327	0.00524288	-0.00145562	-0.00174187	0.00609426	-0.00335059
158	0.0158954	-0.0558939	0.027382	0.00149592	-0.00676443	-0.0298393	0.00188448	-0.00624397	0.0141188	0.0132804
157	-0.00354335	0.0161724	0.00878178	0.0215503	0.0451436	0.00249856	0.0260502	0.00615971	-0.00257153	0.00170837
156	-0.0140959	0.0113861	0.0125539	0.0132904	0.000310401	0.0132054	0.00806424	-0.0194139	-0.0169952	-0.00505284
155	-0.0060692	0.0482704	0.0069801	0.0109008	0.0149002	-0.01699	0.00371088	-0.00261385	0.00644306	-0.00437016
154	0.0619986	0.0337869	0.0269938	-0.0311831	0.0121264	-0.00484837	0.00432544	-0.0203489	0.0170169	-0.00016744
153	-0.0485583	0.02474	-0.0280678	-0.0222269	-0.020513	0.0235581	0.016394	0.0491998	-0.00877387	0.00633005
152	-0.0275755	0.0550201	-0.0214848	0.00711648	-0.0734586	-0.0104372	0.0450472	-0.00260789	-0.0180059	0.0185768
151	0.0128117	0.0172627	-0.0363438	0.10201	0.173835	0.0415986	0.0296131	-0.0389256	-0.0215555	0.0916399

The values of the error of each fitted particle variable are listed below. They correspond to the spectra shown in Section 6.6.1.1 and are obtained for the analysis conditions presented at the beginning of Chapter 6.

C.7 Errors of fitted proton variables

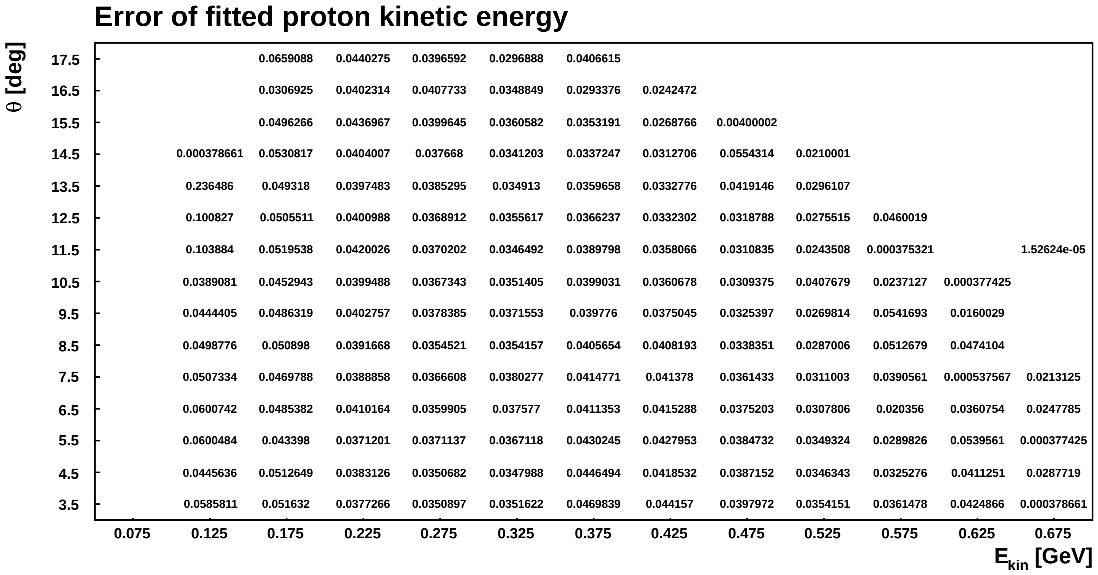

Error of fitted proton kinetic energy

θ [deg] / E_{kin} [GeV]	0.075	0.125	0.175	0.225	0.275	0.325	0.375	0.425	0.475	0.525	0.575	0.625	0.675
17.5			0.0659088	0.0440275	0.0396592	0.0296888	0.0406615						
16.5			0.0306925	0.0402314	0.0407733	0.0348849	0.0293376	0.0242472					
15.5			0.0496266	0.0436967	0.0399645	0.0360582	0.0353191	0.0268766	0.00400002				
14.5		0.000378661	0.0530817	0.0404007	0.037668	0.0341203	0.0337247	0.0312706	0.0554314	0.0210001			
13.5		0.236486	0.049318	0.0397483	0.0385295	0.034913	0.0359658	0.0332776	0.0419146	0.0296107			
12.5		0.100827	0.0505511	0.0400988	0.0368912	0.0355617	0.0366237	0.0332302	0.0318788	0.0275515	0.0460019		
11.5		0.103884	0.0519538	0.0420026	0.0370202	0.0346492	0.0389798	0.0358066	0.0310835	0.0243508	0.000375321		1.52624e-05
10.5		0.0389081	0.0452943	0.0399488	0.0367343	0.0351405	0.0399031	0.0360678	0.0309375	0.0407679	0.0237127	0.000377425	
9.5		0.0444405	0.0486319	0.0402757	0.0378385	0.0371553	0.039776	0.0375045	0.0325397	0.0269814	0.0541693	0.0160029	
8.5		0.0498776	0.050898	0.0391668	0.0354521	0.0354157	0.0405654	0.0408193	0.0338351	0.0287006	0.0512679	0.0474104	
7.5		0.0507334	0.0469788	0.0388858	0.0366608	0.0380277	0.0414771	0.041378	0.0361433	0.0311003	0.0390561	0.000537567	0.0213125
6.5		0.0600742	0.0485382	0.0410164	0.0359905	0.037577	0.0411353	0.0415288	0.0375203	0.0307806	0.020356	0.0360754	0.0247785
5.5		0.0600484	0.043398	0.0371201	0.0371137	0.0367118	0.0430245	0.0427953	0.0384732	0.0349324	0.0289826	0.0539561	0.000377425
4.5		0.0445636	0.0512649	0.0383126	0.0350682	0.0347988	0.0446494	0.0418532	0.0387152	0.0346343	0.0325276	0.0411251	0.0287719
3.5		0.0585811	0.051632	0.0377266	0.0350897	0.0351622	0.0469839	0.044157	0.0397972	0.0354151	0.0361478	0.0424866	0.000378661

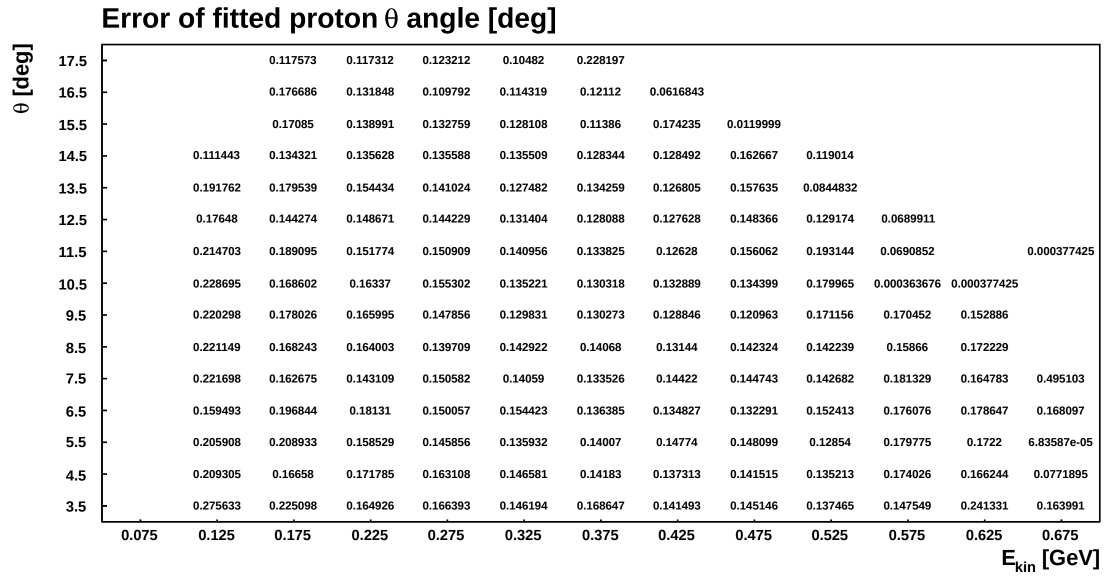
Error of fitted proton θ angle [deg]
θ [deg]
17.5
16.5
15.5
14.5
13.5
12.5
11.5
10.5
9.5
8.5
7.5
6.5
5.5
4.5
3.5
0.117573 0.117312 0.123212 0.10482 0.228197
0.176686 0.131848 0.109792 0.114319 0.12112 0.0616843
0.17085 0.138991 0.132759 0.128108 0.11386 0.174235 0.0119999
0.111443 0.134321 0.135628 0.135588 0.135509 0.128344 0.128492 0.162667 0.119014
0.191762 0.179539 0.154434 0.141024 0.127482 0.134259 0.126805 0.157635 0.0844832
0.17648 0.144274 0.148671 0.144229 0.131404 0.128088 0.127628 0.148366 0.129174 0.0689911
0.214703 0.189095 0.151774 0.150909 0.140956 0.133825 0.12628 0.156062 0.193144 0.0690852 0.000377425
0.228695 0.168602 0.16337 0.155302 0.135221 0.130318 0.132889 0.134399 0.179965 0.000363676 0.000377425
0.220298 0.178026 0.165995 0.147856 0.129831 0.130273 0.128846 0.120963 0.171156 0.170452 0.152886
0.221149 0.168243 0.164003 0.139709 0.142922 0.14068 0.13144 0.142324 0.142239 0.15866 0.172229
0.221698 0.162675 0.143109 0.150582 0.14059 0.133526 0.14422 0.144743 0.142682 0.181329 0.164783 0.495103
0.159493 0.196844 0.18131 0.150057 0.154423 0.136385 0.134827 0.132291 0.152413 0.176076 0.178647 0.168097
0.205908 0.208933 0.158529 0.145856 0.135932 0.14007 0.14774 0.148099 0.12854 0.179775 0.1722 6.83587e-05
0.209305 0.16658 0.171785 0.163108 0.146581 0.14183 0.137313 0.141515 0.135213 0.174026 0.166244 0.0771895
0.275633 0.225098 0.164926 0.166393 0.146194 0.168647 0.141493 0.145146 0.137465 0.147549 0.241331 0.163991
0.075
0.125
0.175
0.225
0.275
0.325
0.375
0.425
0.475
0.525
0.575
0.625
0.675
E_kin [GeV]

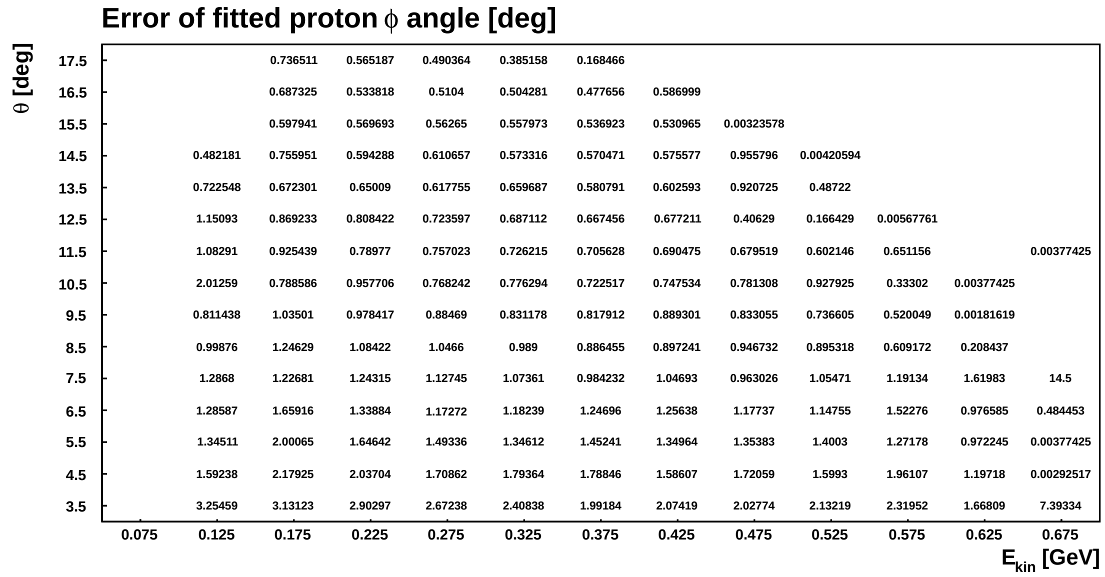
Error of fitted proton φ angle [deg]
θ [deg]
17.5
16.5
15.5
14.5
13.5
12.5
11.5
10.5
9.5
8.5
7.5
6.5
5.5
4.5
3.5
0.736511 0.565187 0.490364 0.385158 0.168466
0.687325 0.533818 0.5104 0.504281 0.477656 0.586999
0.597941 0.569693 0.56265 0.557973 0.536923 0.530965 0.00323578
0.482181 0.755951 0.594288 0.610657 0.573316 0.570471 0.575577 0.955796 0.00420594
0.722548 0.672301 0.65009 0.617755 0.659687 0.580791 0.602593 0.920725 0.48722
1.15093 0.869233 0.808422 0.723597 0.687112 0.667456 0.677211 0.40629 0.166429 0.00567761
1.08291 0.925439 0.78977 0.757023 0.726215 0.705628 0.690475 0.679519 0.602146 0.651156 0.00377425
2.01259 0.788586 0.957706 0.768242 0.776294 0.722517 0.747534 0.781308 0.927925 0.33302 0.00377425
0.811438 1.03501 0.978417 0.88469 0.831178 0.817912 0.889301 0.833055 0.736605 0.520049 0.00181619
0.99876 1.24629 1.08422 1.0466 0.989 0.886455 0.897241 0.946732 0.895318 0.609172 0.208437
1.2868 1.22681 1.24315 1.12745 1.07361 0.984232 1.04693 0.963026 1.05471 1.19134 1.61983 14.5
1.28587 1.65916 1.33884 1.17272 1.18239 1.24696 1.25638 1.17737 1.14755 1.52276 0.976585 0.484453
1.34511 2.00065 1.64642 1.49336 1.34612 1.45241 1.34964 1.35383 1.4003 1.27178 0.972245 0.00377425
1.59238 2.17925 2.03704 1.70862 1.79364 1.78846 1.58607 1.72059 1.5993 1.96107 1.19718 0.00292517
3.25459 3.13123 2.90297 2.67238 2.40838 1.99184 2.07419 2.02774 2.13219 2.31952 1.66809 7.39334
0.075
0.125
0.175
0.225
0.275
0.325
0.375
0.425
0.475
0.525
0.575
0.625
0.675
E_kin [GeV]

C.8 Errors of fitted pion variables

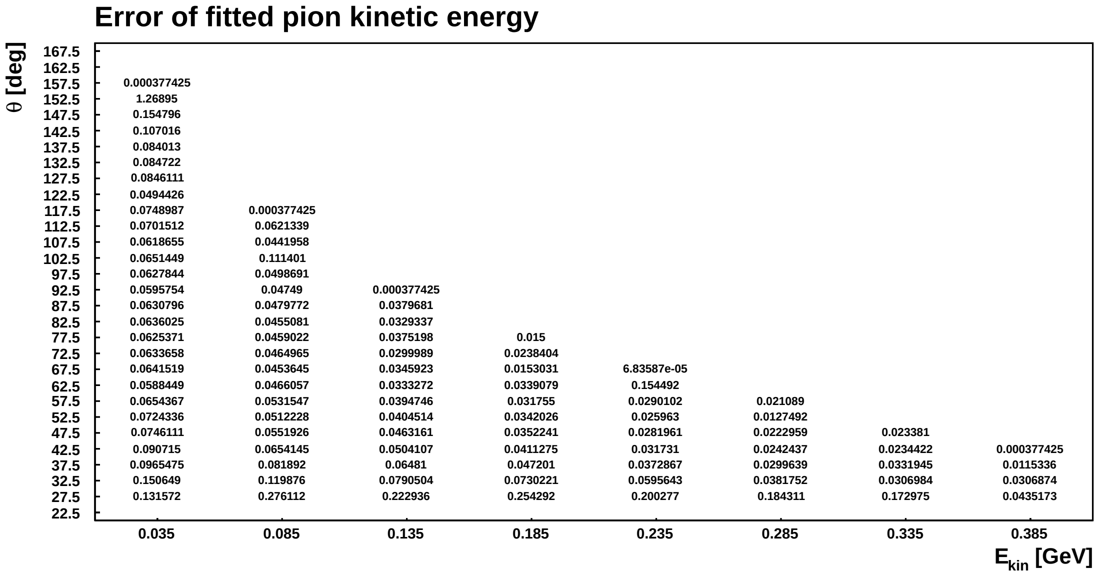

Error of fitted pion kinetic energy

θ [deg]	0.035	0.085	0.135	0.185	0.235	0.285	0.335	0.385
167.5								
162.5								
157.5	0.000377425							
152.5	1.26895							
147.5	0.154796							
142.5	0.107016							
137.5	0.084013							
132.5	0.084722							
127.5	0.0846111							
122.5	0.0494426							
117.5	0.0748987	0.000377425						
112.5	0.0701512	0.0621339						
107.5	0.0618655	0.0441958						
102.5	0.0651449	0.111401						
97.5	0.0627844	0.0498691						
92.5	0.0595754	0.04749	0.000377425					
87.5	0.0630796	0.0479772	0.0379681					
82.5	0.0636025	0.0455081	0.0329337					
77.5	0.0625371	0.0459022	0.0375198	0.015				
72.5	0.0633658	0.0464965	0.0299989	0.0238404				
67.5	0.0641519	0.0453645	0.0345923	0.0153031	6.83587e-05			
62.5	0.0588449	0.0466057	0.0333272	0.0339079	0.154492			
57.5	0.0654367	0.0531547	0.0394746	0.031755	0.0290102	0.021089		
52.5	0.0724336	0.0512228	0.0404514	0.0342026	0.025963	0.0127492		
47.5	0.0746111	0.0551926	0.0463161	0.0352241	0.0281961	0.0222959	0.023381	
42.5	0.090715	0.0654145	0.0504107	0.0411275	0.031731	0.0242437	0.0234422	0.000377425
37.5	0.0965475	0.081892	0.06481	0.047201	0.0372867	0.0299639	0.0331945	0.0115336
32.5	0.150649	0.119876	0.0790504	0.0730221	0.0595643	0.0381752	0.0306984	0.0306874
27.5	0.131572	0.276112	0.222936	0.254292	0.200277	0.184311	0.172975	0.0435173
22.5								

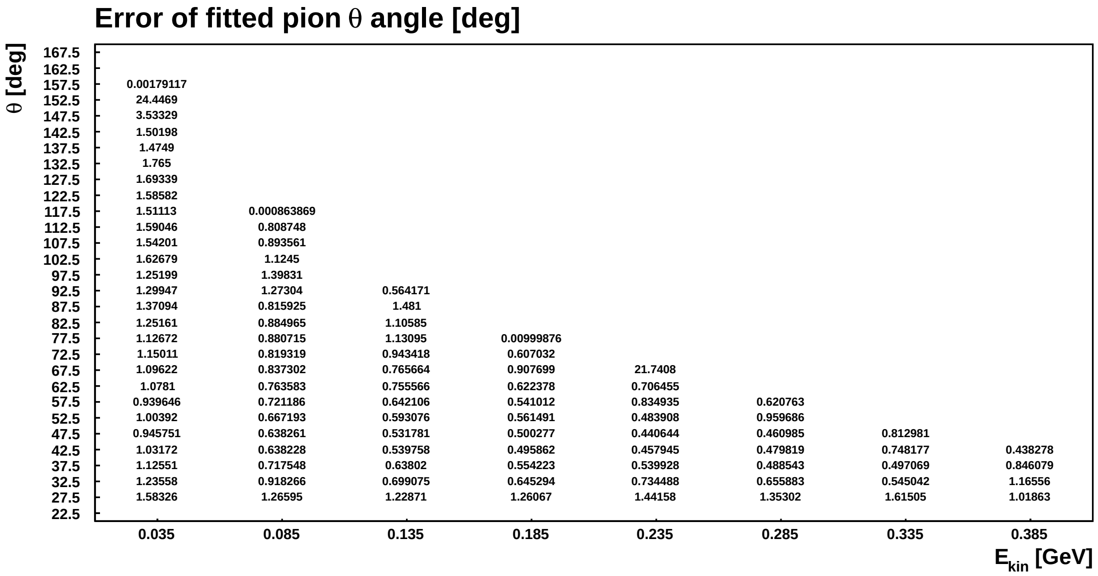

Error of fitted pion θ angle [deg]

θ [deg]	0.035	0.085	0.135	0.185	0.235	0.285	0.335	0.385
167.5								
162.5								
157.5	0.00179117							
152.5	24.4469							
147.5	3.53329							
142.5	1.50198							
137.5	1.4749							
132.5	1.765							
127.5	1.69339							
122.5	1.58582							
117.5	1.51113	0.000863869						
112.5	1.59046	0.808748						
107.5	1.54201	0.893561						
102.5	1.62679	1.1245						
97.5	1.25199	1.39831						
92.5	1.29947	1.27304	0.564171					
87.5	1.37094	0.815925	1.481					
82.5	1.25161	0.884965	1.10585					
77.5	1.12672	0.880715	1.13095	0.00999876				
72.5	1.15011	0.819319	0.943418	0.607032				
67.5	1.09622	0.837302	0.765664	0.907699	21.7408			
62.5	1.0781	0.763583	0.755566	0.622378	0.706455			
57.5	0.939646	0.721186	0.642106	0.541012	0.834935	0.620763		
52.5	1.00392	0.667193	0.593076	0.561491	0.483908	0.959686		
47.5	0.945751	0.638261	0.531781	0.500277	0.440644	0.460985	0.812981	
42.5	1.03172	0.638228	0.539758	0.495862	0.457945	0.479819	0.748177	0.438278
37.5	1.12551	0.717548	0.63802	0.554223	0.539928	0.488543	0.497069	0.846079
32.5	1.23558	0.918266	0.699075	0.645294	0.734488	0.655883	0.545042	1.16556
27.5	1.58326	1.26595	1.22871	1.26067	1.44158	1.35302	1.61505	1.01863
22.5								

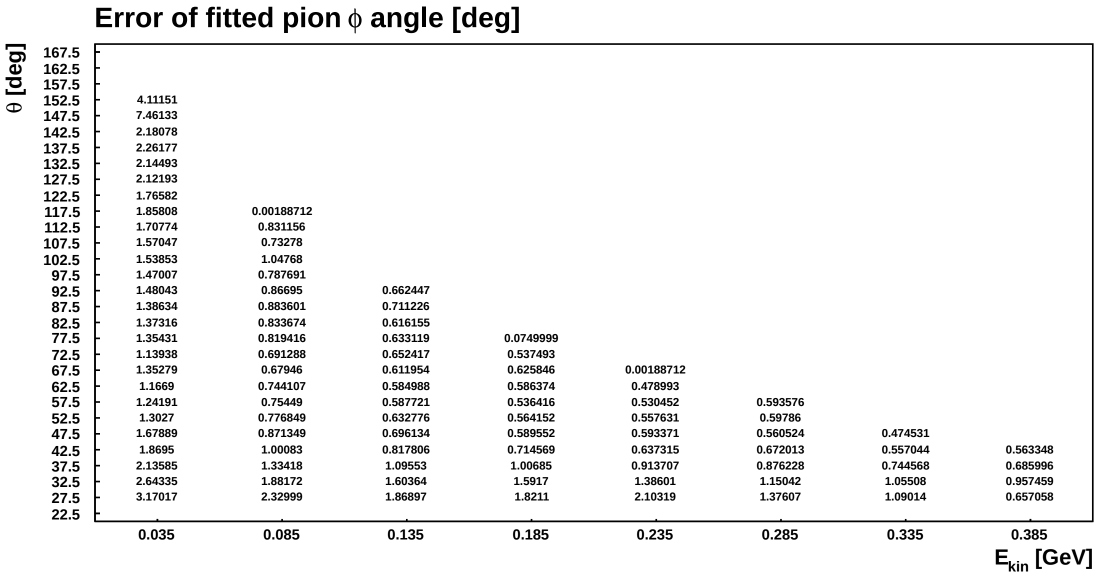

Error of fitted pion ϕ angle [deg]

θ [deg]	0.035	0.085	0.135	0.185	0.235	0.285	0.335	0.385
167.5								
162.5								
157.5								
152.5	4.11151							
147.5	7.46133							
142.5	2.18078							
137.5	2.26177							
132.5	2.14493							
127.5	2.12193							
122.5	1.76582							
117.5	1.85808	0.00188712						
112.5	1.70774	0.831156						
107.5	1.57047	0.73278						
102.5	1.53853	1.04768						
97.5	1.47007	0.787691						
92.5	1.48043	0.86695	0.662447					
87.5	1.38634	0.883601	0.711226					
82.5	1.37316	0.833674	0.616155					
77.5	1.35431	0.819416	0.633119	0.0749999				
72.5	1.13938	0.691288	0.652417	0.537493				
67.5	1.35279	0.67946	0.611954	0.625846	0.00188712			
62.5	1.1669	0.744107	0.584988	0.586374	0.478993			
57.5	1.24191	0.75449	0.587721	0.536416	0.530452	0.593576		
52.5	1.3027	0.776849	0.632776	0.564152	0.557631	0.59786		
47.5	1.67889	0.871349	0.696134	0.589552	0.593371	0.560524	0.474531	
42.5	1.8695	1.00083	0.817806	0.714569	0.637315	0.672013	0.557044	0.563348
37.5	2.13585	1.33418	1.09553	1.00685	0.913707	0.876228	0.744568	0.685996
32.5	2.64335	1.88172	1.60364	1.5917	1.38601	1.15042	1.05508	0.957459
27.5	3.17017	2.32999	1.86897	1.8211	2.10319	1.37607	1.09014	0.657058
22.5								

C.9 Errors of fitted photon variables

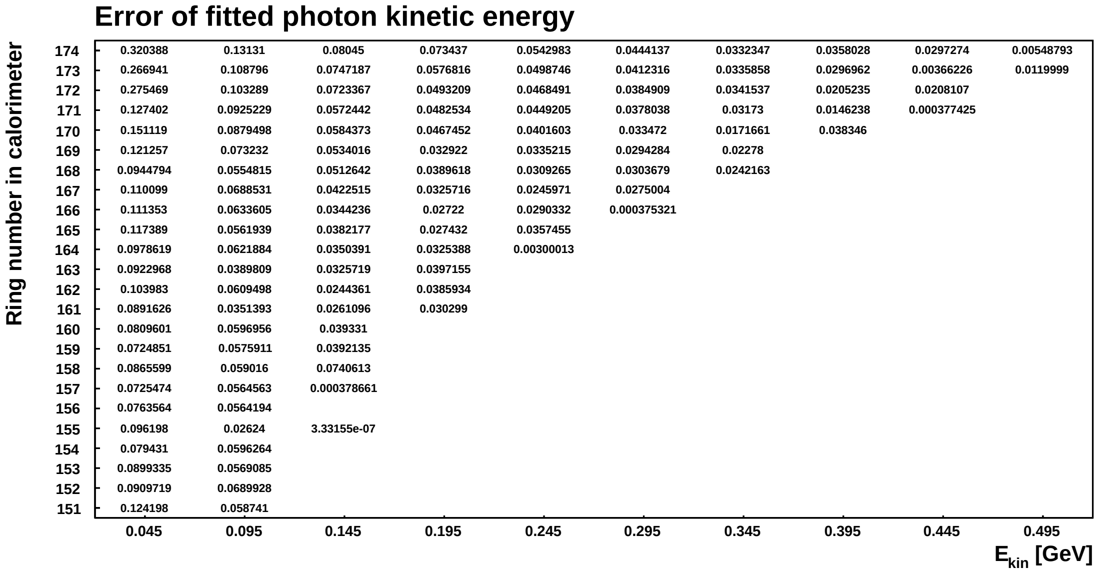

Error of fitted photon kinetic energy

Ring number in calorimeter	0.045	0.095	0.145	0.195	0.245	0.295	0.345	0.395	0.445	0.495
174	0.320388	0.13131	0.08045	0.073437	0.0542983	0.0444137	0.0332347	0.0358028	0.0297274	0.00548793
173	0.266941	0.108796	0.0747187	0.0576816	0.0498746	0.0412316	0.0335858	0.0296962	0.00366226	0.0119999
172	0.275469	0.103289	0.0723367	0.0493209	0.0468491	0.0384909	0.0341537	0.0205235	0.0208107	
171	0.127402	0.0925229	0.0572442	0.0482534	0.0449205	0.0378038	0.03173	0.0146238	0.000377425	
170	0.151119	0.0879498	0.0584373	0.0467452	0.0401603	0.033472	0.0171661	0.038346		
169	0.121257	0.073232	0.0534016	0.032922	0.0335215	0.0294284	0.02278			
168	0.0944794	0.0554815	0.0512642	0.0389618	0.0309265	0.0303679	0.0242163			
167	0.110099	0.0688531	0.0422515	0.0325716	0.0245971	0.0275004				
166	0.111353	0.0633605	0.0344236	0.02722	0.0290332	0.000375321				
165	0.117389	0.0561939	0.0382177	0.027432	0.0357455					
164	0.0978619	0.0621884	0.0350391	0.0325388	0.00300013					
163	0.0922968	0.0389809	0.0325719	0.0397155						
162	0.103983	0.0609498	0.0244361	0.0385934						
161	0.0891626	0.0351393	0.0261096	0.030299						
160	0.0809601	0.0596956	0.039331							
159	0.0724851	0.0575911	0.0392135							
158	0.0865599	0.059016	0.0740613							
157	0.0725474	0.0564563	0.000378661							
156	0.0763564	0.0564194								
155	0.096198	0.02624	3.33155e-07							
154	0.079431	0.0596264								
153	0.0899335	0.0569085								
152	0.0909719	0.0689928								
151	0.124198	0.058741								

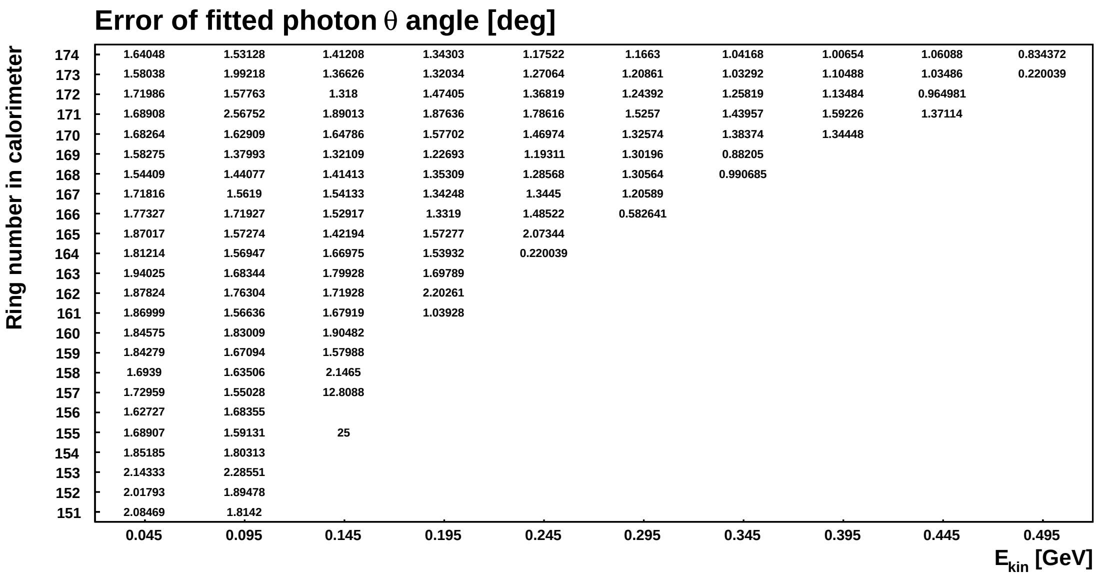

Error of fitted photon θ angle [deg]

Ring number in calorimeter	0.045	0.095	0.145	0.195	0.245	0.295	0.345	0.395	0.445	0.495
174	1.64048	1.53128	1.41208	1.34303	1.17522	1.1663	1.04168	1.00654	1.06088	0.834372
173	1.58038	1.99218	1.36626	1.32034	1.27064	1.20861	1.03292	1.10488	1.03486	0.220039
172	1.71986	1.57763	1.318	1.47405	1.36819	1.24392	1.25819	1.13484	0.964981	
171	1.68908	2.56752	1.89013	1.87636	1.78616	1.5257	1.43957	1.59226	1.37114	
170	1.68264	1.62909	1.64786	1.57702	1.46974	1.32574	1.38374	1.34448		
169	1.58275	1.37993	1.32109	1.22693	1.19311	1.30196	0.88205			
168	1.54409	1.44077	1.41413	1.35309	1.28568	1.30564	0.990685			
167	1.71816	1.5619	1.54133	1.34248	1.3445	1.20589				
166	1.77327	1.71927	1.52917	1.3319	1.48522	0.582641				
165	1.87017	1.57274	1.42194	1.57277	2.07344					
164	1.81214	1.56947	1.66975	1.53932	0.220039					
163	1.94025	1.68344	1.79928	1.69789						
162	1.87824	1.76304	1.71928	2.20261						
161	1.86999	1.56636	1.67919	1.03928						
160	1.84575	1.83009	1.90482							
159	1.84279	1.67094	1.57988							
158	1.6939	1.63506	2.1465							
157	1.72959	1.55028	12.8088							
156	1.62727	1.68355								
155	1.68907	1.59131	25							
154	1.85185	1.80313								
153	2.14333	2.28551								
152	2.01793	1.89478								
151	2.08469	1.8142								

E_{kin} [GeV]

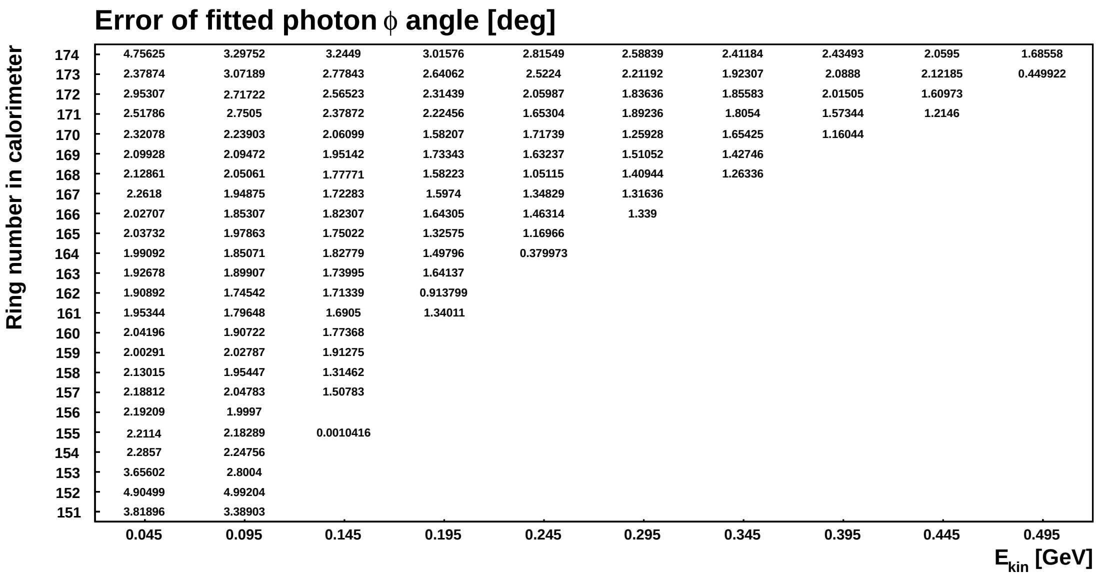

Error of fitted photon ϕ angle [deg]

Ring number in calorimeter	0.045	0.095	0.145	0.195	0.245	0.295	0.345	0.395	0.445	0.495
174	4.75625	3.29752	3.2449	3.01576	2.81549	2.58839	2.41184	2.43493	2.0595	1.68558
173	2.37874	3.07189	2.77843	2.64062	2.5224	2.21192	1.92307	2.0888	2.12185	0.449922
172	2.95307	2.71722	2.56523	2.31439	2.05987	1.83636	1.85583	2.01505	1.60973	
171	2.51786	2.7505	2.37872	2.22456	1.65304	1.89236	1.8054	1.57344	1.2146	
170	2.32078	2.23903	2.06099	1.58207	1.71739	1.25928	1.65425	1.16044		
169	2.09928	2.09472	1.95142	1.73343	1.63237	1.51052	1.42746			
168	2.12861	2.05061	1.77771	1.58223	1.05115	1.40944	1.26336			
167	2.2618	1.94875	1.72283	1.5974	1.34829	1.31636				
166	2.02707	1.85307	1.82307	1.64305	1.46314	1.339				
165	2.03732	1.97863	1.75022	1.32575	1.16966					
164	1.99092	1.85071	1.82779	1.49796	0.379973					
163	1.92678	1.89907	1.73995	1.64137						
162	1.90892	1.74542	1.71339	0.913799						
161	1.95344	1.79648	1.6905	1.34011						
160	2.04196	1.90722	1.77368							
159	2.00291	2.02787	1.91275							
158	2.13015	1.95447	1.31462							
157	2.18812	2.04783	1.50783							
156	2.19209	1.9997								
155	2.2114	2.18289	0.0010416							
154	2.2857	2.24756								
153	3.65602	2.8004								
152	4.90499	4.99204								
151	3.81896	3.38903								

E_{kin} [GeV]

Appendix D

Relative reconstruction efficiencies

The relative efficiencies of the various analysis steps presented in Chapter 5 are listed in Table D.1 for reconstructing $\eta \to \pi^+\pi^-\gamma$ events. The corresponding efficienices for the reconstruction of $\eta \to \pi^+\pi^-\pi^0$ are shown in Table D.2 respectively. The last columns in each of the two tables corresponds to the product of the individual efficiencies. Table D.3 summarises the absolute efficiencies after the basic analysis steps shown in Chapter 5 including the preselection criteria presented in Chapter 4. The event topology differs for $\eta \to \pi^+\pi^-\gamma$ and $\eta \to \pi^+\pi^-\pi^0$ by the number of requested neutral tracks in the Central Detector. The product of the red highlighted values in Table D.1 or D.2 and those presented in Table D.3 leads to the total reconstruction efficiency for the corresponding η decay (which has also been shown in Fig. 5.22).

Relative efficiencies for the 1st analysis approach [%]

Reaction	PID in CD	$\mathrm{MM}^2_{\pi^\pm} < 0.01\,\mathrm{GeV}^2/\mathrm{c}^4$	$E_\gamma > \frac{2\,\mathrm{deg}\times\mathrm{GeV}}{\angle(\pi^\pm,\gamma)}$	**Product**
$\boldsymbol{\eta \to \pi^+\pi^-\gamma}$	59.98	94.03	95	**53.58**
$\boldsymbol{\eta \to \pi^+\pi^-\pi^0}$	53.60	56.54	94.59	**28.67**
$\boldsymbol{\eta \to e^+e^-\gamma}$	1.21	99.16	96.03	**1.15**
$\boldsymbol{pp \to pp\pi^+\pi^-\pi^0}$	51.53	55.67	94.98	**27.25**
$\boldsymbol{pp \to pp\pi^+\pi^-}$	67.12	97.19	37.21	**24.27**

Relative efficiencies for the 2nd analysis approach [%]

Reaction	$E_\gamma > \frac{2\,\mathrm{deg}\times\mathrm{GeV}}{\angle(\pi^\pm,\gamma)}$	$P(\chi^2_{pp\to pp\pi^+\pi^-\gamma}, 4) \geq 0.2$		**Product**
$\boldsymbol{\eta \to \pi^+\pi^-\gamma}$	95.12	18.22		**17.33**
$\boldsymbol{\eta \to \pi^+\pi^-\pi^0}$	94.17	0.60		**0.57**
$\boldsymbol{\eta \to e^+e^-\gamma}$	93.54	0.03		**0.03**
$\boldsymbol{pp \to pp\pi^+\pi^-\pi^0}$	94.63	0.56		**0.53**
$\boldsymbol{pp \to pp\pi^+\pi^-}$	38.34	0.50		**0.19**

Table D.1: *Relative efficiencies for reconstructing $\eta \to \pi^+\pi^-\gamma$ events after using the two analysis approaches discussed within Chapter 5. The reconstruction efficiencies for the preselection, the proton identification, demanding time coincidences and requesting an event topology are not included here.*

Relative efficiencies for the 1^{st} analysis approach [%]				
Reaction	PID in CD	$\mathrm{MM}^2_{\pi^\pm} \geq 0.01\,\mathrm{GeV}^2/\mathrm{c}^4$	Select π^0	**Product**
$\eta \to \pi^+\pi^-\gamma$	59.98	5.95	70.36	**2.51**
$\eta \to \pi^+\pi^-\pi^0$	53.60	43.45	99.99	**23.27**
$\eta \to e^+e^-\gamma$	1.21	0.84	19.17	**0**
$pp \to pp\pi^+\pi^-\pi^0$	51.53	44.33	100	**22.84**
$pp \to pp\pi^+\pi^-$	67.12	2.86	32.45	**0.62**
Relative efficiencies for the 2^{nd} analysis approach [%]				
Reaction	Select π^0	$P(\chi^2_{pp\to pp\pi^+\pi^-\gamma\gamma}, 4) \geq 0.2$		**Product**
$\eta \to \pi^+\pi^-\gamma$	50.69	2.79		**1.41**
$\eta \to \pi^+\pi^-\pi^0$	91.65	17.64		**16.17**
$\eta \to e^+e^-\gamma$	41.21	0		**0**
$pp \to pp\pi^+\pi^-\pi^0$	92.17	17.75		**16.36**
$pp \to pp\pi^+\pi^-$	37.95	0.02		**0.01**

Table D.2: *Relative efficiencies for reconstructing $\eta \to \pi^+\pi^-\pi^0$ events after using the two analysis approaches discussed within Chapter 5. The reconstruction efficiencies for the preselection, the proton identification, demanding time coincidences and requesting an event topology are not included here.*

	Absolute efficiencies [%] for:	
Reaction	$\eta \to \pi^+\pi^-\gamma$	$\eta \to \pi^+\pi^-\pi^0$
$\eta \to \pi^+\pi^-\gamma$	11.75	2.04
$\eta \to \pi^+\pi^-\pi^0$	11.39	7.39
$\eta \to e^+e^-\gamma$	15.23	3.18
$pp \to pp\pi^+\pi^-\pi^0$	6.76	4.40
$pp \to pp\pi^+\pi^-$	0.76	0.18

Table D.3: *Absolute efficiencies for the basic analysis steps discussed in Chapter 5. They include the preselection conditions, proton identification, check for time coincidences and requesting an event topology.*

Appendix E

Determining the E_γ-distribution

The photon energy bin-wise projected missing mass spectra that are used for background subtraction, are summarised in the diagrams below and obtained for the analysis conditions: $P(\chi^2_{pp\to pp\pi^+\pi^-\gamma}, 4) \geq 0.2$ and $E_\gamma > \frac{2\,\mathrm{deg}\times\mathrm{GeV}}{\angle(\pi^\pm,\gamma)}$. The black crosses represent the measured missing mass distribution. The background of each spectrum (red curve) is described by a fourth order polynomial folded with the simulated phase space distribution of $pp \to pp\pi^+\pi^-$ and $pp \to pp\pi^+\pi^-\pi^0$ (see also Eq. 5.18). The signal peak is fitted by the simulated $\eta \to \pi^+\pi^-\gamma$ signal (blue curve). The yellow coloured area in each diagram corresponds to the sum of signal and background fit. The purple dashed lines indicate the integration window for determining the η-peak content after background subtraction. The corresponding values (without efficienicy correction) are plotted in each diagram. The entries, as well as the statistical errors, of the final background and acceptance corrected energy distribution are listed in Table E.1.

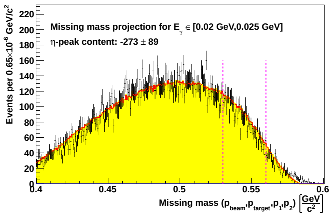

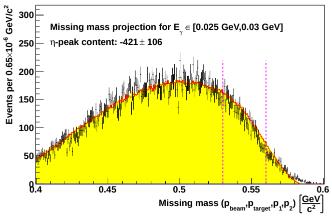

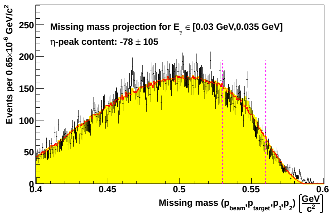

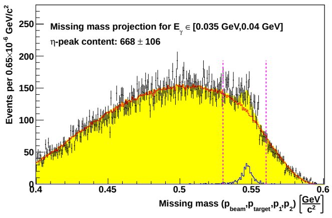

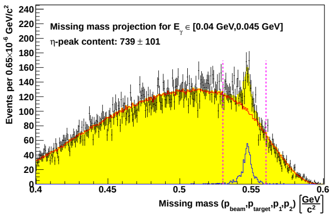

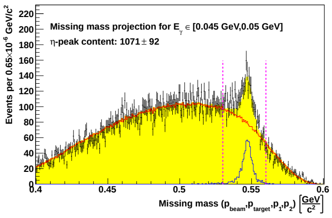

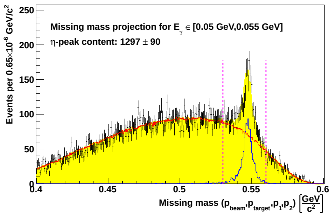

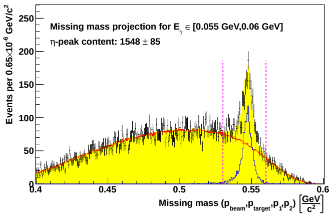

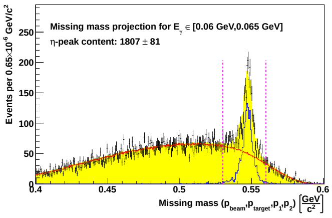

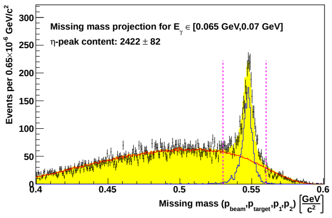
Missing mass projection for $E_\gamma \in$ [0.065 GeV,0.07 GeV]
η-peak content: 2422 ± 82
Events per 0.65·10^{-6} GeV/c^2
Missing mass (p_{beam},p_{target},p_1,p_2) $\left[\frac{GeV}{c^2}\right]$

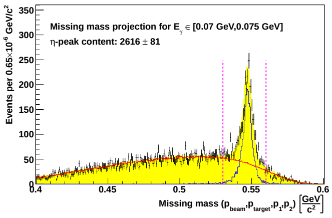
Missing mass projection for $E_\gamma \in$ [0.07 GeV,0.075 GeV]
η-peak content: 2616 ± 81
Events per 0.65·10^{-6} GeV/c^2
Missing mass (p_{beam},p_{target},p_1,p_2) $\left[\frac{GeV}{c^2}\right]$

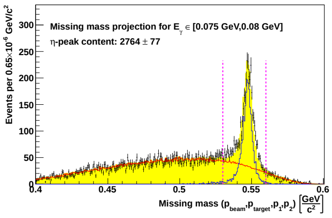
Missing mass projection for $E_\gamma \in$ [0.075 GeV,0.08 GeV]
η-peak content: 2764 ± 77
Events per 0.65·10^{-6} GeV/c^2
Missing mass (p_{beam},p_{target},p_1,p_2) $\left[\frac{GeV}{c^2}\right]$

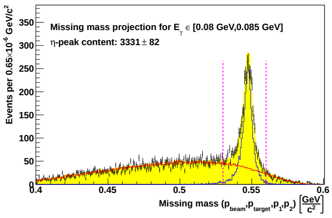
Missing mass projection for $E_\gamma \in$ [0.08 GeV,0.085 GeV]
η-peak content: 3331 ± 82
Events per 0.65·10^{-6} GeV/c^2
Missing mass (p_{beam},p_{target},p_1,p_2) $\left[\frac{GeV}{c^2}\right]$

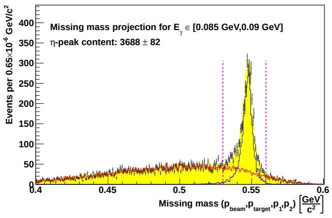
Missing mass projection for $E_\gamma \in$ [0.085 GeV,0.09 GeV]
η-peak content: 3688 ± 82
Events per 0.65·10^{-6} GeV/c^2
Missing mass (p_{beam},p_{target},p_1,p_2) $\left[\frac{GeV}{c^2}\right]$

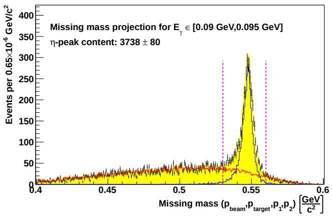
Missing mass projection for $E_\gamma \in$ [0.09 GeV,0.095 GeV]
η-peak content: 3738 ± 80
Events per 0.65·10^{-6} GeV/c^2
Missing mass (p_{beam},p_{target},p_1,p_2) $\left[\frac{GeV}{c^2}\right]$

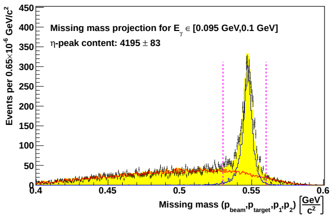
Missing mass projection for $E_\gamma \in$ [0.095 GeV,0.1 GeV]
η-peak content: 4195 ± 83
Events per 0.65·10^{-6} GeV/c^2
Missing mass (p_{beam},p_{target},p_1,p_2) $\left[\frac{GeV}{c^2}\right]$

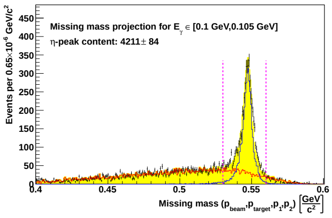
Missing mass projection for $E_\gamma \in$ [0.1 GeV,0.105 GeV]
η-peak content: 4211± 84
Events per 0.65·10^{-6} GeV/c^2
Missing mass (p_{beam},p_{target},p_1,p_2) $\left[\frac{GeV}{c^2}\right]$

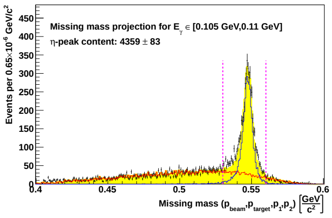
Missing mass projection for $E_\gamma \in$ [0.105 GeV,0.11 GeV]
η-peak content: 4359 ± 83
Events per 0.65·10^{-6} GeV/c^2
Missing mass (p_{beam},p_{target},p_1,p_2) $\left[\frac{GeV}{c^2}\right]$

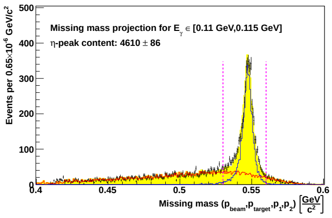
Missing mass projection for $E_\gamma \in$ [0.11 GeV,0.115 GeV]
η-peak content: 4610 ± 86
Events per 0.65·10^{-6} GeV/c^2
Missing mass (p_{beam},p_{target},p_1,p_2) $\left[\frac{GeV}{c^2}\right]$

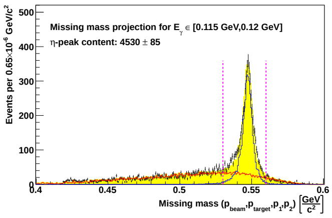
Missing mass projection for $E_\gamma \in$ [0.115 GeV,0.12 GeV]
η-peak content: 4530 ± 85
Events per 0.65·10^{-6} GeV/c^2
Missing mass (p_{beam},p_{target},p_1,p_2) $\left[\frac{GeV}{c^2}\right]$

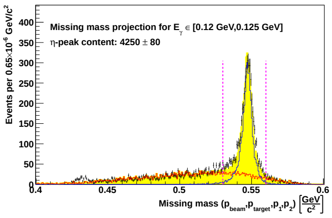
Missing mass projection for $E_\gamma \in$ [0.12 GeV,0.125 GeV]
η-peak content: 4250 ± 80
Events per 0.65·10^{-6} GeV/c^2
Missing mass (p_{beam},p_{target},p_1,p_2) $\left[\frac{GeV}{c^2}\right]$

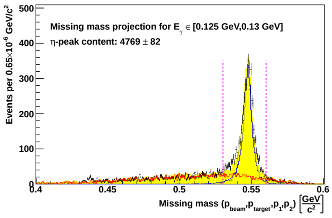
Missing mass projection for $E_\gamma \in$ [0.125 GeV,0.13 GeV]
η-peak content: 4769 ± 82
Events per 0.65·10^{-6} GeV/c^2
Missing mass (p_{beam},p_{target},p_1,p_2) $\left[\frac{GeV}{c^2}\right]$

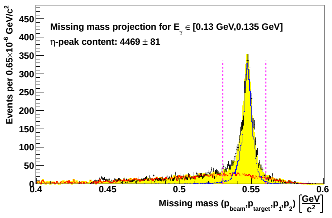
Missing mass projection for $E_\gamma \in$ [0.13 GeV,0.135 GeV]
η-peak content: 4469 ± 81
Events per 0.65·10^{-6} GeV/c^2
Missing mass (p_{beam},p_{target},p_1,p_2) $\left[\frac{GeV}{c^2}\right]$

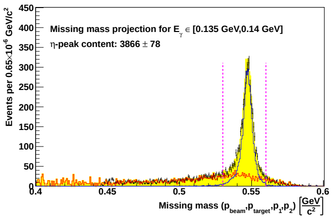
Missing mass projection for $E_\gamma \in$ [0.135 GeV,0.14 GeV]
η-peak content: 3866 ± 78
Events per 0.65·10^{-6} GeV/c^2
Missing mass (p_{beam},p_{target},p_1,p_2) $\left[\frac{GeV}{c^2}\right]$

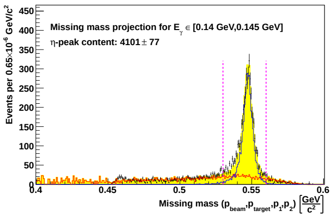
Missing mass projection for $E_\gamma \in$ [0.14 GeV,0.145 GeV]
η-peak content: 4101 ± 77
Events per 0.65·10^{-6} GeV/c^2
Missing mass (p_{beam},p_{target},p_1,p_2) $\left[\frac{GeV}{c^2}\right]$

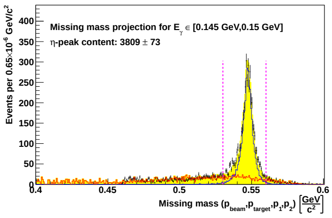
Missing mass projection for $E_\gamma \in$ [0.145 GeV,0.15 GeV]
η-peak content: 3809 ± 73
Events per 0.65·10^{-6} GeV/c^2
Missing mass (p_{beam},p_{target},p_1,p_2) $\left[\frac{GeV}{c^2}\right]$

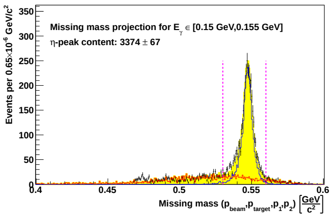
Missing mass projection for $E_\gamma \in$ [0.15 GeV,0.155 GeV]
η-peak content: 3374 ± 67
Events per 0.65·10^{-6} GeV/c^2
Missing mass (p_{beam},p_{target},p_1,p_2) $\left[\frac{GeV}{c^2}\right]$

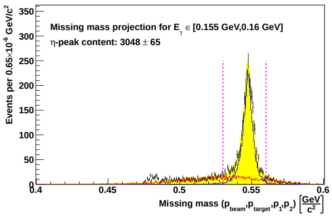
Missing mass projection for E$_\gamma$ ∈ [0.155 GeV,0.16 GeV]
η-peak content: 3048 ± 65
Events per 0.65×10^{-6} GeV/c^2
0
50
100
150
200
250
300
350
0.4
0.45
0.5
0.55
0.6
Missing mass (p$_{beam}$,p$_{target}$,p$_1$,p$_2$) [GeV/c^2]

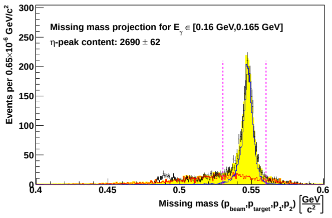
Missing mass projection for E$_\gamma$ ∈ [0.16 GeV,0.165 GeV]
η-peak content: 2690 ± 62
Events per 0.65×10^{-6} GeV/c^2
0
50
100
150
200
250
300
0.4
0.45
0.5
0.55
0.6
Missing mass (p$_{beam}$,p$_{target}$,p$_1$,p$_2$) [GeV/c^2]

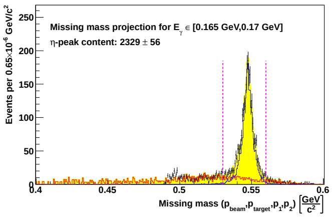
Missing mass projection for E$_\gamma$ ∈ [0.165 GeV,0.17 GeV]
η-peak content: 2329 ± 56
Events per 0.65×10^{-6} GeV/c^2
0
50
100
150
200
250
0.4
0.45
0.5
0.55
0.6
Missing mass (p$_{beam}$,p$_{target}$,p$_1$,p$_2$) [GeV/c^2]

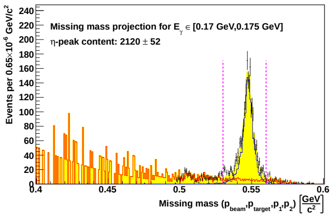
Missing mass projection for E$_\gamma$ ∈ [0.17 GeV,0.175 GeV]
η-peak content: 2120 ± 52
Events per 0.65×10^{-6} GeV/c^2
0
20
40
60
80
100
120
140
160
180
200
220
240
0.4
0.45
0.5
0.55
0.6
Missing mass (p$_{beam}$,p$_{target}$,p$_1$,p$_2$) [GeV/c^2]

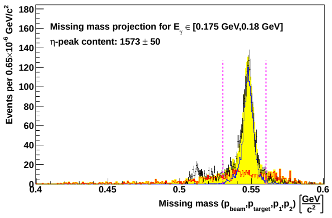
Missing mass projection for E$_\gamma$ ∈ [0.175 GeV,0.18 GeV]
η-peak content: 1573 ± 50
Events per 0.65×10^{-6} GeV/c^2
0
20
40
60
80
100
120
140
160
180
0.4
0.45
0.5
0.55
0.6
Missing mass (p$_{beam}$,p$_{target}$,p$_1$,p$_2$) [GeV/c^2]

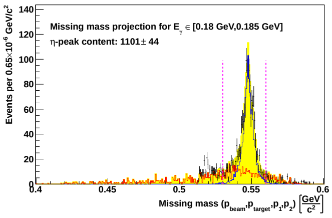
Missing mass projection for E$_\gamma$ ∈ [0.18 GeV,0.185 GeV]
η-peak content: 1101 ± 44
Events per 0.65×10^{-6} GeV/c^2
0
20
40
60
80
100
120
140
0.4
0.45
0.5
0.55
0.6
Missing mass (p$_{beam}$,p$_{target}$,p$_1$,p$_2$) [GeV/c^2]

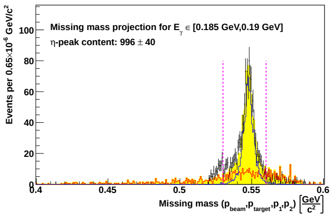
Missing mass projection for E$_\gamma$ ∈ [0.185 GeV,0.19 GeV]
η-peak content: 996 ± 40
Events per 0.65×10^{-6} GeV/c^2
0
20
40
60
80
100
0.4
0.45
0.5
0.55
0.6
Missing mass (p$_{beam}$,p$_{target}$,p$_1$,p$_2$) [GeV/c^2]

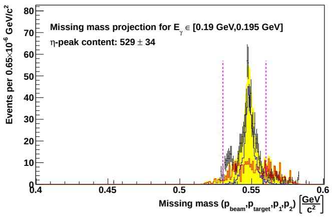
Missing mass projection for E$_\gamma$ ∈ [0.19 GeV,0.195 GeV]
η-peak content: 529 ± 34
Events per 0.65×10^{-6} GeV/c^2
0
10
20
30
40
50
60
70
80
0.4
0.45
0.5
0.55
0.6
Missing mass (p$_{beam}$,p$_{target}$,p$_1$,p$_2$) [GeV/c^2]

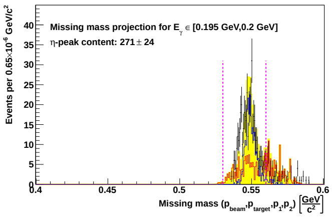
Missing mass projection for E$_\gamma$ ∈ [0.195 GeV,0.2 GeV]
η-peak content: 271 ± 24
Events per 0.65×10^{-6} GeV/c^2
0
5
10
15
20
25
30
35
40
0.4
0.45
0.5
0.55
0.6
Missing mass (p$_{beam}$,p$_{target}$,p$_1$,p$_2$) [GeV/c^2]

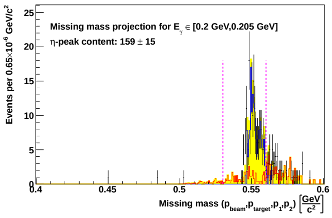
Missing mass projection for E$_\gamma$ ∈ [0.2 GeV,0.205 GeV]
η-peak content: 159 ± 15
Events per 0.65×10^{-6} GeV/c^2
0
5
10
15
20
25
0.4
0.45
0.5
0.55
0.6
Missing mass (p$_{beam}$,p$_{target}$,p$_1$,p$_2$) [GeV/c^2]

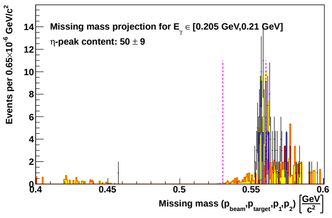
Missing mass projection for E$_\gamma$ ∈ [0.205 GeV,0.21 GeV]
η-peak content: 50 ± 9
Events per 0.65×10^{-6} GeV/c^2
0
2
4
6
8
10
12
14
0.4
0.45
0.5
0.55
0.6
Missing mass (p$_{beam}$,p$_{target}$,p$_1$,p$_2$) [GeV/c^2]

$E_\gamma[GeV]$ (in η-rest frame)	Entries [a.u.]	Stat. error [a.u.]
0.0225	−54494	17827
0.0275	−34868	8771
0.0325	−5101	6809
0.0375	29183	4645
0.0425	28772	3974
0.0475	42728	3724
0.0525	45490	3204
0.0575	55234	3111
0.0625	71674	3315
0.0675	86936	3056
0.0725	92972	3038
0.0775	110591	3295
0.0825	120456	3204
0.0875	133609	3232
0.0925	143169	3401
0.0975	152407	3365
0.1025	160190	3610
0.1075	175584	3767
0.1125	178192	3760
0.1175	179136	3801
0.1225	181874	3948
0.1275	191226	3785
0.1325	181379	3831
0.1375	176449	4129
0.1425	184653	3947
0.1475	176776	3822
0.1525	173339	3905
0.1575	148519	3525
0.1625	137880	3574
0.1675	126947	3402
0.1725	108857	2991
0.1775	84799	2962
0.1825	64242	2897
0.1875	51940	2378
0.1925	31650	1817
0.1975	14969	1570
0.2025	3450	361

Table E.1: *Central values E_γ of photon energy bins and the corresponding entries with statistical errors. The bin width is* 5 MeV.

Appendix F

Determining the pion-photon opening angle distribution

The two proton missing mass spectra corresponding to the angular bins are shown below for the analysis conditions: $P(\chi^2_{pp\to pp\pi^+\pi^-\gamma}, 4) \geq 0.2$ and $E_\gamma > \frac{2\,\mathrm{deg}\times\mathrm{GeV}}{\angle(\pi^\pm,\gamma)}$. The background of the measured data spectra (black crosses) is described in the same manner as presented in Appendix E. The corresponding fitted distributions are represented by the red coloured curves. The blue distributions are obtained from a simulation of $\eta \to \pi^+\pi^-\gamma$ events, which is used to describe the signal region of the individual missing mass spectrum. The sum of fitted signal and background is indicated by the yellow coloured area in each diagram. The remaining peak content after background subtraction is determined between the purple dashed lines and written in each diagram. The final angular distribution after all corrections is summarised in Table F.1

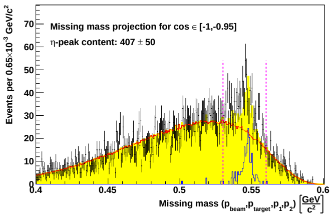

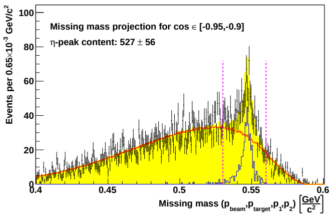

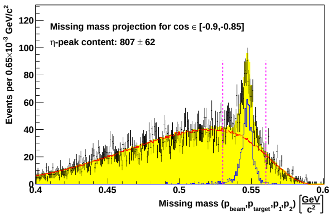

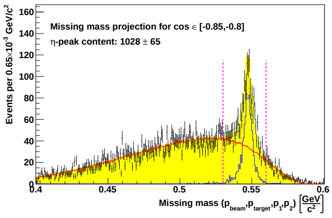

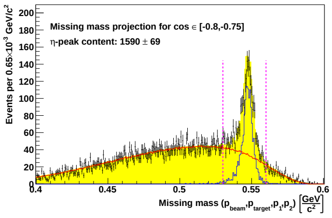

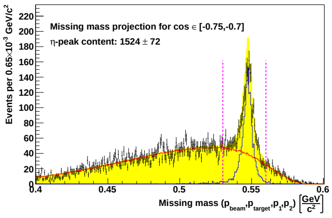

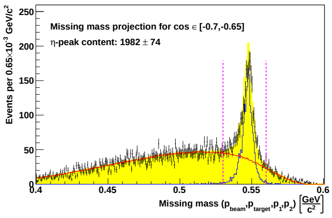

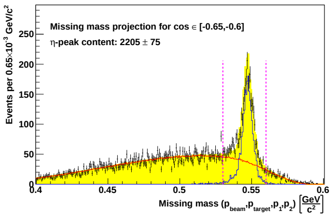

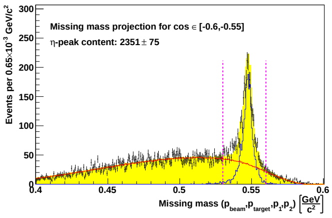

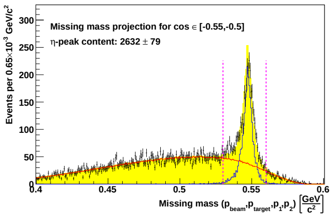
Missing mass projection for cos ∈ [-0.55,-0.5]
η-peak content: 2632 ± 79
Events per 0.65×10⁻³ GeV/c²
0
50
100
150
200
250
300
0.4
0.45
0.5
0.55
0.6
Missing mass (p_beam,p_target,p_1,p_2) [GeV/c²]

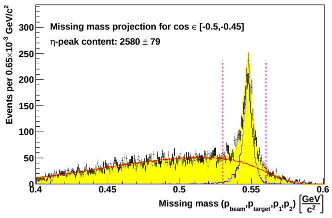
Missing mass projection for cos ∈ [-0.5,-0.45]
η-peak content: 2580 ± 79
Events per 0.65×10⁻³ GeV/c²
0
50
100
150
200
250
300
0.4
0.45
0.5
0.55
0.6
Missing mass (p_beam,p_target,p_1,p_2) [GeV/c²]

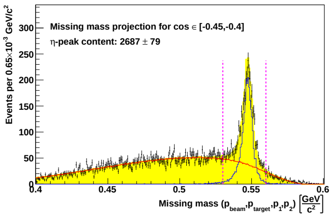
Missing mass projection for cos ∈ [-0.45,-0.4]
η-peak content: 2687 ± 79
Events per 0.65×10⁻³ GeV/c²
0
50
100
150
200
250
300
0.4
0.45
0.5
0.55
0.6
Missing mass (p_beam,p_target,p_1,p_2) [GeV/c²]

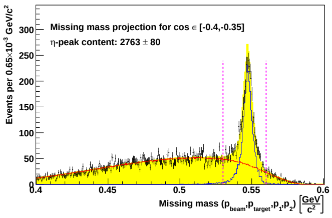
Missing mass projection for cos ∈ [-0.4,-0.35]
η-peak content: 2763 ± 80
Events per 0.65×10⁻³ GeV/c²
0
50
100
150
200
250
300
0.4
0.45
0.5
0.55
0.6
Missing mass (p_beam,p_target,p_1,p_2) [GeV/c²]

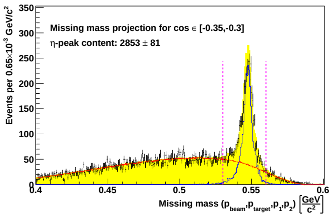
Missing mass projection for cos ∈ [-0.35,-0.3]
η-peak content: 2853 ± 81
Events per 0.65×10⁻³ GeV/c²
0
50
100
150
200
250
300
350
0.4
0.45
0.5
0.55
0.6
Missing mass (p_beam,p_target,p_1,p_2) [GeV/c²]

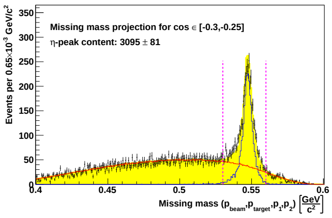
Missing mass projection for cos ∈ [-0.3,-0.25]
η-peak content: 3095 ± 81
Events per 0.65×10⁻³ GeV/c²
0
50
100
150
200
250
300
350
0.4
0.45
0.5
0.55
0.6
Missing mass (p_beam,p_target,p_1,p_2) [GeV/c²]

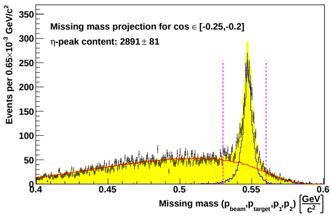
Missing mass projection for cos ∈ [-0.25,-0.2]
η-peak content: 2891 ± 81
Events per 0.65×10⁻³ GeV/c²
0
50
100
150
200
250
300
350
0.4
0.45
0.5
0.55
0.6
Missing mass (p_beam,p_target,p_1,p_2) [GeV/c²]

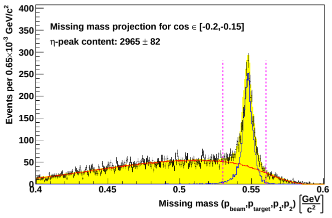
Missing mass projection for cos ∈ [-0.2,-0.15]
η-peak content: 2965 ± 82
Events per 0.65×10⁻³ GeV/c²
0
50
100
150
200
250
300
350
400
0.4
0.45
0.5
0.55
0.6
Missing mass (p_beam,p_target,p_1,p_2) [GeV/c²]

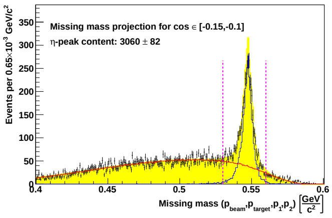
Missing mass projection for cos ∈ [-0.15,-0.1]
η-peak content: 3060 ± 82
Events per 0.65×10⁻³ GeV/c²
0
50
100
150
200
250
300
350
0.4
0.45
0.5
0.55
0.6
Missing mass (p_beam,p_target,p_1,p_2) [GeV/c²]

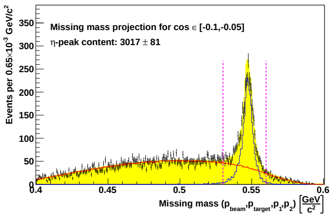
Missing mass projection for cos ∈ [-0.1,-0.05]
η-peak content: 3017 ± 81
Events per 0.65×10⁻³ GeV/c²
0
50
100
150
200
250
300
350
0.4
0.45
0.5
0.55
0.6
Missing mass (p_beam,p_target,p_1,p_2) [GeV/c²]

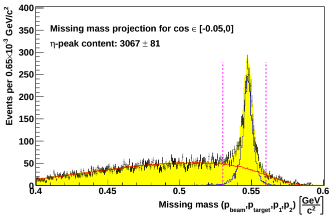
Missing mass projection for cos ∈ [-0.05,0]
η-peak content: 3067 ± 82
Events per 0.65×10⁻³ GeV/c²
0
50
100
150
200
250
300
350
400
0.4
0.45
0.5
0.55
0.6
Missing mass (p_beam,p_target,p_1,p_2) [GeV/c²]

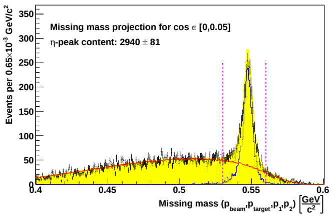
Missing mass projection for cos ∈ [0,0.05]
η-peak content: 2940 ± 81
Events per 0.65×10⁻³ GeV/c²
0
50
100
150
200
250
300
350
0.4
0.45
0.5
0.55
0.6
Missing mass (p_beam,p_target,p_1,p_2) [GeV/c²]

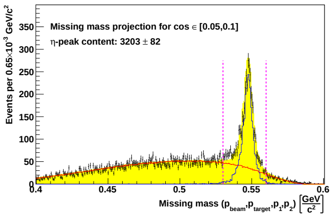
Missing mass projection for cos ∈ [0.05,0.1]
η-peak content: 3203 ± 82
Events per 0.65×10⁻³ GeV/c²
0
50
100
150
200
250
300
350
0.4
0.45
0.5
0.55
0.6
Missing mass (p_beam,p_target,p_1,p_2) [GeV/c²]

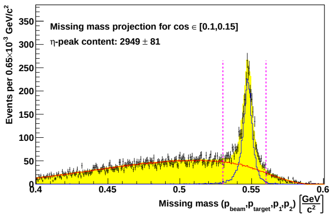
Missing mass projection for cos ∈ [0.1,0.15]
η-peak content: 2949 ± 81
Events per 0.65×10⁻³ GeV/c²
0
50
100
150
200
250
300
350
0.4
0.45
0.5
0.55
0.6
Missing mass (p_beam,p_target,p_1,p_2) [GeV/c²]

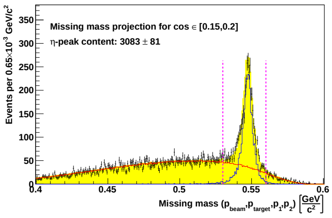
Missing mass projection for cos ∈ [0.15,0.2]
η-peak content: 3083 ± 81
Events per 0.65×10⁻³ GeV/c²
0
50
100
150
200
250
300
350
0.4
0.45
0.5
0.55
0.6
Missing mass (p_beam,p_target,p_1,p_2) [GeV/c²]

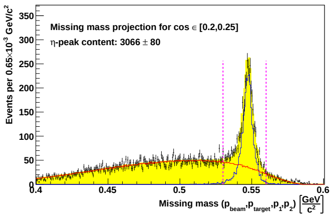
Missing mass projection for cos ∈ [0.2,0.25]
η-peak content: 3066 ± 80
Events per 0.65×10⁻³ GeV/c²
0
50
100
150
200
250
300
350
0.4
0.45
0.5
0.55
0.6
Missing mass (p_beam,p_target,p_1,p_2) [GeV/c²]

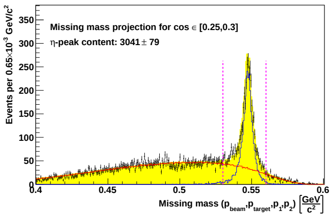
Missing mass projection for cos ∈ [0.25,0.3]
η-peak content: 3041 ± 79
Events per 0.65×10⁻³ GeV/c²
0
50
100
150
200
250
300
350
0.4
0.45
0.5
0.55
0.6
Missing mass (p_beam,p_target,p_1,p_2) [GeV/c²]

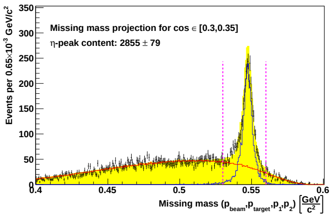
Missing mass projection for cos ∈ [0.3,0.35]
η-peak content: 2855 ± 79
Events per 0.65×10⁻³ GeV/c²
0
50
100
150
200
250
300
350
0.4
0.45
0.5
0.55
0.6
Missing mass (p_beam,p_target,p_1,p_2) [GeV/c²]

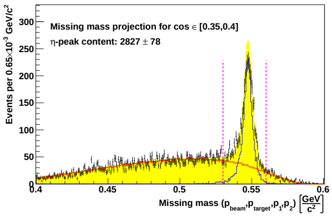
Missing mass projection for cos ∈ [0.35,0.4]
η-peak content: 2827 ± 78
Events per 0.65·10⁻³ GeV/c²
0 50 100 150 200 250 300
0.4 0.45 0.5 0.55 0.6
Missing mass (p_beam,p_target,p_1,p_2) [GeV/c²]

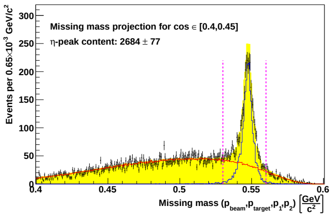
Missing mass projection for cos ∈ [0.4,0.45]
η-peak content: 2684 ± 77
Events per 0.65·10⁻³ GeV/c²
0 50 100 150 200 250 300
0.4 0.45 0.5 0.55 0.6
Missing mass (p_beam,p_target,p_1,p_2) [GeV/c²]

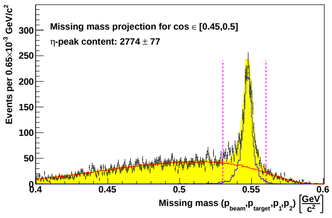
Missing mass projection for cos ∈ [0.45,0.5]
η-peak content: 2774 ± 77
Events per 0.65·10⁻³ GeV/c²
0 50 100 150 200 250 300
0.4 0.45 0.5 0.55 0.6
Missing mass (p_beam,p_target,p_1,p_2) [GeV/c²]

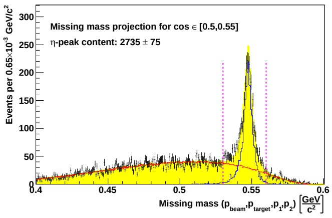
Missing mass projection for cos ∈ [0.5,0.55]
η-peak content: 2735 ± 75
Events per 0.65·10⁻³ GeV/c²
0 50 100 150 200 250 300
0.4 0.45 0.5 0.55 0.6
Missing mass (p_beam,p_target,p_1,p_2) [GeV/c²]

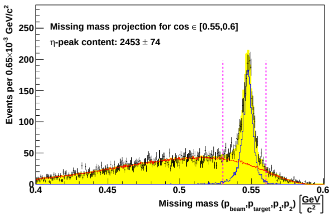
Missing mass projection for cos ∈ [0.55,0.6]
η-peak content: 2453 ± 74
Events per 0.65·10⁻³ GeV/c²
0 50 100 150 200 250
0.4 0.45 0.5 0.55 0.6
Missing mass (p_beam,p_target,p_1,p_2) [GeV/c²]

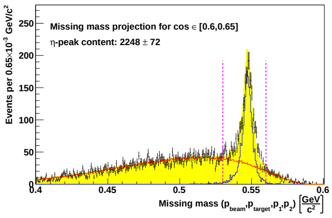
Missing mass projection for cos ∈ [0.6,0.65]
η-peak content: 2248 ± 72
Events per 0.65·10⁻³ GeV/c²
0 50 100 150 200 250
0.4 0.45 0.5 0.55 0.6
Missing mass (p_beam,p_target,p_1,p_2) [GeV/c²]

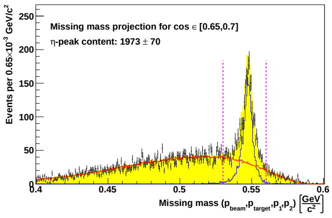
Missing mass projection for cos ∈ [0.65,0.7]
η-peak content: 1973 ± 70
Events per 0.65·10⁻³ GeV/c²
0 50 100 150 200 250
0.4 0.45 0.5 0.55 0.6
Missing mass (p_beam,p_target,p_1,p_2) [GeV/c²]

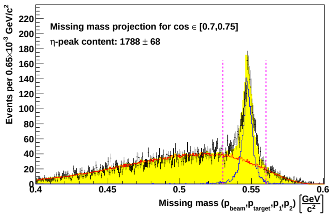
Missing mass projection for cos ∈ [0.7,0.75]
η-peak content: 1788 ± 68
Events per 0.65·10⁻³ GeV/c²
0 20 40 60 80 100 120 140 160 180 200 220
0.4 0.45 0.5 0.55 0.6
Missing mass (p_beam,p_target,p_1,p_2) [GeV/c²]

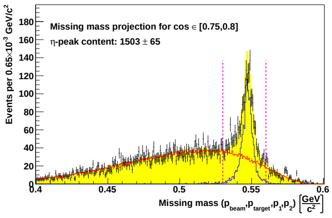
Missing mass projection for cos ∈ [0.75,0.8]
η-peak content: 1503 ± 65
Events per 0.65·10⁻³ GeV/c²
0 20 40 60 80 100 120 140 160 180
0.4 0.45 0.5 0.55 0.6
Missing mass (p_beam,p_target,p_1,p_2) [GeV/c²]

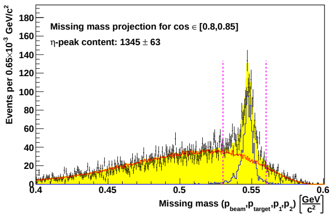
Missing mass projection for cos ∈ [0.8,0.85]
η-peak content: 1345 ± 63
Events per 0.65·10⁻³ GeV/c²
0 20 40 60 80 100 120 140 160 180
0.4 0.45 0.5 0.55 0.6
Missing mass (p_beam,p_target,p_1,p_2) [GeV/c²]

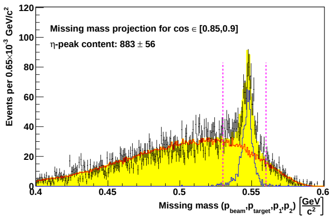
Missing mass projection for cos ∈ [0.85,0.9]
η-peak content: 883 ± 56
Events per 0.65·10⁻³ GeV/c²
0 20 40 60 80 100 120
0.4 0.45 0.5 0.55 0.6
Missing mass (p_beam,p_target,p_1,p_2) [GeV/c²]

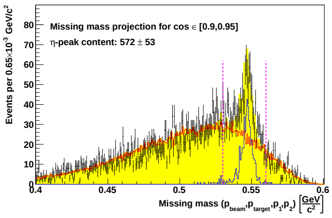
Missing mass projection for cos ∈ [0.9,0.95]
η-peak content: 572 ± 53
Events per 0.65·10⁻³ GeV/c²
0 10 20 30 40 50 60 70 80
0.4 0.45 0.5 0.55 0.6
Missing mass (p_beam,p_target,p_1,p_2) [GeV/c²]

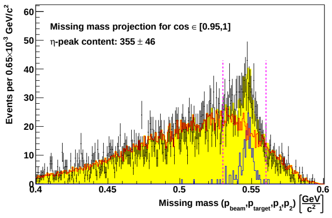
Missing mass projection for cos ∈ [0.95,1]
η-peak content: 355 ± 46
Events per 0.65·10⁻³ GeV/c²
0 10 20 30 40 50 60
0.4 0.45 0.5 0.55 0.6
Missing mass (p_beam,p_target,p_1,p_2) [GeV/c²]

$\cos[\angle(\pi^+,\gamma)]$ (in (π^+,π^-)-rest frame)	Entries [a.u.]	Stat. error [a.u.]
-0.975	20455	4959
-0.925	31706	5155
-0.875	39561	4291
-0.825	50932	4057
-0.775	67449	3553
-0.725	62628	3599
-0.675	85932	3629
-0.625	96392	3643
-0.575	103695	3684
-0.525	109173	3592
-0.475	112405	3765
-0.425	115235	3705
-0.375	121214	3754
-0.325	128858	3920
-0.275	136677	3825
-0.225	130655	3887
-0.175	131285	3863
-0.125	137239	3896
-0.075	134841	3812
-0.025	138752	3852
0.025	134697	3895
0.075	144403	3862
0.125	134869	3860
0.175	139332	3843
0.225	135146	3766
0.275	135442	3733
0.325	125932	3700
0.375	125290	3694
0.425	118439	3680
0.475	128318	3863
0.525	118919	3530
0.575	107800	3634
0.625	98503	3575
0.675	86696	3508
0.725	80104	3607
0.775	69643	3633
0.825	68104	3848
0.875	46771	4031
0.925	29657	4411
0.975	18486	4562

Table F.1: *Central values of the cosine of the pion-photon opening angle bins and the corresponding entries with statistical errors.*

Appendix G

Fitting a constant function to data points

Suppose N data points $y_1, ..., y_N$ with errors $\sigma_1, .., \sigma_N$ shall be fitted by a constant $p0$ via a least squares fit. The parameter $p0$ is found by minimising:

$$\chi^2 = \sum_{i=1}^{N} \Big(\frac{y_i - p0}{\sigma_i} \Big)^2 \tag{G.1}$$

The error $\Delta p0$ is calculated according to:

$$\chi^2 + 1 = \sum_{i=1}^{N} \Big(\frac{y_i - (p0 \pm \Delta p0)}{\sigma_i} \Big)^2 \tag{G.2}$$

which corresponds to a 1σ region for the parameter error of $p0$. Using the definitions:

$$\frac{1}{\sigma_t^2} \equiv \sum_{i=1}^{N} \frac{1}{\sigma_i^2} \tag{G.3}$$

$$m \equiv \sum_{i=1}^{N} \frac{y_i - p0}{\sigma_i^2} \tag{G.4}$$

and solving Eq. G.2 with respect to $\Delta p0$ leads to:

$$\Delta p0 = \mp \sigma_t^2 m \pm \sqrt{(\sigma_t^2 m)^2 + \sigma_t^2} \tag{G.5}$$

Fitting a constant to any distribution of data points will lead, by construction of the least squares minimisation technique, to $m \approx 0$. Thus, the parameter error $\Delta p0$ is dominated by the errors σ_i of the data points y_i, which allows for the approximation:

$$\Delta p0 \approx \pm \sigma_t = \pm \Big[\sum_{i=1}^{N} \frac{1}{\sigma_i^2} \Big]^{-0.5} \tag{G.6}$$

In case that all N data points have the same error $\sigma \equiv \sigma_i = const.$ leads to the simplified relation:

$$\Delta p0 \approx \pm \frac{\sigma}{\sqrt{N}} \tag{G.7}$$

A fit hypothesis is considered to be accepted, if all data points agree within σ_i with the proposed model. This leads to $\langle \chi^2 \rangle = \text{ndf}$ and $Var(\chi^2) = 2 \cdot \text{ndf}$, where ndf denotes the number of degrees of freedom. Hence, a fitted function is supposed to describe the data set, if $\frac{\chi^2}{\text{ndf}} \sim 1$. In the following, two extreme cases that are related to fitting a constant function via Eq. G.1 to a set of data points, shall be discussed:

Case 1: The data points y_i do not follow the expected pattern within σ_i at all (i.e. $(y_i - p0) >> \sigma_i$). This leads to $\chi^2 >>$ ndf. According to that and Eq. G.6, the discrepancy between y_i and $p0$ is underestimated by the returned error $\Delta p0$.

Case 2: The difference $y_i - p0$ is much smaller than σ_i, which causes $\chi^2 <<$ ndf. In this case, the fluctuations between y_i and $p0$ are overestimated by $\Delta p0$.

Assuming that the χ^2 values returned by the least squares fit are distributed normally around ndf with $\sigma = Var(\chi^2) = \sqrt{2\ \mathrm{ndf}}$, allows for a very rough estimate, whether one of the two cases is applicable or not. A definition related to that issue might be:

$$k \equiv \left| \frac{\chi^2 - \mathrm{ndf}}{\sqrt{2\ \mathrm{ndf}}} \right| \tag{G.8}$$

where k corresponds to the distance $k\sigma$ between the mean value ndf and χ^2, within a normal distribution. Depending on the value of k, a quantitative judgement of the obtained χ^2 could be done. However, Eq. G.8 allows no absolute judgement of a fit procedure. Fitting is and will always be a matter, where all available information have to be taken into account. The equations listed here are only a help for evaluating a fit procedure and therefore should be used with caution.

Appendix H

Systematic studies for $\frac{\Gamma(\eta\rightarrow\pi^+\pi^-\gamma)}{\Gamma(\eta\rightarrow\pi^+\pi^-\pi^0)}$, α and β

The variation of $\frac{\Gamma(\eta\rightarrow\pi^+\pi^-\gamma)}{\Gamma(\eta\rightarrow\pi^+\pi^-\pi^0)}$, α and β with respect to different analysis or experimental conditions are listed in the following sections. The error Δ_{stat} represents the statistical error of $\frac{\Gamma(\eta\rightarrow\pi^+\pi^-\gamma)}{\Gamma(\eta\rightarrow\pi^+\pi^-\pi^0)}$, whereas the errors $\Delta\alpha$ / $\Delta\beta$ of α / β are deduced from fitting Eq. 2.29 / Eq. 2.34 to the E_γ- / opening angle distributions, respectively. The selection of a π^0-candidate for the reconstruction of $\eta \rightarrow \pi^+\pi^-\pi^0$ events is fixed to $0.09\,\mathrm{GeV/c^2} \leq$ Invariant mass $(\gamma_1, \gamma_2) < 0.2\,\mathrm{GeV/c^2}$ for all systematic studies, that are presented in the following.

H.1 Varying the kinematic fit probability

The selection of the minimum kinematic fit probabilities $P(\chi^2_{pp\rightarrow pp\pi^+\pi^-\gamma}, 4)$ and $P(\chi^2_{pp\rightarrow pp\pi^+\pi^-\gamma\gamma}, 4)$ is varied in steps of 0.1 and the split-off rejection condition is fixed by: $E_\gamma > \frac{2\,\mathrm{deg}\times\mathrm{GeV}}{\angle(\pi^\pm,\gamma)}$. As discussed in Chapter 6, the minimum fit probabilities are increased in steps of 0.05 for studying systematic effects of the kinematic fit on the relative branching ratio. The intermediate probability steps 0.05, 0.15, 0.25,..., etc. for the relative branching ratio are not listed in Tables H.1 and H.2.

$P(\chi^2_{pp\rightarrow pp\pi^+\pi^-\gamma}, 4)$	≥ 0.1	≥ 0.2	≥ 0.3	≥ 0.4	≥ 0.5	≥ 0.6	≥ 0.7	≥ 0.8	≥ 0.9
$\frac{\Gamma(\eta\rightarrow\pi^+\pi^-\gamma)}{\Gamma(\eta\rightarrow\pi^+\pi^-\pi^0)}$	0.201	0.197	0.192	0.190	0.190	0.192	0.194	0.194	0.191
$\pm\Delta_{stat}$	0.001	0.001	0.002	0.002	0.002	0.002	0.002	0.003	0.004
α [GeV^{-2}]	0.286	0.229	0.189	0.314	0.313	0.202	0.403	0.431	0.378
$\pm\Delta\alpha_{fit}$ [GeV^{-2}]	0.152	0.153	0.155	0.165	0.172	0.173	0.197	0.221	0.282
β	0.357	0.350	0.330	0.328	0.353	0.340	0.403	0.412	0.395
$\pm\Delta\beta_{fit}$	0.053	0.054	0.056	0.059	0.062	0.066	0.075	0.087	0.114

Table H.1: *Values of* $\frac{\Gamma(\eta\rightarrow\pi^+\pi^-\gamma)}{\Gamma(\eta\rightarrow\pi^+\pi^-\pi^0)}$, *$\alpha$ and β obtained for choosing different kinematic fit probabilities* $P(\chi^2_{pp\rightarrow pp\pi^+\pi^-\gamma}, 4)$.

$P(\chi^2_{pp\to pp\pi^+\pi^-\gamma\gamma}, 4)$	≥ 0.1	≥ 0.2	≥ 0.3	≥ 0.4	≥ 0.5	≥ 0.6	≥ 0.7	≥ 0.8	≥ 0.9
$\frac{\Gamma(\eta\to\pi^+\pi^-\gamma)}{\Gamma(\eta\to\pi^+\pi^-\pi^0)}$ $\pm\Delta_{stat}$	0.200 0.001	0.197 0.001	0.196 0.002	0.194 0.002	0.190 0.002	0.187 0.002	0.183 0.002	0.180 0.002	0.174 0.002
α [GeV^{-2}] $\pm\Delta\alpha_{fit}$ [GeV^{-2}]	0.234 0.153	0.229 0.153	0.240 0.154	0.233 0.153	0.248 0.154	0.252 0.154	0.266 0.155	0.275 0.156	0.280 0.157
β $\pm\Delta\beta_{fit}$	0.350 0.054	0.350 0.054	0.348 0.054	0.341 0.054	0.340 0.054	0.337 0.054	0.348 0.055	0.328 0.055	0.315 0.054

Table H.2: *Values of* $\frac{\Gamma(\eta\to\pi^+\pi^-\gamma)}{\Gamma(\eta\to\pi^+\pi^-\pi^0)}$, α *and* β *obtained for choosing different kinematic fit probabilities* $P(\chi^2_{pp\to pp\pi^+\pi^-\gamma\gamma}, 4)$.

H.2 Varying the split-off rejection parameter *A*

The minimum kinematic fit probabilities are fixed to: $P(\chi^2_{pp\to pp\pi^+\pi^-\gamma}, 4) \geq 0.2$ and $P(\chi^2_{pp\to pp\pi^+\pi^-\gamma\gamma}, 4) \geq 0.2$. The split-off rejection parameter A is increased from 1 deg × GeV to 6 deg × GeV in steps of 1 deg × GeV. Values of A larger than 4 deg × GeV are not considered for the estimation of the systematic error (see Chapter 6).

A [deg × GeV]	$= 1$	$= 2$	$= 3$	$= 4$	$= 5$	$= 6$
$\frac{\Gamma(\eta\to\pi^+\pi^-\gamma)}{\Gamma(\eta\to\pi^+\pi^-\pi^0)}$ $\pm\Delta_{stat}$	0.218 0.002	0.197 0.001	0.188 0.001	0.183 0.001	0.178 0.001	0.172 0.001
α [GeV^{-2}] $\pm\Delta\alpha$ [GeV^{-2}]	0.399 0.164	0.229 0.153	0.034 0.145	-0.091 0.144	-0.189 0.144	-0.337 0.144
β $\pm\Delta\beta$	0.411 0.071	0.350 0.054	0.291 0.050	0.214 0.049	0.140 0.049	0.048 0.050

Table H.3: *Values of* $\frac{\Gamma(\eta\to\pi^+\pi^-\gamma)}{\Gamma(\eta\to\pi^+\pi^-\pi^0)}$, α *and* β *obtained for different split-off rejection conditions* $E_\gamma > \frac{A}{\angle(\pi^\pm,\gamma)}$.

H.3 Varying the luminosity range

The analysis conditions are fixed to $P(\chi^2_{pp\to pp\pi^+\pi^-\gamma}, 4) \geq 0.2$, $P(\chi^2_{pp\to pp\pi^+\pi^-\gamma\gamma}, 4) \geq 0.2$ and $E_\gamma > \frac{2\,\mathrm{deg}\times\mathrm{GeV}}{\angle(\pi^\pm,\gamma)}$ within this study. The luminosity ranges are varied according to Table H.4 and H.5.

$\frac{\text{Trigger 17 rate}}{\text{Pellet rate}}$	$[0, 10]$	$[10, 20]$	$[20, 30]$	$[30, 40]$	$[40, 50]$	$[50, 60]$
$\frac{\Gamma(\eta\to\pi^+\pi^-\gamma)}{\Gamma(\eta\to\pi^+\pi^-\pi^0)}$ $\pm\Delta_{stat}$	0.195 0.012	0.191 0.005	0.193 0.003	0.189 0.002	0.193 0.002	0.190 0.003
$\frac{\text{Trigger 17 rate}}{\text{Pellet rate}}$	$[60, 70]$	$[70, 80]$	$[80, 90]$	$[90, 100]$	$[100, 110]$	$[110, 120]$
$\frac{\Gamma(\eta\to\pi^+\pi^-\gamma)}{\Gamma(\eta\to\pi^+\pi^-\pi^0)}$ $\pm\Delta_{stat}$	0.190 0.006	0.199 0.011	0.204 0.013	0.213 0.015	0.189 0.017	0.227 0.032

Table H.4: *Relative branching ratio* $\frac{\Gamma(\eta\to\pi^+\pi^-\gamma)}{\Gamma(\eta\to\pi^+\pi^-\pi^0)}$ *obtained for different luminosity ranges expressed as the ratio* $\frac{\textit{Trigger 17 rate}}{\textit{Pellet rate}}$.

$\frac{\text{Trigger 17 rate}}{\text{Pellet rate}}$	$[0, 30]$	$[30, 60]$	$[60, 120]$
α [GeV^{-2}] $\pm\Delta\alpha$ [GeV^{-2}]	0.364 0.222	0.083 0.155	0.479 0.336
β $\pm\Delta\beta$	0.446 0.091	0.332 0.060	0.420 0.149

Table H.5: α *and* β *values obtained for different luminosity ranges expressed as the ratio* $\frac{\textit{Trigger 17 rate}}{\textit{Pellet rate}}$.

H.4 Varying the signal peak integration

The analysis conditions are the same as presented in the previous section and no specific luminosity range is chosen. A description of the different scenarios can be found in Section 6.6.4.

Scenario	1	2	3	4
$\frac{\Gamma(\eta\to\pi^+\pi^-\gamma)}{\Gamma(\eta\to\pi^+\pi^-\pi^0)}$ $\pm\Delta_{stat}$	0.203 0.002	0.197 0.001	0.192 0.002	0.193 0.002
α [GeV^{-2}] $\pm\Delta\alpha$ [GeV^{-2}]	-0.126 0.146	0.114 0.148	0.282 0.183	0.431 0.233
β $\pm\Delta\beta$	0.211 0.056	0.468 0.054	0.199 0.084	0.206 0.097

Table H.6: *Values of* $\frac{\Gamma(\eta\to\pi^+\pi^-\gamma)}{\Gamma(\eta\to\pi^+\pi^-\pi^0)}$*,* α *and* β *obtained for different scenarios of determining the* η *signal peak content after background subtraction.*

Appendix I

List of acronyms

CLEO Particle detector used at the Cornell Electron Storage Ring (CESR)

KLOE K LOng Experiment

WASA Wide Angle Shower Apparatus

QCD Quantum Chromodynamics

QED Quantum Electrodynamics

ChPT Chiral Pertubation Theory

EFT Effective Field Theories

VMD Vector Meson Dominance

HLS Hidden Local Symmetries

PDG Particle Data Group

CAD Computer-Aided Design

COSY COoler SYnchrotron accelerator

ANKE Apparatus for Studies of Nucleon and Kaon Ejectiles

PAX Polarized Antiproton eXperiments

FD Forward Detector

FRH Forward Range Hodoscope

FPC Forward Proportional Chamber

FTH Forward Trigger Hodoscope

CD Central Detector

MDC Mini Drift Chamber

PSB Plastic Scintillator Barrel

SEC Scintillator Electromagnetic Calorimeter

SQDC Slow Charge-to-Digital Converter

QDC Charge-to-Digital Converter

ADC Analogue-to-Digital Converter

TDC Time-to-Digital Converter

CERN European centre of nuclear physics research

HADES High Acceptance Di-Electron Spectrometer

WMC WASA Monte Carlo

GEANT GEometry ANd Tracking

MC Monte Carlo

Bibliography

[1] B. R. Holstein. Allowed Eta-Decay Modes and Chiral Symmetry. *Phys. Scripta*, T99:55–67, 2002.

[2] M. Benayoun, P. David, L. DelBuono, Ph. Leruste, and H.B. O'Connel. Anomalous η/η' Decays: The Triangle and Box Anomalies. *European Physics Journal*, C31:525–547, 2003.

[3] J. Bijnens, A. Bramon, and Fernando Cornet. Three-Pseudoscalar Photon Interactions in Chiral Pertubation Theory. *Physics Letters*, B237(3,4):488–494, 1990.

[4] F. Stollenwerk, C. Hanhart, A. Kupsc, U.-G.Meißner, and A.Wirzba. Model-independent approach to $\eta \to \pi^+\pi^-\gamma$ and $\eta' \to \pi^+\pi^-\gamma$. *Physics Letters*, B707:184–190, 2012.

[5] The CLEO collaboration. Measurement of prominent η decay branching fractions. *Physics Review Letters*, 99(122001), 2007.

[6] The KLOE collaboration. $\Gamma(\eta \to \pi^+\pi^-\gamma)/\Gamma(\eta \to \pi^+\pi^-\pi^0)$ with the KLOE detector. *Physics Letters*, B718:910–914, 2013.

[7] The WASA-at-COSY collaboration. Exclusive Measurement of the $\eta \to \pi^+\pi^-\gamma$ Decay. *Physics Letters*, B707:243–249, 2012.

[8] Image Credit: Miss MJ. Wikipedia [online]. September 2014 [cited October 2014]. Available from World Wide Web: `http://en.wikipedia.org/wiki/Standard_Model`.

[9] S. Scherer and M. R. Schindler. *A Primer for Chiral Pertubation Theory*, volume 830 of *Lecture Notes in Physics*. Springer, 2012. Available from World Wide Web: `http://www.springer.com/series/5304`.

[10] K. A. Olive et al. (Particle Data Group). Review of Particle Pshysics. *Chin. Phys.*, C38(090001), 2014.

[11] Trassiorf. Premier octet de mésons [online, cited February 2014]. Available from World Wide Web: `http://upload.wikimedia.org/wikipedia/commons/e/e0/Meson-octet.svg`.

[12] A. Bramon, R. Escribano, and M. D. Scadron. The η-η' mixing angle revisited. *Eur. Phys. J.*, C7:271–278, 1999.

[13] C. Berger. *Elementarteilchenphysik*, volume 2. Springer-Verlag, 2006. Available from World Wide Web: `http://www.springer.de`.

[14] P. Adlarson. *Studies of the Decay* $\eta \to \pi^+\pi^-\pi^0$ *with WASA-at-COSY*. PhD thesis, Uppsala University, 2012.

[15] J. Wess and B. Zumino. Consequences of anomalous ward identities. *Physics Letters*, B37(1), 1971.

[16] E. Witten. Global aspects of current algebra. *Nuclear Physics*, B223:422–432, 1983.

[17] L.G. Landsberg. Electromagnetic Decays of Light Mesons. *Phyiscs Reports*, 128(6):301–376, 1985.

[18] D. Coderre. *The Branching Ratio and CP-Violating Asymmetry of* $\eta \to \pi^+\pi^-e^+e^-$. PhD thesis, Ruhr-Universität-Bochum, 2012.

[19] M. Gormley, E.Hyman, Won-Lee, T. Nash, J. Peoples, C. Schultz, and S. Stein. Experimental determination of the dalitz-plot distribution of the decays $\eta \to \pi^+\pi^-\pi^0$ and $\eta \to \pi^+\pi^-\gamma$, and the branching ratio $\eta \to \pi^+\pi^-\gamma/\eta \to \pi^+\pi^-\pi^0$. *Physics Review*, D2:501–505, 1970.

[20] J. J. Thaler, J. A. Appel, A. Kotlewski, J. G. Layter, W.-Y. Lee, and S. Stein. Relative decay rates of $\eta \to \pi^+\pi^-\pi^0$,$\eta \to \pi^+\pi^-\gamma$, $\eta \to \pi^+\pi^-\pi^0\gamma$ and $\eta \to \pi^+\pi^-$. *Physics Review*, D7:2569–2571, 1973.

[21] J. G. Layter, J. A. Appel, A. Kotlewski, W.-Y. Lee, S. Stein, and J. J. Thaler. Study of the dalitz-plot distributions of the decays $\eta \to \pi^+\pi^-\pi^0$ and $\eta \to \pi^+\pi^-\gamma$. *Physics Review*, D7:2565–2568, 1973.

[22] The GAMS-200 collaboration. Study of the radiative decay $\eta' \to \pi^+\pi^-\gamma$. *Z. Phys.*, C50:451–454, 1991.

[23] The CRYSTAL BARREL collaboration. Measurement of the Decay Distribution for η' to $\pi^+\pi^-\gamma$ and Evidence for the box anomaly. *Physics Letters*, B(402):195, 1997.

[24] J. J. Thaler, J. A. Appel, A. Kotlewski, J. G. Layter, W.-Y. Lee, and S. Stein. Charge Asymmetry in the Decay $\eta \to \pi^+\pi^-\gamma$. *Physics Review Letters*, 29(5):313–316, 1972.

[25] M. R. Jane, B. D. Jones, N. H. Lipman, D. P. Owen, B. K. Penney, T. G. Walker, M. Gettner, P. Grannis, and H. Uto. A measurement of the charge asymmetry in the decay $\eta \to \pi^+\pi^-\gamma$. *Physics Letters*, B48:265–268, 1974.

[26] C. F. Redmer. *In search of the Box-Anomaly with the WASA facility at COSY*. PhD thesis, Bergische Universität Wuppertal, March 2010.

[27] D. Prasuhn, J. Dietrich, R. Maier, R. Stassen, H. J. Stein, and H. Stockhorst. Electron and stochastic cooling at COSY. *Nuclear Instruments and Methods in Physics Research*, A 441:167–174, 2000.

[28] H. J. Stein, D. Prasuhn, H. Stockhorst, J. Dietrich, K. Fan, V. Kamerdjiev, R. Maier, I. N. Meshkov, A. Sidorin, and V. V. Parkhomchuk. Present Performance of Electron Cooling at COSY-Jülich. In *18th Conference on Charged Particle Accelerators (RUPAC 2002)*, pages 220–226, 2004. Available from World Wide Web: `http://arxiv.org/pdf/1101.5963.pdf`.

[29] H. Stockhorst, R. Stassen, D. Prasuhn, R. Maier, T. Katayama, and L. Thorndahl. Compensation of mean energy loss due to an internal target by application of a barrier bucker and stochastic momentum cooling at cosy. In *Proceedings of COOL*, Lanzhou, China, 2009.

[30] B. Höistad and J. Ritman. Proposal for the Wide Angle Shower Apparatus (WASA) at COSY-Jülich "WASA at COSY". Technical report, Forschungszentrum Jülich, October 2004.

[31] Curt Ekström and The CELSIUS/WASA Collaboration. The CELSIUS/WASA Pellet Target System. *Phys. Scripta T99*, pages 169–172, 2002.

[32] A. Pricking. *Double Pionic Fusion to* ^{4}He*, Kinematically Complete Measurements over the Energy Region of the ABC Effect.* PhD thesis, Eberhard Karls Universität Tübingen, 2010.

[33] J. Marek. *Measurement of the Reaction* $pp \rightarrow pp\pi^+\pi^-\pi^0$ *with CELSIUS/WASA at* 1.36 GeV. PhD thesis, Uppsala University, 2006.

[34] L. Yurev. Performance of the MDC - central part of wasa - before installation at cosy. Master's thesis, Voronezh State University, 2006.

[35] M. Komogorov, B. Morosov, A. Povtorejko, and V. Tikhomirov. Track recognition algorithm for WASA Mini Drift Chamber (MDC). Technical report, WASA collaboration, 1997.

[36] The CELSIUS/WASA Collaboration. The WASA Detector Facility at CELSIUS. *Nucl. Inst. Meth. in Phys. Res. A 594*, pages 339–350, 2008.

[37] P. N. Vlasov. *Analysis of the* $\eta \rightarrow 3\pi^0$ *decay in the pp interaction.* PhD thesis, Ruhr-Universität-Bochum, September 2008.

[38] V. Hejny. Software:calorimeter calibration [online]. June 2010 [cited March 2014]. Available from World Wide Web: `http://wasasrv.ikp.kfa-juelich.de/WasaWiki/index.php/Software:Calorimeter_calibration`.

[39] Energy calibration of the wasa calorimeter. Private discussion with V. Hejny, March 2011.

[40] The CBELSA/TAPS Collaboration. In-medium ω mass from the $\gamma + Nb \rightarrow \pi^0\gamma + X$ reaction. *Physics Review*, C82:035209, 2010.

[41] H. Kleines, K. Zwoll, P. Wüstner, W. Erven, P. Kämmerling, G. Kemmerling, H. Loenvenich, A. Ackens, M. Wolke, V. Hejny, H. Ohm, T. Sefzick, R. Nellen, P. Marciniewski, K. Fransson, L. Gustafsson, A. Kupsc, and H. Calen. Performance Issues of the New DAQ System for WASA at COSY. *15th IEEE-NPSS, Real-Time Conference*, pages 1–4, April/March 2007.

[42] H. Kleines, W. Erven, P. Wüstner, A. Ackens, G. Kemmerling, M. Wolke, and K. Zwoll. Developement of a High Reoslution TDC Module for the WASA Detector System Based on the GPX ASIC. *IEEE Nuclear Science Symposium Conference Record*, 2:1005–1007, October/November 2006.

[43] K. Fransson. The Trigger System of the CELSIUS/WASA Detector. *Physics Scripta*, T99:176–182, 2002.

[44] V. Hejny, M. Hartmann, and A. Mussgiller. Rootsorter: A New Analysis Framework for ANKE. Forschungszentrum Jülich Annual Report 2002.

[45] R. Brun and F. Rademakers. ROOT - An Object Oriented Data Analysis Framework. *Nucl. Inst. Meth. in Phys. Res.*, A389:81–86, 1997.

[46] I. Froehlich, L. Cazon Boado, T. Galatyuk, V. Hejny, R. Holmann, M. Kagarlis, W. Kuehn, J. G. Messchendorp, V. Metag, M. A. Pleier, W. Pryzgoda, B. Ramstein, J. Ritman, P. Salabura, J. Stroth, and M. Sudol. Pluto: A Monte Carlo Simulation Tool for Hadron Physics. *PoS*, ACAT2007:076, 2007.

[47] CERN Application Software Group Computin and Network Division. GEANT Detector Description and Simulation Tool. Cern program library long writeup w5013, CERN, 1993.

[48] R. Bilger, W. Brodowski, H. Calén, H. Clement, C. Ekström, G. Fäldt, K. Fransson, L. Gustafsson, B. Höistad, A. Johansson, T. Johansson, K. Kilian, S. Kullander, A. Kupsc, G. Kurz, P. Marciniewski, B. Morosov, A. Mörtsell, W. Oelert, V. Renken, R. J. M. Y. Ruber, B. Shwartz, J. Stepaniak, A. Sukhanov, P. Thörngren-Engblom, A. Turowiecki, G. J. Wagner, Z. Wilhelmi, C. Wilkin, J. Zabierowski, and J. Złomańczuk. Measurement of the $pd \rightarrow {}^3\mathrm{He}\eta$ cross section between 930 and 1100 MeV. *Physics Review*, C65(044608), 2002.

[49] The CELSIUS/WASA Collaboration. The $pp \rightarrow pp\pi\pi$ reaction channels in the threshold region. *Physics Letters*, B649:122–127, 2007.

[50] M. Bashkanov, D. Bogoslawsky, H. Calén, F. Cappellaro, H. Clement, L. Demiroers, C. Ekström, K. Fransson, J. Greiff, L. Gustafsson, B. Höistad, G. Ivanov, M. Jacewicz, E. Jiganov, T. Johansson, O. Khakimova, M. M. Kaskulov, S. Keleta, I. Koch, F. Kren, S. Kullander, A. Kupść, A. Kuznetsov, P. Marciniewski, R. Meier, B. Morosov, W. Oelert, C. Pauly, Y. Petukho, A. Povtorejko, R. J. M. Y. Ruber, W. Scobel, T. Skorodko, B. Shwartz, V. Sopov, J. Stepaniak, V. Tchernyshev, P. Thörngren-Engblom, V. Tikhomirov, A. Turowiecki, G. J. Wagner, M. Wolke, A. Yamamoto, J. Zabierowski, and J. Zlomanczuk. Exclusive measurements of $pd \rightarrow {}^3\mathrm{He}\pi\pi$: The ABC effect revisited. *Physics Letters*, B637:223–228, 2006.

[51] S. Zakharian, P. Ladewig-Riebler, and S. Thoer. *Neuronale Netze für Ingenieure.* Vieweg, 1998.

[52] R.M. Hristev. *The ANN Book.* R. M. Hristev, 1998.

[53] A. Hoecker, P. Speckmayer, J. Stelzer, J. Therhaag, E. von Toerne, and H. Voss. *TMVA 4 Toolkit for Multivariate Data Analysis with ROOT Users Guide.* CERN, November 2009.

[54] D. Stefan and T. Wąchała. Application of Neural Networks to Simulated Data for Liquid Argon TPC'S. *ACTA Physica Polonica*, B37(7):2187–2195, 2006.

[55] A. Kupsc. Note on kinematical fit (vers. 2.0). Proposal for kinematic fitting procedure in WASA, November 1995.

[56] B. P. Roe, H.-J. Yang, J. Zhu, Y. Liu, I. Stancu, and G. McGregor. Boosted decision trees as an alternative to artificial neural networks for particle identification. *Nucl. Inst. Meth. in Phys. Res. A 543*, pages 577–584, 2005.

Acknowledgements

Finally, I would like to thank all people who supported me and made it possible to write this thesis. I would like to thank in particular:

- My supervisor Dr. Frank Goldenbaum for his support and the friendly atmosphere during our various discussions.
- Prof. James Ritman for making it possible for me to write this thesis at the Forschungszentrum Jülich, for his helpful advices and for the critical reading of my thesis.
- Dr. Susan Schadmand for helping me to keep on track with my thesis.
- Dr. Volker Hejny and Dr. Andrzej Kupsc for the vivid and helpful discussions during the various FIKA-meetings, for answering all my questions and especially for preventing me from following all my (sometimes silly) ideas.
- Dr. Andreas Wirzba for answering all questions related to theory and reading the theory chapter of this thesis.
- Dr. Christoph Florian Redmer, who analysed this channel in $pd \to {}^{3}\mathrm{He}\eta[\eta \to \pi^{+}\pi^{-}\gamma]$ and answered all my questions about the whole world of WASA and the decay $\eta \to \pi^{+}\pi^{-}\gamma$. If each of my questions was charged with 1 Euro, he would own a private detector by now.
- The whole WASA-at-COSY group for the fruitful discussions during the FIKA-meetings and for the nice collaboration meetings. I would especially like to thank Farha Khan for being a good friend, office mate and supporting me (also with delicious Indian food). I also would like to thank Dr. Patrick Wurm, Siddesh Sawant and Kay Demmich for the various helpful discussions about data analysis. Many thanks to Dr. Daniel Coderre for being such a good friend and the funny discussions we had.
- All members of IKP1 for the friendly atmosphere and the various seminar talks. Special thanks to: Ludovico Bianchi, Lu, Cao, Dariusch Deermann, Rene Dosdall, Ilhan Engin, Dr. Simone Esch, Dr. Albrecht Gillitzer, Andre Goerres, Dr. Florian Hauenstein, Qiang Hu, Sedigheh Jowzaee, Dr. Elisabetta Prencipe, Dr. Matthias Röder, Guenther Sterzenbach, Dr. Tobias Stockmanns, Dr. Huagen Xu and Maria Zurek for the nice time during lunch and other occasions and for the funny and interesting PhD-seminar talks.
- My former colleagues from IKP-Cologne: Dr. Bendikt Birkenbach, Dr. Kerstin Geibel, Dr. Herbert Hess, Dr. Tanja Kotthaus, Dr. Michael and Marijke Seidlitz, Burkhard Siebeck, Dr. Andreas Wendt and Dr. Andreas Wiens.
- All Cologne breweries for their unlimited support with Kölsch.

- My Kendo-fellows: Falko Brögger, Dr. Dominik Christ, Prof. Ulrich Deiters, Sonja Hülsebus, Florian Schulz, Hak-Seung Shin, Mitsuhiro Takamura, all remaining members of the Kendo-Dojo Cologne and of course my arch-enemy Dr. Evertz. Many thanks for the training, the Kan-Geikos and the large amount of Ji-Geikos and Kölsch.

- My Kendo Sensei Roland Niewerth for teaching me and sharing all his inspiring and funny stories.

- My close friends: Alkiviadis Baviolis, Lukas Fink, Bernd Körperich and Alexander Stolz for their strong support and the great time we spent together. Thank you guys!

- My deceased physics teacher Dr. Wilfried Zeiske for being a generous and great mentor.

- My parents for their unlimited love, the never ending support and their patience.

- My younger brother Oliver, who is in some cases much more grown up than I am.

- Friederike for her never ending love and support. I love you!

Erklärung

Ich versichere, die Arbeit selbständig verfasst zu haben, nur die in der Dissertation angegebenen Hilfsmittel benutzt und alle wörtlich oder inhaltlich übernommenen Stellen als solche gekennzeichnet zu haben, und dass die Dissertation in der gegenwärtigen oder einer anderen Fassung noch keinem anderen Fachbereich, keiner Gesamthoch-schule und keiner anderen wissenschaftlichen Hochschule vorgelegen hat.